Synthesis and Phase Evolution of Evaporated Lead Halide Perovskites for Solar Cells:
From *in situ* Analysis to Optoelectronic Properties

Dissertation

zur Erlangung des Doktorgrades der Naturwissenschaften
(Dr. rer. nat.)

der Naturwissenschaftlichen Fakultät II
der Martin-Luther-Universität Halle-Wittenberg

vorgelegt von

Karl Lukas Heinze

Eingereicht am 6. Februar 2024

1. Gutachter: Prof. Dr. Roland Scheer
2. Gutachter: Prof. Dr. Michael Saliba
3. Gutachter: Dr. Paul Pistor

Verteidigt am 23. Oktober 2024

0.1 Abstract

Metal halide perovskites (MHPs) make up a class of materials that have the potential to revolutionize thin film industry. MHPs for perovskite solar cells (PSCs) such as $MAPbI_3$, $FAPbI_3$ or $CsPbI_3$ have high absorptivity due to direct band gaps in the visible region, exhibit high charge carrier mobilities and high defect tolerance. However, research on PSCs strongly focuses on solution-based techniques. Even though thermal evaporation has demonstrated high efficiencies and up-scaling potential it is largely disregarded. Accordingly, a knowledge gap exists between solution-based preparation and properties of perovskite thin films prepared by these techniques and their counterparts prepared via thermal evaporation. For example, the fundamentals of the interplay between variable preparation conditions and processing schemes during thermal evaporation and their impact on film properties have hardly been explored, yet.

Thus, this thesis contributes four peer-reviewed publications on thermal evaporation of MHPs unraveling fundamental insight into the limiting boundaries and prospects of this deposition approach. The use of an *in situ* X-ray diffraction (XRD) setup enables the analysis of the crystal phase evolution during evaporation and annealing processes. This way, the initial nucleation, the evolution of secondary phases and the stoichiometry- and diffusion-limited boundaries for single-phase perovskite growth are explored for the first time and correlated to film properties and device performance.

In [H1], the impact of varying process schemes and conditions on the film formation of $MAPbI_3$ absorbers and the performance of the resulting PSCs is investigated. Flux variations are used to produce seed layers and stoichiometry variations in the perovskite bulk for PSCs in the standard *n-i-p* structure. With the *in situ* XRD, we are able to evaluate the initial nucleation and the development of secondary phases such as PbI_2 and relate these to improvements in device performance.

As a follow-up work, [H2] aims to transfer the results obtained in [H1] to the requirements of PSCs in the inverted *p-i-n* architecture. The comparison between *n-i-p* and *p-i-n* devices can be utilized to separate the influence of varying processing conditions on the initial film formation and bulk growth from interfacial effects occurring at the interfaces to the charge contact layers. In [H2], the impact of different novel dynamic processing schemes applying pre/post-deposition steps of MAI and PbI_2 precursor layers is investigated. Two plausible hypotheses of the working principle behind the device improvement based on electronic models are given. By employing novel dynamic evaporation schemes to both standard *n-i-p* and inverted *p-i-n* structures, an optimized, dynamic growth path is presented for the first time, that allows for improved charge extraction and performance in PSCs.

Due to their advantageous properties compared to $MAPbI_3$, PSCs based on $FAPbI_3$ find higher recognition for future PSC applications. Since $FAPbI_3$ is prone to grow in and/or transition to its undesired, photo-inactive δ phase necessitating an annealing step in common processing schemes, special interest lies in suppressing the δ phase in favor of the α phase at low energy input. In [H3], absorbers based on $FAPbI_3$ are co-evaporated with varying precursor ratios. With the *in situ* XRD, the phases in the growing film are analyzed, aiming at the suppression of secondary phases and the stabilization of single-phase $FAPbI_3$ perovskite.

The growth behaviour at room temperature as influenced by bulk stoichiometric variations (FAI/PbI$_2$ ratio) and compositional variations (introduction of components CsI, PbBr$_2$) is studied and detailed boundaries are determined to enable single-phase α FAPbI$_3$ formation.

Finally, in [H4] the limits of dynamic processing and the kinetics of the diffusion and reaction of the precursor stacks for perovskites based on FAPbI$_3$ are studied in the context of sequential evaporation schemes. For this purpose, the phase evolution of different precursor layer stacks is analyzed by *in situ* XRD during deposition and subsequent annealing. Astonishingly, the same precursor layers with constant individual thicknesses react differently when evaporated in one stacking sequence compared to another. The reaction is dominated by the diffusion of one specific species. The detailed phase analysis via *in situ* XRD allows for the proposal of several processing schemes to optimize the diffusion/conversion of perovskite absorbers based on FAPbI$_3$ in sequential evaporation approaches.

The results presented in this thesis unveil the unexplored potential of dynamic, non-stationary co-evaporation schemes for MHP thin films, give fundamental insights into the phase evolution during growth and derive important recommendations for the future application of optimized growth schemes for perovskite solar cell absorbers.

Publications

[H1] K. L. Heinze, O. Dolynchuk, T. Burwig, J. Vaghani, R. Scheer, P. Pistor, *Scientific Reports* **2021**, *11*, 1 15299.

[H2] R. Heidrich, K. L. Heinze, S. Berwig, J. Ge, R. Scheer, P. Pistor, *Scientific Reports* **2022**, *12*, 1 19167.

[H3] K. L. Heinze, P. Wessel, M. Mauer, R. Scheer, P. Pistor, *Materials Advances* **2022**, *3*, 23 8695.

[H4] K. L. Heinze, T. Schulz, R. Scheer, P. Pistor, *physica status solidi (a)* **2023**, 2300690.

[H5] T. Burwig, K. Heinze, P. Pistor, *Physical Review Materials* **2022**, *6*, 6 065404.

[H6] T. Burwig, K. Heinze, V. Naumann, A. Hähnel, S. Lange, C. Hagendorf, R. Scheer, P. Pistor, In *Proceedings of the 36th European Photovoltaic Solar Energy Conference and Exhibition.* **2019** 728–732.

Contents

1   Introduction

Perovskites were first defined through the discovery of $CaTiO_3$ by Gustav Rose in 1839 [1]. Lead halide perovskites, or more generally metal halide perovskites (MHPs) are a subgroup of the perovskite material group defined by its ternary formula ABX_3. In MHPs, A and B represent monovalent (e.g. methylammonium MA^+) and divalent (Pb^{2+}) cations, respectively, and X is a monovalent anion (I^-). MHPs such as $MAPbI_3$ are highly interesting for solar cell use due to their band gap energy in the visible region, their ambipolar behavior and high absorptivity due to a direct band-to-band transition enabling their use in thin film solar cells. Additionally, perovskite solar cells (PSCs) promise to be cheap, because their components are abundant and they can be prepared at relatively low temperatures requiring low energy usage.

To-date, the solar cell market is dominated by Si. However, the efficiencies of solar cells based on Si are ever so close to their theoretical efficiency limit, plateauing at just below 27 % for the last 6 years [2]. For further innovative progress, this stagnation demands for new materials such as MHPs. PSCs have almost caught up in efficiency with SCs based on Si. Following the first publication on PSCs by Kojima et al. in 2009 [3], their power conversion efficiencies have sky-rocketed reaching 26 % by mid 2023 [2]. To-date the greatest beneficiary of the steep development of PSCs is the monolithic MHP/Si tandem solar cell, increasing its efficiency from 23 % to 33.9 % from 2017 to 2023 [2].

An environmental issue concerning PSCs is the usage of Pb, which is highly toxic due to its harmful effect on the human body functions [4]. Pb-free PSCs are in development by replacing Pb with Sn [5], but their efficiencies and stability lag behind when Pb is completely omitted [6]. Even though multifaceted encapsulation techniques are being investigated to prevent the leakage of the water-soluble Pb [7], the final disposal of the modules needs to be thought through and recycling must be promoted in parallel to the high development of high efficiencies [8]. Furthermore, the greatest challenge for PSCs is their stability, because they suffer from several intrinsic degradation mechanisms that are accelerated under environmental conditions such as heat, moisture and light [9, 10]. However, great improvements have been made from the complete degradation of a PSC within a few hours [11] to a preservation of 100 % of the inital $\sim$15 % efficiency after 10 months of continuous outdoor testing under operation [12].

Due to their immense potential and fast evolution, it seems that PSCs are on the verge of commercialization - with companies such as *Oxford PV*, *Meyer Burger* and *QCells* heavily investing into their research. At this point the decisive factor determining the most feasible preparation technique is its ability to be upscaled for production. Most groups apply easy to handle solution-based spin-coating techniques which provide many advantages on the lab-scale, but cannot be transferred to larger scale production. On the other hand, MHPs prepared via evaporation have an upscaling potential which is comparable to other established inorganic photovoltaic technologies [13]. However, works focusing on the evaporation of MHPs make up less than 1 % of their publications [14].

Therefore, one of the main goals of this thesis is to improve the knowledge on the preparation of MHPs by evaporation and to optimize the process conduct for MHP absorbers for the use in solar cell devices. MHP layers in this work are

prepared via thermal evaporation in a vacuum chamber which has the intrinsic advantage of allowing for scalability. The flagship of our experimental setup is an *in situ* X-ray diffraction (XRD) measurement directly attached to the vacuum chamber. Since layer growth is slower during evaporation compared to solution-based techniques, this allows for real-time display of crystallization and phase evolution during growth which is a unique analysis method for evaporated MHPs.

The herein drafted publications take advantage of the evaporation technique by deliberately varying the individual precursor impingement rates to identify the most advantageous stoichiometric conditions. This allows for the optimization of bulk and interfacial growth by controlling the nucleation conditions and allocating stoichiometric regimes for single-phase growth. The first two publications [H1,H2] focus on the quirks of MAPbI$_3$ deposition via co-evaporation of two materials: lead iodide (PbI$_2$) and methylammonium iodide (MAI). The growth of MAPbI$_3$ can be hard to control due to the dissociation of MAI during evaporation, rendering a high chamber pressure. Consequently, the MAI impinges the sample as several subproducts, which strongly influences adsorption behavior. In [H1], we use this behavior to control the MAI flux by monitoring the chamber pressure closely. This way, we find an optimum MAI/PbI$_2$ ratio for bulk growth in terms of PSC efficiency. Via *in situ* XRD, we observe the growth of PbI$_2$ before MAPbI3 crystallization. Therefore, in a second series, we employ a PbI$_2$ precursor and vary the MAI evaporation onset time. We find optimized conditions for the MHP absorber and achieve up to 14 % efficiency in an *n-i-p* structure. In [H2], we apply these results to a *p-i-n* structure and find the same process conduct to be detrimental for this PSC. Instead, an MAI precursor and a PbI$_2$ post-deposition step yield the best results. On the basis of these results two thought models are developed to explain this optoelectronic behavior.

[H3] investigates the thermal evaporation of FAPbI$_3$. By replacing MA$^+$ with formamidinium (FA$^+$), the intrinsic and thermal stability of the material can be improved, since the FA$^+$ component is less volatile than MA$^+$. However, due to the greater size of FA$^+$ compared to MA$^+$, the perovskite lattice is dilated. Thus, FAPbI$_3$ exhibits competing cubic (E$_g$~1.45 eV) and hexagonal (E$_g$>2 eV) phases at room temperature. For solar cell applications, the cubic phase needs to be incentivized. In [H3], we investigate the influence of stoichiometry in FAPbI$_3$, (Cs,FA)PbI$_3$ and (Cs,FA)Pb(I,Br)$_3$ on the preferentially grown phases and identify stoichiometric regimes in which phase segregation and/or single-phase growth are promoted.

The subsequent publication [H4] analyzes sequential evaporation schemes of FAPbI$_3$, (Cs,FA)PbI$_3$ and (Cs,FA)Pb(I,Br)$_3$. Sequential evaporation promises high control due to consecutive precursor deposition and reduced energy expenditure due to low annealing temperatures. In [H4] the interfacial reaction and diffusion behaviors of the precursor layers CsI, FAI, PbI$_2$ and PbBr$_2$ are examined when deposited in different orders and the results suggest clearly dominant diffusion paths and resulting boundaries for sequential evaporation.

This thesis begins with an introduction to the properties of the herein studied MHPs in section **2 Perovskites for Photovoltaics**. The properties of MAPbI$_3$ and FAPbI$_3$ as well as the issue of degradation are discussed in detail and a summary of the literature on perovskite deposition via evaporation is given. Section **3 Experimental Methodology** introduces the theory on film formation from

the vapor phase and gives an overview of the experimental setup and methods used. In **4 Results and Discussion** the main publications are presented and contextualized by respective opening remarks and closing discussions. Additional results of [H5, H6] are briefly discussed. The last section **5 Summary** concludes this thesis.

2 Perovskites for Photovoltaics

The efficiency of perovskite solar cells (PSCs) has greatly improved over the last decade. A brief look at the national renewable energy laboratory (NREL) efficiency chart [2] shows that PSC efficiencies have quickly made up ground compared to Silicon-based SCs. This is greatly due to the possibilities of modern engineering - which did not exist when Si SCs were first researched. However, the PSCs' fast development is also promoted by the metal halide perovskites' (MHP) chemical versatility, which enables component substitution and mixing to improve their band gap and enhance stability as well as defect tolerance.

The publications within this thesis presented in section **4 Results and Discussion** focus on the evaporation of two fundamental MHP materials: *methylammonium lead iodide* ($CH_3NH_3PbI_3$ or $MAPbI_3$) and *formamidinium lead iodide* ($CH(NH_2)_2PbI_3$ or $FAPbI_3$). In the following section, a brief general introduction is given on MHPs. Then, a literature overview of the properties of $MAPbI_3$ and $FAPbI_3$ is established, as well as a summary of their status quo in research. At last, the vacuum evaporation of perovskites and their components are discussed with respect to the literature.

2.1 Introduction to Halide Perovskites

Organic-inorganic metal halide perovskites can be described by the sum formula ABX_3. A and B are monovalent and divalent cations, respectively, and X is a halide anion as given in table 2.1. The perovskite crystal structure is built from a network of corner-sharing BX_6 octahedra, in which the cuboctahedral centers are each occupied by an A-cation. The simplest crystal structure that can be built from this octahedral network is cubic. By exchanging components A, B and/or X, the lattice can experience a dilation or stress, resulting in tilting of the BX_6 octahedra. The octahedral tilting induces a change in lattice structure: At room temperature $MAPbBr_3$ [15], $FAPbI_3$ and $FAPbBr_3$ favor a cubic structure and $MAPbI_3$ takes on a tetragonal structure and $CsPbBr_3$ [16], $CsPbI_3$ [17] an orthorhombic lattice, to name only a few. However, ABX_3 compounds can also assume non-perovskite low-dimensional (2D) structures e.g. for overly large organic molecular cations such as dimethylammonium or guanidinium [18, 19]. Additionally, double or quartenary perovskites $ABB'X_6$ such as $CsAgBiBr_6$ are being investigated [H6] [20], but to-date, they are not as relevant for PSCs since their efficiencies have been far below the devices based on ternary ABX_3 absorbers [H6].

To determine the capability of an ABX_3 (or $ABB'X_6$) compound to crystallize in a 3D perovskite structure, the Goldschmidt tolerance factor τ in eq. 2.1 can be used. It was originally used for oxide perovskites and expresses the stability and distortion of the respective crystal structure depending on the ionic radii r_{ion} of its components [21].

$$\tau = \frac{r_A + r_X}{\sqrt{2}(r_B + r_X)} \tag{2.1}$$

For about $0.8 < \tau < 1$, a perovskite structure is likely to be stable [28, 29]. r_{ion} of the components employed in this thesis are given in table 2.2. However, for

A^+	B^{2+}	X^-
$CH_2(NH_2)_2$ (FA)	Sn	I
CH_3NH_3 (MA)	Pb	Br
Cs		Cl

Table 2.1: Components for perovskite absorber compositions sorted by their ionic roles of monovalent A-cation, divalent B-cation and monovalent X-anion in the ABX_3 compound. In theory, all combinations are interchangeable, e.g. $FASnI_3$ [22] can be synthesized as well as $CsPbI_3$ [23] or $MASnCl_3$ [24].

Ion	r_{ion}
MA^+	$2.16\,\text{Å}$
FA^+	$2.53\,\text{Å}$
Cs^+	$1.74\,\text{Å}$
I^-	$2.2\,\text{Å}$
Br^-	$1.96\,\text{Å}$
Cl^-	$1.85\,\text{Å}$
Pb^{2+}	$0.98\text{-}1.03\,\text{Å}$

Table 2.2: Ionic radii r_{ion} of perovskite components within the perovskite crystal structure [25–27].

ABX_3 compounds in which X is a halide, τ predicts the ability of the compound to form a perovskite structure with a precision of only about 50 % [28].

An auxiliary value to predict the formation of a perovskite structure is the octahedral factor μ. It predicts the ability of B and X to form BX_6 octahedra via the relation $\mu = r_B/r_X$. For $0.41 < \mu < 0.73$ octahedra formation is anticipated and, thus, a perovskite structure is expected [28, 29]. This leads to a maximum prediction accuracy for compounds forming (non-)perovskite structures of $\sim$80 % [30] to $\sim$85 % [28] depending on the approach.

Bartel et al. introduced an improved tolerance factor τ_{Ba}, which incorporates the octahedral factor and includes the oxidation state n_A of the A-cation as given in eq. (2.2) [28]. This improved the prediction accuracy to $\sim$92 %.

$$\tau_{Ba} = \frac{r_X}{r_B} - n_A \left(n_A - \frac{r_A/r_B}{ln(r_A/r_B)} \right) \tag{2.2}$$

From the theoretical investigations of τ the formation of 100.000 perovskite compounds was predicted [30], while from τ_{Ba} 20.000 new $ABB'X_6$ compounds were anticipated [28]. These numbers indicate an enormous phase space of new compounds to be investigated experimentally.

The investigated viable ABX_3 compositions for PSCs have individual properties including band gap energies E_g that shift with the exchange of single components. E_g is strongly determined by the B-X-B bond angle, which mainly depends on the steric properties and bond lengths of the B and X components [31]. Accordingly, the E_g for the materials mentioned in tab. 2.1 can shift from $1.45\,\text{eV}$ for large A, B and X in $FASnI_3$ [32] to $3.06\,\text{eV}$ for $CsPbCl_3$ [33].

In $MAPbI_3$ and similar compounds, the valence band maximum is provided by I5p and Pb6s orbitals, whereas the conduction band minimum consists of Pb6p

orbitals [31]. Even though A-cations do not directly contribute to photoexcitation of electrons, they influence E_g by inducing different octahedral tilt angles (see section 2.2.1) and therefore B-X-B bond angles [34].

Owing to their similar nature, in modern PSCs A-cations and halides are often mixed to form compounds such as $(Cs_{.05}FA_{.8}MA_{.15})Pb(I_{.8}Br_{.2})_3$ to increase their stability and alter the absorber properties. This property can be used to optimize their E_g to obtain efficiencies closer to the Shockley-Queisser limit for single-junction PSCs [35]. Shifting E_g is especially interesting for tandem solar cells with Si, since the sub-cells need to be current-matched. Si/Perovskite tandem cells have reached a record efficiency of 33.2 % in 2023 [2].

Vegard's law in eq. 2.3 can be used to describe the change of lattice parameters a during mixing of two components V and W with a composition of $V_{1-x}W_x$.

$$a = (1 - z)a_V + z \cdot a_W \tag{2.3}$$

Noh et al. adapted Vegard's law to calculate E_g with the addition of the bowing parameter b in the quadratic expression in eq. 2.4 and determined the values given in eq. 2.5 [36].

$$E_g[MAPb(I_{1-x}Br_x)_3] = E_g[MAPbI_3] + (E_g[MAPbBr_3] - E_g[MAPbI_3] - b)\, x + bx^2 \tag{2.4}$$

$$E_g(x) = 1.57 + 0.39x + 0.33x^2 \tag{2.5}$$

Componential mixing and doping can not only be used to optimize E_g, but also to enhance structural and optical properties of the absorber. Local stoichiometric variations in the layer can have a strong effect on the absorber and PSC characteristics, passivating defects or enhancing charge extraction [37, 38]. However, the features of the fundamental metal-halide perovskites $MAPbI_3$ and $FAPbI_3$ have first to be understood. Therefore, the following section focuses on these two compositions.

2.2 Organic-Inorganic Perovskite Absorber Properties

The first perovskite solar cell (PSC) was produced in 2009 by Kojima et al., who used the design of a dye-sensitized solar cell [3]. $MAPbI_3$ and $MAPbBr_3$ nanoparticles were deposited in an 8-12 μm thick mesoporous TiO_2 structure via spin-coating and reached a short-term maximum efficiency of 3.81 %, which decayed rapidly. Since then, the device architecture has evolved substantially and the total active device thickness of a single-junction PSC is commonly <1 μm [39] [H1,H2].

$MAPbI_3$ was the first absorber used in a PSC and its properties are best researched. It is a good candidate for PSC devices [40, 41] and principal investigations on perovskites [42, 43]. Modern perovskite photovoltaics are dominated by absorbers based largely on the organic molecule formamidinium ($CH(NH_2)_2^+$, FA) - mostly in an optimized triple-cation configuration [44]. Among other properties, $FAPbI_3$ offers an intrinsically more stable compound against heat [45] and light [46], while having a lower bandgap and exhibiting absorption [47] and diffusion [46] properties comparable to $MAPbI_3$.

Therefore, this section describes the features of $MAPbI_3$ in terms of (1) structural properties (2) optoelectronic properties and (3) stability under various conditions and gives a comparison to the qualities of $FAPbI_3$ in each of these these domains.
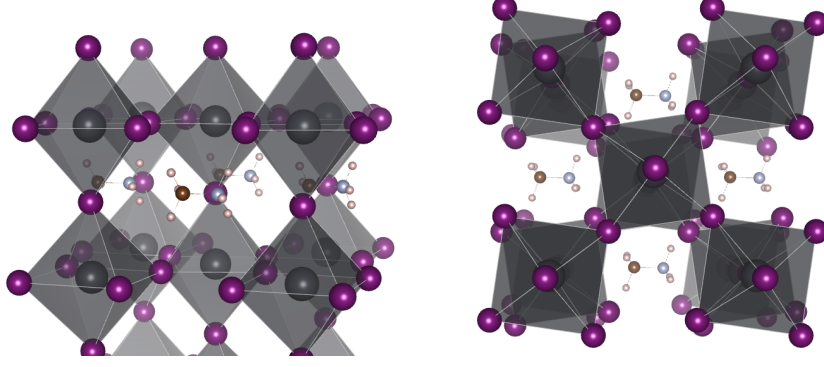
Figure 2.1: Schematic presentation of the tetragonal MAPbI$_3$ crystal structure in a- (left) and c-directions (right). The displayed perovskite structure consists of lead (grey), iodide (violet), carbon (brown), nitrogen (lightblue) and hydrogen (white) atoms. The octahedral rotation around the c-axis can be seen in the right image. Created using Vesta [57] from structural parameters in [58].

2.2.1 Structural properties

MAPbI$_3$

Temp. [K]	Structure	Space Group	Constants [Å]	Angles [°]
0-150	Orthorhombic	Pnma	a=8.91, b=12.68, c=8.66	α=90
150-313	Tetragonal	I4cm	a=8.86, c=12.65	α=90
>333	Cubic	Pm$\bar{3}$m	a=6.31	α=90

Table 2.3: MAPbI$_3$ crystal structures and lattice parameters for orthorhombic [48], tetragonal [49] and cubic [50, 51] phases at 150 K, 298 K and 373 K, respectively.

MAPbI$_3$ crystallizes in a tetragonal structure at room temperature [52] and exhibits a phase transition at 310 K-330 K to its cubic phase [50] and at 120-150 K to its low-temperature orthorhombic phase [53]. The respective lattice parameteres of all three phases are listed in table 2.3.

All MAPbI$_3$ lattice structures can be described as a combination of two building blocks: the inorganic PbI$_6^{4-}$ octahedron and the organic MA$^+$ ion. The tetragonal structure is displayed in fig. 2.1. The MA$^+$ is positioned within a cuboctahedral cage consisting of corner-sharing PbI$_6^{4-}$. The octahedra are sometimes termed PbI$_3-$ to underline their local charge and corner-sharing feature [54, 55]. This term defines the same geometrical construct as PbI$_6^{4-}$. Here, the octahedra are termed PbI$_6^{4-}$ to emphasize their geometrical construct keeping the fact in mind that each I$^-$ is part of two octahedra.

MA$^+$ exhibits a strong dipole moment with the positive charge concentrated at the -NH$_3$ site [56]. The differences between the temperature-dependent lattice structures of MAPbI$_3$ mainly arise from the increasing thermal motion of the MA$^+$ with higher temperatures resulting in different tilt angles between the inorganic octahedra [59]. In the tetragonal and orthorhombic structures, the inorganic octahedra are tilted (Pb-I-Pb angles below 180°) allowing a dilation of the lattice. This ilation is caused by H-I bonds producing three I-sites closer to the -NH$_3$ side

of MA^+ and three I-sites further away on the -CH_3 side [59,60]. Therefore, in the orthorhombic structure the MA^+ is localized off the cuboctahedral center and its orientation is fixed due to the strong H-I bonds on the -NH_3side. In the tetragonal structure, the H-I bonds are weakened due to increasing thermal motion of MA^+. The MA^+ is displaced slightly off-center and restricted to eight different orientations around the c-axis and free rotation around the C-N bond [60,61]. In the tetragonal phase, the only positional irregularity of the PbI_6^{4-} octahedra is a rotation around the c-axis [62].

Since solar cell operating temperatures range from 0 to 85°C [63,64], the most interesting transition for electronic devices based on $MAPbI_3$ is from the tetragonal to the cubic phase. This transition is continuous, resulting from the dilation and increase of Pb-I bond lengths along a- and b-axes relative to the c-axis of the tetragonal unit cell [59]. At the same time the MA^+ shifts towards the cuboctahedral center and assumes one of eight identical positions (x,y,z) to satisfy symmetry [48]. In contrast to the lower temperature phases, the cubic phase allows for quasi-free rotation of MA^+ on the picosecond time scale [56,61] and octahedral tilting is revoked [50].

As mentioned in section 2.1 the octahedral tilting determines the Pb-I-Pb bond angle. An increase in the angles causes a reduction in E_g and a decrease in the angle increases E_g [31]. Consistent with the dependence of E_g on the tilt angle, experiments have shown E_g is higher in the $MAPbI_3$ orthorhombic ($\sim 1.69\,\mathrm{eV}$) than in the tetragonal structure ($\sim 1.58\,\mathrm{eV}$) [65]. However, this correlation is more complicated for the tetragonal-cubic phase transition and the thermal change of E_g within one lattice structure.

When increasing the temperature while remaining within the borders of a structural transition, the change of E_g can be described by eq. (2.6) [66].

$$\left(\frac{dE_g}{dT}\right)_p = \left(\frac{dE_g}{dT}\right)_V + \left(\frac{dE_g}{d\,ln(V)}\right)_T \left(\frac{d\,ln(V)}{dT}\right)_p \tag{2.6}$$

The first term represents electron-phonon coupling due to lattice deformations resulting in a decrease in E_g with increasing temperature. The second term accounts for lattice dilation which causes an increase in E_g. For most inorganic semiconductors the electron-phonon coupling dominates, leading to a decrease of E_g for increasing T. However, the volume expansion coefficient in the tetragonal phase of $MAPbI_3$ is estimated at $3.83 \times 10^{-4}\,\mathrm{K^{-1}}$, which is 50 times higher than for Si ($3 \times 10^{-6}\,\mathrm{K^{-1}}$) [65]), which leads to an increasing E_g with temperature [52,67] compared to other semiconductors, in which the E_g decreases with higher temperatures [68]. From 20°C to 80°C, the bandgap of $MAPbI_3$ rises from 1.595 eV to 1.605 eV [52] by lowering of the valence band maximum.

FAPbI₃

$FAPbI_3$, similar to $MAPbI_3$, exhibits a cuboctahedral corner-sharing PbI_6^{4-} structure determined by octahedral tilting. The structure encompasses the large organic cation FA^+ [69]. It has four polymorphs, of which β (below 151 K) and γ (below 91 K) represent the low-temperature orthorhombic and tetragonal structures, respectively. At temperatures above 151 K, $FAPbI_3$ can crystallize in α and δ phases. Both crystal structures are displayed in fig. 2.2. The cubic (earlier
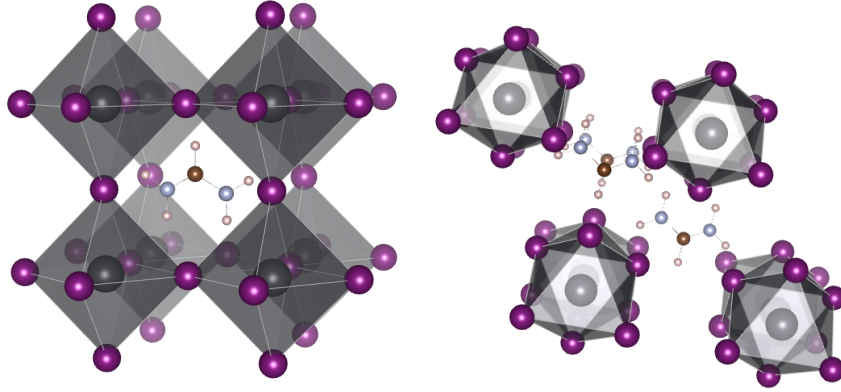
Figure 2.2: Schematic presentation of FAPbI$_3$ cubic α (left) and hexagonal δ (right) crystal structures. The displayed atoms are lead (grey), iodide (violet), carbon (brown), nitrogen (lightblue) and hydrogen (white). Created using Vesta [57] from structural parameters in [70] and [71] for α and δ phases, respectively.

reports referenced the phase as trigonal [71]) α phase is needed for solar cell operation [72], but suffers from a phase transition to the less favorable δphase due to the large tolerance factor of $t =1.04$ (see eq. (2.1)). A structural summary of all phases can be found in table 2.4.

When reducing the temperature from 300 K to 250 K in the stabilized α phase, the lattice shrinks and E_g is reduced by about 0.017 eV [73]. As in MAPbI$_3$, the transition to the lower temperature tetragonal phase of FAPbI$_3$ decreases its Pb-I-Pb bond angle below 180° and increase the bandgap due to weaker orbital overlap.

In the cubic α phase the FA$^+$ agitates around an equilibrium position in which -NH$_2$ groups point at opposite faces of the octahedral cube [74]. Other than MA$^+$ which exhibits a strong dipole moment, FA$^+$ interacts weakly with the inorganic sublattice forming weak FA-I bonds [46]. The weak dipole moment of FA$^+$ is due to its homogeneously distributed electron density along the N-C-N bond and its resonance stabilization [75, 76]. Consequently, the FA$^+$ orientation is not

Temp. [K]	Phase	Structure	Space Group	Constants [Å]	Angles [°]
<140	γ	tetragonal	P4/mbm	a=8.87, c=6.28	α=90
140-285	β	tetragonal	P4/mbm	a=8.90, c=6.31	α=90
285-423	δ	hexagonal	P63mc	a=8.66, c=7.90	α=90, γ=120
>285	α	cubic	Pm$\bar{3}$m	a=6.36	α=90

Table 2.4: Temperature-dependent lattice structure parameters of FAPbI$_3$ [71,77]. The cubic α phase exists at room temperature, but intrinsically transforms to the δ phase, if not artificially stabilized [69]. The α phase is intrinsically stable above T$_{trans}$=423 K=150°C.

stable, but still limited to certain orientations. It transitions rapidly along these orientations, performing 90° flips on a picosecond time scale [74]. The cubic phase in basal FAPbI$_3$ at ambient conditions is only stable above T_{trans}=150°C [78]. It undergoes a transition to the thermodynamically more stable δ phase below T_{trans}

and in a humid environment, if not artificially stabilized [77]. This is mainly due to lattice stress in the (111) direction in the α phase, which is reduced by the phase transformation [27].

The FAPbI$_3$ δ phase is a non-perovskite phase since it exhibits a face-sharing octahedral structure [79]. It has a high E_g along with low absorption and conductivity, rendering it unfavorable for PSCs. During solar cell operation, the absorber qualities suffer strongly from α→δ transition (see section 2.2.3), which is why many works report on the stabilization of the FAPbI$_3$ α phase [79–83]. To combat the unwanted phase transformation, fabrication methodologies termed composition engineering [84] [H3], dimensionality engineering [85], strain engineering [H3] [27] and crystallization modulation [86] are used.

A general approach to suppress the transformation to the δ phase is to lower the Goldschmidt tolerance factor of FAPbI$_3$ by alloying with MA, Cs or others. MA and Cs occupy the same lattice sites as FA and due to their smaller sizes the effective ion radius is reduced. Therefore, the overall tolerance factor of the mixed-cation perovskite drops to the range of 0.8-1. Additionally, the stronger dipole moment of MA$^+$ increases structural stability. Thus, T_{trans} is reduced to 125°C and the transformation barrier to the FAPbI$_3$ δ phase is greatly increased even below the T_{trans} [87].

2.2.2 Optoelectronic properties

Strong absorption, high conductivity and defect tolerance are only some of the optoelectronic properties that make organic-inorganic perovskites special and attractive for solar cell applications. Here, their charge carrier dynamics are explained in terms of carrier creation via absorption, subsequent recombination dynamics, the influence of self-doping on the charge carrier characteristics as well as the occurring hysteresis phenomenon.

MAPbI$_3$

The absorption of photons in MAPbI$_3$ is based on a direct bandgap provided by I 5p - Pb 6s antibonding orbitals for the valence band maximum (VBM) and by the Pb 6p orbital for the conduction band minimum (CBM) [31]. The organic cation has an indirect influence on E_g by its steric properties and is essentially decoupled from free charge carrier transport which occurs in the inorganic sublattice [88]. Halide substitution with Br can be employed to steadily increase the E_g in a mixed-halide absorber MAPb(I,Br)$_3$ according to eq. (2.5). Compared to MAPbI$_3$, the valence band is lowered in MAPb(I,Br)$_3$. In the Br-rich absorber MAPbBr$_3$ the conduction band is lifted compared to MAPb(I,Br)$_3$ [89] increasing the bandgap to a maximum value of 2.3 eV [90].

MAPbI$_3$ exhibits a steep absorption onset with an Urbach Energy of 14 meV [91,92] at its bandgap energy (E_g) of 1.6 eV [93]. The absorption coefficient rises from 1×10^4 at E_g to 1×10^5 cm^{-1} at photon energies ≥2.5 eV. The E_g is 0.4 eV larger than the optimum according to Shockley-Queisser, but is still in a good position for single-junction solar cells, allowing for a theoretical solar cell efficiency above 30 % (compared to 34 % for the absolute theoretical maximum) [35].

FAPbI₃

Many advantageous properties of MAPbI₃ can also be found in FAPbI₃. Along with a low Urbach energy of $15\,\text{meV}$ (or even $13\,\text{meV}$, if prepared in a specific way [94]), slightly stronger absorption than MAPbI₃ in the visible region from $1\times10^4\,\text{cm}^{-1}$ to $1\times10^5\,\text{cm}^{-1}$ [95], absorption edge at $870\,\text{nm}$ [96], greater diffusion lengths [47, 78, 97], FAPbI₃ has a direct bandgap with an E_g of $1.45\,\text{eV}$, more suitable for single-junction solar cells.

Similar to MAPbI₃, valence band maximum (VBM) and conduction band minimum (CBM) consist of I(5p)/Pb(6s) and Pb(6p) orbitals, respectively [31, 98]. However, the density of states in FAPbI₃ is higher at the VBM due to extra contribution from the I(5s) orbitals.

The low E_g of FAPbI₃ could be one of its greatest advantages. When alloying with Sn to produce a mixed FAPb₀.₅Sn₀.₅I₃ perovskite, its E_g can be reduced even further to 1.2-1.28 eV [99, 100]. This so-called band gap bowing occurs, even though the pure FASnI₃ as well as FAPbI₃ have a higher E_g than the mixture. For the mixture of two compounds at a proportion of x, E_g is described by eq. 2.7 [101]. Herein, the bowing parameter b describes the deviation from the linear relationship as given by Vegard's law in eq. (2.3). For $FA(Pb_{1-x}Sn_x)I_3$ b is $0.73\,\text{eV}$ [102]. For a mixed absorber $(MA_{0.24}FA_{0.65}Cs_{0\cdot15})(Pb_{0.35}Sn_{0.65})I_3$ a low E_g of $1.23\,\text{eV}$ was obtained [103].

$$E_g = (1 - x) \cdot E_g(\text{FAPbI}_3) + x \cdot E_g(\text{FASnI}_3) + bx \cdot (x - 1) \tag{2.7}$$

This can make FA-based cells interesting as bottom cells for perovskite-perovskite tandem applications as well [99, 104, 105]. A-cation substitution increases not only structural stability, but also electronic properties. FAPbI₃ has been doped with $15\,\%$ MA$^+$ to suppress α→δ phase transition from 25 to 250°C [76, 106]. No lattice shrinkage or change in E_g was observed, but the free charge carrier lifetime increased from ns to several μs, possibly by decreasing the number of grain boundaries. The benign property of MA$^+$ was attributed to its dipole moment which is ten times larger than that of FA$^+$, stabilizing the octahedral structure due to stronger I-H hydrogen bonds [76].

Recombination Characteristics

MAPbI₃

Optoelectronic devices find their limitations in the recombination of free charge carriers. Polycrystalline thin films exhibit a large number of grain boundaries at which defects may accumulate forming carrier trapping/recombination centers. Recombination processes can be distinguished in terms of radiative and non-radiative paths, of which the non-radiative processes mainly limit free charge carrier transport as their life times are lowest. Non-radiative recombination processes include Auger recombination, defect-assisted recombination (Shockley-Read-Hall (SRH)), electron-phonon interactions and carrier-carrier-scattering. SRH recombination occurs via defects that are located "deep" in (close to the center of) the band gap, meaning that electrons and holes have to overcome similar energy differences in order to recombine at such a defect. The charge carriers reach the deep defect via a string of phonon interactions, strongly facilitating non-radiative

recombination. The rate of SRH recombination depends on the concentration of deep defects in the band gap and their capture cross sections as well as electron and hole concentrations. During Auger recombination, the excess energy during a non-radiative band-to-band transition results in a kinetic excitation of an electron within the conduction band (or hole within the valence band), which subsequently dissipates its excess energy by interacting with the atoms in the lattice. SRH recombination is the dominant mechanism at lower carrier concentrations, Auger recombination dominates for higher concentrations, because three charge carriers participate during Auger recombination and its rate therefore depends on the multiplied concentration of these three charge carriers (electron-electron-hole or electron-hole-hole) [107]. Si solar cells are doped to reduce SRH recombination, which in turn increases Auger recombination. This limits their maximum PCE to $\sim$29 % compared to their SQ-limit of $\sim$33 % [108]. In contrast, MAPbI$_3$ exhibits greatly reduced Auger-recombination at operating conditions, enabling low losses compared to the SQ-limit and a high fill factor of $\sim$90.4 % [108].

The external luminescence efficiency (L_{ext}) indicates the probability of a recombination event to be radiative [108, 109]. L_{ext} can be expressed in dependence of radiative, SRH and Auger recombination via eq. 2.8, where B_{int} is the internal radiative coefficient estimated for MAPbI$_3$ at $1.34 \times 10^{-10}\,\mathrm{cm^3 s^{-1}}$ (for Si $B_{int,Si}$=3 $\times$ $10^{-15}\,\mathrm{cm^3 s^{-1}}$ [107]), P_{esc} is the probability of escape of an internally emitted photon, n is the excess carrier density, A_{SRH}=τ_{SRH}^{-1} is the SRH constant, P_{par} accounts for parasitic absorption and C_{Auger}, estimated at $1.1 \times 10^{-28}\,\mathrm{cm^6 s^{-1}}$ [110] ($C_{Auger,Si}$=1 $\times$ $10^{-30}\,\mathrm{cm^6 s^{-1}}$ [107]), is the Auger coefficient.

$$L_{ext} = \frac{B_{int}P_{esc}n^2}{A_{SRH}n + B_{int}(P_{esc} + P_{par})n^2 + C_{Auger}n^3} \quad (2.8)$$

Of the different types of recombination paths radiative and Auger recombination are intrinsic, enabling an assessment for the potential of a material to qualify as a viable solar cell absorber. Pazos-Outón et al. assumed radiative and Auger recombination (Auger limit) in their simulations of a PSC and found that the maximum efficiency was barely affected compared to the case when assuming only radiative recombination (radiative limit), showcasing the intrinsic potential of MAPbI$_3$ [108]. This is enabled by the fast decrease in Auger recombination proportional to n^3 from V_{OC} towards the operating voltage. Radiative recombination decreases more slowly due to its n^2 dependence. Even though V_{OC} decreases from radiative limit to Auger limit, the operating voltage can be closer to V_{OC} in the Auger limit compared to the radiative limit. This leads to an increased fill factor (FF) and an almost equivalent theoretical efficiency of 30.45 % in the Auger limit compared to 30.5 % in the radiative limit. For this effect the ratio of radiative to Auger recombination in MAPbI$_3$ is the deciding factor - B_{int} being relatively large for MAPbI$_3$.

However, in the presence of SRH recombination the operating voltage falls more rapidly than V_{OC}. Life times τ_{SRH} of $\sim$100 μs are necessary to maintain maximum efficiency [108]. Such life times have been realized for MAPbI$_3$ single crystals [111], but they remain one order of magnitude lower for real solar cells and the FF remains below 0.85 [40, 112]. Nonetheless, Yin et al. have found that intrinsic deep defects enabling SRH recombination in MAPbI$_3$ have high formation energies [113]. This enables long theoretical carrier life times. Deep

defects include antisites I_{Pb} (I at a lattice site normally occupied by Pb), I_{MA} and Pb_I as well as the interstitial defect Pb_i, all of which exhibit formation energies above $3\,\text{eV}$ according to Yin et al.

In general, solar cells absorbers can be doped to decrease SRH recombination. However, this in turn increases Auger recombination [114]. The doping density can be optimized so that overall recombination is minimized. For perovskite solar cells the optimum doping density is low due to the large Auger coefficient, so the potential reduction of the overall recombination by reduction of SRH recombination through doping is limited [108]. $MAPbI_3$ exhibits several intrinsic shallow defects that lead to self-doping [115]. In the following, the self-doping effect by intrinsic defect types in $MAPbI_3$ are discussed.

Self-Doping of MAPbI$_3$

$MAPbI_3$ is often assumed to be an intrinsic semiconductor, accordingly the junction for standard (inverted) PSCs is written as *n-i-p* (*p-i-n*) [116, 117]. However, $MAPbI_3$ can exhibit strong *n*- and *p*-doping depending on its composition, i.e. MAI/PbI_2 ratio. This ratio is strongly influenced by film formation methods, precursor composition and process conditions. Wang et al. grew a film from a stoichiometric precursor solution and observed strong *n*-type doping with an electron concentration of $1.28 \times 10^{17}\,\text{cm}^{-3}$, while a ratio of PbI_2/MAI of 0.93 was measured in the final layer - accompanied by *p*-doping of $4.0 \times 10^{-16}\,\text{cm}^{-3}$ [115]. A later study by Hellmann et al. confirmed that $MAPbI_3$ layers deposited via co-evaporation exhibited *n*-type doping, independent of the substrate (*p*-type NiO or *n*-type SnO_2 [118]. This results in an *n-p*-heterojunction at the perovskite/HTL interface, which is responsible for the V_{OC} in the device [118]. Accordingly, the main potential drop can be found at the perovskite-ETL junction in an MAI-rich sample with *p*-type doping [119]. Thus, PSCs should be treated as *n-n-p* and *p-n-n* devices instead of *n-i-p* and *p-i-n*, respectively [118].

Several types of defects are prone to appear that lead to doping, including vacancies, interstitials and antisites of all three components MA, Pb and I. During PbI_2 excess the three main defect types are: I^- vacancy (V_I, *n*-type), Pb interstitial (Pb_i, *n*-type), and MA^+ vacancy (V_{MA}, *p*-type) [113]. Due to relatively high formation energies of Pb_i and V_{MA} the *n*-type doping in films with PbI_2 excess is ascribed to the V_I vacancies caused by MAI insufficiency. The electron mobility increases proportionally to the PbI_2 excess due to an *n*-type doping [115, 120]. Upon strong MAI excess three defects dominate: Pb_2^+ vacancy (V_{Pb}, *p*-type) due to PbI_2 insufficiency, MA^+ interstitial (MA_i, *n*-type) due to MAI excess and I^- vacancy (V_I, *n*-type) due to I insufficiency [113]. Of these, V_{Pb} forms with the highest probability and therefore the occurring *p*-type doping in MAI rich films is attributed to this defect [115].

FAPbI$_3$

In $FAPbI_3$, spin-orbit coupling reduces E_g, induces band-splitting and enables long carrier life times [121]. Reported experimental electron-hole life times range from 700 to $1400\,\text{ps}$ [122] and calculations found recombination to occur within one ns [123]. Low trap densities of $1.13 \times 10^{10}\,\text{cm}^{-3}$ and large hole carrier mobilities of $35\,\text{cm}^2\text{V}^{-1}\text{s}^{-1}$ were reported for $FAPbI_3$ single crystals [124] and

$27\,\mathrm{cm^2V^{-1}s^{-1}}$ for polycrystalline films [125]. Diffusion lengths of $3.1\,\mu\mathrm{m}$ [125] and $25\,\mu\mathrm{m}$ [126] were reported in polycrystalline films enabling free charge carriers to reach the electric contract layers and enable current extraction. Upon mixing with Br the charge recombination rate constants can be further increased according to calculations [125]. Yang et al. have significantly prolonged the life time to $1105\,\mathrm{ns}$ by encorporating excess I ions which increased the crystallite size, reducing the amount of grain boundaries and therefore the trap density [127].

$FAPbI_3$ is prone to several defect types including vacancies, interstitials and antisites of all components FA, Pb and I. Only the antisite defects FA_I (FA at an I lattice site), I_{FA}, I_{Pb} and Pb_I as well as the interstitial Pb_i cause deep defect levels in the bandgap [128].

All defects implying Pb displacements have very high formation energies in Pb-rich, I-rich and stoichiometric conditions, which makes their contribution to recombination rates unlikely [128]. The FA_I antisite defect (in Pb-rich conditions) and the I_{FA} antisite defect (in I-rich conditions) have much lower formation energies than MA_I and I_{MA} in $MAPbI_3$ under given conditions. FA_I and I_{FA} antisites create deep defect levels in the bandgap which are most likely attributed to the weak van der Waals interactions between FA^+ and PbI_6^{4-} octahedra. Therefore, they can easily act as recombination centers for SRH recombination and decrease carrier life times in $FAPbI_3$.

In order to suppress the formation of the most influential defect FA_I, theoretical observations point towards an I-rich and n-doped absorber [128]. In I-rich conditions, Pb_2^+ vacancies have the lowest formation energies in $FAPbI_3$ [128]. Reduction of deep-level defects by additional supply of I was also shown experimentally [127]. Pb_2^+ vacancies were found to increase electron-hole recombination time to tens of ns [123]. This results from the mitigation of atomic motion and non-adiabatic electron-phonon coupling, which was identified as the main contributor to electron-hole recombination. Additionally, Pb_2^+ vacancies create shallow defects (traps) from which the trapped electrons can thermally escape without recombining, leaving E_g unaffected. It was observed that shallow defects can strongly regulate recombination, therefore enabling a high open-circuit voltage [129].

By A-site alloying (e.g. $(MAFA)PbI_3$) the defect formation energies can be greatly increased, reducing their problematic influence [128]. Cs^+ and Rb^+ have been shown to reduce SRH recombination and promote the extraction of free charge carriers by suppressing interfacial defects and offering a reduced resistance to holes at the perovskite/HTL interface and a low series resistance in general [130].

Hysteresis/ Ion Movement

MAPbI$_3$

If not prepared and/or treated in the right way, PSCs suffer from a significant hysteresis in their current-voltage curves, resulting in higher efficiencies in the reverse (V_{OC} to j_{SC}) compared to the forward direction (j_{SC} to V_{OC}). This hysteresis is caused by the charging of a parasitic capacitance, causing a temporary current-ramp induced by ion movement [131]. Hysteresis can cause structural instability the layer [132].

The severity of hysteresis in a PSC can be described by the hysteresis index (HI) in eq. (2.9) [133]. The HI states

$$HI = \frac{\int_{SC}^{OC} J_{rev}(V) - J_{forw}(V) dV}{\int_{SC} OC J_{rev}(V) dV} \qquad (2.9)$$

the relative integrated J-V curve loss in forward (forw) direction compared to reverse (rev) direction.

Experiments by Li et al. suggested that I^- migration through the grain boundaries towards the positive electrode was responsible for the hysteresis [134]. This is fairly likely, since V_I are the most mobile species in $MAPbI_3$ [135] exhibiting a diffusion coefficient of 10×10^{-8} to $10 \times 10^{-9} \, cm^2 s^{-1}$ [136]. Son et al. suggested the cause of hysteresis was not only ion migration, but also the formation of I^- Frenkel defects near the cathode during illumination [137]. To prevent the formation of Frenkel defects KI was incorporated in small amounts. K^+ energetically favors the interstitial defect site and occupies it, blocking the I^- defect. The formation energy of the K^+ interstitial defect was further decreased for mixed-cation perovskites, rendering the KI treatment even more effective. Incorporation of Li (Cs) did not result in reduction of hysteresis due to their smaller (larger) ionic radii making it unlikely for them to passivate the Frenkel defect. Another study showed that the addition of extrinisic mobile ions such as small alkali metals Li and Na can even enhance hysteresis [138].

However, ion migration should not be the sole factor causing hysteresis. A combination of simulation and experiment was employed to observe ion migration in both standard and inverted PSC devices, but found hysteresis in the standard device structure (n-i-p) would only occur in the presence of strong interfacial recombination [139, 140]. Accordingly, modification of interfaces and contact layers was successful in averting hysteresis by reducing defect concentration at the interfaces [141–145].

Resulting from the above mentioned studies, hysteresis is a considerable issue in PSCs, but can be combatted successfully by chosing the correct transport layers, interfacial layers and perovskite dopants.

FAPbI₃

The hysteresis phenomenon in $FAPbI_3$ is mostly mentioned as a by-product of hysteresis in $MAPbI_3$-based PSCs and even recent reviews do not address distinct hysteresis phenomena separately for the two absorber types [133, 146, 147]. This makes sense, since j-V hysteresis is largely ascribed to halide (vacancy) migration, as discussed above and not to the behavior of the organic MA^+ ions. This concept remains true for the FA^+ molecule.

FA^+ performs two types of movements in the PbI_6^{4-} cage: (i) motions around the center (time constant 470 fs) (ii) 90° flips with reorientation of the FA^+ N-C-N axis between two cuboctahedral faces (time constant 2.8 ps) [74]. Therefore, formatino of long-lived (anti)ferroelectric domains in $FAPbI_3$ can be ruled out and hysteresis can be ascribed to ion migration and interfacial recombination as in $MAPbI_3$.

2.2.3 Degradation Mechanisms

The intrinsic stability of $MAPbI_3$ is limited due to several overlapping effects and might be the decisive property restricting its competitiveness with $FAPbI_3$-based compounds. As for many other materials, the exposure of $MAPbI_3$ to O_2 and humidity can drive processes decomposing the perovskite. Additionally, the MA cation is volatile leading to an intrinsic instability of the perovskite compound [148].
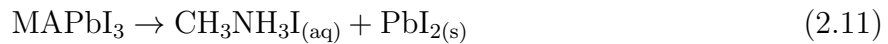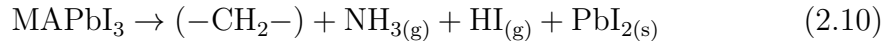
On the other hand, $FAPbI_3$ is chemically non-inert which results in photo- and moisture instability of the $FAPbI_3$ structure [46]. Furthermore, the pristine cubic α phase exhibits anisotropic lattice strain, incentivizing a transition to the δ phase [27]. $FAPbI_3$ is thermodynamically more stable than $MAPbI_3$, but needs temperatures as high as 150°C to crystallize in its α phase [77]. In 2.2.1 the problematic of the α→δ phase transition was pointed out. This section focuses in more detail on the origins of instability in both perovskite absorber types.

Humidity Induced Degradation

Solar cells suffer from constant exposure to humidity during their lifetime. Therefore, degradation processes resulting from their reaction with the omnipresent humidity have to be understood and combatted. The use of vacuum evaporation chambers and gloveboxes for preparation and storage during this thesis minimizes the degradation effects caused by exposure to humidity. Nonetheless, the humidity within the *in situ* glovebox (see section 3.2) could not be reduced to 0. Additionally, the exposure of samples to oxygen can occur during transfer to measurement setups (other than the *in situ* XRD) and measurement at air (see section 3.4). Therefore, humidity-induced degradation needs to be considered for the samples within this thesis.

$MAPbI_3$

An early suggestion as to the degradation pathway of $MAPbI_3$ caused by humidity is in the chemical eq. 2.10. Therein, outgassing of N and I were assumed to be responsible for the degradation [149]. Another proposed degradation path involved the loss of MAI by aqueous dissolution via the chemical eq. 2.11 [150].

$$MAPbI_3 \rightarrow (-CH_2-) + NH_{3(g)} + HI_{(g)} + PbI_{2(s)} \tag{2.10}$$

$$MAPbI_3 \rightarrow CH_3NH_3I_{(aq)} + PbI_{2(s)} \tag{2.11}$$

However, several groups [151–153] agree upon a two-step degradation mechanism proposed by Leguy et al. [154]: (i) Reversible formation of the monohydrate $MAPbI_3 \cdot H_2O$ in chemical eq. 2.12 (ii) Irreversible formation of the dihydrate $MA_4PbI_6 \cdot 2H_2O$ in chemical eq. 2.13

$$4MAPbI_3 + 4H_2O \rightleftharpoons 4\left[MAPbI_3 \cdot H_2O\right] \tag{2.12}$$

$$\rightleftharpoons MA_4PbI_6 \cdot 2H_2O + 3PbI_2 + 2H_2O \tag{2.13}$$

$$MA_4PbI_6 \cdot 2H_2O_{(s)} \rightarrow 4MAI_{(aq)} + PbI_{2(s)} + 2H_2O_{(l)} \tag{2.14}$$
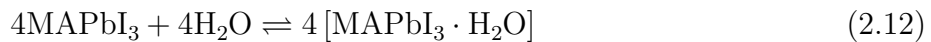
The formation of the dihydrate is expected to lead to phase separation under excess water as given in reaction 2.14. This reaction is expected to be irreversible due to dissolution of MA^+ [154].

To combat degradation via water infiltration, the choice of the top transport layer (TL) is decisive. The TL either allows permeation of H_2O molecules - exposing the perovskite layer to hydration - or provides a hydration barrier [155]. Hygroscopic dopants such as LiTFSI or 4-*tert*-Butylpyridine in hole TL such as Spiro-MeOTAD strongly enhance degradation [156]. Therefore, non-hygroscopic TLs are crucial for perovskite stability.

FAPbI$_3$

Even though FA is less volatile than MA, FAPbI$_3$ is prone to degradation reactions with the surrounding atmosphere, especially H_2O [157], which can trigger the formation of the impurity phase $NH_4PbI_3 \cdot 2H_2O$ [71]. The main degradation mechanism induced by the reaction of FAPbI$_3$ with H_2O is the dissolution of the α phase at grain surfaces and interfaces and subsequent formation of the δ phase [79]. Accordingly, the grain and subgrain surface area should be reduced to mitigate a strong surface reaction. Therefore, larger grains are preferred to suppress the α→δ phase transition.

The δ phase formation is likely to occur along the strained (111) direction (see section 2.2.1) of the α phase [27]. Since the α (111) and δ (0001) planes exhibit the same atomic arrangement (close-packing planes of FA and Pb), the strain in (111) direction helps to nucleate the δ phase formation. This opens an energetically favorable path to the moisture-enhanced α→δ phase transformation.

According to density functional theory (DFT) calculations, upon exposure of FAPbI$_3$ to humidity the H_2O molecule binds to the hydrogen atoms of the N moiety of FA$^+$ [158]. This hydrogen bond forms since the theoretical distance between O and H-N (1.7-2.0 Å) is lower than the sum of their van der Waals radii (2.6 Å). The H atoms in H_2O then orient towards I, stably hydrating the perovskite. Lattice calculations were done for an H_2O mole fraction of x=1/8, 1/4, 1/2 and 7/8 in FAPbI$_3$, unveiling a minimum in unit cell volume and α→δ transformation energy at 1/4 due to the hydrogen bonds with the host structure FAPbI$_3$ [158]. For higher H_2O contents the α→δ transformation energy increases again. Simultaneously, H_2O intercalates into the perovskite structure and causes further volume expansion. This makes the remaining α phase domains less stable. However, the layered δ phase is not as sensitive to volume expansion and remains stable upon H_2O intercalation. In summary, exposure of FAPbI$_3$ to high humidity will lead to the absorption and diffusion of H_2O into the lattice until a molar fraction of 1/4 is reached. Then, the α→δ transformation is energetically most favorable and occurs before further water intercalates into the monohydrate δ-FAPbI$_3 \cdot H_2O$ and stabilizes the δ phase with respect to the α phase.

In an opposite approach, Wang et al. included a large amount of water into the crystal structure of FAPbI$_3$ to try to stabilize it against transition to the δ phase [159]. Three different hydrated phases of FAPbI$_3$ were observed for different molar ratios of H_2O/FAPbI$_3$: ε >(1:1), ϑ (2:1) and μ (3:1). The PCE stability was increased from 2 to 25 days by employing an ε phase absorber based PSC, but the initial PCE was reduced from 19 % to 0.25 %, showcasing the possibilities and complications with this idea [159].

Countless investigations have been run to improve the stability of FAPbI$_3$ during exposure to humidity. When a part of the I share was substituted with Br [160] and/or part of FA with MA [27] the lattice strain was released and resistance

to the humidity-induced phase transformation was enhanced. Substitution of FA with smaller cations such as Cs and MA and the smaller halide Br reduces the cuboctahedral volume, which strengthens the FA-I as well as the Pb-I interactions and can increase the grain size [46].

The choice of the HTL as a substrate layer in *p-i-n* solar cells was found to significantly influence the stability of the α phase against the $\alpha{\rightarrow}\delta$ phase transition during exposure to H_2O [37, 80]. In a wet-chemical experiment, the HTL [2-(3,6-Dimethoxy-9H-carbazol-9-yl)ethyl] phosphonic Acid (MeO-2PACz) was found to stabilize the α phase under exposure to high relative humidity [37]. In this regard MeO-2-PACz outperformed other commonly used HTLs, such as PTAA, NiO and PEDOT:PSS. The positive effect of MeO-2PACz was attributed to its free phosphate groups. In a co-evaporated experiment, MeO-2PACz was employed in combination with excess FAI [80]. Here, the free phosphate groups were said to efficiently bind to the FAI via hydrogen bonds [161], thereby increasing the structural stability of FAPbI$_3$ by enabling an increased incorporation of FAI into the layer [80].

However, humidity can also be exploited to improve device performance. Lin et al. exposed sequentially vapor deposited thin films to humidity directly after preparation (before annealing) [158]. Films exposed to high humidity exhibited a faster and more homogeneous transformation to the α phase while also showing substantially higher solar cell efficiencies of 20 % compared to 13 % for film exposed to low humidity conditions. The beneficial effect of high humidity exposition directly after preparation was attributed to the lower $\delta{\rightarrow}\alpha$ phase transition energy at certain molar ratios of H_2O in the structure.

Oxygen Induced Degradation

Another critical degradation mechanism originates from the reaction of oxygen with excited electrons in the perovskite. Therefore, this reaction is especially severe during exposure to light or under forward bias due to a higher concentration of excited electrons [11]. Similar to humidity-induced degradation, the sample exposure to oxygen within this thesis is minimized due to the use of a high-vacuum chamber and gloveboxes. However, the oxygen content within the *in situ* glovebox (see section 3.2) could not be reduced to 0. Further, the samples can react with oxygen during transfers and measurements at air (see section 3.4). Therefore, oxygen-induced degradation needs to considered.

MAPbI$_3$

When comparing degradation of MAPbI$_3$ imposed by humidity and oxygen, the reaction with oxygen was found to be the dominant mechanism [11]. When O_2 is introduced to the perovskite, the excited electrons cause the formation of the superoxide O_2^-, which can deprotonate the organic cation via eq. 2.15 [162].

$$MAPbI_3 + O_2^- \rightarrow CH_3NH_2 + PbI_2 + \frac{1}{2}I_2 + H_2O \qquad (2.15)$$
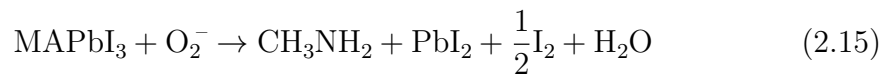
This leads to a fast degradation of the MAPbI$_3$ surface, but further degradation in the bulk is hindered due to the formation of a solid oxidation product (PbO) at the surface [163].

To combat oxygen induced degradation, the formation of the superoxide can be hindered by employing encapsulation layers or charge transport layers that also function to block O_2 infiltration [7]. Intrinsically, the formation of the superoxide can be suppressed by improving charge extraction, so the excited electrons are not likely to contribute to the formation of O_2^- [11, 162, 164].

FAPbI$_3$

A publication investigating the effects of isolated O_2-exposure for the pure FAPbI$_3$ compound was not found. However, Guo et al. studied Cs/Rb-doped FAPbI$_3$ surface structures and compares H_2O and O_2 exposure [165]. They found the surface bonds formed by O_2 and the respective surface group (Pb, I, Cs or Rb) to be much weaker than the bonds formed with the O in H_2O. According to Guo et al. O_2 can easily diffuse along the surface due to its weak bonds. Still, both adsorbed species O_2 and H_2O lead to a similar shift in absorption in the surface structure, greatly diminishing absorption in the visible region and shifting the band gap onset by $0.2\,eV$ compared to the bulk [165]. In another work, the oxygen-induced instability of MAPbI$_3$ is greatly alleviated by replacing $20\,\%$ of MA with FA [166]. This positive effect is ascribed to the energetically less favorable deprotonation of FA compared to MA and to a lower ion conductivity in the FA-based perovskite, reducing the degradation transport rate from the surface towards the bulk.

Degradation in Vacuum

Degradation in vacuum is significantly slower compared to degradation in air. The transformation of MAPbI$_3$ during 1 month under $10 \times 10^{-3}\,mbar$ is comparable to 24h in humid air [167]. Nonetheless, since vacuum preparation and characterization techniques play a central role in perovskite research, degradation mechanisms under vacuum have to be considered.

MAPbI$_3$

MAPbI$_3$ decomposition effects in vacuum or during exposure to air and humidity can both originate from the loss of MAI components [167]. At low pressures, MAPbI$_3$ can suffer from outgassing of organic components, such as CH_3NH_2, HI, CH_3I, NH_3 and I_2 [168], which leads to the formation of PbI$_2$. The loss of volatile organic components originates at extended defect sites or discontinuities such as grain boundaries [167]. The removal of I via outgassing of CH_3I and I_2 enables the reorientation of the PbI_6^{4-} octahedra to the 2D PbI$_2$ structure, therefore enabling phase separation.

However, the volatilization of organic components under illumination in vacuum is partially reversible as described in eq. (2.16) [168].

$$MAPbI_3 \rightleftharpoons PbI_{2(s)} + Pb_{(s)}^0 + CH_3NH_{2(g)} + HI_{(g)} \tag{2.16}$$
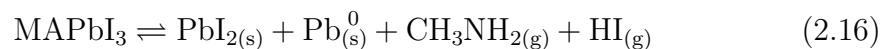
Eventually, further loss of MAI enables the decomposition of residual PbI$_2$ to Pb^0 and mobile I_2^- ions, which significantly accelerate the self-degradation of MAPbI$_3$ by deprotonation of MA$^+$ [169].

Br-rich perovskite MAPb(I,Br)$_3$ can be far less susceptible to I$_2^-$ induced degradation due to the stronger Pb-Br bond and larger electronegativity of Br, but poses other limitations due to the structural differences of the respective single-halide perovskite [170].

FAPbI$_3$

Degradation under vacuum is not as well explored for FAPbI$_3$. Since FAI dissociates upon evaporation [171], it can be assumed that FAI - similar to MAI - exhibits an intrinsic volatility, albeit lower than MAI.

A singular experiment for thermal evaporation of the mixed-cation mixed-halide PSCs based on (MAPbBr$_3$)$_{0.17}$(FAPbI$_3$)$_{0.83}$ has been conducted by Guo et al. [172]. During operation under 1×10^{-3} mbar, they observed a shrinking of the lattice and separation into FAPbI$_3$ and (MAPbBr$_3$)$_{0.17+x}$(FAPbI$_3$)$_{0.83-x}$. According to their DFT calculations, the mixed-perovskite has a negative activation energy for phase separation during operation under vacuum, whereas it is found to be positive in a nitrogen atmosphere at ambient pressure.

Light-Induced Degradation/Halide Migration

PCSs under illumination in absence of other factors have been shown to pass device stability tests exceeding 1000 h in terms of PCE [173–175]. This high stability can be enabled by good encapsulation or storage in an inert atmosphere. However, as soon as one of heat [168], humidity [157], oxygen [155] or reverse bias [176] are involved, illumination becomes a driving force for degradation.

MAPbI$_3$

MAPbI$_3$ solar cells can suffer fast degradation upon exposure to light [162]. The effects of light-induced degradation are strongest when combined with the presence of O$_2$. Then, the chemical deprotonation reaction 2.15 can be severe [162]. When isolating the effects of illumination on MAPbI$_3$ halide migration occurs away from the illuminated area [177]. This leads to an increase in photoluminescence intensity in the illuminated area, likely due to the formation of point defects such as halide vacancies caused by the migration. However, halide vacancies can serve as non-radiative recombination centers, impeding charge transport [178].

By (partially) substituting I with Br in the compound MAPb(I$_{1-x}$Br$_x$)$_3$, the bandgap can be increased and adjusted to e.g. tandem solar cell use. Problematically, MAPb(I$_{1-x}$Br$_x$)$_3$ suffers from halide phase segregation under illumination, resulting in I-rich and Br-rich domains [179]. The light-induced segregation begins above a threshold excitation intensity and the segregation speed is enhanced with increasing intensity [89]. The low-bandgap I-rich phases will effectively act as carrier traps, since all photoluminescence originates from the lower energy state provided in the I-rich phase compared to the Br-rich phase due to the halide-induced shift in valence band minimum and conduction band maximum [10]. Astonishingly, as long as no further degradation occurs demixed halide perovskites slowly remix in the dark and so halide segregation is not viewed as a long-term stability problem by some [10].

Separated I-rich and Br-rich phases are estimated to correspond to x=0.2 for the I-rich majority phase and x=0.7 for the Br-rich minority phase [93]. The phase separation can take its reverse reaction by entropic mixing under darkness, even though this inverse process is slower than the original segregation [89, 180].

The combination of charge carriers with long life times, electron-phonon coupling and mobile halides was found to drive the formation of I-rich clusters in MAPb(I,Br)$_3$ [181]. The cluster size is 8 to 10 nm of diameter, whereas the stoichiometry of the remaining bulk would not change.

In a theoretical study by Yun et al. using first-principal calculations, the initial halide segregation process is explained by the lower surface potential of grain boundaries compared to the bulk [182]. This leads to upward bending of the bands towards the grain boundaries [182]. The band-bending induces a positive space charge causing I migration towards and along the grain boundaries. The strongly bound Br is less mobile and therefore less likely to migrate, leading to segregation of I-rich and Br-rich phases.

In a DFT-based study a reduction of the charge carrier diffusion length as well as lower excitation intensities were predicted to suppress halide segregation [89]. At $100\,mWcm^{-1}$ electron/hole diffusion lengths below 13 nm are necessary to mitigate halide segregation. This can be realized for mesoporous PSCs, but not in a planar architecture.

An experimental approach by Yoon et al. showed that strong halide deficiency (excess) leads to slower (faster) halide segregation in the layer [183]. However, the recovery kinetics are effected in the same way, enabling faster recovery from segregation in the dark for layers with halide excess. The faster segregation in films with halide excess goes against the idea that halide migration occurs via halide vacancy transport. However, it is explained by the I's (Br's) shorter diffusion distance to an I-rich (Br-rich) domain.

A greatly improved structural stability with a large Br/I ratio of 2/3 can be realized by modifying the lattice by partially replacing MA with 10 % Cs [184]. This allows for stable solar cell operation for above 60 min. Finally, a mixture of MA, Cs and FA allows for a stable and widely tunable mixed-halide perovskite absorber finding its application in the most successful PSCs [44, 185, 186]. In general, the predominant use of FA instead of MA can adopt many of the positive assets of MAPbI$_3$ while combatting the intrinsic instability of the MA component.

FAPbI$_3$

Within the work of this thesis, single-halide FAPbI$_3$ and double-halide FAPb(I,Br)$_3$ as well as double-cation (Cs,FA)PbI$_3$ absorbers were prepared in [H3,H4] and their optic properties studied in [H3]. In the prospect of the applicatin of FAPbI$_3$-based absorbers as solar cells, the importance of their light-induced degradation mechanisms should be understood in order to consider the correct counter-measures during prepartion.

he C-N bonds of FA$^+$ exhibit a resonance characteristic theoretically stabilizing it against HI release under illumination [22]. This renders FAPbI$_3$ more stable in light than MAPbI$_3$ [187,188]. Still, FAPbI$_3$ slowly degrades under illumination, even in vacuum [189]. The decomposition speed of FAPbI$_3$ is dependent on the wavelength of the incoming light [189]. Specifically, photo-degradation is occurs

only for photon energies above the band gap energy (E_g) of the metal halide [190].

As in MAPbI$_3$, illumination leads to the formation of iodine vacancies V$_I$ whose concentration increases with stronger illumination, enhancing non-radiative recombination [178]. The formation of V$_I$ triggers further degradation effects. The V$_I$ react with their charge-balanced defect V$_{FA}$, which triggers PbI$_2$ nucleation [189]. This subsequently leads to irreversible formation of Pb(0) and outgassing of I$_2$.

When exposing FAPbI$_3$ to blue-light in vacuum, the decomposition can therefore be explained via a two-step process: (i) segregation of PbI$_2$ due to evaporation of FAI components (eq. 2.17) and (ii) subsequent formation of metallic Pb(0) during evaporation of I$_2$ (reaction (2.18)) [189]:

$$FAPbI_3 \rightarrow PbI_2 + \text{co-products} \tag{2.17}$$
$$PbI_2 \rightarrow Pb(0) + \text{co-products} \tag{2.18}$$
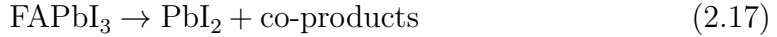
Strong excess use of FAI or I$_2$ leads to the formation of I$_3^-$ via the redox-reaction (2.19). This triggers an additional path for photo-assisted

$$I_2 + I^- \rightarrow I_3^- \tag{2.19}$$

perovskite degradation. Through reaction with the photocatalyst I$_3^-$ and photons $h\nu$, FAI and PbI$_2$ are separated via the chemical reaction (2.20) again leaving the PbI$_2$ to decompose to Pb(0) via the reaction (2.21).

$$3FAPbI_3 + h\nu + I_3^- \rightarrow 3I_3^- + 3FA^+ + 3PbI_2 + 2e^- \tag{2.20}$$
$$PbI_2 + h\nu \rightarrow I_2 + Pb(0) \tag{2.21}$$

Additionally, under llumination the formation energy of the interstitialI$_i$ is increased, which leads to strong formation of I$_2$ and I$_3^-$ in absorbers with high I excess, recursively accelerating degradation as discussed via chemical reactions (2.20) and (2.21 [189]).

Similar to other degradation effects, photodegradation can be combatted by cation mixing. Substituting 10 % of FA with Cs leads to an extended stability determined via absorbance [46]. Under 1 sun illumination in 50 % relative humidity, 50 % of the initial absorption was maintained for 16 h for (Cs,FA)PbI$_3$ instead of 12 h for FAPbI$_3$. Deng et al. improved the photostability of (Cs,FA)PbI$_3$ by adding 0.25 % excessive FAI, while maintaining the initial PCE (without degradation) of 20.2 % [178]. This treatment passivates iodine vacancies and mitigates ion migration and the generation of defects during illumination, leading to a ten-fold increased stability compared to CsI/FAI deficient devices.

Some groups observed slow cation migration and demixing in mixed-cation absorbers under illumination in the time scale of several hours [191–193]. However, others did not make this observation, but instead observed a rise in efficiency during the first hours of operation [10, 194, 195]. This was ascribed to reduction of recombination due to lattice expansion and strain reduction at the interfaces.

2.3 Evaporating Perovskites

A plethora of preparation techniques for perovskite thin films have been studied, of which several reviews give a detailed overview [196–199]. Herein, the focus will be set on establishing technical and physical knowledge of the preparation of perovskite absorbers by evaporation in view of the methods used in [H1–H6].

Evaporation techniques are considered to be easily up-scalable in comparison to solution-based deposition techniques and evaporation is applicable to any given substrate morphology, which is important when e.g. considering deposition onto a structured Si substrate for tandem solar cells [80]. Within the field of perovskite thin film evaporation one needs to differentiate between several techniques. During chemical vapor deposition (CVD) the evaporated components are transported in an inert-gas atmosphere at pressures of 0.01 to 10×10^3 mbar [200] and perovskite growth rates of $60 \, \text{nm} \, \text{min}^{-1}$ can be achieved [201]. However, perovskite solar cells (PSCs) prepared by CVD lag behind in efficiency [202]. Chambers used for physical vapor deposition (PVD) are usually operated under high vacuum from 10×10^{-5} to 10×10^{-6} mbar. In consequence, PVD is expected to provide high-purity layers. This shows in high efficiencies of above 24 % [39] almost on par with the record efficiency for PSCs of 26.1 % prepared by a solution-based technique [2].

During PVD of perovskites, the binary halide salts AX (MAI, MACl, FAI, CsI...) and BX_2 (PbI_2, $PbBr_2$, $PbCl_2$...) and others are usually evaporated from individual sources. The components then react on the substrate during evaporation and post-annealing to form the perovskite phase. Since the components are evaporated individually, a variety of process conducts for multi-step and dynamic approaches are possible.

PVD has been employed in metal halide perovskite thin film preparation as early as 2013 [203]. The focus was laid on simple co-evaporation depositing $PbCl_2$ and MAI on the substrate simultaneously [203]. The optimal ratio of $PbCl_2$:MAI was found to be 1:4, resulting in a strong excess of MAI in the pre-annealed film. During annealing (and $MAPb(I_{1-x}Cl_x)_3$ perovskite formation), loss of mass and thickness indicated the volatilization of the organic component. Further, the X-ray diffraction (XRD) measurements showed no inclusion of Cl in the final film, indicating loss of Cl during annealing and the formation of pure $MAPbI_3$. In other works, the Cl content in such layers was estimated to be below 5 %, if any [204]. Here, the excess of MAI ensured a strong reaction of the organic and inorganic components, which dictates the success of perovskite formation and eventually PSC efficiency.

In 2014, sequential PVD of (1) $PbCl_2$ and (2) MAI was used for the first time to fabricate $MAPb(I_{1-x}Cl_x)_3$ [205]. It was observed that at room temperature only a 25 nm thick $PbCl_2$ layer can be fully reacted by MAI vapor. Increasing the temperature to an optimum of 75°C enabled the transformation of a 150 nm thick $PbCl_2$ layer to the perovskite phase, finding the sweet spot between sufficient MAI adsorption and diffusion reaction. At 65°C the reaction kinetics were too weak leaving behind residual $PbCl_2$. At 85 C, which was also the MAI crucible temperature, the reaction of the MAI on the hot sample surface resulted in impurities in the final layer. By this, the *in situ* substrate temperature was already highlighted as an important factor in perovskite film formation, especially when MAI is used.

In the following year, Teuscher et al. made two further vital observations during co-evaporation of PbI_2 and MAI [206]. They recognized that MAI evaporates nearly omnidirectionally, necessitating additional parameters apart from the crucible temperature to ensure reproducible deposition. A consequence of omnidirectional evaporation is a high partial pressure of MAI in the chamber. Teuscher et al. assumed that the chamber pressure consisted mainly of the MAI partial pressure. The chamber pressure was kept constant during evaporation by coupling it to the MAI crucible temperature in an attempt to control the MAI evaporation rate via the chamber pressure. Finally, the optimum PbI_2/MAI ratio was measured at 1:0.96 yielding an efficiency of 12 % [206]. With this, the idea to dynamically vary the stoichiometry within the film via pressure-controlled flux control was introduced.

The role of the MAI partial pressure was extensively studied in 2018 by Baekbo et al. who observed that the MAI had a low sticking coefficient on the sample and chamber walls and would constantly re-desorb, maintaining high partial pressure [207]. The sticking coefficient on the sample was improved by providing a $PbCl_2$ precursor layer for the MAI to react with. The thickness of the $PbCl_2$ layer determined the amount of MAI that would be able to condense. With the help of a mass spectrometer attached to the vacuum chamber, a partial decomposition of the MAI precursor during evaporation was observed. The main products of this decomposition were CH_3NH_2 and HI and smaller amounts of the MAI-dimer $(CH_3NH_3I)_2$ via chemical reactions (2.22) and 2.23.

$$2CH_3NH_3I \leftrightarrow (CH_3NH_3I)_{2(g)} \tag{2.22}$$

$$CH_3NH_3I \leftrightarrow CH_3NH_{2(g)} + HI_{(g)} \tag{2.23}$$
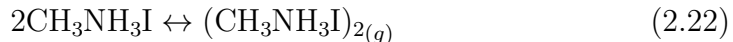
The formation of several decomposition products explains the high partial pressure during evaporation of MAI and leads to another conclusion confirming earlier works: since the decomposition products have to react on the surface to form MAI, high impingement rates and therefore high partial pressures (higher than usual PVD chamber pressures) are needed to ensure transformation to the perovskite phase.

Initial growth behavior of perovskite thin films with MAI is strongly determined by the sticking factor of MAI. However, results on the nucleation of MAI-based perovskites differ. Borchert et al. showed that material impurities, which vary from one MAI batch to the next, increase MAI sticking and are an influential factor in terms of MAI condensation [208]. Two studies employed X-ray photoelectron spectroscopy (XPS) and ultraviolet photoelectron spectroscopy (UPS) and XRD and detected a thin PbI_2 layer prior to perovskite growth due to low MAI sticking-factor on the substrate [209, 210] . In another report by Olthof et al. crystallization during co-evaporation was observed to depend strongly on the substrate type [211]. They found no unreacted PbI_2 to be present during the first stages of the process and organic precursor layers enabled a faster crystallization of the perovskite phase than metal oxides. On metal oxide precursor layers (ITO and MoO_3), perovskite growth was slowed down due to re-volatilization of the deposited materials because the metal oxide precursors acted as catalysts [211]. Thus, a passivation layer had to be deposited prior to the commencement of perovskite growth. Organic precursors (polyethylenimine ethoxylate, PEIE and Poly(3,4-ethylenedioxythiophene)-poly(styrenesulfonate), PEDOT:PSS) enabled

faster condensation of both MAI and PbI_2 causing perovskite growth from the beginning.

Cojocaru et al. co-evaporated $MAPbI_3$ on TiO_2 and weak charge extraction in the PSC, presumably due to a high concentration of interfacial traps located at the TiO_2/$MAPbI_3$ interface [212]. An organic phenyl-C_{61}-butyric acid methyl ester (PCBM) interlayer was used to enhance charge extraction and greatly increase the efficiency of the cell.

During co-evaporation of MAI and PbI_2 in an experiment by Parrott et al. the perovskite exhibited Volmer-Weber type island growth (see section 3.1) up to a thickness of $8\,nm$, fully covering the quartz substrate starting from $10\,nm$ [213]. In this publication, the island growth was made out as the root cause for low crystallite sizes in co-evaporated layers. Furthermore, the substrate was predicted to strongly influence the crystallization process and the choice of optimal substrate was suggested to largely improve the film quality in terms of grain size. A lattice matched substrate could enable epitaxial growth and incentivize Frank-van der Merwe type layer-by-layer growth (see section 3.1), drastically increasing crystallite sizes and therefore efficiency and stability.

The $MAPbI_3$ crystallite size can also be controlled by the substrate temperature [214]. The colder the substrate, the greater the MAI adsorption and MAI/PbI_2 ratio in the final film and the larger the perovskite crystallites were determined to be. However, large ($\sim 1\,\mu m$ crystallites grown by improved MAI adsorption proved detrimental for PSC performance. Presumably the large share of organic components causes high trap densities within the grains hindering charge transport. Instead, a PbI_2 excess obtained by a process at relatively high substrate temperature (room temperature) was the most successful in terms of device performance. A benign PbI_2 excess is a commonly observed property in PSC and is assigned to a trap passivating effect of the PbI_2 at grain boundaries [215]. The effect of greater MAI incorporation on the layer properties was exploited in a dynamic co-evaporation approach [40]. Depending on the PSC structure, the MAI/PbI_2 ratio was gradually reduced (p-i-n structure) or increased (n-i-p) throughout the course of the evaporation by gradually decreasing/increasing the MAI partial pressure in the chamber. This induced Fermi-level grading in the absorber and led to ¿20 % efficiency consistently [40].

Using TEM imaging Rothmann et al. observed the interplay of PbI_2 and perovskite ($MAPbI_3$ and $FAPbI_3$) growth during evaporation [216]. Specifically, PbI_2 was shown to intergrow with the perovskite without the formation of grain boundaries between the two phases. PbI_2 adapted to the perovskite lattice by assuming a distorted phase, deviating from its usual hexagonal structure and PbI_2 domains interweaved with perovskite domains on all sides. The perovskite domains exhibited a shift of half a unit cell across the PbI_2. From this it was presumed, that the PbI_2 is not a result of degradation a posteriori, but acts as a seed to perovskite growth.

As elaborated in section 2.2, modern PSCs have shifted from the use of $MAPbI_3$ to $FAPbI_3$, since the latter offers several advantages such as a lower bandgap and higher stability against heat due to FAI being less volatile as MAI (see section 2.2.3). Nonetheless, stable evaporation of FAI requires special caution, because can also dissociate upon evaporation, forming formamidine ($CHNHNH_2$) and I_2, but also triazine ($C_3H_3N_3$) and cyanide (HCN) [171]. There-

fore, the chamber pressure can increase during evaporation of FAI and has to be considered as an important process parameter. The evaporation temperature must be chosen carefully, since the local pressure at the evaporation source orifice can increase faster than in the rest of the chamber, yielding a low mean free path and therefore low FAI impingement and deposition rates on the sample. At $\sim$200°C, FAI degrades completely, but sufficiently high deposition rates can be reached at lower temperatures with low influence on the pressure. Consequently, FAI evaporation is easier to control than MAI evaporation, but careful process gauging has to be done.

When preparing the $MAPbI_3$ tetragonal perovskite phase via co-evaporation, no post-annealing is necessary, since the tetragonal phase is stable at room temperature [214]. This is different for $FAPbI_3$ because the hexagonal δ $FAPbI_3$ phase is energetically more favorable than the cubic α perovskite phase at room temperature (see section 2.2.3). To obtain the α phase via co-evaporation, Borchert et al. needed a short post-annealing step at 170°C [72]. Still, they were able to achieve $FAPbI_3$ co-evaporation with homogeneous coverage on large-area substrates and reduce the root mean square roughness compared to other deposition methods.

The post-annealing temperature in a co-evaporation process can be reduced to 135°C by partial substitution of FA with Cs and I with Br [217]. The choice of poly(triaryl amine) (PTAA) as the HTL and precursor layer yielded larger crystallites and α phase crystallization was possible at 5 % excess PbI_2 in this configuration. The crystallization of the α phase was enabled at room temperature, when [2(3,6-dimethoxy-9H-carbazol-9-yl)ethyl]phosphonic acid (MeO-2PACz) was used as hole transport and seed layer in a *p-i-n* structure and an FAI excess was deposited [80]. The free phosphonic acid groups of MeO-2PACz can interact strongly with FAI, forming hydrogen bonds [161]. This could enable an increased incorporation of FAI into the layer, which stabilizes the α phase and yields efficiencies up to 24.6 % [80].

Sequential evaporation of $FAPbI_3$ can enable easier process control and be done in less complicated setups using only one quartz crystal monitor [218]. When evaporating FAI on top of a PbI_2 precursor layer, Yan et al. found the reaction during annealing was limited by the diffusion of FAI and organic species were not observed throughout the final layer, leaving large amounts of unreacted PbI_2 after 30 min of annealing [219]. The reaction of PbI_2 and FAI was enhanced by depositing CsBr as a third and final layer before post-annealing. The triple-layer stack reacted faster allowed perovskite formation within 5 min of annealing. A similar feat was achieved by Feng et al. by evaporating CsI after successive PbI_2 and FAI evaporation [220]. This approach allowed low-temperature annealing at 60°C and high efficiency of 21 %. Li et al. have performed a very successful sequential process conduct resulting in 24 % efficiency [39]. Their approach consists of a first step in which the inorganic precursors PbI_2, $PbCl_2$ and CsI are co-evaporated and a second step during which FAI is deposited. This is followed by annealing at 170°C to drive the reaction and interdiffusion.

3 Experimental Methodology

This section explains the theoretical background of thin film growth in a vacuum chamber and the characterization techniques employed within this thesis. First, vacuum thin film growth is theoretically elaborated including the steps of phase transition, vapor transport and nucleation. For a practical literature review on perovskite evaporation refer to section 2.3. Subsequently, the actual preparation setup including the vacuum chamber and device characterization via *in situ* XRD is presented. Finally, complementary measurement techniques including GI-WAXS (grazing incidence wide angle X-ray scattering), SEM (scanning elctron microscopy), EDX (electron dispersive X-ray spectroscopy), *j-V* (current density - voltage) analysis, PL (photoluminescence) and time resolved photoluminescence (TRPL) are briefly discussed.

3.1 Film Formation from the Vapor Phase

This thesis is centered around the preparation of thin films by physical vapor deposition (PVD), i.e. via thermal evaporation of source material in a vacuum chamber. In this subchapter, a review on the fundamentals of thin film evaporation is given along the lines of Maissel and Glang [221][1] as well as Frey and Khan [222]. According to Maissel and Glang, the deposition via PVD can be split into three steps which are considered individually in the order:

1. Phase transition from condensed (solid or liquid) to a gaseous state (sublimation or evaporation)
2. Vapor transport from source to sample
3. Particle impingement on the substrate, re-condensation on its surface and nucleation

The above-mentioned steps are used as a structure for the the following theoretical explanations. Step 3 is discussed in terms of impingement and nucleation separately.

3.1.1 Sublimation and/or Evaporation

When a material is evaporated, the rate of its phase transition from solid/liquid (condensed phase) to the vapor phase depends on the applied source temperature T_{eva}. Accordingly, T_{eva} also determines the amount of material present in the vapor phase in the vacuum chamber, i.e. its partial pressure. The materials saturation vapor pressure (or equilibrium pressure) p_v is reached when both condensed and vapor phases exist in equilibrium. Then, an equal number of particles undergo the transition from the condensed to the vapor phase as in the opposite direction. p_v scales non-linearly with the temperature and a high p_v corresponds to a high volatility of the material. p_v can be calculated by means of the Clausius-Clapeyron equation 3.1 [221, p. 1-9].

$$\frac{dp_v}{dT} = \frac{\Delta H_{eva}}{T(V_v - V_s)} \tag{3.1}$$

---

[1]The page number in "Handbook of Thin Film Technology" by Maissel and Glang is reset with the beginning of each chapter. Therefore, the page number 2-11 corresponds to page 11 of chapter 2.

ΔH_{eva} is the standard free enthalpy of evaporation, i.e. the heat necessary to vaporize the condensed material. ΔH_{eva} corresponds to the difference between H_v and H_{cond}, the enthalpies of vapor and condensed phases, respectively. V_v (V_c) are the molar volumes of vapor (condensed phase).

The saturation vapor pressure $p_{v,AB}$ in mbar of a compound material AB that does not dissociate upon transition to the vapor phase can be calculated using its standard Gibb's free energy of evaporation $\Delta_{eva}G°(T)$ at the specific temperature T via eq. 3.2 [221, p. 1-11]. $\Delta_{eva}G°(T)$ is given by the difference of the material's chemical potentials $\mu_v(T)$ and $\mu_{cond}(T)$ at the temperature T and standard pressure in the vapor and condensed phases, respectively.

$$log(p_{v,AB}) = -\frac{\Delta_{eva}G°(T)}{RT}log(e) \cdot 10^3 \tag{3.2}$$

For a compound AB that dissociates into the vapor components A and B_2 via $AB \rightarrow A + \frac{1}{2}B_2$, the evaporation involves diffusion of A and B surface atoms with recombination to B_2 molecules prior to entering the gas phase. In this case, the equilibrium between condensed and vapor phases is given when the product of partial pressures p_A and p_{B_2} equals a temperature-dependent pseudo-saturation vapor pressure constant $K_{p_v}(T) = p_A p_{B2}^{1/2}$ given by eq. 3.3 [221, p. 1-69].

$$log(K_{p_v}(T)) = -\frac{\Delta_{eva}G(T)}{RT}log(e) \tag{3.3}$$

In the following, the evaporation of a single, non-dissociating material is considered. The material's vapor pressure p_v dictates the amount of material that can be present in the vapor phase. Therefore, it also defines the evaporation rate of the material through the evaporation source orifice. Hertz determined the evaporation rate to be proportional to the difference between p_v at the surface temperature of an evaporating liquid ($\sim T_{eva}$) and the partial pressure $p_{p,s}$ acting on its surface [223]. The number of particles dN evaporating during dt from a surface area A can be calculated via eq. 3.4. The negative term $p_{p,s}$ accounts for the pressure exerted on the evaporation surface by a backstream of particles to said surface. Hertz concluded that a liquid cannot exceed a given maximum evaporation rate R_{max} at a constant temperature and R_{max} would require particles to leave the surface in the same number as would be necessary to apply p_v on the surface of the evaporating liquid. Additionally, none of the leaving particles would be allowed to return, rendering $p_{p,s} = 0$.

$$\frac{dN}{Adt} = (2\pi m k_B T)^{-\frac{1}{2}}(p_v - p_{p,s}) \tag{3.4}$$

$$\frac{dN}{Adt} = \xi(2\pi m k_B T)^{-\frac{1}{2}}(p_v - p_{p,s}) \tag{3.5}$$

The backstreaming particles undergo a phase transition back to the liquid phase and do not contribute to $p_{p,s}$ anymore. However, a fraction $(1 - \xi)$ of particles is reflected from the evaporating surface, stays in the vapor phase and still contributes to the partial pressure of the evaporated material. The evaporation coefficient ξ can be determined by the ratio of observed vacuum evaporation rate (via measurement) and theoretically possible value (via eq. 3.4). Eq. 3.4 then

becomes the Hertz-Knudsen equation 3.5 [224]. Knudsen found the maximum evaporation rate for a perfectly clean surface of Hg to be $(2\pi m k_B T)^{-\frac{1}{2}} p_v$ [224].

The Hertz-Knudsen equation was initially established for evaporation from the liquid phase. Langmuir showed that it can also be applied to evaporation from free solid surfaces (no shear stress parallel to the surface) [225]. The total mass evaporation rate Π_{eva} of the solid can be determined by multiplying the Hertz-Knudsen equation with the molecular mass m as given in eq. 3.6. The total evaporated mass M_{eva} can then be determined by the double integral in eq. 3.7. This type of evaporation from free solid surfaces is termed free evaporation or Langmuir evaporation [225].

$$\Pi_{eva} = m\frac{dN}{Adt} = \left(\frac{m}{2\pi k_B T}\right)^{\frac{1}{2}} (p_v - p_s) \tag{3.6}$$

$$M_{eva} = \int_t \int_A \Pi_{eva}\, dAdt \tag{3.7}$$

To further understand the phase transition step, an idealized isothermal spherical evaporation source which maintains p_v is assumed (Knudsen source). The material's evaporation surface is large compared to the small orifice [221, p. 1-27]. The Knudsen source assumes infintesimally thin walls which do not allow scattering or absorption of gaseous material travelling through the orifice, hence $\xi = 1$, since all particles that pass the orifice leave the source. Langmuir determined that if the diameter of the orifice with area A_o is less than 0.1 of the vapor particles' mean free path length $\bar{\lambda}$ (see next section and eq. 3.8), the particle flux per second through A_o is $A_o(2\pi m k_B T)^{-\frac{1}{2}}(p_v - p_{p,s})$ [225].

The theory of evaporation for crystalline solids is more complicated than for liquids due to the binding forces holding the atoms within the lattice. Surface atoms or cornering atoms are weaker bound than bulk atoms due to their lower number of neighbours and therefore their removal from the lattice for evaporation is easier. Volmer described that an atom would free itself from most of its nearest neighbours before diffusing along the surface in a semi-bound state and finally evaporating [226]. The evaporation of crystalline solids can therefore be described as the reverse of their growth process due to the process of enacting or counteracting of binding energies defining their state.

Polycrystalline metals with monatomic vapors such as Ag, Cu or Be can yield evaporation coefficients ξ of 1 when their surface is clean, but when the surface of Be is subjected to oxygen its ξ was reduced to 0.02 due to chemisorption of O and resulting surface impurities [221]. Polycrystalline solids that evaporate as polyatomic molecules (Se, Te, P, C) and compounds that dissociate upon evaporation (NH_4Cl, Al_2O_2) are subject to more complicated processes and their ξ varies from ≈ 1 for Te_2 vapor to $\approx 10 \times 10^{-7}$ for P_2 and P_4.

3.1.2 Vapor Transport

The mean energy in eV of vapor particles leaving the evaporation source amounts to $mv^2/2 = \frac{3}{2}k_B T = 1.29T$ [222] with the particle mass m, its velocity v and temperature T. Thus, vapor particles travel at high speeds, but are slowed and redirected by collisions with other particles along their path. The average path a particle travels between two collisions is given by the mean free path $\bar{\lambda}$. For

an approximation of $\bar{\lambda}$ it is assumed that only the considered particle is moving at a speed of $\bar{c}$ while all other particles are at rest. All particles are assumed to have the same diameter σ so that the moving particle collides with those particles whose centers lie within a cross-sectional area of $\pi\sigma^2$ in its path. It follows that collisions will only occur in a volume $\pi\sigma\bar{c}dt$. Multiplication with the particle volume density $\frac{N}{V}$ yields the collision frequency $\frac{N}{V}\pi\sigma\bar{c}dt$, from which $\bar{\lambda}$ is derived in eq.3.8 [221, p. 1-22]. When the relative motion of all other particles is

$$\bar{\lambda} \approx \left(\frac{N}{V}\pi\sigma^2\right)^{-1} \tag{3.8}$$

$$\bar{\lambda} \approx \frac{k_B T}{p\pi\sigma^2\sqrt{2}} \tag{3.9}$$

considered and the gas pressure p substituted for $\frac{N}{V}$ as for an ideal gas, the expression becomes eq. 3.9.

The actual free path length x of a single particle is based on a statistical distribution by eq. 3.10. The fraction N/N_0 corresponds to the fraction of molecules that have not collided after travelling a collision-free distance of x.

$$\frac{N}{N_0} = exp\left(\frac{-x}{\bar{\lambda}}\right) \tag{3.10}$$

Further corrections to $\bar{\lambda}$ need to be made when considering that particles do not scatter like solid spheres but exert attractive and repulsive forces upon each other. Therefore, effective collision cross sections should be considered which vary with the type of experiment. For calculation of the latter refer to ref. [227]. For N_2 molecules, the effective diameter lies at $\sim 3.74\,\text{Å}$ [227], which yields an effective cross-section of $43\,\text{Å}^2$. Using the above information, $\bar{\lambda}$ of PbI_2 in a N_2 background atmosphere at $2.5 \times 10^{-5}\,\text{mbar}$ can be approximated. Since no measurable pressure change occurs upon evaporation of PbI_2 in our chamber the vapor particle density of PbI_2 is neglected. Using the ideal gas law the particle density of N_2 becomes $n_{N2} = p/(k_B T) = 6.08 \times 10^{17}\,\text{m}^{-3}$ at $298\,\text{K}$. The ionic radii r_{ion} of Pb^{2+} and I^- in a PbI_2 vapor molecule are $1\,\text{Å}$ and $1.6\,\text{Å}$, respectively. The effective radius of PbI_2 is approximated at $\sigma_{PbI_2} = r_{Pb^{2+}} + 2r_{I^-}$ which gives $\sigma_{PbI_2} = 4.2\,\text{Å}$ and a cross-sectional area $\pi\sigma_{PbI_2}^2 = 55.4\,\text{Å}$. It follows using eq. 3.9 that $\bar{\lambda}_{PbI_2} = 2.1\,\text{m}$ in the given low pressure N_2 atmosphere.

Upon co-evaporation of other materials such as MAI the $\bar{\lambda}_{PbI_2}$ can be reduced, since the chamber pressure is increased by the partial pressures of the other materials. This effect is specifically strong for co-evaporation with MAI, since MAI dissociates into multiple products upon evaporation [207], each increasing the chamber pressure via their partial pressure.

3.1.3 Particle Impingement

Following the evaporation of particles that leave the source through its orifice and their transport through high vacuum, a statistical share of the particles according to eq. 3.10 impinge on the sample surface. Similar to the evaporation rate in eq. 3.4, the impingement rate $\frac{dN}{A_r\,dt}$ of particles with individual mass m on

a receiving substrate area A_r can be expressed with the materials partial pressure $p_{p,sub}$ at the substrate surface via eq. 3.11 [221, p. 1-21].

$$\frac{dN}{A_r\, dt} = (2\pi m k_B T)^{-\frac{1}{2}} p_{p,sub} \tag{3.11}$$

Assuming a Knudsen evaporation source (section 3.1.1) and an area at shortest distance l to the source orifice, the received mass dM_r on the sample per unit area dA_r can be described via the cosine-law in eq. 3.12 [221, p. 1-34].

$$\frac{dM_r}{dA_r} = \frac{M_{eva}}{\pi l^2} cos(\phi) cos(\theta) \tag{3.12}$$

M_{eva} is the total evaporated mass according to eq. 3.7 in section 3.1.1. ϕ gives the particle emission angle with respect to the normal of the source orifice whereas θ denotes the incidence angle of particles with respect to the surface normal of the unit area dA_r they impinge.

Usually, the evaporation source orifice is disk-shaped and the substrate is plane-parallel to the orifice. For this case, the thickness of a condensed mass M_r in a volume $dA_r\, d$ on the substrate can be calculated via eq. 3.13 [221, p. 1-55] with the density ρ of the growing material.

$$d = \frac{1}{\rho}\frac{dM_r}{dA_r} \tag{3.13}$$

Then, the distribution of d on the sample is centrosymmetrical around the projection of the orifice. This means d at a certain location on the sample can be described by its distance y to the center of the projection of the orifice. A fraction of a ring element dA_o of the disk orifice can be expressed as $dA_o = r\, d\alpha\, dr$ with the ring radius r pointing towards dA_o from the center of the orifice and the angle α between y and the projection of r onto the sample. Specifically, α is in-plane with the sample. Transferring this geometry to the cosine-law it follows $cos\,\phi = cos\,\theta = h/l$ with the shortest distance l between dA_o and dA_r and the distance h between the parallel planes of substrate and orifice, respectively. Finally, the thickness d at dA_r becomes the triple integral across α, r and the time t in eq. 3.14 [221, p. 1-57] with Π_{eva} as defined in eq. (3.6).

$$d = \int_t \int_r \int_\alpha \frac{\Pi_{eva}\, d\alpha\, dr}{\pi\, \rho}\frac{h^2}{l^4}dt \tag{3.14}$$

Via approximation by a series development the thickness distribution along the sample with d_0 at $l = 0$ then becomes eq. 3.15 [221, p. 1-59]

$$\frac{d}{d_0} \approx \frac{1 + (r/h)^2}{[1 + (y/h)^2]^2 + [1 - (y/h)^2](r/h)^2} \tag{3.15}$$

For this approximation of the thickness gradient it was assumed that all impinging particles condensate. However, condensation is a more complex process as discussed in the following.

3.1.4 Adsorption, Nucleation and Condensation

In the previous sections a material's phase transition, vapor transport and impingement onto a sample were considered. Actual condensation, nucleation and growth into a thin film are determined by further conditions that are discussed in the following.

The equilibrium impingement rate on a substrate is determined by a material's p_v at their respective source temperature T_S as given by eq. 3.11. The condensation on the substrate depends on the respective partial pressure $p_{p,sub}$ at the substrate. Considering source and sample with evaporation characteristics according to the cosine-law (eq. 3.12), a mass evaporation rate from the source as given in eq. 3.6 and an impingement rate on the sample in terms of eq. 3.11, $p_{p,sub}$ can be expressed via eq. 3.16 [221, p. 1-89].

$$p_{p,sub} = \frac{A_o \, cos(\phi) cos(\theta)}{\pi l^2} p_v(T_{eva}) \tag{3.16}$$

Condensation on the surface of a substrate from the vapor phase occurs when the material's $p_{p,sub}$ is equal to or higher than its p_v at the substrate surface temperature T_{sub}, i.e. when the vapor is supersaturated with respect to the temperature of the substrate surface. The relationship between condensing vapor particles to impinging particles is given by the condensation coefficient χ with $0 < \chi \leq 1$. Since T_{sub} is usually low compared to T_{eva}, the vapor is commonly supersaturated with respect to the substrate surface leading to a high χ. A higher T_{sub} decreases the number of condensing particles, i.e. decreases χ until the critical temperature T_c is reached at which all particles are reflected from the substrate surface. T_c can be raised by increasing the impingement rate. Materials with lower evaporation temperatures in general exhibit a lower χ at a constant T_{sub}. This is well known for e.g. MAI and referred to as a low "sticking factor" in many works [207, 214] [H1]. χ can be improved by using a seed layer - in the case of MAI it has been shown that PbI_2 can be employed [H1].

Condensation is considered as the process of a phase transition from the vapor to a condensed phase. This phase transition occurs via adsorption at a surface, nucleation and the formation of large agglomerates that become stable at a critical size. In order to examine condensation more closely, the intermediate steps are considered.

Adsorption

Vapor particles emitted from an evaporation source have a mean kinetic energy of $1.29\,T_{eva}$ eV with the source temperature T_{eva}. In order for adsorption to occur, the particle needs to equilibrate with the substrate rapidly. The probability for equilibration with the surface is given in eq. 3.17 [221, p. 8-5] by the thermal-accommodation coefficient α_T with $0 < \alpha_T \leq 1$.

$$\alpha_T = \frac{E_{i,kin} - E_{des}}{E_{i,kin} - E_{des,eq}} = \frac{T_{i,kin} - T_{des}}{T_{i,kin} - T_{des,eq}} \tag{3.17}$$

$E_{i,kin}$, E_{des} and $E_{des,eq}$ correspond to the incidental kinetic energy and to the energy of a desorbed (i.e. reflected) atom before and after equilibration with the substrate, respectively. The given temperatures are defined accordingly. It was

shown that incoming vapor particles can lose all their $E_{i,kin}$ unless they are very light or have extremely high $E_{i,kin}$ (corresponding to $6000\,\mathrm{K}$) [221]. The high likeliness of their energy loss can be explained by the short time scale during which it occurs: $2/\nu$ - with the frequency of substrate phonons ν. $\chi = 1$ as assumed in the previous section is therefore not unlikely for many materials.

Assuming no stable condensation of vapor particles, an equilibrium between impinging and re-evaporating particles is reached. The substrate coverage by adsorbed molecules n_{ad} is then determined by the impingement rate R via eq. 3.18 [221, p. 8-7]. ΔG_{des} and ν_{des} are the Gibb's free activation energy required for a desorption process and the desorption frequency, respectively.

$$n_{ad} = \frac{R}{\nu_{des}} exp\left(\frac{\Delta G_{des}}{k_B T}\right) \tag{3.18}$$

The adsorbed vapor particles travel along the surface until they desorb or reach a fixed position by forming a stronger bond with the surface atoms. This is most likely to occur at defects due to the larger amount of unterminated bonds. Since the binding energy between a vapor particle and the substrate is usually lower than the binding energy between two vapor particles, most particles diffuse until they find another and subsequently remain in a fixed position. If $R \rightarrow 0$ so that the likelihood of two adsorbed particles meeting can be neglected, the substrate coverage by adsorbed atoms is nullified. The mean time an adsorbed molecule resides on the substrate surface is τ_{ad} and can then be given in eq. 3.19 [221, p. 8-7].

$$\tau_{ad} = \frac{1}{\nu_{des}} exp\left(\frac{\Delta G_{des}}{k_B T}\right) \tag{3.19}$$

Consequently, most condensation theories postulate an equilibrium of the density of adsorbed particles and define a critical size, at which agglomerates become more likely to grow further than to dissociate and desorb.

Agglomerate Formation and Nucleation - The Capillarity Model

In order for adsorbed vapor particles to agglomerate, the particles' residence time τ_{ad} (eq. 3.19) on the sample needs to be high enough so that two adsorbed particles can find each other, since their interaction with each other is usually stronger than with the substrate and can render their state on the surface more stable. Put differently, the impingement rate R of particles on the sample has to be high enough, so that at any given point there are always adsorbed particles within their surface-traveling distance of each other in their adsorbed state. For this condition to be satisfied, a supersaturation greater than 1 at T_{sub} is necessary to allow for the adsorption to be greater than desorption. Only then, the adsorbed particles can agglomerate and eventually - if the agglomerates reach a stable size - nucleate. A nucleated agglomerate (nucleus) has reached a stable condensed state and does not dissociate, but it accumulates more particles and grows further, as long as supersaturation is given.

The capillarity model uses the Gibb's free energies G of the agglomerate's respective surfaces, interfaces and volume to define its stability. The model gives the difference ΔG between the agglomerate's adsorbed/nucleated state and its

fully dissociated state in the vapor phase depending on its average linear dimension r in eq. 3.20 [221, p. 8-8]. Accordingly, an agglomerate with positive ΔG is unstable and likely to dissociate and an agglomerate with negative ΔG has reached a stable, nucleated state. The capillarity model postulates that, in order for an agglomerate to nucleate, a maximum in ΔG - a critical ΔG_c has to be overcome, before negative ΔG can be acquired.

$$\Delta G = a_1 r^2 \sigma_{agg-vac} + a_2 r^2 \sigma_{agg-sub} - a_2 r^2 \sigma_{sub-vac} + a_3 r^3 \Delta G_{cond} \qquad (3.20)$$

ΔG in eq. 3.20 consists of 4 terms. The surface (between agglomerate and vacuum) term $a_1 r^2 \sigma_{agg-vac}$ uses the agglomerate's surface area $a_1 r^2$ (a_n are constants that take into account the agglomerate's shape) and the surface's Gibb's free energy $\sigma_{agg-vac}$ to account for the increase of ΔG during growth of the agglomerate's surface. The summand $a_2 r^2 \sigma_{agg-sub}$ defines the interfacial (between agglomerate and substrate) G analogously with the interfacial area $a_2 r^2$ and the energy term $\sigma_{agg-sub}$. The third surface area term $a_2 r^2 \sigma_{sub-vac}$ contributes the loss of G of the substrate surface area that is covered up during formation and development of the agglomerate. It is considered negatively, since the substrate's surface G is reduced by the agglomerate's coverage. Finally, the term $a_3 r^3 \Delta G_{cond}$ incorporates the agglomerate's volume ($a_3 r^3$) contribution. ΔG_{cond} is the difference between G of a condensed particle in the bulk and the same particle's G in its vapor state as a monomer. ΔG_{cond} is defined by the film material's volume V of a single particle (monomer), the impingement rate R of particles on the substrate and the re-evaporation rate R_{bulk} of bulk particles in eq. 3.21 [221, p. 8-8]. R/R_{bulk} is the supersaturation ratio with $R > R_{bulk}$.

$$\Delta G_{cond} = -\frac{k_B T}{V} ln \frac{R}{R_{bulk}} \qquad (3.21)$$

Small agglomerates with high surface-to-volume ratios have high surface energies which can make them unstable. When an agglomerate grows, the dissociation probability increases at first due to an increase in surface area and, accordingly, ΔG grows due to the surface terms. The maximum ΔG is reached when the agglomerate reaches a critical size (it is then called critical nucleus). The corresponding $r = r^*$ is determined by eq. 3.22 via differentiation of eq. 3.20 [221, p. 8-8].

$$r^* = \frac{-2(a_1 \sigma_{agg-vac} + a_2 \sigma_{agg-sub} - a_2 \sigma_{sub-vac})}{3 a_3 \Delta G_{cond}} \qquad (3.22)$$

A critical nucleus has the most unstable agglomerate size - i.e. highest Gibb's free energy ΔG with respect to its complete dissociation and evaporation - due to its large surface-to-volume ratio and corresponding high surface energy. Removing an atom from a critical nucleus will make it more likely to dissociate. However, adding an atom to a critical nucleus makes it more stable and increases its likelihood to grow in size and form a permanently condensed deposit (nucleus). For $r > r^*$ the r^3 term in eq. 3.20 dominates and the agglomerate's stability increases rapidly due to the binding force between agglomerated particles exerted by the condensation energy ΔG_{cond} in the bulk.

The capillarity model explains the principal necessity of an agglomerate to reach a certain size in order to stabilize its condensed state sufficiently well.

However, it applies bulk surface energies to small agglomerates, making calculations for small critical agglomerate sizes r^* inaccurate. For small r^*, the Atomic Small-cluster Model is more exact, because it defines a potential internal energy E_N giving the energy of dissociation of an agglomerate containing N atoms into N desorbed monomers. More details can be found in ref. [221].

Film Growth Modes

Following the formation of critical nuclei the growth of a thin film is finally enabled. Pashley et al. have distinguished four stages of growth via *in situ* electron microscopy [228]: i) nucleation and island growth ii) joining of islands iii) channel and hole formation iv) growth of continuous film. Depending on the saturation vapor pressure, impingement rate, source and substrate temperatures, adhesion and cohesion energies and other parameters, the islands develop varying contact angles to the substrate and grow smaller or larger before joining and forming a continuous film.

Three distinct modes are usually considered: i) layer-by-layer (Frank-van der Merwe) ii) island (Volmer-Weber) iii) layer-plus-island (Stranski-Krastanov) growth [222]. A low specific surface free energy (SFE) of the agglomerate incentivizes layer-plus-island growth. This mode requires similar lattice parameters for substrate and deposit, which allows for initial epitaxial growth up to a critical thickness. Subsequently island formation releases strain caused by lattice misftis between the substrate and deposit [229]. Higher SFEs first lead to island growth and eventually, for very high SFE, to layer-by-layer growth in order to minimize the surface-to-volume ratio. These two growth types are not limited to lattice-matched deposits and substrates. Island growth is usually favored for cases when the cohesion energy (between particles of the evaporated material) is larger than the adhesion energy (between material and substrate). This causes the material to agglomerate rather than spreading out homogeneously to form a uniform layer [230]. Accordingly, layer-by-layer growth is favored when the adhesion energy is greater than the cohesion energy.

Defects During Growth

During the early stages of nucleation, the small island-type grains will perform single-crystal-like growth. Upon touching with other islands the formation of grain boundaries can lead to defects.

Dislocations are the type of defect most frequently encountered in evaporated films. Dislocations are linear defects that exhibit an abrupt change in the atomic arrangement and will usually end in another defect or extend to the boundary of the crystal. They can be the origin of lattice rotations or displacements between the respective joining islands. They may also result from interfacial stress release between substrate and film. Still, most dislocations develop while islands join and channels/holes on the substrate surface are covered up.

Another natural origin of defect formation are grain boundaries that can also form when islands join. In general, the higher T_{sub} during evaporation or annealing, the larger the grains will become since the film will decrease its total energy by reducing its grain boundary area. Lower T_{sub} will lead to smaller grain sizes. R also influences grain formation. At high rates the adsorbed particles

will not be able to diffuse before being buried under the next layer of impinging vapor particles, potentially inhibiting diffusion and promoting lattice faults. However, the rate needs to be above a certain threshold in order to dominate over the temperature-induced effects. Below this threshold solely T_{sub} determines the grain size. Above the threshold higher rates will decrease grain sizes.

Since higher T_{sub} also enhances diffusion, because of the higher mobility of the involved particles and their enhanced ability to reach an "ideal" position within the lattice, lattice defaults in the bulk are reduced. Lower T_{sub} in turn increase the surface area, possibly by allowing protruding peaks to shadow the substrate surface and film area from impinging vapor particles.

3.2 Thin Film Preparation

3.2.1 Setup for Evaporation of Perovskite Absorbers

For deposition of perovskite absorbers a high vacuum chamber with a base pressure of 2×10^{-5} mbar was used. The vacuum chamber is a self-made hollow steel cuboid designed by our group (photograph in fig. 3.2). A turbo molecular pump (TMP) and a fore-pump are firmly attached. The installation is fixed on an aluminum setup and can be moved through the laboratory on wheels in order to allow for the exchange of different vacuum chambers for different materials (CuInGaSe, CuZnSnSe, InS) in the *in situ* XRD system (see chapter 3.3).

During this thesis, up to 5 evaporation sources were used in the chamber. This included two *Radak II* [231], two *CreaTec Dual Filament Cells (DFC)* [232] and one low temperature *CreaPhys Organic Molecular Evaporator* [233]. Each evaporation source is fixed on a high-vacuum flange which is attached to the floor of the vacuum chamber. Through the respective flanges, the source temperatures are controlled by each respective power supply and monitored using type C thermocouples. The respective materials are placed in so-called liners made of pyrolytic boron nitride (PBN) or aluminum oxide. The liners can then be placed inside the evaporation sources. Information on the materials and sources used in this thesis can be found in table 3.1.

Up to six substrates can be placed on a molybdenum substrate holder during deposition (see fig. 3.1. To allow for more homogeneous film coverage between different substrates mostly up to four substrates were used per run. The central substrate is situated 2 cm below the others on two ledges that allow the sample to be hit by *in situ* lasers and X-ray. The X-ray enters and exits the chamber through *Kapton* windows in the side walls of the chamber and is used to observe the evolution of crystalline structures via XRD. Red and infrared lasers for laser light scattering (LLS) enter and exit through flanges at the floor of the chamber. LLS also responds to amorphous structures and is used as a secondary, qualitative measure for deposition speed. It is very useful for this purpose, because, other than the QCM, the measurement is performed directly on the central sample. Thus, the information is directly comparable to the *in situ* XRD measurement. However, it is not utilized for quantitative evaluation of our experiments since error values are too large.

The deposition rate is measured via a quartz crystal monitor (QCM) with a base frequency of 6 MHz. The QCM's position is adjusted to the same height as the substrate holder, as close as possible to the substrate, but in a way that
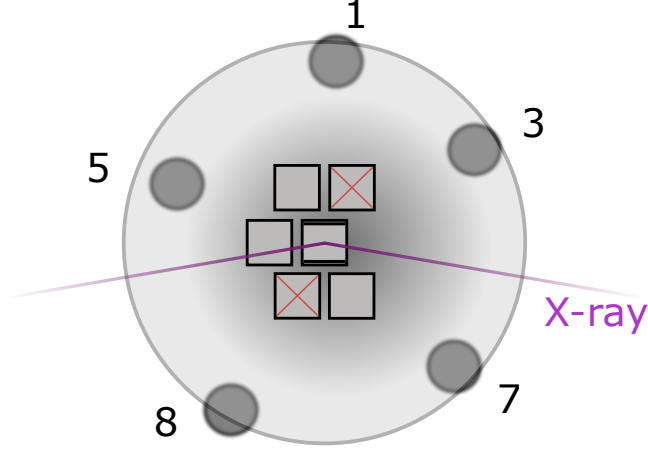
Figure 3.1: Illustration of the substrate holder and evaporation sources from above. The source numbers correspond to those given in table 3.1. Up to six samples can be placed in the holder, but only four samples were used per evaporation process. Two sample spots were not used, as indicated by the red crosses. The X-ray beam hits the center sample from below, which is located lower than the other samples on two ledges. This allows the sample illumination by the X-ray beam on an area stretching from the left edge of the sample to the right for low incident angles.

no substrate is shadowed by it. The change in mass Δm is quantified via the oscillation frequency change Δf of the QCM via the Sauerbrey eq. 3.23. The initial frequency of the QCM amounts to f_0=5.98 MHz, its area A=1.53 cm^2, its density ρ_q=2.65 gcm^{-3} and the shear modulus μ_q=2.95 $\times$ 10^{11} gcm^{-1}s^{-2}. In order to calculate the as-grown thickness $\Delta d = \Delta m/(\rho_{mat} \cdot A)$ on the sample, the Sauerbrey equation is modified by the grown material's density ρ_{mat} via eq. 3.24. The QCM area A is then omitted. The tooling factor T_f in eq. 3.24 accounts for the difference in growth rate between QCM and sample due to their different positions in the chamber.

T_f is determined via flux rate measurements. The thickness determined via QCM during a flux rate measurement is compared to the thickness determined via scanning electron microscope (see section 3.4.2) for every evaporation source and material. Then, the live thickness measurement via QCM can be related to the actual material thickness on the sample for future processes using T_f according to eq. 3.24.

$$\Delta m = -\frac{A\sqrt{\rho_q\mu_q}}{2f_0^2}\Delta f \tag{3.23}$$

$$\Delta d = -\frac{\sqrt{\rho_q\mu_q}}{2f_0^2\rho_{mat}} \cdot T_f \tag{3.24}$$

The data in [H1] was collected while the evaporation setup was used without an attached *in situ* glovebox , so that the samples were exposed to air when opening the chamber. For later publications [H2–H4,H4] an *in situ* glovebox provided by *Sylatech GmbH* (a different glovebox was used for transport layer preparation, see
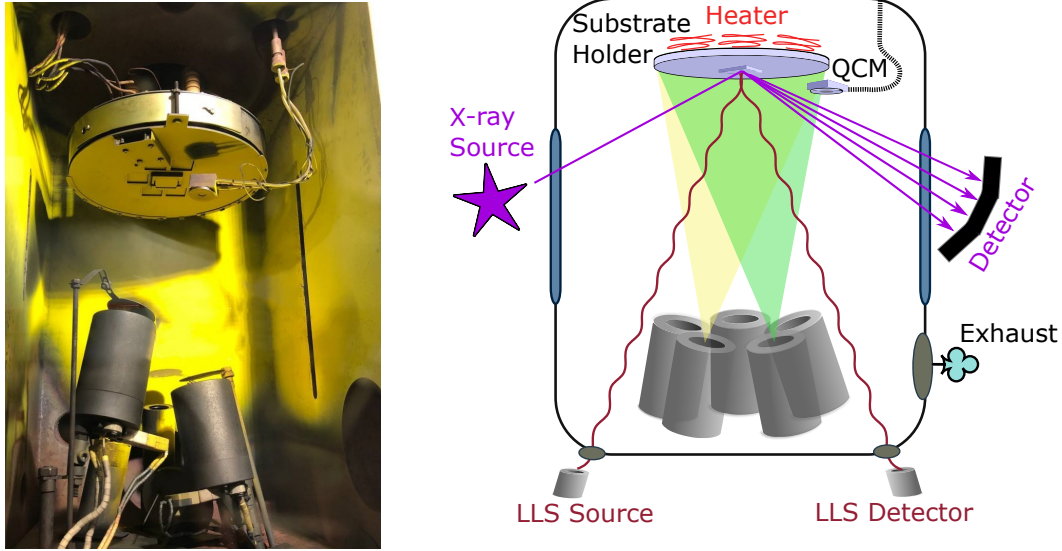
Figure 3.2: Photograph (left) and scheme (right) of the evaporation chamber.

section 3.2.2) was attached to the vacuum chamber. This enables the handling of newly prepared samples under inert gas (N_2) atmosphere in order to greatly reduce degradation effects incentivized by O_2 and H_2O vapor (see chapter 2.2.3). The samples could also be stored in the *in situ* glovebox's N_2 atmosphere for better structural durability before being exposed to air for measurements. The *in situ* glovebox reduced the O_2 and H_2O contents to values between 15 ppm to 70 ppm.

Source No.	Type	Materials	Temperature Range [°C]
1	*CreaPhys* [233]	FAI	120-200
3	*CreaTec* [232]	PbI_2	280-320
5	*CreaTec* [232]	CsI	390-420
7	*Radak* [231]	$PbBr_2$	390-420
8	*Radak* [231]	C_{60}	370

Table 3.1: Evaporation source types, their main materials and respective temperature ranges.

3.2.2 Solar Cell Architectures

To complete the solar cell stacks, electron/hole transport layer (ETL/HTL) as well as contact layers have to be deposited. Specific processing parameters are provided in [H1, H2]. Essentially, in the *n-i-p* solar cell configuration in [H1], an ITO substrate was used. As ETL, a nanoparticle SnO_2 layer was spin-coated at air and a C_{60} layer was deposited in the *in situ* vacuuum chamber, which was
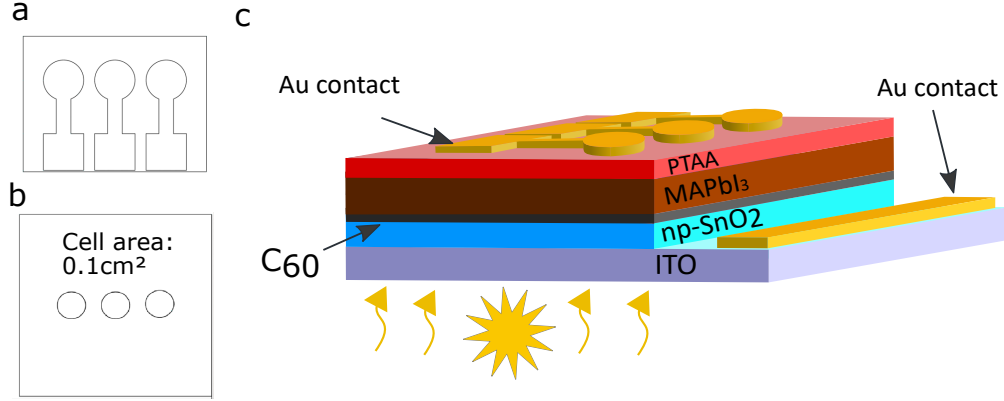
Figure 3.3: **a**: Shadow mask for evaporation of Ag/Au. It defines the area of the sample that is covered with Ag/Au during evaporation. **b**: Shadow mask for current density-voltage (*j-V*) measurement defining the cell area of $0.1\,\mathrm{cm}^2$. **c**: Schematic representation of the cell structure of the *n-i-p* solar cell in [H1] after Au evaporation. For *j-V* measurement, the cells are illuminated from the bottom and can be contacted individually via the rectangular-shaped back contacts. In [H2] the same contacting architecture is used for evaporation of Ag onto the *p-i-n* solar cell.

also used for perovskite deposition. After perovskite deposition, PTAA was spin-coated in a glovebox provided by *Sylatech GmbH* as the HTL and the contact layer Au was evaporated in a designated vacuum chamber. The O_2 and H_2O concentrations in the glovebox were kept below $50\,\mathrm{ppm}$, respectively, at all times. In the *p-i-n* structure, NiO was deposited via electron beam evaporation on an ITO substrate. After perovskite evaporation the buffer layer phenyl-C_{61}-butyric acid methyl ester (PCBM) and ETL ZnO were deposited via spin-coating in the same glovebox used for HTL preparation in *n-i-p* structure. Finally, Ag was evaporated as a contact layer in the respective designated chamber.

The Au and Ag evaporation patterns define the solar cell structure on the sample. A shadow mask is used to cover the sample during Au and Ag evaporation - apart from the predefined cell area and the respective contacting areas. The shadow mask for evaporation is shown fig. 3.3 **a**. It allows the deposition of three cells per sample. Fig. 3.3 **b** shows the shadow mask for current density-voltage (*j-V*) measurement. It defines a total area of $0.1\,\mathrm{cm}^2$ for the *j-V* measurement. The scheme in fig. 3.3 **c** demonstrates the sample coverage after evaporation of the contact layer. For *j-V* measurement, the sample illuminated from the bottom through the ITO layer and is contacted at the long Au contact on the right side and the respective cell's rectangular contact on the left side.

3.3 (*In Situ*) X-Ray Diffraction

The evaporation setup used in this thesis is designed as to allow an *in situ* X-ray diffraction (XRD) measurement. The uniqueness of the herein employed setup lies within the observation of the crystallization and reaction during thin film growth. In the following a brief introduction to XRD in general is given and the *in situ* XRD setup and data evaluation are explained. For further details on XRD

theory the reader can refer to other educational works [234, 235].

3.3.1 Standard X-Ray Diffraction

When an X-ray photon with wavelength λ interacts with an electron, it can scatter elastically. During elastic scattering, the electron is very briefly excited from its ground state. During transition back to its ground state it re-emits a photon with the same wavelength λ as the initial incoming photon. A crystal structure comprises a large amount of atoms and their electrons in a periodical structure. The atomic order can be described as families of equidistant identical lattice planes, which are specified by their reciprocal axis intercepts - their Miller indices h, k and l.

$$d_{hkl} = \frac{1}{\sqrt{\frac{h}{a}^2 + \frac{k}{b}^2 + \frac{l}{c}^2}} \tag{3.25}$$

A family of lattice planes is then referred to as (hkl) and the distance d_{hkl} between two adjacent planes is given by eq. 3.25 for lattice structures with orthogonal axes.

The wavelength of X-ray radiation is in the same range as the distances between lattice planes. Therefore, XRD offers the possibility to resolve these planes via constructive/destructive interference by photons diffracted at the same (hkl) family. As the photons penetrate the crystal, their wavelength λ and the considered lattice plane distance d_{hkl} determine the diffraction angle θ at which constructive interference occurs. This is described by the Bragg condition in eq. 3.26 with the diffraction order n.

$$n\lambda = 2d_{hkl} \cdot sin(\theta) \tag{3.26}$$

$$\tag{3.27}$$

Two X-ray photons with the same wavelength λ diffracted at the same angle θ by two atomic shells on parallel lattice planes from the same family (hkl) will constructively interfere, if the extra distance that one of the photons has to cover is equal to a multiple of their wavelength λ. As the distance between to adjacent lattice planes d_{hkl} decreases the diffraction angle at which constructive interference will occur increases, if λ is constant. A scheme of the Bragg condition is depicted in fig. 3.4.

The intensity $I_{diff,hkl}$ of the diffracted radiation is proportional to square of the absolute value of the structure factor $|F(hkl)|^2$ of the respective family of lattice planes (hkl). $I_{diff,hkl}$ therefore depends on the type of atoms and their electronic structures [234]. The structure factor can be approximated via eq. 3.28 using the atoms' positions $\vec{r_j} = (x_j, y_j, z_j)$ in the unit cell and the momentum transfer $\vec{r^*} = (h, k, l)$, which describes the respective diffraction plane in reciprocal space.

$$F(hkl) = \sum_{j=1}^{n_{Atoms}} f_j(\vec{r^*}) \cdot exp^{2\pi i \, (\vec{r^*} \cdot \vec{r_j})} \tag{3.28}$$

$$f_j(\vec{r^*}) = \int_V \rho_j(\vec{r} - \vec{r_j}) \, d^3\vec{r} \tag{3.29}$$

The atomic form factor $f_j(\vec{r^*})$ is the fourier-transformed electron density of the respective atom type in its relaxed ground state, as given in eq. 3.29. Here, V is
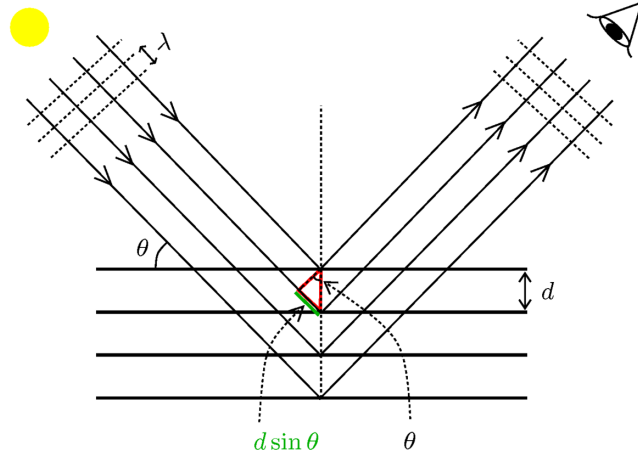
Figure 3.4: Schematic X-ray diffraction. X-rays with wavelength λ enter from the top left and diffracted X-rays are detected at the top right corner. The incidence angle of the X-rays is θ. The X-rays are diffracted at lattice plane family (hkl) with interplanar spacing d_{hkl}. Constructive interference occurs for specific λ, θ and d_{hkl} as given by the Bragg condition in eq. 3.26 and explained in the text. Adapted from reference [236]. Copyright via Creative Commons.

defined as the volume in which the atom's electron density distribution is different from zero.

Constructive interference occurs for those (hkl) whose normal vectors are orthogonal to the surface of the thin film so that the lattice planes are aligned in parallel with the surface. For an ideal polycrystalline film this condition is satisfied for all (hkl), since crystallites with all possible orientations exist. The crystal structures observed within this thesis comprise several perovskite phases such as the cubic (α) and hexagonal (δ) $FAPbI_3$ and tetragonal $MAPbI_3$ as well as their individual components. The most prominent diffraction planes and respective 2θ angles of all phases can be found in table 3.2. Their literature intensities are usually expressed in relative intensities. For cubic $FAPbI_3$ the most intense peak is the (100) peak produced by diffraction at $\theta =$ 13.9° [77]. The corresponding $d_{100} =$ 6.359 Å is also the edge length of the cubic unit cell and corresponds to the distance between two Pb atoms. The (100) family of planes is therefore the stack of plains spanned by parallel linear series of Pb-Pb-Pb... atoms. Since the Pb atoms have by far the highest electron density of all atoms in the lattice, their diffraction intensity given by the $F(hkl)$ and $f_j(\vec{r^*})$ will yield the highest relative intensity of all peaks, as experimentally verified [77]. The relative intensity I_{100} of the (100) peak is closely followed by I_{200} resulting from a family of planes with half the distance d_{200} compared to d_{100}. Therefore, the diffraction peak (200) is the result of stacked parallel planes with in-plane series of Pb-I-Pb-I... and I-V-I-V... with vacant virtual lattice points V at the center of the outer planes of the cubic unit cell.

The next highest intensity I_{210} is a result of a series of I atoms at the centers of the edges of the unit cell paired with a parallel sequence of Pb-I-Pb-I... atoms. Full θ-θ scans of $FAPbI_3$ and $MAPbI_3$ are shown in [H3] and [H1], respectively.

As discussed above, the intensity of a peak is determined by the structure factor of the respective (hkl). However, the number of lattice planes (number

and size of crystallites/domains with the same orientation) contributing to the constructive interference also influence the intensity. Therefore, the influence of a substrate lattice or a seed layer inducing orientational preferences [H1] can also enhance or reduce specific (hkl) intensities. Additionally, conditions enabling growth of larger crystallites/domains can also enhance peak intensities.

The domain size in a strain-free lattice structure can be approximated via an average crystallite linear dimension D depending on the measured peak width β via the Scherrer equation 3.30 . θ is the Bragg angle, λ is the wavelength of the X-ray radiation and K is a crystal shape-related value usually set to 0.9. β_0 corresponds to the peak broadening caused intrinsically by the instrumental setup, so $\beta - \beta_0$ yield the physical peak width.

$$D = \frac{K \cdot \lambda}{(\beta - \beta_0) \cdot cos\,\theta} \tag{3.30}$$

However, the peak width is normally influenced by the domain size and the strain present in the material induced e.g. by epitactic growth or defects. The peak width has different angular dependencies on domain size and strain, namely $1/cos\,\theta$ and $tan\,\theta$, respectively [244]. Therefore, the total peak broadening β_t can be described via eq. (3.31).

$$\beta_t^2 = \left[\frac{0.9 \cdot \lambda}{(\beta - \beta_0) \cdot cos\,\theta}\right]^2 + (4\epsilon \cdot tan\,\theta)^2 + \beta_0^2 \tag{3.31}$$

In general, a peak broadened mainly by grain size can be approximated using a Lorentzian profile [245] as given by $L(x, \Gamma)$ in eq. (3.32) with the position x_0 of the peak maximum and the full width at half maximum (FWHM, Γ). If interplanar strain is the main contribution to peak broadening, the peak profile is best described by a Gaussian function in eq.(3.33). A split pseudo-Voigt function $pV(x)$ combines and weighs both contributions of $L(x, \Gamma)$ and $G(x, \Gamma)$ to the peak profile as given in eq. (3.34) and is therefore used within this thesis. The factor η weighs the respective contributions. Since $L(x, \Gamma)$ and $G(x, \Gamma)$ are normed, the maximum peak height is given by I. The fitting in this thesis is done via the program *PDXL* version 2.8.1.1 by *Rigaku inc.*

$$L(x, \Gamma) = \frac{1}{\pi} \frac{\Gamma/2}{(x - x_0)^2 + \Gamma/2)^2} \tag{3.32}$$

$$G(x, \Gamma) = \frac{1}{\sigma\sqrt{2\pi}} exp\left(-\frac{(x - x_0)^2}{2\sigma^2}\right) \tag{3.33}$$

$$pV(x) = I \cdot (\eta G(x, \Gamma) + (1 - \eta)L(x, \Gamma)) \tag{3.34}$$

The X-ray photons enter the chamber through a *Kapton* window (as described in section 3.2) and hit the sample (scheme in fig. 3.2). After scattering by the sample they exit through another *Kapton* window on the opposite side and are then captured by the linear X-ray detection array. We employ a Cu X-ray tube providing Cu-K$_\alpha$ radiation with a wavelength of 1.54 Å. The occuring K$_\beta$ intensity is attenuated to 5 % of K$_\alpha$ by a Ni filter. The electron acceleration voltage for creation of the X-ray radiation is set to 35 kV and the current to 40 mA which results in a total power of 1.4 kW.

The system applies a 1D linear detector consisting of three *Mythen 1K* detector modules attached to the goniometer for the angular resolved detection of the scattered X-rays. The detector setup enables the measurement of a 28° range of scattering angles every 60 s. For *ex situ* θ-θ scans the sample remains in place while X-ray source and detector array move along the goniometer circle in steps of 1°, always matching incidence and exit angles θ of source∠sample and sample∠detector-center, respectively. θ-θ scans are measured from 10° to 50°. At each θ, a 28° measurement is recorded and the central 1° recorded by the detector-center is used for evaluation so that θ is maintained as the exit angle. For this measurement type to be effective, multicrystalline samples are required, since X-ray source and detector are static and will only detect planes with a normal vector splitting the 2θ angle in half. The measurement of a single crystal could suffer from unfittingly oriented crystal planes, which might not be observed.

The film is illuminated by a divergent beam along its whole width. The center part of the X-ray beam hits the sample at angle θ and reaches the detector at the same angle with respect to the sample, satisfying the Bragg condition for some (hkl). The divergent part of the beam hits the sample edges at angles of $\theta + \Delta$ and $\theta - \Delta$, respectively. The divergent beam parts are then diffracted towards the detector at angles of $\theta - \Delta$ and $\theta + \Delta$, respectively, yielding a total diffraction angle of 2θ and contributing to the measured peak intensity at this diffraction angle. It follows that this correlation holds for the whole beam along the sample width.

3.3.2 *In situ* Measurement

In situ XRD is ideally suited to analyze the initial thin film growth as well as the film's undergoing structural and crystallographic evolution during external influences as elaborated in ref. [246]. It is well-established for growth during solution-based processes [247–249] or temperature-dependent changes [48,59,191]. Even degradation mechanisms caused by humidity and elevated temperatures have been investigated via *in situ* XRD [250,251] or *in situ* GIWAXS [252] (grazing incident wide angle X-ray scattering, see section 3.4.1).

The distinctiveness of the *in situ* XRD setup employed in this thesis is that it allows for real-time observation of developing phases during evaporation and post-treatment, e.g. post evaporation or annealing. For better comprehension of the *in situ* measurement, an illustration of the color-coded intensity plot (colorplot) is given in fig. 3.5. For this measurement, incidence and exit angles were set to $\theta =$11°. The detector-center is then at 22° and the detector limits are at 8° and 36°, respectively. In Step 1 a 60 s long measurement is plotted - shown on the left. The rectangular peaks at 17.2° and 26.7° are artefacts caused by the gaps between the three detector modules. During Step 2 the measurement plot is converted to a line. The original x-axis θ values remain the same, but the intensity (originally y-axis) is color-coded. Finally, in Step 3 the string of color-coded single measurements results in an *in situ* XRD colorplot (Step 3), as shown on the right of fig. 3.5. In the colorplot, the y-axis corresponds to the diffraction angle 2θ, the x-axis is the relative process time during which the data were taken and the intensity is color-coded.
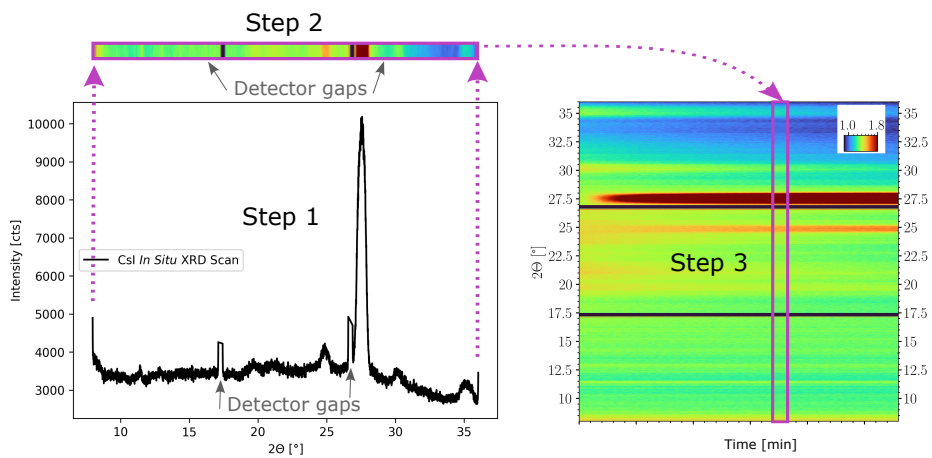
Figure 3.5: Illustration to show the formation of the *in situ* XRD color plot. In Step 1 a diffractogram is recorded over a duration of 60 s. Step 2 illustrates the change of diagram type. Here, the x-axis remains as in Step 1, but the y-axis (intensity) is converted to a color scale. In Step 3, the diffractogram is turned 90° so that a time-correlated course of peak progression can be observed in the color plot from left to right. In this case a CsI flux measurement can be observed, in which mainly the CsI (110) and the corresponding K_β peaks can be observed at 27.5° and 24.5°, respectively.

Material	Crystal Structure	Space Group	Lattice Plane	XRD 2θ Angle	Rel. Int.	Source
CsI	cubic	Pm-3m (221)	(110)	27.59°	1000	[237]
MAI	tetragonal	-	(002)	19.71°	600	[238]
			(101)	19.93°	1000	
			(110)	24.57°	800	
FAI	mono-clinic	P21/a (14)	($\bar{1}$21)	24.73°	1000	[239]
			(111)	24.91°	698	
			(002)	25.64°	532	
PbI$_2$	hexagonal	P-3m1 (164)	(001)	12.67°	250	[240]
			(002)	25.51°	40	
			(101)	25.92°	1000	
PbI$_2$	rhombo-hedral	R-3m (166)	(101)	22.91°	351	[241]
			(104)	28.30°	1000	
PbBr$_2$	ortho-rhombic	Pnam (62)	(200)	22.03°	310	[242]
			(111)	23.70°	730	
			(220)	28.96°	530	
			(211)	30.55°	1000	
MAPbI$_3$	tetragonal	I4cm (108)	(002)	13.99°	547	[49]
			(110)	14.13°	1000	
			(004)	28.19°	376	
			(220)	28.47°	570	
			(114)	31.66°	291	
			(222)	31.91°	429	
FAPbI$_3$	cubic	Pm-3m (221)	(100)	13.92°	1000	[77]
			(110)	19.73°	148	
			(111)	24.23°	151	
			(200)	28.05°	825	
			(210)	31.44°	690	
FAPbI$_3$	hexagonal	P63mc (186)	(100)	11.79°	1000	[71]
			(201)	26.28°	688	
FAPbBr$_3$	cubic	Pm-3m (221)	(100)	14.77°	1000	[243]
			(110)	20.95°	325	
			(200)	29.80°	589	

Table 3.2: Most prominent XRD 2θ peaks for crystal phases of materials found within this thesis.

3.4 Other Characterization Methods

The central technique used in this thesis is the *in situ* XRD analysis as explained in section 3.3. However, several complementary methods are used to provide further information on the grown materials, crystals and phases. Grazing incidence wide angle X-ray scattering (GIWAXS) yields information on the orientational distribution of crystal phases in the film close to the surface. A scanning electron microscope (SEM) is used to image the morphology of the thin film. These cross-sectional and top view images help to understand the growth process and distribution of species/phases along the thickness of the layer. Energy dispersive X-ray spectroscopy (EDX, also EDS) resolves the atomic constituents and their relative amounts in the bulk. Current density-voltage (j-V) analysis is essential for interpretation of solar cell parameters and performance. Finally, Photoluminesce (PL) and time-resolved photoluminescence (TRPL) grant additional insight into the optoelectronic properties in the bulk and at the interfaces.

3.4.1 Grazing Incidence Wide Angle X-Ray Scattering

Grazing Incidence Wide Angle X-Ray Scattering (GIWAXS) is a useful tool to investigate the orientational distribution of a polycrystalline thin film. Similar to XRD, an X-ray beam is used to initiate constructive interference on the sample as explained in section 3.3. The main differences to XRD consist of (i) the low angle of the incidence beam ("grazing"), which makes the measurement more surface sensitive (ii) a 2D detector allowing the observation of almost 180° rotational distribution ("wide angle") of the observed lattice planes.

In order to explain the underlying measurement principle, another concept for determining constructive interference in XRD is introduced. The Laue equation in eq.(3.35) in the reciprocal space is equivalent to the Bragg eq. (3.26) [234]. $\vec{k_{in}}/\lambda$ and $\vec{k_{out}}/\lambda$ correspond to the directions of incoming and diffracted wave vectors, respectively, with length $1/\lambda$.

$$\vec{q} = \frac{\vec{k_{out}}}{\lambda} - \frac{\vec{k_{in}}}{\lambda} \overset{!}{=} \vec{G} \qquad (3.35)$$

If their difference $\vec{q}$ is equal to an arbitrary reciprocal lattice vector $\vec{G}$, constructive interference will occur at these conditions.

A graphical interpretation can be given as displayed in fig. 3.6. The reciprocal lattice is given by the respective lattice vectors $\vec{a}^*$ and $\vec{b}^*$. The vector $\vec{k_{in}}$ of the incoming wave is determined by the experimental setup and points towards the origin O of the reciprocal lattice. The vector $\vec{k_{in}}/\lambda$ with length $1/\lambda$ starts at P and ends at O. The so-called Ewald sphere (here: 2D circle) with radius $1/\lambda$ is drawn around P and its size is determined by the X-ray wavelength. For every reciprocal lattice point (end point of a reciprocal lattice vector $\vec{G}$) that lies on the surface of the Ewald-sphere, the vector $\vec{k_{out}}/\lambda$ from P towards this lattice point fulfills the Laue equation for constructive interference. The angle between $\vec{k_{in}}$ and $\vec{k_{out}}$ is 2θ. If the wavelength λ is too large, the Ewald-sphere radius will be so small that no lattice points can be found within the sphere and no constructive interference can occur. In the common presentation of GIWAXS measurements, the data is Fourier-transformed. The resulting plot can be interpreted as a projection
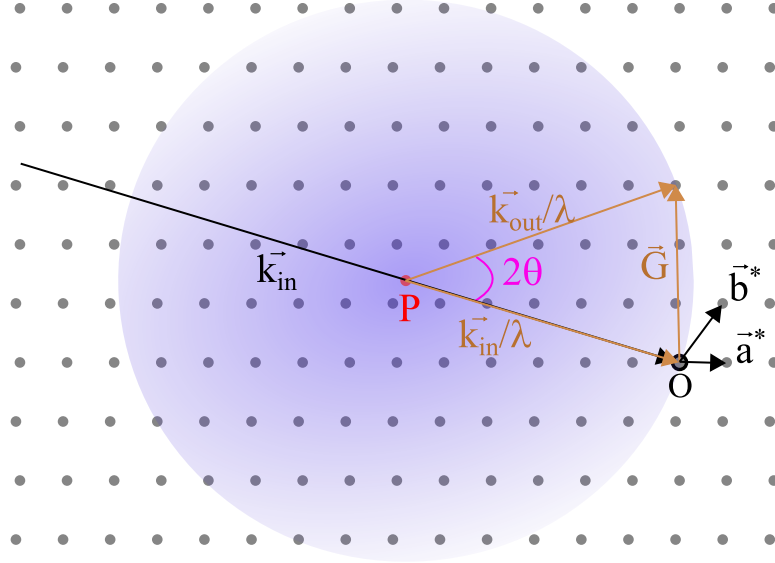
Figure 3.6: Construction of the Ewald-sphere for interpretation of the Laue condition in eq. (3.35) for constructive interference.

of the Ewald-sphere. For further details on the measurement technique refer to [253, 254]. GIWAXS measurements were performed in a $SAXSLAB$ setup (*Retro-F*, Copenhagen, Denmark) at 20-40 μbar. Details of the setup are best described in ref. [255].

3.4.2 Scanning Electron Microscopy

An scanning electron microscopy (SEM) is a useful tool to observe the microscopic structure of a sample. An SEM focuses an electron beam onto a sample and uses the back-scattered electrons (BSE) and secondary electrons (SE) to produce an image of its morphology. An SEM setup is also needed to enable electron dispersive X-ray spectroscopy (EDX), which is discussed in the following section 3.4.3.

More specific, SEs result from inelastic scattering of the incoming electrons with the atoms in the sample. SEs have energies below 100 eV, enabling an average travel distance of 1 to 2 nm in a solid, since the probability of elastic scattering is inversely proportional to the kinetic energy [256]. It follows that SE imaging allows a resolution of the topography of a sample, but lacks information of the sample properties below the surface. BSEs result from elastic scattering with the nucleus' close to the surface of the sample. The kinetic energy of BSEs is high. Consequently, they can reach the detector from deeper within the sample compared to SEs. However, due to the depth of the acquired signals, the resolution is reduced. The BSE's detected intensity is related to the respective atomic number (Z). Therefore BSE images allow to resolve the distribution of heavy atoms within the sample.

For this thesis, a *Zeiss Supra* 40 *VP* with two Everhart-Thornley detectors [257] was used. The angular detector (AD) for SEs is attached inside the chamber in a certain angle with respect to the electron beam. The second so-called "in-lens" detector is situated within the SEM pillar. It uses the electrostatic lense

of the electron beam to extract SEs that travel back in the opposite direction of the beam. The working distance (WD) of the AD has a lower limit since the SEM pillar will cover the sample at low WD as seen from the AD. An optimum resolution was achieved at comparably low working distances of 2 to 3 cm (inlens) and 7 to 8 cm (angular) between detector and sample. The SEM allowed a gun vacuum of 10×10^{-10} mbar and a chamber vacuum of 10×10^{-6} mbar. When investigating organic perovskites in an SEM one needs to be careful as not to damage the sample at hand, since the electron beam can disintegrate the organic component [216, 258]. Therefore, low acceleration voltages between 2 to 5 kV were used for the electron beam with low beam apertures of 20 to 30 μm. To prevent charging of the sample, a conducting carbon tape was employed to establish contact between the area of interest on the sample and the grounded substrate holder. This is especially relevant when imaging the cross-section of thin films on non-conductive substrates such as glass/ITO (indium tin oxide) or glass/FTO (fluorine-doped tin oxide). Otherwise if no conductive tape is used to cover the non-conducting glass, heavy charging of the latter will lead to unstable measurement conditions that impede well-resolved imaging.

3.4.3 Energy Dispersive X-Ray Spectroscopy

Determining the atomic composition and atomic distribution in a sample is key for the interpretation of its crystal and optoelectronic properties and is a crucial feedback for the adjustment of evaporation fluxes via the obtained film stoichiometry. Energy dispersive X-ray spectroscopy (EDX) allows a measurement of the atomic ratios within a sample. An incoming electron beam excites electrons from the outer shells. The replenishment of the inner-most orbital happens through relaxation of electrons from energetically higher orbitals. This leads to the emission of characteristic X-ray photons which can be analyzed for quantification of elemental ratios.

The characteristic radiation of atoms is denoted through two letters specifying the energetic transition. The first letter (K, L, M etc.) indicates the main quantum number of the initially vacant orbital, so K corresponds to n = 1. An index (α, β, γ etc.) names the original state of the relaxing electron by giving the difference in main quantum number of the transition, where α corresponds to Δn = 1. For a transition from n = 2 to n = 1 (K_α), the change in orbital quantum number Δl needs to be 1. Therefore, two transitions $K_{\alpha 1}$ and $K_{\alpha 2}$ exist where the index 1 stands for the higher energy transition.

To prevent perovskite degradation by electron beam exposure the acceleration voltage was kept between 8 and 10 kV during EDX measurements. For this reason, Pb M-lines ($M_{\alpha 1}$, $M_{\beta 1}$, $M_{\gamma 1 \text{ etc.}}$ and I, Br and Cs L-lines were measured and evaluated. The most prominent transitions are listed for the elements Pb, I, Br and Cs in tab. 3.3. H cannot be measured via EDX due to its low emission energies, which do not pass the Beryllium window protecting the detector. C and N can theoretically be detected, but their transition energies are also low and therefore strong superposition with other emission prevents their reproducible quantification in our setup.

For the EDX measurements within this thesis, a *Bruker* EDX detector was attached to the *Zeiss Supra* 40 *VP* SEM. In order to avoid visible electron beam degradation, for the measurements presented here a low magnification of 500 was

Element	$K_{\alpha1}$ [keV]	$K_{\alpha2}$ [keV]	$L_{\alpha1}$ [keV]	$L_{\alpha2}$ [keV]	$M_{\alpha1}$ [keV]
Pb	74.969	72.804	10.552	10.449	2.346
I	28.612	28.317	3.938	3.926	-
Br	11.924	11.878	1.480	1.480	-
Cs	30.973	30.625	4.287	4.272	-
C	0.277	-	-	-	-
N	0.392	-	-	-	-

Table 3.3: Energies of characteristic X-ray radiation for the elements found in organic lead halide perovskites discussed in this thesis [259]. I, Br and Cs M transition energies are not used for quantification. C and N $K_{\alpha1}$ transition energies are too low to enable a reproducible quantification with the detector used during this thesis.

used, which causes a low electron/area exposure. For quantification, a *Bruker* program was used that employs a standardless peak to background (P/B) ZAF (atomic number "Z", absorption "A" and fluorescence factors) fitting.

3.4.4 Current Density - Voltage Analysis

To determine a solar cell's (SC) ability to convert solar to electric power, the power conversion efficiency (PCE) has to be obtained. During a current density-voltage (j-V) measurement, the SC is illuminated by a standardized AM 1.5 light spectrum at room temperature while its power output is determined for certain voltages during a voltage sweep. From the j-V measurement the short-circuit current density (j_{SC}), the open circuit voltage (V_{OC}), the fill factor (FF) and the PCE are determined, which allow a comparison to other SCs.

To describe the j-V behavior of a thin-film SC in its simplest form, a diode equation can be used according to eq. 3.36 [260]. j and V are the current density and voltage measured at the electrodes, j_{ph} is the photogenerated current density, j_0 is the reverse-bias saturation current density, R_{sh} and R_s are shunt and series resistances, respectively. n, q, k_B and T correspond to the ideality factor, unit charge, Boltzmann-constant and temperature, respectively.

$$j = j_{ph} - j_0 \cdot \left[exp\{ \frac{q(V+jR_s)}{nk_BT} - 1 \} \right] - \frac{V+jR_s}{R_{sh}} \tag{3.36}$$

For a MAPbI$_3$ p-i-n SC a two diode model proved to be more precise for fitting experimental data [261]. In this case, the diode term $j_0 \cdot exp\{...\}$ term would be replaced by two diode terms which are given in 3.37. This model is developed from the assumption that only non-radiative (first term, n=1) and shockley-read-hall (SRH) recombination (second term, n=2) paths play a role [107]. In an equivalent circuit the two theoretical diodes are in parallel to each other and to R_{sh} while R_s is connected in series.

$$-j_{01} \; exp\{ \frac{q(V+jR_s)}{k_BT} \} - j_{02} \; exp\{ \frac{q(V+jR_s)}{2k_BT} \} \tag{3.37}$$

For numerical drift-diffusion modeling of the j-V behaviou the poisson equation, carrier continuity equations at steady state and drift diffusion equations are used [107] and enable theoretical device optimization [262].

The measurement of a PSC j-V curve has to be done delicately, since PSCs can exhibit hysteresis (see section 2.2.2) and short-term stability (see section 2.2.3. If a PSC shows hysteresis, an extended measurement protocol should be followed to determine the actual quality of the cell by varying the voltage sweep speed [137, 263]. In any case, observing the stabilized j/PCE in addition to the j-V curve helps to improve understanding and comparability of the PSC. Additionally, dark j-V curve measurements can give valuable insight into charge carrier properties, such as charge carrier mobilities, trap densities and ion densities [42].

The setup used during this thesis was controlled by a *LabView* program operating a *Keithley 2400* source measure unit. The light stemmed from a 300 W *Omnilux* lamp which provided $100\,\text{mW/cm}^2$ AM 1.5 illumination at $25\,°\text{C}$. A sample comprised three cells, each with an area of $0.096\,\text{cm}^2$ defined by a shadow mask.

3.4.5 Photoluminescence

Photoluminescence spectroscopy (PL) is the measurement of the emitted luminescence light spectrum of a material driven by optic excitation. E.g. one can obtain information on the band gap energy E_g. As such, PL is a valuable complementary measurement to the pure structural method of XRD.

Upon illumination of a semiconductor with photons of sufficient energy, electrons are excited from the valence band (VB) into the conduction band (CB). Due to the continuous distribution of energy states within the bands, the excitation can be driven by photons with energies larger than E_g. The excited electrons (holes) relax towards the CB minimum (VB maximum) and can recombine through radiative and non-radiative recombination. The former leads to emission of (photo-) luminescence, while the latter can lead to heating of the sample. Therefore, PL can be used to determine the E_g of a material and to observe its phase purity. E_g is mostly given by the dominant peak in the obtained luminescence spectrum. If several peaks exist in the spectrum, several phases might exist. E.g. in mixed-halide perovskites, phase separation through halide migration (see 2.2.3) can cause two peaks in the PL spectrum, if the energy of the exciting photons is large enough to excite both electronic transitions.

Further, the PL intensity can give information on the preferred recombination mechanisms. The higher the intensity, the higher (lower) the probability of radiative (non-radiative) recombination processes. In fact, in a well defined and calibrated setup, the quasi-Fermi level splitting of phase pure layer can be determined by measuring its absolute intensity [264]. In the context of PSCs, steady-state PL e.g. has been used to identify the limiting components and interfaces [265, 266].

The luminescence spectrum $Y_{PL}(E)$ of a semiconductor as given in eq. 3.38 is dependent on the absorptivity $a(E)$ of the semiconductor and the quasi-fermi-level splitting ΔE_f [267]. ϕ_{bb} is the blackbody spectrum emitted into a hemisphere at temperature T, given in eq. 3.39.

$$Y_{PL}(E) = a(E)\phi_{bb}(E) \cdot exp\left(\Delta E_f/(k_B T)\right) \qquad (3.38)$$

$$\phi_{bb} = \frac{2\pi E^2}{h^3 c^2} \, \frac{1}{exp(E/kt) - 1} \qquad (3.39)$$

A review by Kirchartz et al. provides detailed insights into further quantification paths [264].

The band gap energy E_g can be determined from a measured spectrum by fitting the respective peak via a Gaussian-function G as shown in eq. 3.40. λ, σ and μ denote the wavelength, the variance and the expected value (E_g), respectively.

$$G(\lambda) = \frac{1}{\sigma\sqrt{2\pi}} \, exp\left(-\frac{1}{2} \, \frac{(\lambda - \mu)^2}{\sigma^2}\right) \tag{3.40}$$

During this thesis a *Labram HR Evolution* was used to perform PL spectroscopy. The excitation laser with the highest photon energy had a wavelength of 532 nm. Since the higher the incoming photon energy, the broader the energetic range of excitation in the sample and the more information can be gained, the 532 nm laser was always used. The minimum laser intensity of 0.01 % and 50-fold magnification were used to protect the sample from light-induced degradation. Details on light-induced degradation can be found in section 2.2.3.

3.4.6 Time Resolved Photoluminescence

The time-resolved (or transient) photoluminescence (TRPL) measurement gives insight into the decay times of excited carriers. It can be used to determine the kinetics of charge transfer and/or recombination on ns-timescales. E.g. TRPL allows the quantification of the key recombination rate constants such as Shockley–Read–Hall (SRH), bimolecular, and Auger recombinations [268, 269]. Non-radiative decay times can be analyzed by measuring the decay of excited charge carriers through their radiative recombination, i.e. the photoluminescence (PL). According to eq. 3.38, the PL is directly dependent on the quasi-fermi level splitting and therefore the density of the excited charge carriers. However, the interpretation of TRPL results often poses a challenge due to the large number of influential factors that need to be considered [264].

The transient decay of excited carriers can be described by solving eq. 3.41. n (p) and τ_n (τ_p) denote the electron (hole) charge carrier concentrations and their decay times at given conditions, respectively. k_{rad} is the coefficient for radiative recombination, which assumes values between 5.9×10^{-11} and 8.7×10^{-10} cm^{3}s^{-1} for MAPbI$_3$. p_r gives the probability for an emitted photon to be reabsorbed in the layer. The equation

$$-\frac{dn}{dt} = \left[k_{rad}(1 - p_r)n^2 + \frac{n}{\tau_p + \tau_n}\right] \tag{3.41}$$

yields different solutions for the majority carrier density n for high-level injection ($n=p$) and low-level injection ($n \ll p$). At high-level injection the decay is faster at shorter times and higher excitation due to the quadratic term of the radiative recombination. Later and during low excitation conditions, the exponential decay via SRH recombination dominates the decay. Further explanations can be found in a review by Kirchartz et al. [264].

Upon fitting the measured transient by multiexponential functions, several decay times can be determined according to eq. 3.42. τ_1 (A_1) and τ_2 (A_2) represent decay times (amplitudes) of different recombination mechanisms. Depending on

the injection and the properties of the layer, single-exponential decay can be preferred for fitting.

$$f(t) = A_1 \, exp\left(\frac{-t}{\tau_1}\right) + A_2 exp\left(\frac{-t}{\tau_2}\right) \tag{3.42}$$

The employed measurement technique is named "Time-Correlated Single Photon Counting" (TCSPC). Details can be found in references [270,271]. The TCSPC is enabled by the *PicoQuant GmbH*'s chip card *TimeHarp 200* which reads trigger and detector pulses and feeds its data to the software. The decay times are measured in bins, which can be set between 28 and 896 ps. The measurement ends as soon as one of these bins has reached 1000 counts. The laser's energy is 1.94 eV. The laser pulse length is 88 ps with a pulse repetition rate that can be set between 10 kHz and 20 MHz. It is important that the repetition rate is such that the excited sample has enough time to relax to its pristine (dark) state. The pulse energy amounts to 12.6 pJ with a focus area of 4.5×10^{-10} cm^2 and an intensity of 267 nJcm^{-2}. *PicoQuant GmbH*'s ultraviolet to near-infrared detector *PMA-192* is used to detect wavelengths between 270 and 850 nm.

4 Results and Discussion

4.1 General Remarks

The present thesis studies the deposition of perovskite thin film absorbers in a vacuum chamber by thermal evaporation of metal and organic halide precursors. A unique *in situ* X-ray diagnostics setup is attached to the evaporation chamber to monitor the film growth.

As outlined in section 2.2, the majority of research on perovskite thin films is based on solution-based processing, namely spin-coating techniques. Spin-coating can be useful in a laboratory environment due to its low equipment prices and fast fabrication feedback. However, spin-coating comes with several disadvantages such as the use of toxic solvents and the low material yield (below 10)% [272]. Additionally, the sample size for deposition of homogeneously thick films is limited due to the difference in radial velocity along the sample during rotation, making spin-coating unfeasible for upscaling of device sizes. Solution-based techniques [197] such as ink-jet printing [273] or blade coating [274] are being investigated aiming to overcome some of these limitations and pave the way towards larger scales. Nonetheless, but these are still solution-based.

Physical vapor deposition (PVD) by thermal evaporation is a promising technique to solve and/or mitigate most of the above problems, offering a solvent-free and scalable approach, but it is still underexplored (below 1 % of perovskite-related publications investigated vapor-based processing) [14]. Intrinsically, PVD is slower than one-step spin-coating, because a high vacuum needs to be applied to the evaporation chamber and the material is deposited in the range of Å/s to nm/s compared to deposition via a single droplet during spin-coating [275]. However, the intrinsically low rate of PVD can be overcompensated by the spatially extended deposition area, which enables large-area deposition [72], and the use of several sources at once to increase the overall deposition speed. In addition, PVD offers a homogeneous deposition independent of the substrate morphology [276]. Albeit its small research community, the resulting upscaling potential of fully evaporated PSCs is in the range of established inorganic photovoltaic technologies [13].

PVD has a specific intrinsic advantage, that has not been exploited. For solution-based techniques the precursor mixture is fixed by means of the prepared solution/ink. Therefore, the mixture is set prior to the deposition without the possibility to change this during the process. However, since PVD is a protracted deposition technique, the fluxes of different precursors can be varied and adjusted during the process in what is termed dynamic processing in this thesis. Up to now static processes with fixed precursor fluxes have been studied. Prior to the start of this thesis, the organic halides were known to dissipate upon sublimation, complicating the deposition process due to the high partial pressure of the organic components [207, 277]. The perovskite growth was promoted by the initial nucleation of organic species [211] and inorganic species [209, 210] depending on the substrate. However, the influence of the initially nucleating species on the perovskite phase development and, importantly, solar cell performance, remained largely unexamined, even though the significance of grain-boundaries [278] and interfaces [279] had been clear and significant efforts have been made to optimize these [143].
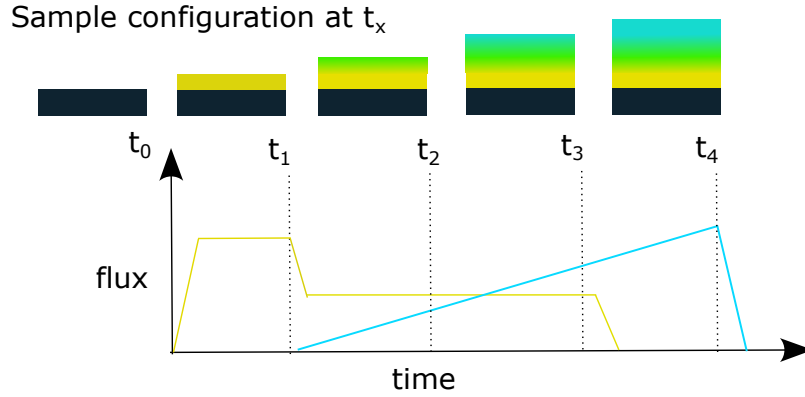
Figure 4.1: Schematic depiction of dynamic processing. During co-evaporation of multiple components (here: two) their individual fluxes are varied to specifically adjust the depth-dependent stoichiometry in the prepared thin film absorber.

Deliberately dynamizing the evaporation process allows for better control of the absorber film growth. Dynamic processing enables depth dependent variations of the stoichiometry from interfaces to bulk, such as cation and halide contents and AX/BX_2 ratios (see fig. 4.1). Accordingly, nucleation and bulk growth conditions can be decoupled and adjusted individually and the control of specific properties of interface/bulk/surface as well as gradients are made possible. In pursuit of optimized co-evaporation by dynamic processing routes for PSCs, the following questions emerge:

(Q_1) What are the stoichiometric ranges in which single-phase perovskite growth is enabled and in which ranges is the segregation of secondary phases promoted?

(Q_2) What influence does the stoichiometry have on the optoelectronic properties of the absorber, e.g. is there an optimum stoichiometry for photovoltaic performance in PSCs?

(Q_3) How do initial growth conditions impact the bulk crystal growth? Is the initial growth perpetuated towards the bulk? In that respect, what are favorable nucleation conditions?

(Q_4) How will varying deposition conditions impact solar cell performance, i.e. is it possible to fine-tune the optoelectronic properties of the absorber interface towards the electron transport layer (ETL) and hole transport layer (HTL) through dynamic processing?

(Q_5) What are the limits of dynamic processing? Can diffusion be controlled so that a full reaction of sequentially deposited layers is possible?

The phase formation at different stoichiometric conditions is one of the main investigations within this thesis, which, among other topics, aims to showcase the potential of optimized stoichiometry for PSCs. To interpret the influence of depth-dependent stoichiometry locally, a general understanding of the influence of stoichiometry on the absorber growth has to be established first. Therefore,

56

[H1] looks for optimized growth conditions for deposition of MAPbI$_3$ via co-evaporation of MAI and PbI$_2$ in an *n-i-p* structure. Both [H1] and [H2] analyze dynamic evaporation of MAPbI$_3$ absorbers for PSCs in an *n-i-p* [H1] and a *p-i-n* [H2] structure, respectively.

After delving into dynamically evaporated MAPbI$_3$ PSCs, perovskite absorbers based on FAPbI$_3$ are investigated due to their advantageous properties discussed in sections 2.2 and 2.3. However, as FAPbI$_3$ at room temperature is a polymorph, the growth of FAPbI$_3$ brings along additional complications compared to MAPbI$_3$. Specifically, the formation of the photo-inactive δ phase has to be avoided. Aiming to determine the best conditions for the preferential α phase formation, the stoichiometry (FAI/PbI$_2$ ratio) and composition (addition of other components such as CsI) of absorbers based on FAPbI$_3$ are varied in [H3]. Subsequently, the influence of precursor stacking sequence on the phase development and diffusion are explored in [H4] by sequential evaporation of mixed absorbers based on FAPbI$_3$.

One reason for the low amount of research on crystallization behavior in connection with PSC performance may be the rare availability of *in situ* PVD characterization techniques [280]. In this thesis, *in situ* XRD is employed to elucidate the thin film growth, because it gives detailed insight into the time-dependent evolution of crystal phase formation and segregation. *In situ* XRD is used to observe the dependence of the final film on its initial crystallization behavior, to shine light on the film-depth-dependent preferential phase formation and to connect this to the absorbers' other properties and their performance in PSCs.

Along the lines of the questions formulated above, the present thesis studies the deposition of perovskite absorbers in a vacuum chamber by the PVD of metal and organic halide precursors. The works published within the realm of this thesis investigate the effect of (i) stationary processing schemes for bulk stoichiometry variations and (ii) non-stationary, dynamic processing schemes during which the flux of each individually evaporated material is changed within the deposition to grow thin films with compositional gradients or sequentially evaporated layer stacks.

4.2 Dynamic Co-Evaporation of MAPbI$_3$ for n-i-p Solar Cells

Opening Remarks

The static co-evaporation of MAI and PbI$_2$ for deposition of MAPbI$_3$ represents the fundamental approach for vapor deposition of perovskites, since MAPbI$_3$ is the most-researched material for PSCs (see section 2.2). Several works on the evaporation of MAPbI$_3$ exist, as discussed in section 2.3. However, the initial growth mechanisms are not understood in detail and the initial nucleation behavior is still subject of discussion, since the perovskite growth can be promoted either by organic or by inorganic species and depends strongly on the substrate [208, 209, 211]. Further, the effects of MAI and PbI$_2$ stoichiometry on device performance and stability have been unconclusively discussed.

Tumen-Ulzii et al. demonstrated strong degradation induced by excess PbI$_2$ and relate good structural and device stability to the absence of unreacted PbI$_2$ [281]. Liu et al. found excess PbI$_2$ to enhance the degradation of the crystal structure, but not the efficiency of the PSC [282]. On the other hand, Jacobsson et al. achieved higher efficiencies for slight PbI$_2$ excess, but better crystallite quality for PbI$_2$ deficient devices and they encourage further research to combine the advantages of both growth types [215] - indirectly encouraging alternative preparation methods to connect improved crystal properties and PSC performance. Therefore, the significance of perovskite composition has been recognized, but a localization of benign and malign compositional variations has not been systematically investigated. More importantly, a dynamic variation of the growth conditions in an attempt to decouple nucleation and bulk growth has not been conducted.

[H1] strives to investigate the nucleation and initial film formation of MAPbI$_3$ absorbers deposited via PVD, and to study the impact of stoichiometry variations on the crystal growth behavior, preferential phase formation and PSC device performance. *In situ* XRD and static/dynamic deposition schemes are used to analyze the initial and bulk stoichiometry-dependent crystal phase evolution. First, the bulk stoichiometry is varied in a static processing scheme and related to crystal growth - as inquired by (Q_1) - and PSC performance - referring to (Q_2). After identifying an optimum bulk stoichiometry in terms of PSC performance, a dynamic variation of the optimized evaporation process is conducted by chosing different MAI evaporation onset times. This way, PbI$_2$ precursor layers with different thicknesses are deposited, inducing a local PbI$_2$ excess at the ETL/perovskite interface during the initial perovskite nucleation. Thereby, favorable nucleation conditions for crystal growth are determined [(Q_3)] and a way to fine-tune the perovskite/ETL interface for PSCs is introduced [(Q_4)].

scientific reports

OPEN

Importance of methylammonium iodide partial pressure and evaporation onset for the growth of co-evaporated methylammonium lead iodide absorbers

Karl L. Heinze[1], Oleksandr Dolynchuk[2], Thomas Burwig[1], Jaykumar Vaghani[1], Roland Scheer[1] & Paul Pistor[1]✉

Vacuum-based co-evaporation promises to bring perovskite solar cells to larger scales, but details of the film formation from the physical vapor phase are still underexplored. In this work, we investigate the growth of methylammonium lead iodide (*MAPbI₃*) absorbers prepared by co-evaporation of methylammonium iodide (*MAI*) and lead iodide (*PbI₂*) using an in situ X-ray diffraction setup. This setup allows us to characterize crystallization and phase evolution of the growing thin film. The total chamber pressure strongly increases during *MAI* evaporation. We therefore assume the total chamber pressure to be mainly built up by an *MAI* atmosphere during deposition and use it to control the *MAI* evaporation. At first, we optimize the *MAI* to *PbI₂* impingement ratios by varying the *MAI* pressure at a constant *PbI₂* flux rate. We find a strong dependence of the solar cell device performance on the chamber pressure achieving efficiencies > 14% in a simple n-i-p structure. On the road to further optimizing the processing conditions we vary the onset time of the *PbI₂* and *MAI* deposition by delaying the start of the *MAI* evaporation by *t* = 0/8/16 min. This way, *PbI₂* nucleates as a seed layer with a thickness of up to approximately 20 nm during this initial stage. Device performance benefits from these *PbI₂* seed layers, which also induce strong preferential thin film orientation as evidenced by grazing incidence wide angle X-ray scattering (GIWAXS) measurements. Our insights into the growth of *MAPbI₃* thin films from the physical vapor phase help to understand the film formation mechanisms and contribute to the further development of *MAPbI₃* and related perovskite absorbers.

In recent years, perovskite solar cells (PSCs), have been subject to intense research due to the outstanding optoelectronic properties of the perovskite absorber[1,2] and the ease of fabrication through a variety of simple preparation methods[3,4]. Low processing temperatures[5,6], high compositional versatility[7–11] and potential usage in cheap, high efficiency single-[12,13] as well as multi-junction (tandem) solar cells (SCs)[14,15] have further stimulated research interests.

Methylammonium lead iodide (*MAPbI₃*) was the first and has been one of the most investigated materials for perovskite absorbers. Due to their low expense and simplicity in fabrication, up to now most groups have been using wet-chemical deposition approaches such as spin-coating in order to produce *MAPbI₃* layers for structural and optoelectronic analysis as well as photovoltaic applications[16–18]. Although up-scaling of wet-chemical deposition methods is being investigated[3,4], their large scale preparation is still an open issue in terms of reproducibility, process yield and homogeneity[19]. On the other hand, the historic development of organic light emitting diodes (OLEDs) has shown that physical vapour deposition (PVD) is well suited for thin-film depositions at large scales and has great potential to succeed in the transition from laboratory production to

[1]Thin Film Photovoltaics, Institute of Physics, Martin-Luther-University Halle-Wittenberg, 06120 Halle, Saale, Germany. [2]Experimental Polymer Physics, Institute of Physics, Martin-Luther-University Halle-Wittenberg, 06120 Halle, Saale, Germany. ✉email: paul.pistor@physik.uni-halle.de

industrial fabrication. Single-junction power conversion efficiencies of above 20% have already been obtained for co-evaporated $MAPbI_3$ PSCs by various groups in a p-i-n configuration[20,21] and above 16% in an n-i-p device[20].

From a variety of different vacuum-based deposition approaches, co-evaporation of the constituent binary halides is arguably the most simple one, and good progress has been made in fabricating efficient devices with this technique. Already in 2013, PVD of $MAPb(I_{1−x}Cl_x)_3$ via dual-source co-evaporation of methylammonium iodide (MAI) and $PbCl_2$ showed an advantageous film coverage, an improved layer thickness homogeneity and an increase in SC performance compared to a spin-coated counterpart[22].

Following works have shown that despite the apparent simplicity of the process, precursor evaporation and the details of the film formation are rather complex. Especially the evaporation and deposition of MAI was found to be difficult to control. For example, upon heating, MAI evaporates non-directionally and is not withheld by a crucible shutter but diffuses globally into the evaporation chamber. There, it substantially increases the total chamber pressure and is in general not unambiguously detected by standard deposition control techniques such as quartz crystal microbalances (QCM)[23]. Therefore, Ono et al. suggested a new approach to monitor the MAI evaporation and deposition rate. They relied on using two QCMs, instead of one, where one QCM was facing away from the evaporation sources while the other was facing them directly. With this approach, they managed to verify homogeneous deposition on a $5 \times 5\ cm^2$ sample using X-ray diffraction (XRD)[24]. Later, Liu et al. suggested that MAI dissociates during evaporation and is then incorporated into a previously evaporated PbI_2 layer, introducing the idea that not all MA-sites in the perovskite might be occupied by MA, but also organic dissociates such as CH_3[25]. In 2016, Hsiao et al. showed a two-step approach, depositing PbI_2 before converting it to perovskite by evaporating MAI at chamber pressures ranging from $10^{−5}$ to $10^{−3}$ Torr[26]. For a heated chamber and sample they found MAI excess as well as deficit were harmful for the performance of their fully evaporated cells[26]. In 2018, Baekbo et al. investigated the MAI evaporation behaviour more closely[27]. They installed additional quartz crystal monitors facing away from the evaporation cells and/or with previously evaporated lead halide layers and confirmed earlier results showing a rather low sticking factor for MAI and that its deposition was non-directional. Using mass spectrometry they discovered that MAI dissociated into mainly two compounds: CH_3NH_2 and HI[27]. Borchert et al. found MAI impurities to play a significant role in increasing the MAI deposition rate, while not playing a role in the SC performance, as long as deposition speed was well controlled[28]. In 2020, Rothmann et al. provided high-resolution scanning transmission electron microscopy (STEM) images of formamidinium lead iodide ($FAPbI_3$) as well as $MAPbI_3$ absorber layers, revealing the inter-coordinated growth of PbI_2 and $MAPbI_3$ domains. According to this study, a slight excess of PbI_2 is not harmful for perovskite growth, because it adopts a modified 2H-structure with a seemingly defect-less interface to $MAPbI_3$, also not inducing any lattice defects in the $MAPbI_3$ crystal[29].

Even though $MAPbI_3$ PVD processing and the non-standard MAI sublimation behavior has been intensively investigated in the past, details of the optimal MAI processing conditions, such as flux control and optimal flux ratios for co-evaporated absorbers as well as the nature of the film formation remain subject to discussion. More specifically, the impact of the MAI flux on the nucleation process, and the general growth path have not been unambiguously clarified.

For example, different substrates have been shown to implicate agglomeration of different species at the interfaces. Zhou et al. observed the formation of a thin PbI_2 layer when depositing it on a single-crystalline ZnO (0001) surface via PVD[30]. Olthof et al. detected an organic molecule rich interfacial passivation layer prior to the commencement of the actual crystal growth when depositing $MAPbI_3$ via PVD on MoO_3, Polyethylenimine ($PEIE$), and poly-3,4-ethylendioxithiophene polystyrene sulfonate ($PE-DOT:PSS$) in contrast to a PbI_2 rich interface layer while depositing on indium tin oxide (ITO)[31]. Xu et al. also observed the formation of an interfacial PbI_2 at the initial growth stage for ITO, $PEDOT/ITO$, Si and glass substrates and found a thin PbI_2 interlayer to be detrimental for device performance[32]. Contradictory to other publications stating that excess PbI_2 is beneficial to performance due to a passivation of interfaces and grain boundaries[33,34], they improved their performance by removing this interlayer and achieved efficiencies of 14.35%[32].

Another property that has not been investigated thoroughly enough up to now is the influence of crystal orientation on the quality of the perovskite absorber in a SC structure. To the best of our knowledge, attempts to correlate the preferential crystal orientation of $MAPbI_3$ absorbers with device performance have only been done for wet-chemical deposition techniques. This said, crystal orientation in polycrystalline perovskite thin films depends strongly on the preparation conditions and is believed to influence electric and electronic properties, as well as improve charge carrier mobility and SC parameters[35,36]. Chen et al. managed to improve the SC performance by implementing a uniform (110) orientation in their $MAPbI_3$ absorber compared to a randomly oriented film[37]. At the same time, another investigation has come to the conclusion that orientation plays a minor role compared to defects and impurities in the bulk and at the interface[38].

Consequently, several open questions remain regarding the optimum film deposition parameters, details of the $MAPbI_3$ film formation as well as the influence of orientation on the optoelectronic properties of the absorber. To the best of our knowledge, no attempts have been made to optimize the onset time for the different evaporation components or the thickness of a PbI_2 seed layer. In this work, we investigate the film formation process under varying processing parameters such as the MAI to PbI_2 evaporation rates for optimized PSCs. We deposit $MAPbI_3$ via PVD using dual-source co-evaporation in a self-made vacuum chamber while simultaneously monitoring the crystallization path and phase evolution during deposition in quasi real-time with an in situ XRD (ISXRD) setup attached to the vacuum chamber. Firstly, we adjust the MAI pressure in the chamber in three steps, while leaving the PbI_2 rate constant. The total chamber pressure has been shown to be correlated to the MAI evaporation[26,39] and is assumed to be made up predominantly by the MAI partial pressure. In consequence, the MAI impingement rate (MAI flux towards the substrate surface) was adjusted by controlling the total chamber pressure. Following this line, the chamber pressure was fixed at either $4 \times 10^{−5}$ mbar, $7.5 \times 10^{−5}$ mbar or $1.5 \times 10^{−4}$ mbar. Secondly, in order to deliberately influence the nucleation conditions, the onset (starting) time of the
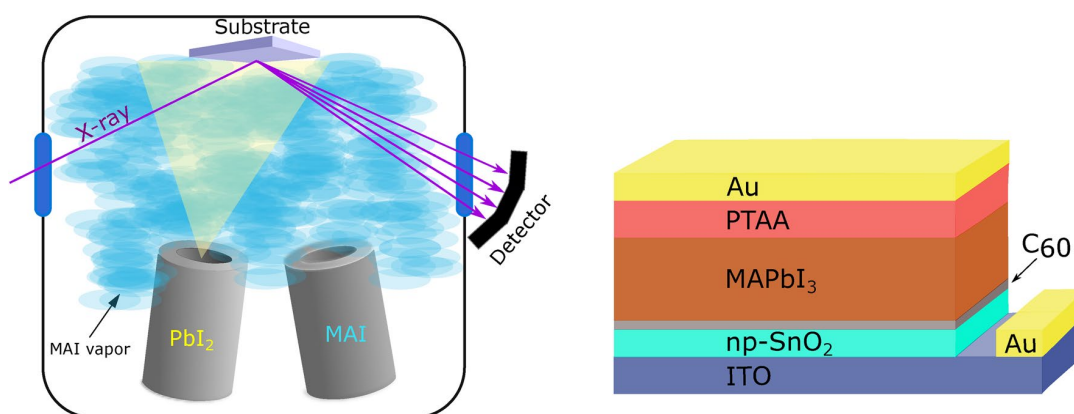
Figure 1. Left: sketch of the vacuum chamber used for the phase analysis with in situ XRD during the deposition of $MAPbI_3$ by co-evaporation. The evaporation of MAI leads to an overall increase of the global chamber pressure, which in turn was used to control the incorporation of MAI into the film. Right: sketch of the solar cell architecture used in this work.

MAI and PbI_2 depositions was systematically varied. This way, a thin PbI_2 precursor layer was deposited before starting the MAI co-deposition. The onset time of MAI evaporation was delayed for $t = 0$–16 min with respect to the PbI_2 onset. A strong correlation of these dynamic processing conditions with the device performance was found. Additionally, with wide angle X-ray scattering (WAXS) we were able to associate the different processing conditions to the growth of perovskite absorbers with rather distinct preferential orientations and relate our findings to the performance of efficient $MAPbI_3$ SCs.

Experimental details

Sample preparation.   For all processes we used 15 ohm/sq indium tin oxide (*ITO*) coated glass substrates (2.5×2.5 cm^2), provided by Kintec Company. The substrates were cleaned in 1% hellmanex solution in de-ionized water, isopropylic alcohol and acetone in an ultrasonic bath for 10 min each. The *ITO* samples were then treated in an ozone plasma for 10 min. Subsequently, 200 µl of a 2.6% colloidal dispersion of tin oxide nanoparticles (*np-SnO$_2$*) was deposited via spin coating at 3000 rpm for 30 s[40]. An additional ozone plasma treatment for 10 min followed before transferring the samples into the vacuum deposition chamber.

Perovskite deposition.   A sketch of the evaporation system with attached in situ X-ray diffraction setup is depicted in Fig. 1, together with a scheme of the device configuration used in this contribution. Base pressure for the start of all processes was between 2 and 2.5×10^{-5} mbar due to residual leakage through the capton windows that allow the ISXRD measurements to be realized (see below). First, C_{60} was evaporated for 5 min at 370 °C to form a 10 nm thick buffer layer. Upon cooling of the C_{60} crucible, the PbI_2 and MAI crucibles were heated to 288 °C and 110/115/125 °C, respectively, which resulted in a PbI_2 flux of 0.2 Å/s, determined via the QCM and scanning electron microscopy (SEM). The MAI crucible temperature was then continually adjusted to keep a constant predetermined chamber pressure (either 4×10^{-5} mbar, 7.5×10^{-5} mbar or 1.5×10^{-4} mbar) during the $MAPbI_3$ deposition. For this approach, a constant leakage rate and pump capacity is assumed, resulting in a stationary base pressure. The additional chamber pressure increase is then determined by an equilibrium established between evaporation of MAI dissociates and the particle drain caused by pumping. The impingement rate of MAI dissociates on the substrate therefore directly depends on the chamber pressure under working conditions. The total film thickness was monitored using a quartz crystal microbalance, the total chamber pressure with an Edwards WRGS-NW35 wide range gauge.

Solar cell completion and measurement.   After $MAPbI_3$ deposition, the samples were briefly (< 15 min) exposed to air before being sealed in a vacuum-tight bag, and then transferred to a nitrogen filled glovebox within the next 30 min. The hole transport layer Poly(triaryl) amine (*PTAA*) was then prepared by spin coating 100 µl of a solution of 6 mg *PTAA* dissolved in 400 µl of toluene, to which 3 µl of 34 mg/ml lithium bis(trifluoromethanesulfonyl)imide (*Li-TFSI*) in acetonitrile and 3 µl of 4-tert-butylpyridine (*4-tBP*) 1:1 in acetonitrile were added. Spin coating took place at 3000 rpm for 30 s. An 80–100 nm thick Gold layer was evaporated in a separate vacuum chamber at 10^{-5} mbar and 2 Å/s.

Current–voltage characteristics.   Current–voltage characteristics were recorded in the dark and under illumination at standard conditions (100 mW/cm^2, 25 °C) produced by a 300 W Omnilux halogen lamp employing a Keithley 2400 source measure unit. An active area of 0.096 cm^2 for the SC measurements was defined by applying appropriate shadow masks.

Film property measurements.   The ISXRD measurements were performed through exchangeable capton windows in the evaporation chamber using Cu-K$_\alpha$ radiation with a wavelength of 1.54 Å generated at 1.4 kW (35
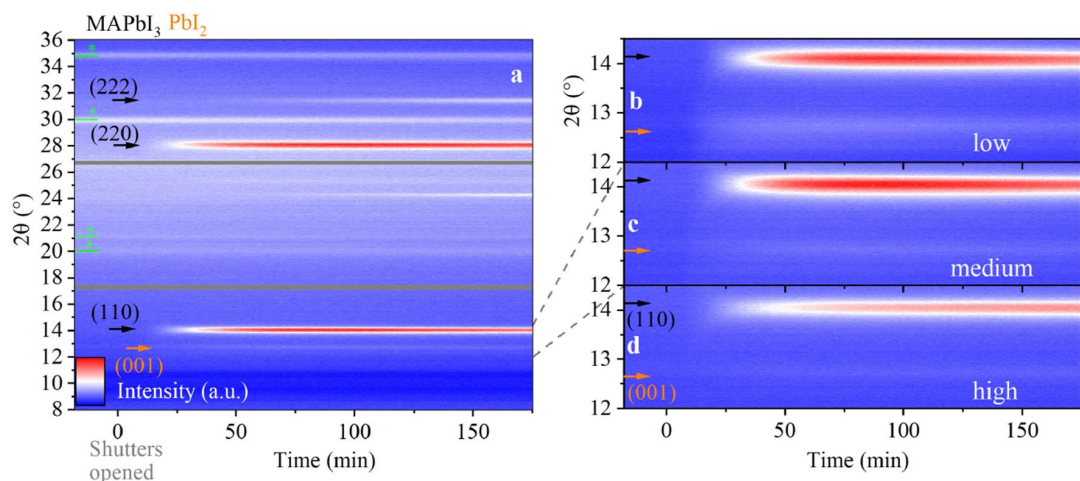
Figure 2. In situ XRD colormaps for vapor deposition $MAPbI_3$ at medium (7.5×10^{-5} mbar, **a,c**), low (4×10^{-5} mbar, **b**) and high (1.5×10^{-4} mbar, **d**) pressure. The black arrows indicate the perovskite peaks, while orange and green arrows are used to indicate the PbI_2 and substrate peaks, respectively.

kV, 40 mA). Three Dectris Mythen 1 K detector modules are assembled in a row enabling the measurement of 2θ angles covering a range of $28°$. The incidence angle was set to $11°$ resulting in the center of the detector setup (at twice the incidence angle) at a 2θ angle of $22°$. This allows an in situ measurement from $8°$ to $36°$. Due to the detector assembly (3 modules), there are two blind spots in the diffractograms roughly around $17.3°$ and $26.7°$. The K_β radiation is attenuated through a Ni filter to 5% of the K_α intensity. The θ–2θ measurements were performed in the same setup right after completion of the evaporation. For the θ–2θ scans, only the central detector module was used. For more details on the ISXRD setup, please refer to reference[41]. Grazing incidence wide-angle X-ray scattering (GIWAXS) was measured at a pressure of 20–40 μbar in a SAXSLAB laboratory setup (Retro-F) (Copenhagen, Denmark) as described elsewhere[42]. The setup used for a reference θ–2θ scan is described in detail in the supplementary information. SEM was performed with a Zeiss Supra 40 VP.

Results

Processing conditions were varied and analyzed in view of differences in the perovskite growth and solar cell (SC) performance. At first, the MAI to PbI_2 flux ratio during deposition was varied. For this, the PbI_2 flux was kept constant, while the MAI flux onto the substrate was increased for different deposition runs by controlling the total chamber pressure. Depositions with three different total chamber pressures (low, medium, high) were made and compared. Secondly, using the optimum total chamber pressure, the evaporation onset times of the two components MAI and PbI_2 were varied. The PbI_2 evaporation onset was set to $t = 0$ while the MAI onset time was varied in three steps: $t = 0/8/16$ min. This resulted in PbI_2 seed layers with different thicknesses prior to the start of the MAI deposition.

***MAI* pressure variation.**　$MAPbI_3$ perovskite layers were deposited at three different total chamber pressures (low: 4×10^{-5} mbar, medium: 7.5×10^{-5} mbar, high: 1.5×10^{-4} mbar) corresponding to three different MAI fluxes impinging on the substrate. The growth of the perovskite films was monitored with the ISXRD and the corresponding diffractograms are shown as colormaps in Fig. 2a–d. Here, X-ray intensity is color-coded and the process time evolves from left to right. Figure 2a exemplarily shows the complete evolution of the ISXRD scans for the deposition at medium pressure. The main peaks (e.g. (220) and (110)) of $MAPbI_3$ can clearly be identified after several minutes of deposition. Figure 2b–d show details of the evolution of the $MAPbI_3$ (110) and the PbI_2 (001) diffraction peaks of the low, medium and high pressure case for comparison. For the high pressure case, the $MAPbI_3$ (110) peak intensity is lowest and nearly no PbI_2 is detected.

The MAI crucible temperature and the development of the total chamber pressure are illustrated in Fig. 3a. The heatings of the PbI_2 and MAI crucibles started simultaneously. After reaching their respective set temperatures, both shutters were opened and the deposition started (at $t = 0$ min). Once the MAI crucible is warmed up, the total chamber pressure rises continuously until reaching the targeted pressure (at $t = 20$ min). In order to keep the total chamber pressure constant, the MAI crucible temperature then has to be reduced stepwise. The inset in the top part of Fig. 3a visualizes a direct comparison of the development of the total chamber pressure for the low, medium and high pressure cases.

In Fig. 3b, the evolution of the $MAPbI_3$ (110) and PbI_2 (001) peaks are shown. The peak areas were extracted from the corresponding ISXRD measurements by fitting a quasi-Voigt peak to the respective fixed diffraction angle. Since $MAPbI_3$ (110) K_β and PbI_2 (001) K_α peaks appear at the same angle at $12.7°$, the K_β peak of the $MAPbI_3$ (110) Bragg reflection had to be considered and substracted for this analysis.

At low pressure (4×10^{-5} mbar), the PbI_2 peak forms rapidly and grows to a final peak area twice as large as for medium pressure (7.5×10^{-5} mbar) and 4 times higher than for high pressure (1.5×10^{-4} mbar). If we take
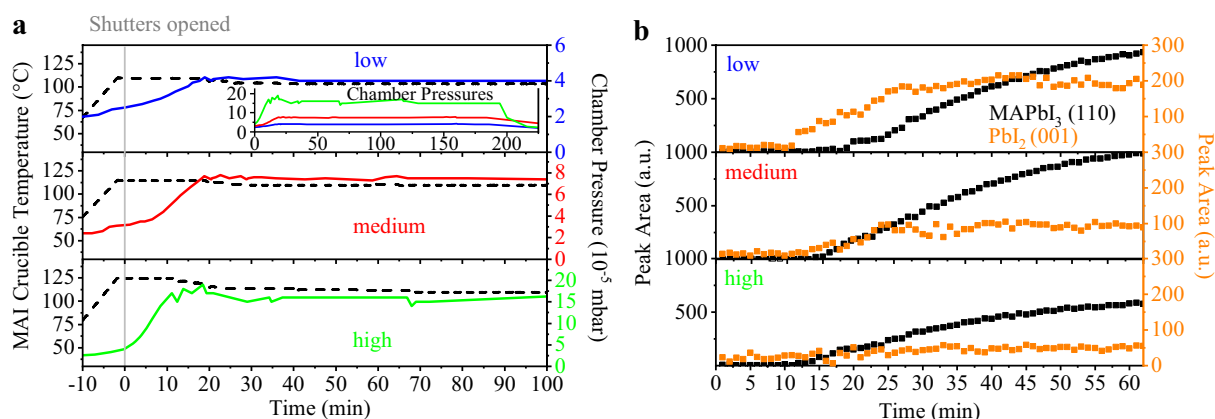
Figure 3. Characterizing initial growth while varying the chamber pressure: (**a**) *MAI* crucible temperature and chamber pressure during the first 100 min of each evaporation process. Inset: chamber pressure plotted for the whole duration of the processes for direct comparison. (**b**) Peak areas for *MAPbI₃* (110) and *PbI₂* (001) peaks for the ISXRD scans for the first 60 min of each evaporation process after opening the shutters.
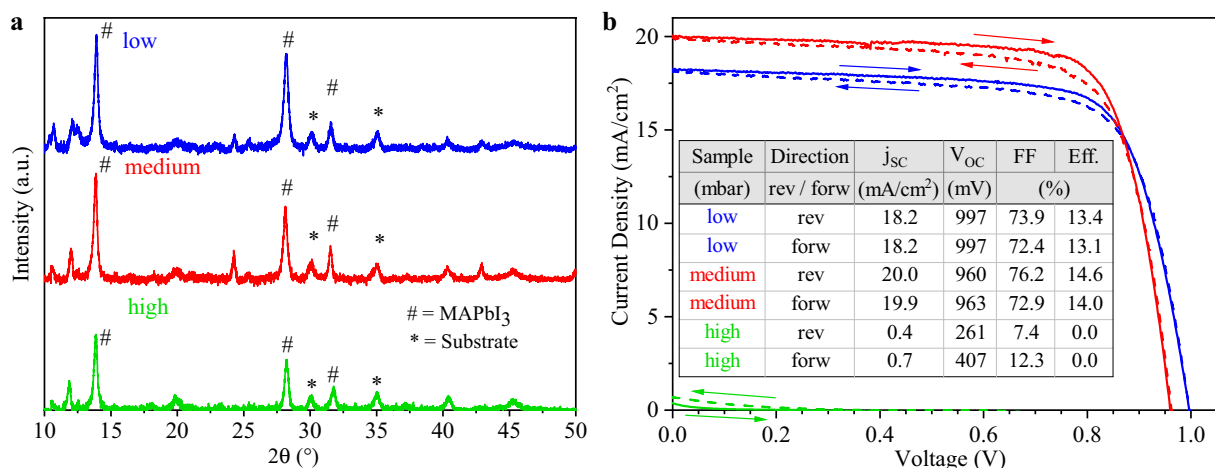

Figure 4. (**a**) XRD scans of the pristine *MAPbI₃* layers prepared at different chamber pressures. (110), (220) and (222) peaks for *MAPbI₃* are indicated by a sharp (#) at 13.9°, 28.2° and 31.5°, respectively. Substrate peaks are labeled with an asterisk (∗). (**b**) Current–voltage characteristics for champion cells fabricated at different chamber pressures recorded at 15 mV/s.

the integrated intensity to be proportional to the amount of crystalline material in these thin films, this result shows that for the low pressure case, the low *MAI* flux leads to an excess of *PbI₂* forming especially at the beginning of the perovskite deposition.

We specifically find that at low pressure, *PbI₂* starts to form well before *MAPbI₃*. This means that for the low pressure case a thin *PbI₂* layer nucleates on the substrate which then acts as a seed layer for the subsequent perovskite growth. In the ISXRD, we observe that the *PbI₂* (001) peak clearly starts to evolve several minutes before the *MAPbI₃* (110) peak. This sequential growth becomes less evident for increasing chamber pressures. In line with the prior argument, a plausible explanation is that the higher *MAI* flux leads to an earlier start of *PbI₂* conversion to *MAPbI₃*. As expected, the total peak area of (001) *PbI₂* is also reduced with increased pressure. Interestingly, according to the quartz crystal microbalance measurement, the total deposition rate is reduced with increasing pressure (see supplementary information (SI) Fig. S1) resulting in final thicknesses of 395 nm, 360 nm and 325 nm for low, medium and high pressure, respectively. We explain this by a decrease of the *PbI₂* flux rate due to reduction of the mean free path length caused by an increased number of *MAI* molecules on the way from the crucible to the substrate. Since the *MAI* molecules have a low probability of sticking to the sample if they do not encounter free *PbI₂* to react with[27,28], a large excess of *MAI* is not expected to lead to an increased growth rate by itself. Following this argument, it comes by no surprise that the perovskite growth as monitored by the ISXRD measurement of the *MAPbI₃* (110) peak is also slowed down at higher pressure.

In Fig. 4a, θ–2θ scans of the final films are shown. Sharp (110), (220) and (222) peaks at 13.9°, 28.2° and 31.5°, respectively, are found, corresponding to the tetragonal room temperature phase of *MAPbI₃*. (110) and (220) peak areas are larger when the pressure is reduced, whereas the intensity of the (220) peak remains almost unchanged.

5
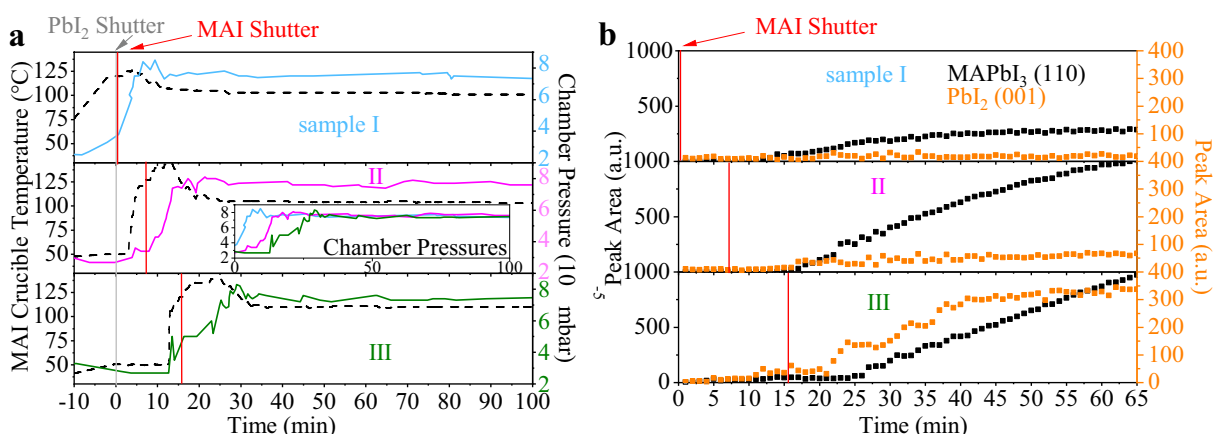
Figure 5. Characterizing initial growth during starting time variation: (**a**) course of the *MAI* crucible temperature (solid lines) and corresponding development of chamber pressure (dashed lines) during the first 100 min for samples I, II and III corresponding to different *MAI* evaporation onset times of $t = 0/8/16$ min. The grey and red lines indicate the evaporation onset times for PbI_2 and *MAI* shutters. The inset shows a direct comparison of chamber pressures. (**b**) Evolution of (110) $MAPbI_3$ (black) and (001) PbI_2 (orange) peaks for samples I, II and III.

This indicates that a more preferential crystallite orientation comes along with increased PbI_2 contents. The peaks at 12° are interpreted as a setup artifact, since they are already present before the deposition starts. A slight shift in the peak positions as compared to powder references[43] will be addressed below.

Figure 4b depicts the current–voltage measurements for the respective best cells. The $MAPbI_3$ layer prepared at medium pressure performed best, with 14.8% and 14.0% measured in reverse and forward voltage sweep direction, respectively, demonstrating the small hysteresis for these devices. Compared to the low pressure preparation, the short circuit current density (j_{SC}) is improved from 18.2 to 20.0 mA/cm², with minor increases also in open circuit voltage (V_{OC}) and fill factor (FF). While the preparation at high pressure conditions did show the formation of single phase perovskite material, the absorbers from these conditions did not perform well in devices, with an efficiency of the best cell staying below 0.1% with nearly no short circuit current. It is assumed that this is due to additional organic phases (such as MAI) forming within the absorber bulk or at the interface to C_{60}. This leads to the conclusion that the co-evaporation of *MAI* and PbI_2 is not a simple self-adjusting process, where excess organic species would simply not be incorporated into the perovskite phase, but instead the control of the flux ratios is rather crucial for the formation of high quality SC absorber material. While a lack of *MAI* (excess of PbI_2) seems to be tolerable to some extent, *MAI* excess is strongly detrimental. This can be seen in the respective SEM images (Fig. S2 of the SI), where the low and medium pressure samples show similar, 100 nm large grains, while high pressure sample exhibits a secondary, organic molecule rich phase.
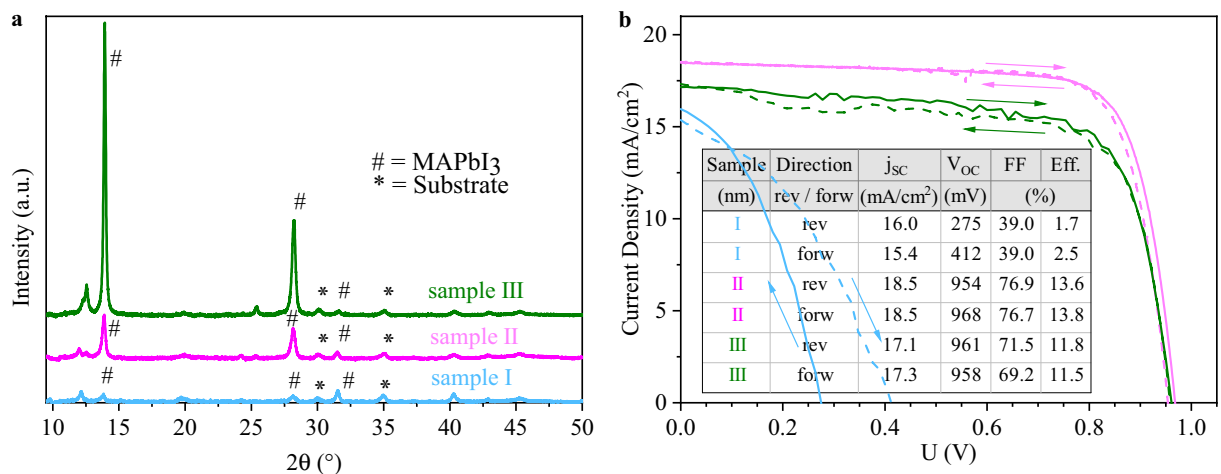
***MAI* onset time variation.** Above, the medium chamber pressure of 7.5×10^{-5} mbar yielded the highest efficiency devices for a given PbI_2 flux rate. In the following experiments, this optimized chamber pressure and the PbI_2 flux rate were kept constant. As we know from previous experiments, the vapor phase surface interaction plays an important role for the nucleation and starting point of the perovskite crystallization, therefore the initial deposition conditions are especially important for the further growth process. In consequence, we analyzed the impact of varied onset times for the *MAI* and PbI_2 evaporation on $MAPbI_3$ growth.

We delayed the starting time of the *MAI* evaporation (crucible temperature ramp up and shutter opening) for several minutes ($t = 0/8/16$ min) with respect to PbI_2 evaporation onset at $t = 0$ min. These predeposition sequences resulted in pure PbI_2 precursor layers of 0/10/20 nm thickness (according to the PbI_2 flux of 0.2 Å/s) that served as seed layers for the subsequent $MAPbI_3$ depositions. The nominal chamber pressure was reached at $t = 5/17/30$ min as can be seen in Fig. 5a. For simplicity, the resultant samples will be called samples I, II and III in the following passage.

In this variation, the *MAI* crucible heating ramp was set much faster than in the *MAI* pressure variation, in order to better define the starting time of the *MAI* evaporation. In consequence, the total chamber pressure also builds up faster than in the chamber pressure variation described above. For comparison, the total chamber pressure evolution for medium chamber pressure and best device in the previous section approximately corresponds to sample II in this onset time variation. The $MAPbI_3$ thicknesses were 330 nm, 300 nm and 280 nm for samples I, II and III, respectively.

Figure 5b depicts the evolution of the $MAPbI_3$ (110) and PbI_2 (001) peaks in our ISXRD scans (see Fig. S3 in the SI). For samples III and II the PbI_2 (001) peak starts evolving at $t = 15$ min and $t = 10$ min, respectively. It saturates quickly at 50 cps deg for sample II, but increases up to 300 cps deg for sample III, indicating that a predeposited 20 nm pure PbI_2 layer facilitates further PbI_2 growth. The $MAPbI_3$ (110) peak starts evolving at $t = 10/15/25$ min for samples I, II and III, respectively. Preconditioning of sample III leads to a linear (110) peak growth that does not show any signs of saturation during the time scale considered in Fig. 5b. These peaks can

Sample	Direction	j_{SC}	V_{OC}	FF	Eff.
(nm)	rev / forw	(mA/cm²)	(mV)	(%)	(%)
I	rev	16.0	275	39.0	1.7
I	forw	15.4	412	39.0	2.5
II	rev	18.5	954	76.9	13.6
II	forw	18.5	968	76.7	13.8
III	rev	17.1	961	71.5	11.8
III	forw	17.3	958	69.2	11.5

Figure 6. (**a**) θ–2θ scans of samples I, II and III corresponding to *MAI* evaporation onset times of t = 0/8/16 min. (**b**) Current–voltage characteristics for the best *MAPbI₃* cells prepared from samples I, II and III.

be compared for the finished samples in the θ–2θ scans in Fig. 6a. For sample I, no *PbI₂* is observed in Fig. 5b. Instead, an early increment of the *MAPbI₃* (110) peak can be seen. This is to be expected, since *MAI* and *PbI₂* fluxes were increased in parallel, leading to an instant conversion of the deposited *PbI₂* to *MAPbI₃*.

The strong impact of the *MAI* onset time on the *MAPbI₃* crystal growth can be seen in the θ–2θ scans displayed in Fig. 6a. By delaying the onset time, a strong increase in the preferential orientation of crystallites in the *MAPbI₃* absorber is observed. The *MAPbI₃* (110) peak area increases sharply from samples I and II to III, indicating a greater proportion of the (110) lattice planes being oriented parallel to the substrate surface. Interestingly, the opposite effect occured for the (222) peak at 31.5°. This peak was more pronounced for an earlier onset and was largest for sample I, as expected from the powder diffraction reference with random orientation[43]. This leads to the preliminary conclusion that delaying the *MAI* evaporation onset and consequently depositing a thicker *PbI₂* precursor layer induces *MAPbI₃* crystallite growth with (110) facets orientated in parallel to the substrate surface. Decreasing crystalline domain sizes lead to a peak broadening of the XRD peaks. If the crystallite size was the only origin of peak broadening, the crystallite size would be inversely proportional to the full width at half maximum (FWHM) of the XRD peaks according to the Scherrer equation. While the limited access to the other factors determining the peak broadening in our series prevents a precise quantification of the crystallite size, the FWHM values of the peak fitting analysis presented in Table S1 of the supporting information can still be used for a qualitative discussion. For the series with the delayed *MAI* onset time, we observe a clear decrease of the (110) and (220) FWHM for an increasing onset time, together with the strong increase in peak intensity. In contrast to this, a decrease of the (222) FWHM is observed. This data allows to conclude that the crystallite size along the (110) direction increases with increasing *PbI₂* thickness. Along with the orientational analysis coming up in the next paragraphs, this observation clearly indicates that the *PbI₂* layer not only induces a preferred orientation of the perovskites but also causes its directional growth.

We notice a shift in the diffraction angles compared to a powder diffraction reference provided by Xie et al.[43]. We measured sample I in another setup to account for the shift in our results and note an increase in lattice constant and resulting peak shift to smaller diffraction angles for our sample compared to the reference (see Fig. S4 in the SI).

Current–voltage characteristics of the best devices from the starting time variation are shown in Fig. 6b. Similar to the high pressure case, for sample I very low V_{OC} and FF were measured in both reverse and in forward direction resulting in an average efficiency of 2.1%. The highest efficiencies were achieved for sample II owing to a significantly larger j_{SC} by 1.4 and 1.2 mA/cm² and FF by 5.4 and 7.5% for reverse and forward directions, respectively, compared to sample III. This resulted in the sample II best cell's efficiencies of 13.6 and 13.8% in reverse and forward directions, respectively.

In order to further characterize the distribution of the crystal orientation for different *MAI* evaporation onset times, we also performed wide-angle X-ray scattering (WAXS) measurements. The intensity plots in reciprocal space can be seen in Fig. 7a–c. The images were taken for the same sample sizes and beam parameters and similar layer thicknesses, so it can be assumed that the irradiated volume is similar for all samples. The angle of incidence was 6.7° in order to create a setting close to the Bragg conditions for the *PbI₂* (001) and *MAPbI₃* (110) peaks and fully resolve their intensities along the q_z axis. This is important, as the transformation of the planar detector image into reciprocal space results in blind areas along the q_z axis originating from the Ewald sphere curvature. After transformation, the intensities of *PbI₂* (001) and *MAPbI₃* (110) located on the q_z axis are nearly equivalent to those measured during the θ–2θ scans presented before (Fig. 6a). Because we chose a high angle of incidence, the sample horizon is located at q_z= 5 nm⁻¹. Additional WAXS measurements obtained at a small incidence angle of 0.5° confirm that no relevant information on the lattice plain orientation is lost due to the high horizon (see Fig. S5 in the SI). The rings corresponding to the *MAPbI₃* (110) and *PbI₂* (001) reflection are marked with arrows. While the *MAPbI₃* (110) reflection can be clearly identified for all three samples, significant
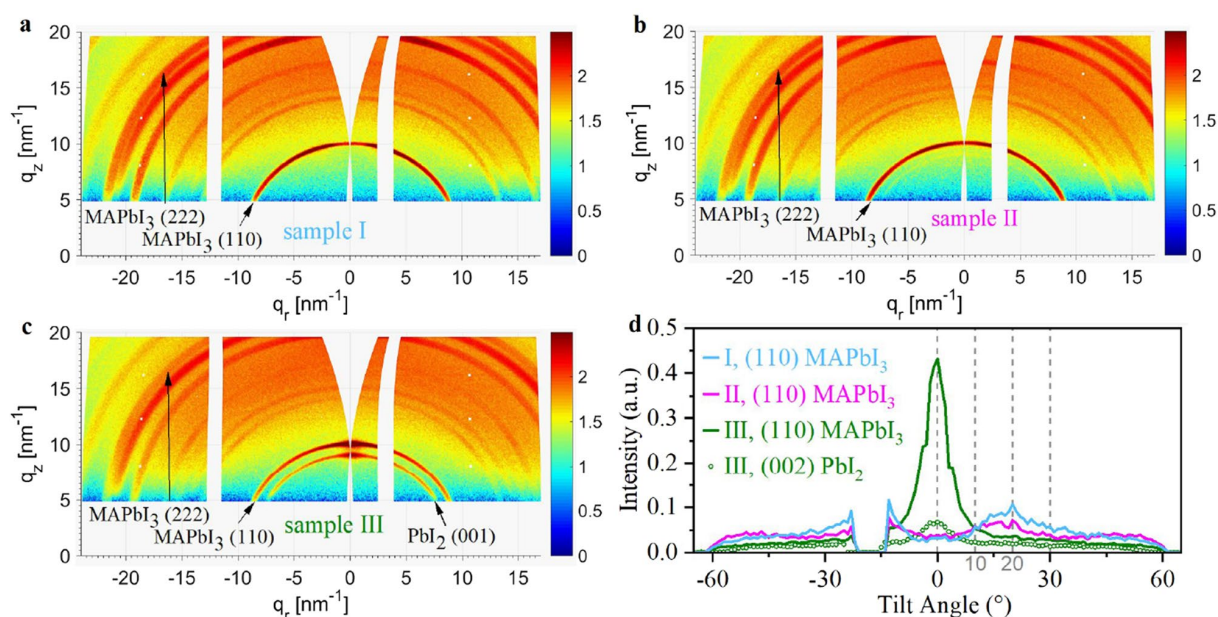
Figure 7. WAXS reciprocal space maps of samples I (**a**), II (**b**) and III (**c**) measured at an incident angle of 6.7°. (**d**) The tilt angle dependent peak intensity distribution for the (110) $MAPbI_3$ and (002) PbI_2 diffraction rings. $MAPbI_3$ (222) is not fully visible. The tilt angle is defined with respect to the q_r-axis as illustrated in Fig. S6 of the supplementary information.

PbI_2 (001) contributions are only found for sample III. On the $MAPbI_3$ (110) ring, the highest intensity is found on the meridian at $q_r = 0$ for sample III, while for samples I and II the maximum intensity is not perpendicular to the sample normal and has an offset of about 20° with respect to the sample normal.

This is further illustrated in Fig. 7d, which shows the intensity distribution of the $MAPbI_3$ (110) peak for all three samples under study and one PbI_2 (001) peak for sample III in dependence of the tilt angle with respect to q_r. These data were extracted directly from the detector images instead of the reciprocal graphs, since from there it can be processed directly in the imaging software. As the incident angle of 6.7° almost satisfies the Bragg conditions for the discussed crystal peaks, no angular transformation was applied to these peaks upon conversion of the detector images into the reciprocal space. Therefore, the dependencies in Fig. 7d actually represent the peak intensity distributions in the reciprocal space. The tilt angle is chosen with respect to the sample normal, so that the q_z axis corresponds to a tilt angle of 0° (illustrated in Fig. S6 in the SI). For sample III, it is clearly visible that the PbI_2 orientation is transferred on to the perovskite (110) orientation. This supports the hypothesis that the $MAPbI_3$ grows topotactically on the PbI_2. For sample II we observe a strong decrease in intensity at 0°. Instead, the preferential growth of the (110) plain is tilted by ~20°, which is clearly indicated by the broad peak ranging from 10° to 30° and centered at 20°. For sample I this effect is even stronger. The same can be assumed at -20°, where the detector gap partially masks the intensity distribution. Since the (110) plain is tilted with respect to the q_z axis, another crystal plain is expected to be preferentially oriented along the q_z axis. This is evidenced in Fig. 6a, where the (222) peak intensity was enhanced from sample III to II and I. The angle between the (222) and (110) lattice planes in $MAPbI_3$ can be calculated to be 26.4°[44], which lies within the previously indicated tilt angle maximum in the range of 10°–30° and therefore confirms this train of thought.

Discussion

We have investigated different conditions for the MAI evaporation in the deposition processes of $MAPbI_3$ via co-evaporation. We optimized the processing conditions in terms of device efficiency by controlling the MAI flux indirectly via the total chamber pressure. This allowed a more reproducible deposition than other processing parameters such as the MAI crucible temperature or control via the quartz microbalance. We observed asymmetries in the influence of an excess of MAI and PbI_2, as an MAI excess during deposition (high chamber pressure) or a too early start of MAI evaporation completely prevented the deposition of device-grade absorber material, while a mild excess of PbI_2 was beneficial or tolerable especially at the initial stages of the deposition.

For various vapor deposition techniques, it is assumed that the $MAPbI_3$ perovskite phase is grown by intercalation of organic ions into a PbI_2 structure[45–47]. This growth path is demonstrated by sequential processing, where a PbI_2 precursor layer is converted into $MAPbI_3$ by post-treatment with MAI vapor[26,48]. During evaporation of MAI, the deposition rate of MAI is governed by its vapor partial pressure. During sequential deposition, the PbI_2 layer is converted top-down. If the MAI chamber pressure is too low, this leaves a residual PbI_2 layer at the bottom[26]. In our experiments, we show a partly sequential (delayed) growth path, which was shown to also result in residual PbI_2 in the final films, as was observed in the ISXRD. As we decreased the MAI impingement rate, the intensity of the PbI_2 (001) peak in the XRD also increased, pointing towards a reduced conversion to

MAPbI$_3$. This corresponds well to the *MAI* pressure variation in the sequential deposition process presented by Hsiao et al.[26].

On multiple occasions, excess *PbI*$_2$ has been shown to improve device performance of *MAPbI*$_3$ solar cells[23,49–51] by passivating interfacial bonds and bulk defects, as well as improving crystal growth[52] and reducing hysteresis. In our experiments, remains of minor *PbI*$_2$ secondary phase contributions were detectable for the medium and low pressure processes. A greater amount of *PbI*$_2$ in the bulk, indicated by a *PbI*$_2$ peak in the respective ISXRD scan, could also lead to a passivation of the grain boundaries and was observed to enhance preferential orientation. For the high pressure process, sufficient pressure to convert *PbI*$_2$ to *MAPbI*$_3$ is reached early, leading to full conversion of *PbI*$_2$ and presumably causing an excess of organic species (Fig. S2 in the SI). A high organic content can lead to a fast current-induced degradation of the absorber layer[53], which would further obstruct charge transport. A resulting organic molecule barrier at the interface[54] can cause insufficient charge transport and decreasing photo current[46]. The effect of *MAI* excess completely restraining solar cell efficiencies has not been as clear in another study, where major *MAI* excess up to 45% could still yield solar cells with the best efficiencies in that study, although these were distinctly less reproducible than cells with absorbers containing less *MAI*[23]. Our *MAI* evaporation onset delay measurements confirmed that *PbI*$_2$ is especially important as a seed layer at the C_{60}/*MAPbI*$_3$ interface for producing high efficiency devices. This observation tips the on-going discussion on beneficial/detrimental aspects of a *PbI*$_2$ excess[32,33,52] towards a positive influence of the latter.

When growing a crystalline layer, its growth path will be decided by a minimization of free energy, whether this is via topotactical growth or surface agglomerates[55,56]. This means that the substrate type and/or the subjacent layer may strongly influence the crystal growth in vapor phase depositions[31,57]. We provide evidence, that in the same way, the crystallite orientation is influenced. In our experiments, depositing *MAPbI*$_3$ on ITO/*np-SnO*$_2$/C_{60}, with no evaporation onset delay for *MAI*, growth of (110) lattice plains tilted by 10° to 30° with respect to the sample normal was induced (Fig. 7). These effects have not been investigated for perovskite absorbers, but play a decisive role for other materials. For example, it has been shown that the interaction of *PMMA* with the substrate is weakened for an increasing layer thickness[58]. For *ZnO*, the optical properties were found to depend on the thickness of a buffer layer[55]. Also, when depositing BaTiO$_3$ the electronic and structural properties were strongly influenced by the thickness of a LaNiO$_3$ buffer layer on a Si substrate[59]. The broad range of preferential growth directions in our perovskite film without *MAI* evaporation onset delay point to different influences from subjacent ITO, *np-SnO*$_2$ and C_{60} layers, where no dominating effect can be isolated. Delaying the *MAI* onset by 8 min, we observe a shift from wide-spread crystallite orientation towards a slightly preferential growth direction. Further increasing the onset delay, the orientation of the perovskite is almost completely dominated by a *PbI*$_2$ seed layer. The purely inorganic *PbI*$_2$ seed layer is highly oriented itself, likely due to interaction with the substrate. The seed layer screens the substrate from the perovskite and incentivizes a clear crystallite orientation in *MAPbI*$_3$, topotactic with the orientation of the *PbI*$_2$ seed layer.

An approach towards explaining this phenomenon can be taken via the route of different growth paths. For stoichiometric dual-source PVD, *MAPbI*$_3$ follows Volmer–Weber island growth, resulting in randomly oriented small grains with sizes below 100 nm[60]. Typically, Volmer–Weber growth occurs when the cohesion energy between molecules of the deposited material is greater than the adhesion energy between the material and the sample[60]. In this case, agglomerations of the deposited material grow in vertical direction from the sample surface, while the surface-coverage advances slowly. When the adhesion energy is larger, layer-by-layer (Frank–van der Merwe) growth is expected, in which case the considered surface is covered quickly. This could be the case for *PbI*$_2$ seeds in our experiments, since it grows in a highly oriented manner. It has often been shown, that lead halides improve the sticking factor for *MAI*[27,28], and *MAI* can intercalate into the *PbI*$_2$ lattice to form *MAPbI*$_3$[26,61]. This hints towards an increase in adhesion energy for *MAI* on the substrate covered with *PbI*$_2$. In consequence, a transition to layer-by-layer growth for the perovskite could take place, thus inducing the observed preferential orientation.

The orientation is suspected to influence the fundamental properties of perovskites[35]. However, it is expected to play a minor role for the optical properties of *MAPbI*$_3$, and the correlations between electronic properties and preferential orientation have not yet been clarified[38]. Dedicated to this question, Chen et al. studied the wet-chemical post-deposition of *MACl* on spin-coated *MAPbI*$_3$[37]. By the post-deposition procedure, the grain size was increased and preferential orientation of the perovskite crystallites improved, resulting in a reproducible increase in SC efficiencies from average values of 11–15%. Since the V_{OC} was not improved, the increase in efficiency was not attributed to larger crystallite sizes or a possible trap site passivation by *Cl*. It was rather attributed to the improved orientation and a corresponding decrease in series resistance[37]. From our SCs' performances it cannot be deduced, whether changing orientation plays a role for charge transport and SC performance. On the one side, the strong impact of the *PbI*$_2$ seed layer on preferential orientation of *MAPbI*$_3$ was shown. On the other side, the importance of the seed layer for SC performance could be seen, but without direct proof that this is related to film orientation, as it could also be caused for example by a passivating effect of the residual *PbI*$_2$ layer. The thickest *PbI*$_2$ layer at latest *MAI* evaporation onset could improve charge transport in the bulk while, due to its low conductivity, also acting as a barrier at the C_{60}/*MAPbI*$_3$ interface. Further focused investigation observing the coupling of the preferential crystallite growth and SC performance are suggested in the future.

Conclusion

In this study, we introduced the chamber pressure as a parameter for controlling the methylammonium iodide (*MAI*) evaporation and respective impingement rate during the growth of methylammonium lead iodide (*MAPbI*$_3$) absorbers for perovskite solar cells. We observed a strong influence of chamber pressure on the absorber film formation and, consequently, on cell performance. At a given *PbI*$_2$ flux of 0.2 Å/s, we found an optimum chamber pressure for *MAI* deposition at 7.5×10^{-5} mbar. Increasing the chamber pressure further up

to 1.5×10^{-4} mbar was strongly detrimental to the functionality of the absorber, presumably because of an excess of organic species in the bulk and/or at the electron transport layer interface. At optimum chamber pressure, a small amount of excess PbI_2 was found and efficiencies above 14% were achieved with low hysteresis.

Using a specially designed in situ setup, we were able to investigate the initial absorber growth for the first time using X-ray diffraction (XRD). At optimum chamber pressure, we noticed that initially a PbI_2 layer is deposited, which then acted as a seed for perovskite growth. This observation is in accordance with the slow rise in chamber pressure, which was characteristic for the evaporation of MAI.

A controlled deposition of PbI_2 seed layers showed that PbI_2 has a strong influence on the crystallization and growth behaviour of the perovskite. Without PbI_2 seed layer, low intensity XRD peaks were observed and the prepared solar cells showed efficiencies below 3%. Delaying the MAI onset time by 8–16 min. drastically enhanced XRD peak intensities and led to efficient solar cells.

This work based on ISXRD provides a detailed characterization of the thin film growth using a new pressure-reliant approach for the deposition of $MAPbI_3$ perovskite absorbers. We provide further evidence that PbI_2 plays a paramount role at the interface and for the initial growth of the perovskite, vastly determining also the bulk of the absorber in perovskite solar cells. Consequently, we show that the use of thin PbI_2 seed layers enables the growth of highly crystalline and high quality organic–inorganic perovskites with physical vapor deposition techniques, which opens new optimization pathways and process developments for the deposition of perovskite thin films from the physical vapor phase.

References

1. De Wolf, S. *et al.* Organometallic halide perovskites: Sharp optical absorption edge and its relation to photovoltaic performance. *J. Phys. Chem. Lett.* **5**, 1035–1039. https://doi.org/10.1021/jz500279b (2014).
2. O'Regan, B. C. *et al.* Optoelectronic studies of methylammonium lead iodide perovskite solar cells with mesoporous TiOInformation: Separation of electronic and chemical charge storage, understanding two recombination lifetimes, and the evolution of band offsets during J–V hysteresis. *J. Am. Chem. Soc.* **137**, 5087–5099. https://doi.org/10.1021/jacs.5b00761 (2015).
3. Razza, S., Castro-Hermosa, S., Di Carlo, A. & Brown, T. M. Research update: Large-area deposition, coating, printing, and processing techniques for the upscaling of perovskite solar cell technology. *APL Mater.* **4**, 091508. https://doi.org/10.1063/1.4962478 (2016).
4. Li, D. *et al.* A review on scaling up perovskite solar cells. *Adv. Funct. Mater.* https://doi.org/10.1002/adfm.202008621 *(2020)*.
5. Yang, D. *et al.* High efficiency planar-type perovskite solar cells with negligible hysteresis using EDTA-complexed SnO2. *Nat. Commun.* **9**, 3239 (2018). https://www.nature.com/articles/s41467-018-05760-x.
6. Yang, D. *et al.* Achieving 20% efficiency for low-temperature-processed inverted perovskite solar cells. *Adv. Funct. Mater.* **29**, 1807556. https://doi.org/10.1002/adfm.201807556 (2019).
7. Igbari, F. *et al.* Composition stoichiometry of Cs2AgBiBr 6 films for highly efficient lead-free perovskite solar cells. *Nano Lett.* **19**, 2066–2073. https://doi.org/10.1021/acs.nanolett.9b00238 (2019).
8. Guo, Y. *et al.* Growth control and defect passivation toward efficient and low-temperature processed carbon based CsPbIBr 2 solar cell. *Organ. Electron.* **83**, 105731 (2020).
9. Yuan, S. *et al.* High efficiency MAPbI 3-x Cl x perovskite solar cell via interfacial passivation. *Nanoscale* **10**, 18909–18914 (2018). https://pubs.rsc.org/en/content/articlelanding/2018/nr/c8nr05504a.
10. Liang, L. *et al.* The humidity-insensitive fabrication of efficient CsPbI 3 solar cells in ambient air. *J. Mater. Chem. A* **7**, 26776–26784 (2019). https://pubs.rsc.org/en/content/articlelanding/2019/ta/c9ta10597b.
11. Bush, K. A. *et al.* Compositional engineering for efficient wide band gap perovskites with improved stability to photoinduced phase segregation. *ACS Energy Lett.* **3**, 428–435. https://doi.org/10.1021/acsenergylett.7b01255 (2018).
12. Jung, E. H. *et al.* Efficient, stable and scalable perovskite solar cells using poly(3-hexylthiophene). *Nature* **567**, 511–515 (2019). https://www.nature.com/articles/s41586-019-1036-3.
13. Best Research-Cell Efficiency Chart. https://www.nrel.gov/pv/cell-efficiency.html. Library Catalog: www.nrel.gov.
14. Meng, L., Wei, Z., Zuo, T. & Gao, P. Finding junction partners for CsPbI3 in a two-terminal tandem solar cell: A theoretical prospect. *Nano Energy* **75**, 104866 (2020).
15. Xu, J. *et al.* Triple-halide wide-band gap perovskites with suppressed phase segregation for efficient tandems. *Science* **367**, 1097–1104 (2020). https://science.sciencemag.org/content/367/6482/1097.
16. Bi, D., El-Zohry, A. M., Hagfeldt, A. & Boschloo, G. Improved morphology control using a modified two-step method for efficient perovskite solar cells. *ACS Appl. Mater. Interfaces* **6**, 18751–18757. https://doi.org/10.1021/am504320h (2014).
17. Caselli, V. M. *et al.* Charge carrier dynamics upon sub-bandgap excitation in methylammonium lead iodide thin films: Effects of urbach tail, deep defects, and two-photon absorption. *ACS Energy Lett.* **5**, 3821–3827. https://doi.org/10.1021/acsenergylett.0c02067 (2020).
18. Mohanty, I., Mangal, S., Jana, S. & Singh, U. P. Stability factors of perovskite (CH3NH3PbI3) thinfilms for solar cell applications: A study. *Mater. Today Proc.* **20**, 10 (2020).
19. Li, Z. *et al.* Scalable fabrication of perovskite solar cells. *Nat. Rev. Mater.* **3**, 1–20 (2018). https://www.nature.com/articles/natrevmats201817.
20. Momblona, C. *et al.* Efficient vacuum deposited p-i-n and n-i-p perovskite solar cells employing doped charge transport layers. *Energy Environ. Sci.* **9**, 3456–3463 (2016). https://pubs.rsc.org/en/content/articlelanding/2016/ee/c6ee02100j.
21. Li, J. *et al.* Highly efficient thermally co-evaporated perovskite solar cells and mini-modules. *Joule* **4**, 1035–1053 (2020).
22. Liu, M., Johnston, M. B. & Snaith, H. J. Efficient planar heterojunction perovskite solar cells by vapour deposition. *Nature* **501**, 395–398 (2013). https://www.nature.com/articles/nature12509.
23. Kim, B.-S., Gil-Escrig, L., Sessolo, M. & Bolink, H. J. Deposition kinetics and compositional control of vacuum-processed CH3NH3PbI3 perovskite. *J. Phys. Chem. Lett.* **11**, 6852–6859. https://doi.org/10.1021/acs.jpclett.0c01995 (2020).
24. Ono, L. K., Wang, S., Kato, Y., Raga, S. R. & Qi, Y. Fabrication of semi-transparent perovskite films with centimeter-scale superior uniformity by the hybrid deposition method. *Energy Environ. Sci.* **7**, 3989–3993 (2014). http://xlink.rsc.org/?DOI=C4EE02539C.
25. Liu, L., McLeod, J. A., Wang, R., Shen, P. & Duhm, S. Tracking the formation of methylammonium lead triiodide perovskite. *Appl. Phys. Lett.* **107**, 061904. https://doi.org/10.1063/1.4928662 (2015).
26. Hsiao, S.-Y. *et al.* Efficient all-vacuum deposited perovskite solar cells by controlling reagent partial pressure in high vacuum. *Adv. Mater.* **28**, 7013–7019. https://doi.org/10.1002/adma.201601505 (2016).

27. J. Bækbo, M., Hansen, O., Chorkendorff, I. & K. Vesborg, P. C. Deposition of methylammonium iodide via evaporation-combined kinetic and mass spectrometric study. *RSC Adv.* **8**, 29899–29908 (2018). https://pubs.rsc.org/en/content/articlelanding/2018/ra/c8ra04851g.

28. Borchert, J. *et al.* Impurity tracking enables enhanced control and reproducibility of hybrid perovskite vapor deposition. *ACS Appl. Mater. Interfaces* **11**, 28851–28857. https://doi.org/10.1021/acsami.9b07619 (2019).

29. Rothmann, M. U. *et al.* Atomic-scale microstructure of metal halide perovskite. *Science* **370** (2020). https://science.sciencemag.org/content/370/6516/eabb5940.

30. Zhou, X., Li, X., Liu, Y., Huang, F. & Zhong, D. Interface electronic properties of co-evaporated MAPbI3 on ZnO(0001): In situ X-ray photoelectron spectroscopy and ultraviolet photoelectron spectroscopy study. *Appl. Phys. Lett.* **108**, 121601. https://doi.org/10.1063/1.4944591 (2016).

31. Olthof, S. & Meerholz, K. Substrate-dependent electronic structure and film formation of MAPbI 3 perovskites. *Sci. Rep.* **7**, 40267 (2017). https://www.nature.com/articles/srep40267.

32. Xu, H. *et al.* Resolving the detrimental interface in co-evaporated MAPbI3 perovskite solar cells by hybrid growth method. *Organ. Electron.* **69**, 329–335 (2019).

33. Euvrard, J., Gunawan, O. & Mitzi, D. B. Impact of PbI2 passivation and grain size engineering in CH3NH3PbI3 solar absorbers as revealed by carrier-resolved photo-hall technique. *Adv. Energy Mater.* **9**, 1902706. https://doi.org/10.1002/aenm.201902706 (2019).

34. Roose, B., Dey, K., Chiang, Y.-H., Friend, R. H. & Stranks, S. D. Critical assessment of the use of excess lead iodide in lead halide perovskite solar cells. *J. Phys. Chem. Lett.* **11**, 6505–6512. https://doi.org/10.1021/acs.jpclett.0c01820 (2020).

35. Ono, L. K., Park, N.-G., Zhu, K., Huang, W. & Qi, Y. Perovskite solar cells-towards commercialization. *ACS Energy Lett.* **2**, 1749–1751. https://doi.org/10.1021/acsenergylett.7b00517 (2017).

36. Li, Y. *et al.* Enhanced power conversion efficiency and preferential orientation of the MAPbI3 perovskite solar cells by introduction of urea as additive. *Organ. Electron.* **73**, 130–136 (2019).

37. Z. Chen, A. *et al.* Crystallographic orientation propagation in metal halide perovskite thin films. *J. Materi. Chem. A* **5**, 7796–7800 (2017). https://pubs.rsc.org/en/content/articlelanding/2017/ta/c7ta02203d.

38. Muscarella, L. A. *et al.* Crystal orientation and grain size: Do they determine optoelectronic properties of MAPbI3 perovskite?. *J. Phys. Chem. Lett.* **10**, 6010–6018. https://doi.org/10.1021/acs.jpclett.9b02757 (2019).

39. Kottokkaran, R., Gaonkar, H. A., Abbas, H. A., Noack, M. & Dalal, V. Performance and stability of co-evaporated vapor deposited perovskite solar cells. *J. Mater. Sci. Mater. Electron.* **30**, 5487–5494. https://doi.org/10.1007/s10854-019-00842-y (2019).

40. Jiang, Q. *et al.* Enhanced electron extraction using SnO2 for high-efficiency planar-structure HC(NH2)2PbI3-based perovskite solar cells. *Nat. Energy* **2**, 1–7 (2016). https://www.nature.com/articles/nenergy2016177.

41. Pistor, P., Borchert, J., Fränzel, W., Csuk, R. & Scheer, R. Monitoring the phase formation of coevaporated lead halide perovskite thin films by in situ X-ray diffraction. *J. Phys. Chem. Lett.* **5**, 3308–3312. https://doi.org/10.1021/jz5017312 (2014).

42. Tariq, M., Dolynchuk, O. & Thurn-Albrecht, T. Effect of substrate interaction on thermodynamics of prefreezing. *Macromolecules* **52**, 9140–9148. https://doi.org/10.1021/acs.macromol.9b01499 (2019).

43. Xie, J. *et al.* Study on the correlations between the structure and photoelectric properties of CH3NH3PbI3 perovskite light-harvesting material. *J. Power Sources* **285**, 349–353 (2015).

44. Han, W.-S., Kang, S.-O. & Suh, I.-H. An easier way to calculate the crystallographic interplanar angles. *Korean J. Crystallography* **18**, 7–9 (2007). https://www.koreascience.or.kr/article/JAKO200727454708849.page.

45. Lohmann, K. B. *et al.* Control over crystal size in vapor deposited metal-halide perovskite films. *ACS Energy Lett.* **5**, 710–717. https://doi.org/10.1021/acsenergylett.0c00183 (2020).

46. Jacobsson, T. J. *et al.* Unreacted PbI2 as a double-edged sword for enhancing the performance of perovskite solar cells. *J. Am. Chem. Soc.* **138**, 10331–10343. https://doi.org/10.1021/jacs.6b06320 (2016).

47. Ha, S. T. *et al.* Synthesis of organic–inorganic lead halide perovskite nanoplatelets: Towards high-performance perovskite solar cells and optoelectronic devices. *Adv. Opt. Mater.* **2**, 838–844. https://doi.org/10.1002/adom.201400106 (2014).

48. Abbas, H. A. *et al.* High efficiency sequentially vapor grown n-i-p CH3NH3PbI3 perovskite solar cells with undoped P3HT as p-type heterojunction layer. *APL Mater.* **3**, 016105. https://doi.org/10.1063/1.4905932 (2015).

49. Zhang, T., Guo, N., Li, G., Qian, X. & Zhao, Y. A controllable fabrication of grain boundary PbI2 nanoplates passivated lead halide perovskites for high performance solar cells. *Nano Energy* **26**, 50–56 (2016).

50. Chen, Q. *et al.* Controllable self-induced passivation of hybrid lead iodide perovskites toward high performance solar cells. *Nano Lett.* **14**, 4158–4163. https://doi.org/10.1021/nl501838y (2014).

51. Kim, Y. C. *et al.* Beneficial effects of PbI2 incorporated in organo-lead halide perovskite solar cells. *Adv. Energy Mater.* **6**, 1502104. https://doi.org/10.1002/aenm.201502104 (2016).

52. Park, B.-w. *et al.* Understanding how excess lead iodide precursor improves halide perovskite solar cell performance. *Nat. Commun.* **9**, 3301 (2018). https://www.nature.com/articles/s41467-018-05583-w.

53. Rothmann, M. U. *et al.* Structural and chemical changes to CH3NH3PbI3 induced by electron and gallium ion beams. *Adv. Mater.* **30**, 1800629. https://doi.org/10.1002/adma.201800629 (2018).

54. Kottokkaran, R., Gaonkar, H. A., Bagheri, B. & Dalal, V. L. Efficient p-i-n inorganic CsPbI3 perovskite solar cell deposited using layer-by-layer vacuum deposition. *J. Vacuum Sci. Technol. A* **36**, 041201. https://doi.org/10.1116/1.5029253 (2018).

55. Hong, R., Shao, J., He, H. & Fan, Z. Influence of buffer layer thickness on the structure and optical properties of ZnO thin films. *Appl. Surf. Sci.* **252**, 2888–2893 (2006).

56. Maissel, L. I., Glang, R. & Budenstein, P. P. Handbook of thin film technology. *J. Electrochem. Soc.* **118**, 114C. https://doi.org/10.1149/1.2408101/meta (1971).

57. Chiang, Y.-H., Anaya, M. & Stranks, S. D. Multisource vacuum deposition of methylammonium-free perovskite solar cells. *ACS Energy Lett.* **5**, 2498–2504. https://doi.org/10.1021/acsenergylett.0c00839 (2020).

58. Xia, W., Mishra, S. & Keten, S. Substrate vs free surface: Competing effects on the glass transition of polymer thin films. *Polymer* **54**, 5942–5951 (2013).

59. Qiao, L. & Bi, X. Effect of LaNiO3 buffer layer thickness on the microstructure and electrical properties of (100)-oriented BaTiO3 thin films on Si substrate. *Thin Solid Films* **517**, 3784–3787 (2009).

60. S. Parrott, E. *et al.* Growth modes and quantum confinement in ultrathin vapour-deposited MAPbI 3 films. *Nanoscale* **11**, 14276–14284 (2019). https://pubs.rsc.org/en/content/articlelanding/2019/nr/c9nr04104d.

61. Hsieh, T.-Y., Huang, C.-K., Su, T.-S., Hong, C.-Y. & Wei, T.-C. Crystal growth and dissolution of methylammonium lead iodide perovskite in sequential deposition: Correlation between morphology evolution and photovoltaic performance. *ACS Appl. Mater. Interfaces* **9**, 8623–8633. https://doi.org/10.1021/acsami.6b12303 (2017).

Acknowledgements

Author contributions

Funding

Competing interests

The authors declare no competing interests.

Additional information

Supplementary Information The online version contains supplementary material available at https://doi.org/10.1038/s41598-021-94689-1.

Correspondence and requests for materials should be addressed to P.P.

Reprints and permissions information is available at www.nature.com/reprints.

Publisher's note Springer Nature remains neutral with regard to jurisdictional claims in published maps and institutional affiliations.

Concluding Discussion

The influence of overall stoichiometry on crystal growth and phase evolution (Q_1) as well as optoelectronic properties and PSC performance (Q_2) are studied in [H1] by the MAI pressure variation. The absorber stoichiometry is varied within the bulk of $MAPbI_3$ via the pressure-controlled MAI impingement rate and a medium pressure of 7.5×10^{-5} mbar is optimal. Via *in situ* XRD, a PbI_2 rich initial growth is observed. In the final film, however, the existence of a segregated PbI_2 layer is not conclusively shown via an XRD θ-θ scan. In the following, an assessment of the impact of stoichiometry on crystal growth - towards answering (Q_1) - is made. If not otherwise mentioned, the approaches in the cited literature are also based on thermal evaporation.

Since PbI_2 formation is observed during the low pressure approach in [H1] - for which excess PbI_2 impingement is assumed - the excess PbI_2 seems more likely to segregate than to intercalate into the perovskite lattice or agglomerate at grain boundaries. A transmission electron microscopy (TEM) study performed by Rothmann et al. examined the interplay of PbI_2 excess and perovskite growth [216]. They observed that PbI_2 and $MAPbI_3$ domain transitions can be free of grain boundaries and instead have continuous atomic patterns [216]. Therefore, a PbI_2 excess might be favorably incorporated into the perovskite grains - while maintaining the perovskite's crystallinity - or at least a tolerance for PbI_2 excess might exist that still allows for the full potential of perovskite properties to unfold.

On the other hand, no segregated MAI is observed in the high pressure approach in [H1] - for which excess MAI impingement is assumed. Thus, the MAI could be more likely to excessively exist within the crystal lattice at interstitial or antisites or at grain boundaries. However, considering only the results in [H1], excess MAI may also form an amorphous phase that XRD would not detect. Lohmann et al. varied the substrate temperature for $MAPbI_3$ deposition without changing the impingement rate of PbI_2 and MAI during co-evaporation [214]. Their results showed that MAI does not segregate at low excess, instead evoking an increase in perovskite crystal size and accumulating at grain boundaries. Gallet et al. find a strong increase in crystallinity of $MAPbI_3$ at high MAI excess [283]. The improved crystallinity observed in the literature seems to contradict the results in [H1] where a presumed bulk excess of PbI_2 was observed to lead to an increase of XRD peaks instead of an MAI excess. However, in [H1] this result may be smeared by the PbI_2 rich nucleation conditions - which were automatically present for lower overall MAI pressure - inducing strong preferential orientation as discussed above.

Further, Gallet et al. observed the formation of a low-dimensional perovskite phase at high MAI excess [283]. In a solution-based study by Klein et al. a low-dimensional phase was not observed at an MAI/PbI_2 ratio of up to two, but at higher MAI excess [284]. Song et al. spin-coated $MAPbI_3$ thin films with a wide variation of MAI/PbI_2 ratios and proposed a binary phase diagram that postulates PbI_2 segregation for PbI_2 excess and MAI integration up until an MAI/PbI_2 ratio of 3, at which the δ low-dimensional phase (δ-LDP) is preferentially formed at room temperature [285]. In the intermediate range of MAI excess, stacked perovskite sheets/layers are formed, that are separated by organic layers [22]. The amount of layers without organic separation decreases with increasing MAI content, thus culminating in the δ-LDP for high MAI excess [285]. Concluding the

stoichiometry dependent phase formation inquired via (Q_1), excess PbI_2 is more likely to segregate than MAI and low excess MAI is first incorporated into the crystal structure or accumulated at grain boundaries before a low-dimensional, non-perovskite phase is formed at higher MAI excess. In addition, the literature results suggest an increase in crystallinity with more MAI.

Furthermore, the dependence of solar cell device performance on bulk stoichiometry as inquired by (Q_2) was studied in [H1] and optimum conditions were determined at medium chamber pressure. Similar to our study, Lohmann et al. found MAI excess to have a stronger negative impact on device performance than PbI_2 excess, necessitating a PbI_2 rich growth for their best PSC devices [214]. Xu et al. [286] and Gallet et al. [283] find the formation of a low-dimensional phase at MAI excess to gravely impact device performance. Both works did not observe residual/segregated PbI_2 in their optimized films yielding the highest efficiencies suggesting an evenly balanced bulk stoichiometry or slight MAI excess. Kim et al. measured the highest average PSC efficiency of $\sim 18\%$ in a p-i-n device for a bulk stoichiometry with 5% excess of PbI_2 [287]. The average efficiency and the reproducibility were reduced at increased PbI_2 excess of 15% and MAI excess of 45%. Even though they obtained the highest individual efficiency at 45% MAI excess, they did not evaluate lower organic excess in their study and did not provide XRD data for any of the films. Summing up the evaluation of (Q_2), it seems conditions close to balanced bulk stoichiometry are preferred for solar cell performance. Few quantitative evaluations are made, but according to Kim et al. [287] the optimum range may lie within 15% PbI_2 excess and 45% MAI excess.

(Q_3) addresses the impact of initial growth conditions on the bulk growth and how the initial behavior is perpetuated towards the bulk. Several works have postulated the initiation of $MAPbI_3$ growth during co-evaporation by the deposition of a lead halide seed layer, subsequently enhancing MAI condensation and enabling perovskite formation and valid evidence has been provided towards this behavior [207, 210, 287]. E.g. Rothmann et al. used TEM to investigate $MAPbI_3$ growth at PbI_2 excess and observed an intergrowth of PbI_2 and $MAPbI_3$ at the atomic level with modified PbI_2 lattice structures and no interfaces between the two phases [216]. They deduced that $MAPbI_3$ growth is therefore seeded by PbI_2 grains. This is supported by [H1] since the formation of PbI_2 peaks precedes $MAPbI_3$ peaks in the *in situ* XRD data. Only during the high pressure approach no initial PbI_2 formation was observed. However, this may be due to the fast reaction of the initial PbI_2 seed layer with the large amount of MAI in the atmosphere, thus rendering the low amount of original PbI_2 undetectable. Therefore, it is still reasonable to assume that PbI_2 condensation precedes perovskite formation.

Concerning the perovskite growth depending on the nucleation conditions along the lines of (Q_3), in the MAI onset delay variation in [H1] a clear trend is observed. The greater the onset delay, the stronger the orientational homogeneity of the resulting $MAPbI_3$. The PbI_2 seed layer clearly induces topotactic $MAPbI_3$ growth as observed by the same orientation of PbI_2 (001) and $MAPbI_3$ (110) peaks via GIWAXS. With longer MAI onset delay a more intense PbI_2 peak remains in the final XRD diffractogram indicating a larger amount of residual PbI_2 at the substrate interface. Analogously, the $MAPbI_3$ (222) peak is enhanced for lower PbI_2 seed layer thickness and higher MAI content during nucleation. There-

fore, the PbI_2 is also effectively shielding the perovskite against the orientational growth induced by the substrate. Something that is not noted in [H1] is the continuous increase of the perovskite peaks during evaporation at elevated onset delay, which is prolonged with a thicker PbI_2 seed layer - yielding an increasingly steep and inclined growth in perovskite peak area. Therefore, within the realm of [H1], (Q_3) concerning the perpetuation of initial growth conditions towards the bulk can be answered by the results in figs. 5, 6 and 7 and the intergrowth behavior observed for PbI_2 and $MAPbI_3$ by Rothmann et al. [216].

Due to the assumption that PbI_2 initiates $MAPbI_3$ growth, the separation of the influence of bulk stoichiometry $[(Q_2)]$ and interfacial stoichiometry on PSC performance $[(Q_4)]$ is difficult at this point since the localization of grains from individual phases cannot be realized. This also arises from the lack of reliable elemental quantification throughout the depth of the thin film, which would allow to distinguish the compositions of bulk and interfaces in the literature. Some information can be gained by *in situ* XRD or approaches mimicking *in situ* XRD by subsequent preparation of layers with different thicknesses under the same conditions and analyzing each layer to gain information on depth-dependent stoichiometry and phase composition [286]. However, there are a limited number of methods for analysis on the actual depth-dependent final film composition. Very few studies employed glow discharge optical emission spectroscopy (GDOES) [288, 289] or time-of-flight secondary ion mass spectroscopy (ToF-SIMS) [290, 291] to determine the change in depth-dependent composition for perovskites, but quantified results are not obtained by these techniques. A dedicated study focusing on (Q_2) and (Q_4) via one of these techniques could potentially be very successful.

However, the influence of stoichiometric interfacial modification $[(Q_4)]$ by itself is most easily addressed by dynamic evaporation processes performed within this thesis. A deliberate delay of MAI onset time allows for the variation of the thickness of a PbI_2 seed layer and an optimum delay of $8\,min$ is found in terms of PSC performance in [H1]. By this, the advantageous process control during dynamic processing is clearly demonstrated, since an onset delay is necessary for functioning PSCs in [H1] and no onset delay ($0\,min$) is detrimental towards PSC performance. In view of (Q_4), the possible origins of the electronic advantages induced by a PbI_2 rich nucleation will be briefly discussed in the following.

Since local PbI_2 excess can induce n-type doping in the bulk [115, 292] - this could also occur at the interface between perovskite and ETL, which may in turn lead to an increase in the electron mobility and enhance charge extraction. Additionally, excess PbI_2 in the bulk has been shown to passivate bulk defects in $MAPbI_3$ [215]. Therefore, a rich PbI_2 nucleation step could reduce the formation of defects at the interface that might otherwise be created upon reaction of MAI components with the substrate. However, if a thick unreacted PbI_2 layer is present at the interface as in the experiment with an MAI onset delay of $16\,min$, charge transport between the perovskite and ETL is reduced as observed by the decrease in j_{sc}. This may be due to the low electron mobility in polycrystalline PbI_2 of under $0.01\,cm^2V^{-1}s^{-2}$ [293] compared to $67.2\,cm^2V^{-1}s^{-1}$ in $MAPbI_3$ [294].

Xu et al. studied the suppression of a PbI_2 layer at the perovskite/ETL interface of evaporated PSCs in the n-i-p structure $FTO/TiO_2/PCBM/MAPbI_3/Spiro$-MeOTAD/Au [286]. They suppressed the PbI_2 interlayer by two different ap-

proaches by (i) using a thin spin-coated $MAPbI_3$ precursor before a subsequent $MAPbI_3$ co-evaporation step and (ii) the conversion of a thin PbI_2 precursor by exposure to MAI vapor for an optimized period of time before $MAPbI_3$ co-evaporation. Both approaches improved their average device efficiency from 9% up to (i) 12% and (ii) 13% (maximum of 14% for (ii)), respectively. In their final optimized device, they do not detect segregated PbI_2 within the absorber via XRD. Even though the approaches in [286] and [H1] seem to point in oppositional directions, their final results are quite comparable. By deliberately depositing a PbI_2 seed layer before converting this seed layer to $MAPbI_3$ and subsequently using co-evaporation, Xu et al. employ a similar PbI_2 rich initial nucleation for their most efficient device as we have done in [H1]. (Q_4) is covered more deeply in [H2] and section 4.3.

4.3 Dynamic Co-Evaporation of MAPbI$_3$ for *p-i-n* Solar Cells

Opening Remarks

Inverted *p-i-n* MAPbI$_3$ PSCs to-date can outperform standard structure *n-i-p* PSCs [295, 296]. In addition, *p-i-n* PSCs can be more compatible with low-temperature processing, exhibit lower hysteresis [297–299] and be more suitable for use in tandem cells [80, 195] clearly showing the importance of investigating both structures.

Based on [H1] the enhancement in solar cell performance by PbI$_2$ rich nucleation can not be ascribed specifically to an improved bulk crystallization and/or modified interface properties, although some evidence has been provided supporting the latter effect. This leaves the impact of interfacial modifications as addressed by (Q_4) open for further discussion. Inverted solar cells in the *p-i-n* structure present a convenient design to continue this investigation.

If, in fact, the influence of PbI$_2$ rich nucleation on the bulk crystal growth is advantageous for the optoelectronic properties in a PSC device, this is expected to occur in *n-i-p* as well as *p-i-n* device architectures. Similarly, potential interface passivation by PbI$_2$ would also be advantageous in the *p-i-n* structure. On the other hand, if the change in local electronic properties induced by PbI$_2$ carries the most weight concerning the impact on PSC performance, PbI$_2$ rich nucleation might even bear a disadvantage for *p-i-n* PSCs. Therefore, the inverted structure provides a suitable framework for continuing the study on the advantages of dynamic processing schemes.

Based on the optimum bulk growth conditions determined in [H1], in [H2] a focus is set on dynamic co-evaporation of MAI and PbI$_2$ to elucidate the impact of stoichiometric variations at the interfaces to electron transport (ETL) and hole transport layers (HTL) in the inverted structure. For this purpose, the pre- and post-evaporation of thin PbI$_2$ and MAI layers is studied.

scientific reports

OPEN

Impact of dynamic co-evaporation schemes on the growth of methylammonium lead iodide absorbers for inverted solar cells

Robert Heidrich [1,3], Karl L. Heinze [1✉], Sebastian Berwig[1], Jie Ge[1], Roland Scheer[1] & Paul Pistor [1,2✉]

A variety of different synthesis methods for the fabrication of solar cell absorbers based on the lead halide perovskite methylammonium lead iodide (MAPbI$_3$, MAPI) have been successfully developed in the past. In this work, we elaborate upon vacuum-based dual source co-evaporation as an industrially attractive processing technology. We present non-stationary processing schemes and concentrate on details of co-evaporation schemes where we intentionally delay the start/end points of one of the two evaporated components (MAI and PbI$_2$). Previously, it was found for solar cells based on a regular n-i-p structure, that the pre-evaporation of PbI$_2$ is highly beneficial for absorber growth and solar cell performance. Here, we apply similar non-stationary processing schemes with pre/post-deposition sequences for the growth of MAPI absorbers in an inverted p-i-n solar cell architecture. Solar cell parameters as well as details of the absorber growth are compared for a set of different evaporation schemes. Contrary to our preliminary assumptions, we find the pre-evaporation of PbI$_2$ to be detrimental in the inverted configuration, indicating that the beneficial effect of the seed layers originates from interface properties related to improved charge carrier transport and extraction across this interface rather than being related to an improved absorber growth. This is further evidenced by a performance improvement of inverted solar cell devices with pre-evaporated MAI and post-deposited PbI$_2$ layers. Finally, we provide two hypothetical electronic models that might cause the observed effects.

Lead halide perovskite semiconductors have excelled in recent years as versatile semiconductors in a variety of opto-electronic applications[1,2]. Most prominently, laboratory scale solar cells, both in single junction ($\eta > 25$ %) and tandem configuration with Si ($\eta > 29.5$%), have shown rapidly increasing record efficiencies well beyond expectations[3].

Apart from device stability, main concerns in view of an industrial uptake of the technology are the scalability and reproducibility of the implemented fabrication processes. While many technological advances on small, laboratory scale solar cells have been obtained with wet-chemical methods (e.g. spin-coating, printing), some vacuum-based approaches have also been successfully implemented.

Liu et al. reported the fabrication of efficient, planar perovskite solar cells by dual source co-evaporation, using methylammonium (MA) and PbCl$_2$ as precursors reaching efficiencies above 15%[4]. Several other groups have followed this route (with either PbI$_2$ or PbCl$_2$ as lead halide precursors)[5] and in 2019 the use of optimized contact layers by Bolink et al. led to efficiencies exceeding 20%[6]. Co-evaporation generally leads to compact, homogeneous films, is fast and easily scalable and offers an improved processing control under reproducible conditions. The two main approaches used nowadays are based either on a) simultaneous, stationary co-evaporation from different sources or b) sequential processing, where first only one component is deposited (normally the lead halide, e.g. PbI$_2$). This precursor layer is then converted into the perovskite, e.g. through exposure to an MAI atmosphere or by deposition of the MAI followed by an annealing[7,8].

Attempts to partly combine the two approaches are rare, i.e. to move to non-stationary co-evaporation where the application of the two precursors is not completely synchronized and stationary. This is even more

astonishing, as this is in fact one of the main advantages of co-evaporation in comparison to solution-based processing: the amount and ratio of precursors arriving at the substrate can be varied during processing. As an example for other photovoltaic technologies, high efficiency co-evaporated solar cells based on chalcopyrite $Cu(In,Ga)Se_2$ absorbers are prepared with a complex Cu-poor/Cu-rich/Cu-poor evaporation scheme leading to optimal absorber properties and a carefully designed band gap gradient within the absorber[9].

In this sense, non-stationary co-evaporation not only bears the potential to vary the composition of the absorber during growth, but also to initiate or terminate the growth with specific precursor compositions. Furthermore, it is rather difficult in an industrial in-line fabrication, where the substrates are normally transported across a series of linear evaporation sources, to ensure the continuously homogeneous, stationary flux of constant precursor ratios to the substrate, as is the case in a stationary laboratory setup.

These considerations motivated us to investigate the impact of pre-evaporating of precursors, starting the evaporation with seed layers instead of a continuous evaporation. This approach continues our previous work in this direction for solar cells in a regular n-i-p configuration[10]. To the best of our knowledge, this is so far the only work considering such kind of asynchronous, non-stationary co-evaporation, where we found that a pre-evaporation of PbI_2 seed layers was greatly beneficial to the solar cell performance. We argumented, that the PbI_2 seed layer initiated crystallization, increased the sticking coefficient and led to the growth of a MAPI absorber with improved properties. However, ultimately it remained unclear whether the performance improvement originated from an improved absorber growth (as a result of the different nucleation on the PbI_2 seed layer) or due to an improved interface to the electron transport layer (ETL).

In order to elucidate this question, here, we present our first results on novel pre/post-evaporation schemes for inverted perovskite solar cells based on a p-i-n structure with NiO as hole transport layer (HTL) and an ETL double layer based on [6,6]-Phenyl C61 butyric acid methyl ester (PCBM) and ZnO. We use different pre/post-deposition schemes of MAI and PbI_2 and report their impact on absorber growth in terms of crystallization and morphology and on performance in complete solar cell devices.

The motivation to use an inverted solar cell configuration is two-fold: On the one hand, it allows us to directly compare the results obtained in our previous work and study the impact of pre/post-evaporation schemes for an inverted contact layer configuration (PbI_2 pre-evaporation onto the HTL instead of the ETL layer). On the other hand, the use of an inverted device configuration is motivated by our longterm goal to fabricate tandem devices, where a solar cell in p-i-n configuration is needed to ensure the correct direction of the current flow in the top cell with respect to the diode of the bottom cell (p-type Si or chalcopyrite solar cell).

Experimental methodology

Solar cells were prepared on glass substrates coated with transparent conductive indium-tin-oxide (ITO) layers in an inverted p-i-n structure. The used stacked cell architecture is based on NiO as hole transport layer (HTL) and a bilayered electron transport layer (ETL) made of phenyl-C61-butyric acid methyl ester (PCBM) and ZnO nanoparticles. The complete solar cell consists of a glass/ITO/NiO/MAPI/PCBM/ZnO/Ag layer stack. Details concerning the sample preparation, ETL/HTL deposition parameters, the solar cell fabrication and characterization methodology can be found in the supporting information.

The co-evaporation of MAPI absorbers was carried out in a high vacuum chamber (base pressure 10^{-5}mbar) with two evaporation sources filled with MAI and PbI_2, respectively. The setup is described in detail in the work by Heinze et al., where dynamic processing schemes including the pre-deposition of different seed layers were developed for regular solar cells in n-i-p structure in the same system[10]. Further experimental details on the evaporation setup and the characterization methodologies can be found in the supporting information.

The MAPI absorbers were synthesized by co-evaporating MAI and PbI_2. Optimal deposition parameters concerning the optimal flux ratios for near stoichiometric absorber compositions had been determined previously (see reference[10]). Following this work, we ramped both crucibles to their respective target temperature in 900s. A constant PbI_2 source temperature of 288°C was used for all experiments. The target temperature for the temperature ramp of the MAI crucible was set to 115°C. Due to its high vapor pressure and particle scattering[5], MAI does not evaporate directionally. As a consequence, the MAI flux cannot be easily controlled by the source temperature alone, nor the installed quartz crystal microbalance. In accordance with[10,11], the MAI flux was therefore controlled by adjusting the MAI source temperature in order to maintain a constant working pressure within the evaporation system. The optimal constant working pressure had been previously determined and was set to 7.5×10^{-5}mbar[10].

Our evaporation setup is equipped with an in situ X-ray diffraction setup (in situ XRD). It consists of a Cu Kα X-ray source and linear detector array arranged at opposite sides of the vacuum chamber. The X-rays enter and leave the chamber through Kapton windows allowing the recording of XRD scans in an angular 2Θ-range of 28°. Details on the experimental setup can be found in the supporting information and in references[10,12].

In this work, MAPI absorbers were deposited on glass/ITO/NiO substrates in a variation of four different evaporation schemes. Every process was carried out with at least 4 samples (3 solar cells on each sample) allowing a small statistical comparison. A nitrogen filled glovebox is directly attached to our evaporation system, allowing the sample/source material insertion/extraction under inert working conditions. The four different evaporation schemes are schematically illustrated in Fig. 1 and will be named throughout this work with the following abbreviations.

The entire evaporation time was 10100s for Eva 1-3 and 10700s for Eva 4. Pre- or post-evaporation times were set to 600s leading to total absorber thicknesses in the range of 300nm. According to our previously performed flux measurements, the layer thickness during the pre/post-evaporation sequences of 600s is in the range of 10nm to 20nm.
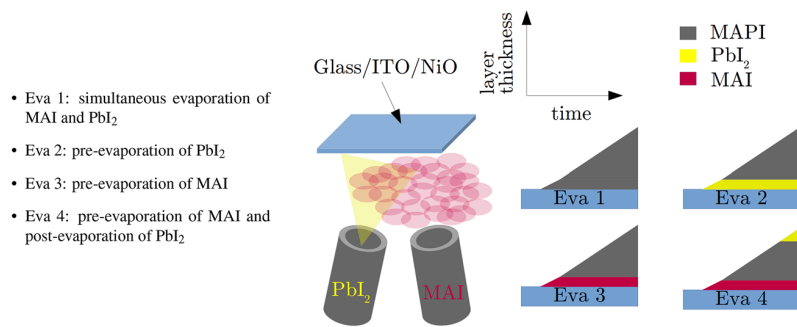
Figure 1. Schematic representation of the co-evaporation schemes using PbI_2 and MAI precursors on glass/ITO/NiO substrates to grow MAPI. While PbI_2 evaporates as a molecular stream, MAI is distributed homogeneously in the chamber, increasing the total chamber pressure[13,14]. Different evaporation schemes (Evaporation 1-4) by choice of different initial/final evaporation conditions have been tested and compared with regard to their impact on the crystal growth and the electronic properties of the absorber.
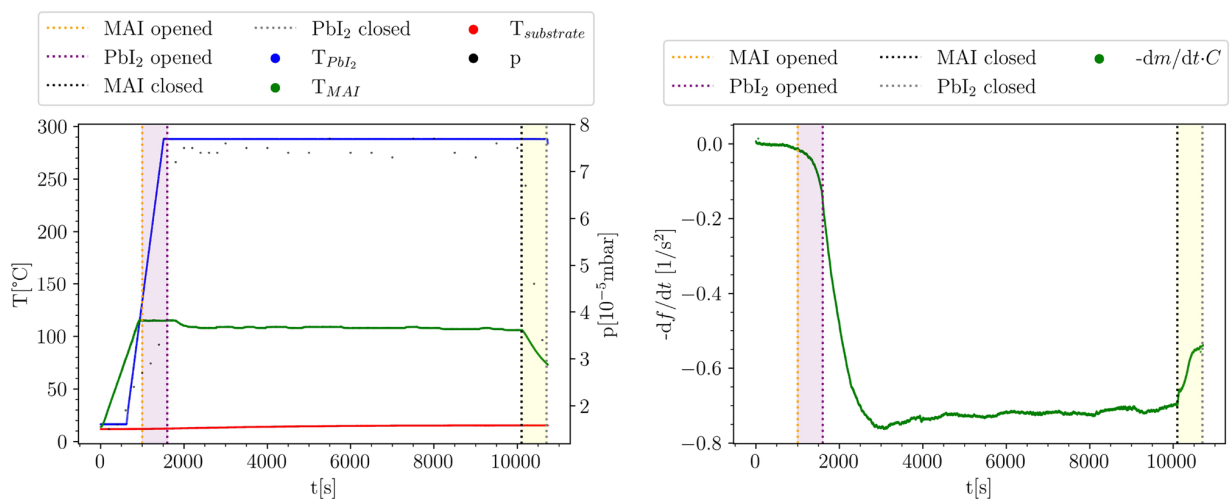

Figure 2. Pre-evaporation of MAI in combination with post-deposition of PbI_2 (Eva 4). The left plot shows the temperatures and pressure for the whole evaporation time, the right image visualizes the time derivative of the frequency calculated from the measured frequency by the QCM.

After the MAPI evaporation was finished, 3 out of 4 samples were further processed to solar cells in a nitrogen atmosphere by adding a PCBM/ZnO electron transport layer (ETL). Finally, Ag contacts were evaporated in a separate vacuum chamber. j-V characteristics of the solar cells were measured under simulated AM1.5 illumination. Details on the sample preparation and contact layer deposition can be found in the supporting information. On the remaining sample, TRPL, SEM and EDX measurements were conducted in this order. For SEM analysis, the sample was cut in half allowing cross-sectional imaging.

Results

Evaporation process. Figure 2 shows EVA 4 as an example for the evolution of the crucible temperatures, chamber pressure (left) and the quartz crystal micro balance (QCM) reading for the evaluation of the deposited mass (right). A comparison of the remaining evaporation schemes can be found in the supporting information. The shutter control for the pre-deposition of MAI and post-deposition of PbI_2 was adjusted to the heating scheme as indicated with dashed lines in the plots. Pre- and post-deposition intervals are marked by the colored rectangles (purple: MAI pre-evaporation, yellow: PbI_2 post-evaporation). For the pre-deposition of MAI, the MAI deposition was started 600s earlier and accordingly, the post-deposition of PbI_2 in Eva 4 was carried out by turning off the MAI heater, closing the MAI shutter and continuing with the deposition of PbI_2. The substrates were not actively heated and the substrate temperature stayed approximately constant for all evaporations starting at $T_{subs} = 12$ °C and reaching $T_{subs} = 16$ °C at the end of the process.

At the right hand side of Fig. 2, the time derivative of the QCM frequency is displayed. This quantity is proportional to the rate of deposited mass modified by material constants of the quartz crystal and visualizes the deposition kinetics[15]. The development of the time derivative of the QCM frequency shows that some mass is already deposited before the shutters were opened, which is explained by the non-directional evaporation
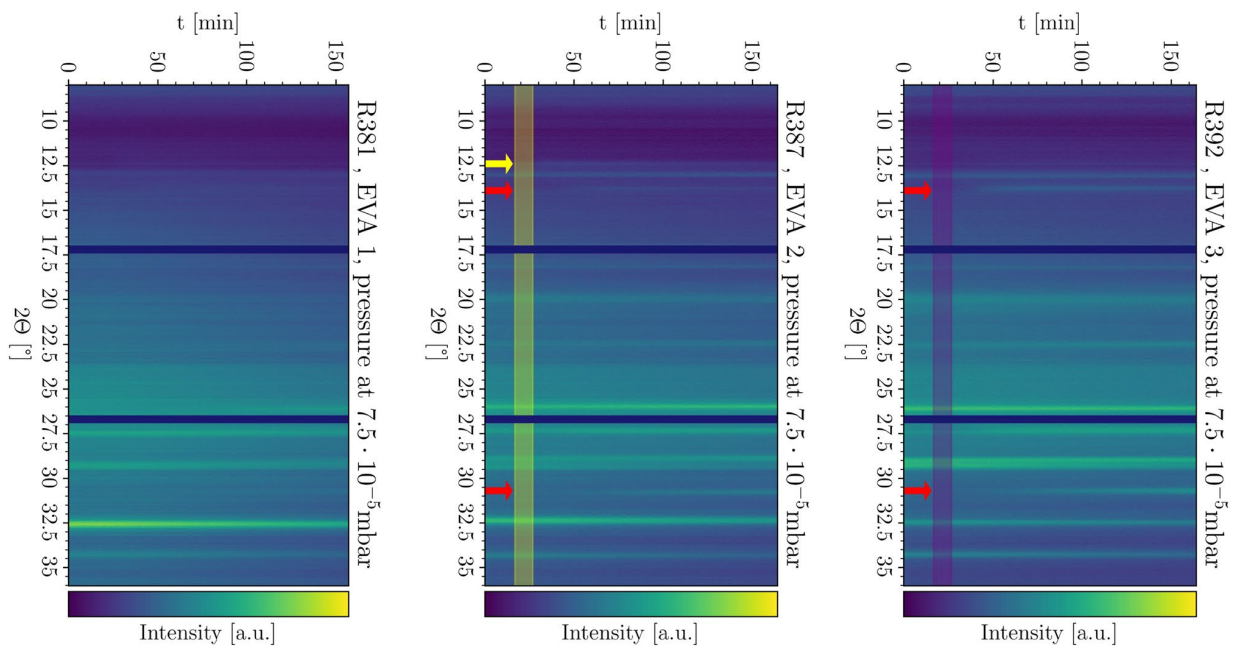
Figure 3. In situ XRD scans of Eva 1 (left), Eva 2 (middle) and Eva 3 (right). The yellow arrow marks the significant PbI_2 peak while the red arrows indicate the significant MAPI peaks[16,17]. Pre-evaporation intervals are marked by colored rectangles (yellow: PbI_2 pre-evaporation, purple: MAI pre-evaporation).

behaviour of MAI[13,14]. After the MAI shutter was opened, the slope increases, in accordance with the observed increase in chamber pressure (left). When the PbI_2 shutter is opened, the slope increases again until a stable deposition is reached at approximately 3000s after the process was started. When the MAI shutter is closed the deposition rate decreases slightly due to the missing MAI flux indicating the post-deposition of PbI_2.

The deposition processes were monitored with the in situ XRD system attached to the evaporation chamber as displayed in Fig. 3. Here, the evolution of the XRD intensity is color-coded in color maps where the x-axis represents the evolution of process time and the y-axis represents the diffraction angle. The color maps are normalized to the maximum value of each measurement. All peaks which are visible from the beginning either belong to the substrate (glass/ITO/NiO) or the substrate carrier and will not be discussed here. The detector assembly has two blind spots at $17.5°$ and $26.5°$.

Eva 1 did not show any signs of crystallization or crystalline thin film growth; no peaks correlated to MAPI, MAI or PbI_2 were observable. However, visually, the substrates were dark after the co-evaporation process and SEM cross-sections confirmed deposition of a thin film of 300nm. For the case of Eva 2, a PbI_2 (001) peak at $12.5°$ [16] can be observed starting approximately 30min after the beginning of the process. After approximately 60min, tetragonal MAPI (110) and (114) peaks[17] at $14°$ and $31.5°$, respectively, become visible. For the third evaporation scheme with MAI pre-evaporation (EVA 3), no PbI_2 peak was detected. The tetragonal MAPI peaks appeared earlier at approximately 45min and with increased intensity relative to the substrate peaks.

SEM and EDX measurements. Figure 4 displays cross-sectional scanning electron microscope (SEM) images of the absorbers. The absorber thickness of Eva 1-3 was measured to be approximately 300nm, only Eva 4 was slightly thinner at approximately 250nm. In between the absorber and the ITO layer (ca. 180nm), the NiO layer can be identified as a slim, bright line with distinct grain structure and a thickness of approximately 25nm. The morphology of the EVA 1 absorber in Fig. 4 shows round particles and some porosity, while for the absorber of Eva 2 no distinct granular structure is observed, but a rather homogeneous cross-section. For Eva 3 and Eva 4, clearly distinguishable granular structures of few tens to one hundred nanometers can be distinguished. Further discussion and morphology images can be found in the supporting information.

Detecting lighter elements like carbon or nitrogen was not possible with sufficient accuracy in the used setup[18], impeding the direct quantification of methylammonium via EDX. In Table 1 the results of the EDX measurements for Pb and I are listed for comparison of all processes. The stoichiometric perovskite has the chemical formula ABX_3[19] leading to a nominal $\frac{I}{Pb}$ ratio of 3. We evaluate the stoichiometry according to the [I] to [Pb] ratio $\frac{I}{Pb}$, where values above 3 would be expected for MAI-rich absorbers and values below 3 indicate PbI_2-rich perovskites. We conclude that all absorbers had a near stoichiometric composition, with Eva 1, 2 and 4 being slightly PbI_2-rich, while Eva 3 (with pre-deposited MAI) was slightly MAI-rich (I/Pb ratio of 3.08).

TRPL measurements. The influence of a post-deposited PbI_2 top layer (Eva 4) was analyzed qualitatively by TRPL measurements of the absorber from the top side. Figure 5 only displays the lowest $(0,001 \cdot I_0)$ and high-
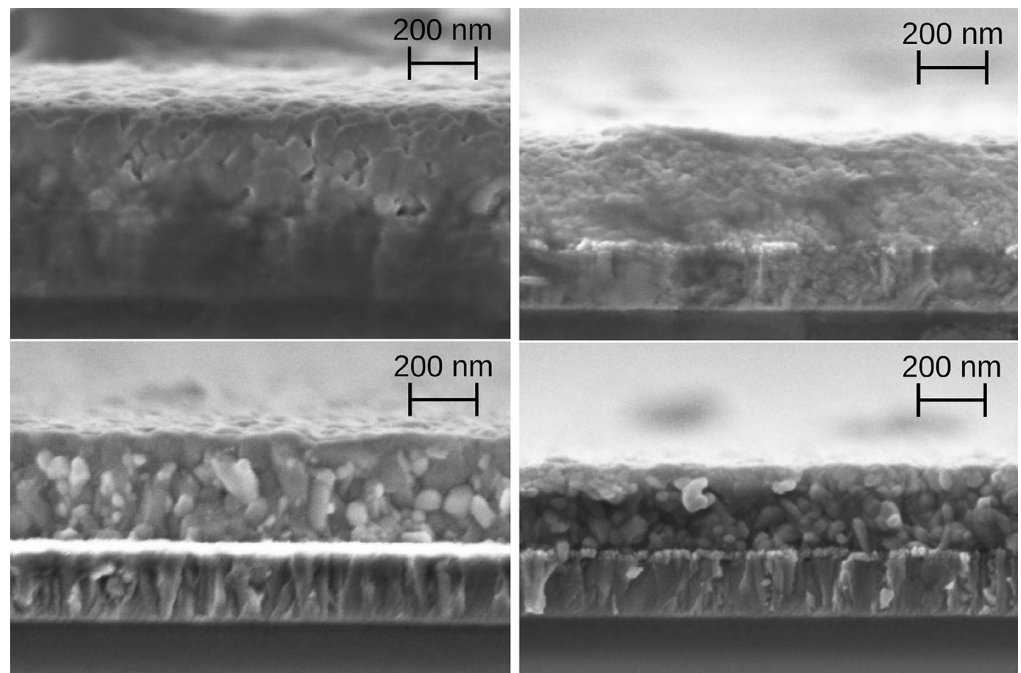
Figure 4. Cross-sectional SEM images of the perovskite absorbers of Eva 1 (top left), Eva 2 (top right), Eva 3 (bottom left) and Eva 4 (bottom right). The magnification was fixed at 80000.

	Eva 1	Eva 2	Eva 3	Eva 4
I atom [%]	73.47	74.03	75.49	74.23
Pb atom [%]	26.53	25.97	24.51	25.77
$\frac{I}{Pb}$	2.77	2.85	3.08	2.88

Table 1. EDX measurement of the absorbers from different evaporation processes. The atomic fractions were normalized to 100%. A relative error of 4% for all measurements was considered as reasonable and calculated by the EDX software.
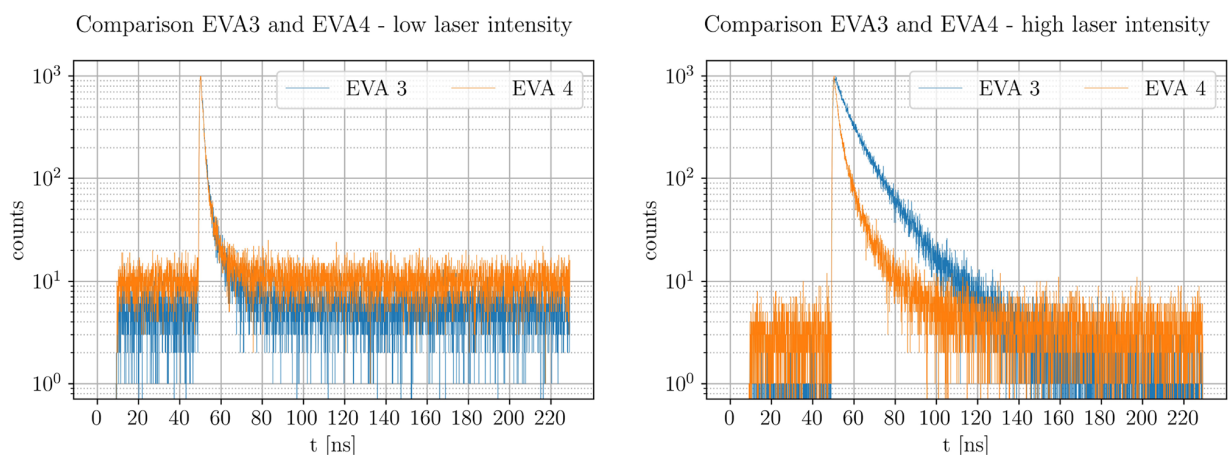
Figure 5. Comparison of TRPL measurements of Eva 3 and Eva 4 with low laser intensity ($0,001 \cdot I_0$, left) and high laser intensity (I_0, right). The incident beam was focused on the absorber top side, which was also the area of photon detection. Attenuation of the laser intensity to $0,001 \cdot I_0$ was made possible by using a neutral gray filter.
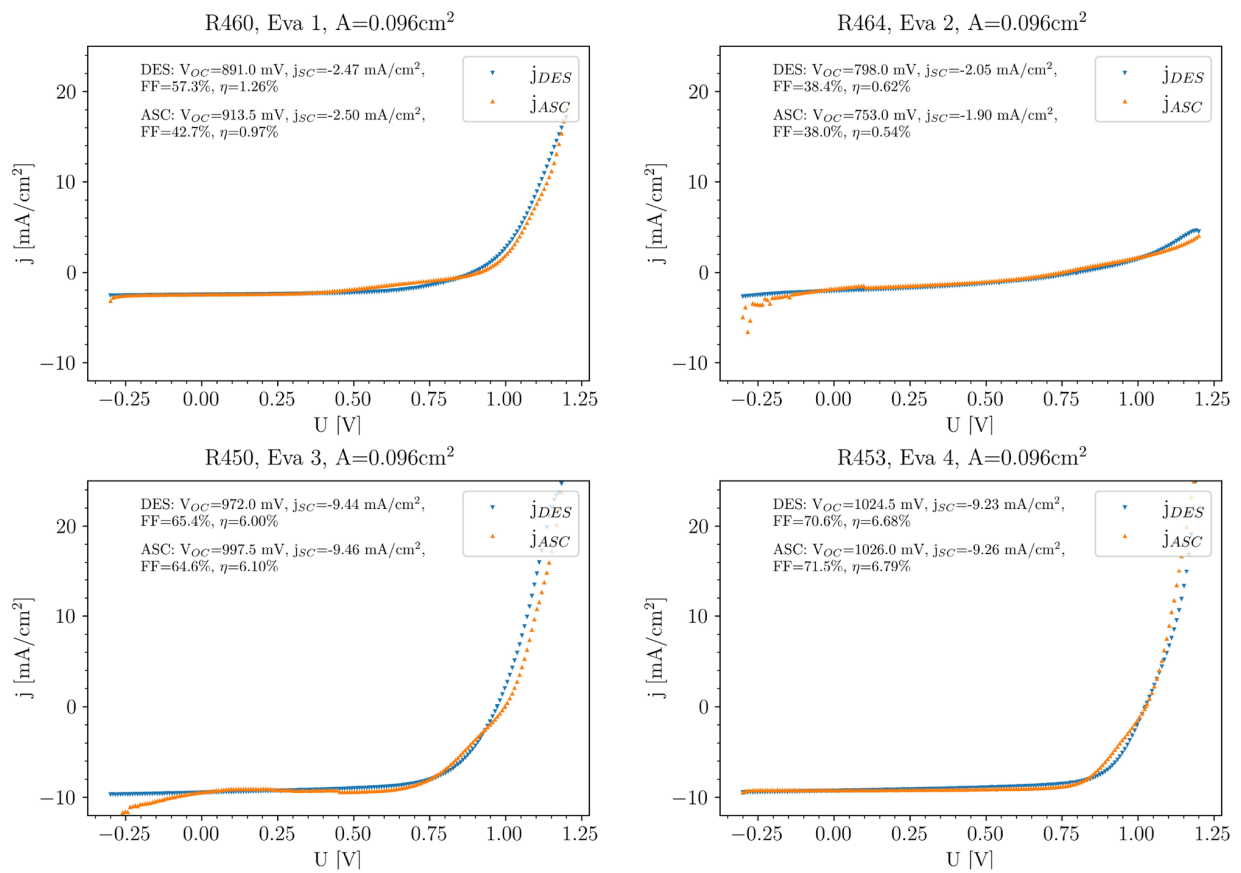
Figure 6. j-V characterisation of Eva 1 (top left), Eva 2 (top right), Eva 3 (bottom left) and Eva 4 (bottom right).

	$V_{OC} \pm$ SD [V]	$j_{SC} \pm$ SD [mA/cm^2]	$\eta \pm$ SD [%]	FF $\pm$ SD [%]
Eva 1	0.90 ± 0.03	2.78 ± 1.01	1.22 ± 0.39	51.31 ± 7.63
Eva 2	0.94 ± 0.04	1.64 ± 0.69	0.52 ± 0.24	34.67 ± 2.18
Eva 3	0.96 ± 0.03	8.01 ± 0.90	4.31 ± 1.03	54.87 ± 9.29
Eva 4	1.02 ± 0.00	7.83 ± 1.24	5.86 ± 0.76	73.75 ± 2.05

Table 2. Average and standard deviation (SD) of the solar cell parameters corresponding to the different evaporation schemes. The total amount of measured solar cells and the parameter distribution for the corresponding statistical value is displayed in the supporting information.

est laser (I_0) intensities that were used in a series of different intensities. We did not detect any photo degradation during these measurements and during subsequent control measurements.

In general, the observed photoluminescence decays are not strictly mono-exponential, indicating a combination of recombination processes[20]. The decay times for the low intensity curves are approximately similar for both evaporation schemes. A built-in electric field rapidly separating the generated charge carriers is one possible explanation for the short decay times at low injection levels, an effect that would be counterbalanced by the generated photovoltage at higher injection levels. At high illumination conditions, the measured signal is significantly different between Eva 3 and Eva 4. The faster decay of Eva 4 could be explained by improved charge carrier extraction due to the post-evaporated lead iodide layer. This would result in less charge carrier accumulation and therefore quenching of the TRPL signal.

j-V analysis. After completing the solar cell devices by deposition of ETL and contact layers, j-V curves were measured under simulated AM1.5 sun light in ascending and descending voltage sweep directions. The j-V curves of the best performing solar cells measured in ascending and descending direction are plotted for each evaporation run exemplary in Fig. 6, while averaged solar cell parameters are listed in Table 2. A more detailed analysis of the data distribution of the solar cell parameters for each evaporation scheme can be found in the supporting information.

The best solar cell for the simultaneous (no pre-/post-deposition) evaporation scheme (Eva 1, top left graph in Fig. 6) resulted in a device with rectifying behaviour, an open circuit voltage around 900mV, low fill factor (42 % in ascending and 57 % in descending direction) and little hysteresis. Due to the rather low short circuit current density of less than 3mA/cm^2, the efficiency of the best device for this evaporation scheme was limited to approximately 1 %. When PbI$_2$ is pre-evaporated (EVA 2, top right graph), the performance of the corresponding solar cells is even lower, mainly because of the drastically decreased fill factor (38% in both directions). The j-V curve now nearly shows no rectifying behaviour and the average efficiency of all solar cells from this evaporation scheme was limited to well below 1 %. This stands in clear contrast to our expectations and the results from Heinze et al. in[10], where the PbI$_2$ pre-evaporation had led to an increased short circuit current density and overall performance in n-i-p based solar cells.

On the contrary, a large improvement in the short circuit current density was observed for EVA 3 (bottom left), were MAI instead of PbI$_2$ was pre-evaporated. For this evaporation scheme, solar cell efficiencies exceeding 6 % were obtained. A further improvement was observed by additional post-deposition of PbI$_2$ (Eva 4, bottom right): here, the efficiency of the best solar cell is elevated to 6.7 % (descending) and 6.8% (ascending). This increase is mainly due to the better open circuit voltage exceeding 1V and an improved fill factor (above 70 %).

Overall solar cell efficiencies of the devices presented in this work are well below the current state-of-the-art of evaporated perovskite solar cells. Despite this, a clear impact of the evaporation scheme on the solar cell performance can be observed in both the j-V curves of the best cells and the list of averaged parameters. We would like to stress the fact that we have reproduced these results and that the co-evaporation methodology and equipment employed here are identical to the ones presented in our previous publication ([10]) and therefore have proven to provide absorber-grade MAPI with reasonable efficiencies. Despite our efforts, in the inverted p-i-n configuration we have not been able so far to produce solar cells with co-evaporated MAPI exceeding 8% efficiency, in contrast to the regular n-i-p configuration where we achieved efficiencies around 15%. As the same processing conditions have been applied, we believe that the main problems of our p-i-n devices lay still in the contacting layers, which demand further optimization.

The main reasoning for this is that the deposition parameters used in this work corresponded to the ones used in our prior publication on the regular solar cell structure, where indeed satisfying device efficiencies had been obtained. The underperformance of the devices presented in the current work is therefore not expected to be related to the absorber growth conditions per se, but must be somehow related to the variation of the substrate/contact layers.

However, in view of the comparable processing conditions we are able to draw several valuable and important conclusions taking into account our current and the previous work as will be discussed in the following.

Discussion

Bækbo et al. showed that decomposition of MAI into smaller structures (mainly HI and CH$_3$NH$_2$) occurs when MAI is evaporated[13]. The adsorption kinetics were described by Kim et al. discussing the adsorption of PbI$_2$ and MAI on the substrate surface[21]. Both groups only measured a minor impact of the MAI flux on the quartz crystal balance. Therefore the suggestion of Kim et al. was made that the nucleation process consists of a seed layer of PbI$_2$ which is used as preferential bond for the MAI components. MAPI is then formed by diffusion processes of MAI through the seed PbI$_2$ layers. These diffusion processes were also described for PbCl$_2$ by Bækbo et al. and Chen et al. while the latter work showed a conversion of a 150nm PbCl$_2$ layer into MAPbCl$_3$[13,22]. For simultaneous evaporations, Parrott et al. showed that the growth starts with nucleation of small islands of 8nm height[23]. Heinze et al. showed that an initial crystallization of PbI$_2$ is possible during simultaneous evaporation depending on the targeted chamber pressure[10].

Here, we observed that the pre/post-deposition of one of the two precursors in dual source co-evaporation of perovskite absorbers has a strong impact on the absorber properties and solar cell performance. Interestingly, PbI$_2$ seed layers (Eva 2) neither lead to better crystallization nor improved solar cell performance. The in situ XRD showed that the PbI$_2$ seed layers pre-deposited in Eva 2 were not fully converted to MAPI, but remained unreacted throughout the deposition. Therefore, a diffusion-driven formation of MAPI was, at least, not completed. Heinze et al. reported an increase of solar cell efficiency with the pre-evaporation of PbI$_2$ in the n-i-p structure, even with remaining PbI$_2$ XRD peaks[10]. We therefore conclude that the PbI$_2$ itself is not necessarily detrimental to the absorber, e.g. by introducing deep defects at the MAPI/PbI$_2$ interface. On the contrary, PbI$_2$ has been claimed to have a passivating effect in several works[24,25]. The detrimental effect of the PbI$_2$ seed layers in this work are therefore attributed to their location at the HTL side in the p-i-n structure. In fact, depositing PbI$_2$ at the ETL side of the device through post-deposition showed an improvement (EVA 4), similar to the seed layers in the n-i-p structure of Heinze et al[10].

Furthermore, it was seen that only the processes with an MAI seed layer (Eva 3 and Eva 4) achieved an absorber structure with a distinct granular structure, and an improved solar cell performance. Muscarella et al. showed that the crystal plane orientation does not necessarily determine the electronic or optic properties, but Hsiao et al. assume a positive effect of larger grains because of less interfaces as recombination centres between the contacts[14,26].

Ou et al. found that the electronic properties of MAPI highly depend on the MAI/PbI$_2$ ratio allowing different doping states from p-doped to n-doped which is caused by the placement of donor defects in the crystal lattice[27]. However, the electronic properties are not only influenced by the electrons and holes as charge carriers. Eames et al. showed the ionic migration of iodine and therefore effects on the band diagram in dependence of the stoichiometry to occur in MAPI[28]. The EDX measurements revealed that the films prepared during the course of this work were on average either nearly stoichiometric, or slightly PbI$_2$-rich. With reference to the work of Ou et al., this implies that the MAPI absorbers on average are intrinsic or n-doped to different extents.
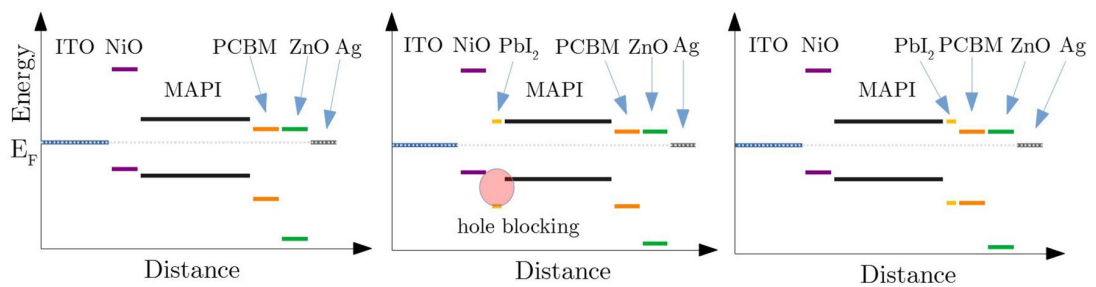
Figure 7. Schematic illustration of possible band diagrams including unconverted layers of lead iodide. The left image shows the solar cell with a fully converted MAPI absorber without residual PbI_2 (Eva 1). The middle image shows the solar cell with an additional layer of PbI_2 on top of the NiO (Eva 2). The right image shows the case of an unconverted lead iodide layer on top of the MAPI absorber (Eva 4).
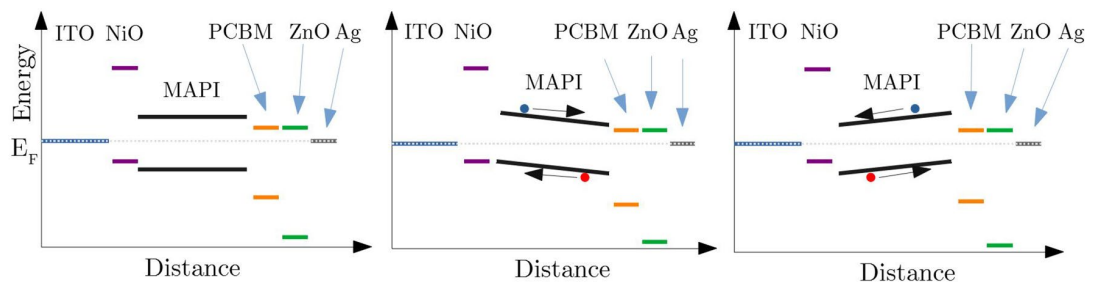
Figure 8. Schematic illustration of the band diagrams resulting from doping gradients within the MAPI absorber. Here, the blue circle illustrates the electrons and the red circle the holes. The left image shows the solar cell with a fully converted MAPI absorber without stoichiometry variations/gradients (Eva 1). The middle image shows a MAPI absorber with MAI-rich stoichiometry at the NiO interface and PbI_2-rich stoichiometry at the ETL interface (Eva 4). The right image shows a MAPI absorber whose stoichiometry is PbI_2-rich at the NiO interface and MAI rich on top of the absorber (Eva 2).

In order to explain the measured differences in solar cell performance, we present two hypothetical models as thought experiments. Figures 7 and 8 show illustrations of these possible effects of the different evaporation schemes on the electronic structure of our devices. The graphs present schematic sketches of possible band diagrams, where the placements of valence band, conduction band and Fermi level correspond to the literature data as measured by PES in references[24,29–33].

According to these data from literature, due to the band offset in the valence band, an incomplete conversion of the PbI_2 layer covering the NiO (Eva 2) would lead to a hole blocking barrier as displayed in the band diagram presented in Fig. 7. Such an energy barrier for the holes traveling towards the HTL might drastically decrease the solar cell performance. Numerical calculations based on experimental data already showed the possibility and effect of such a band offset for a PbI_2/MAPI interface[34].

If unconverted PbI_2 (Eva 4) is placed on top of the absorber, however, the effect would be opposite: Here, adjacent to the ETL, a blocking of the holes while letting the electrons pass through would actually support the filtering effect of the ETL.

TRPL measurements show that the decay times for high illumination intensities are reduced for the samples with PbI_2 post-deposition. One possible explanation is a larger density of trapping defects in the case of the pure MAPI layer or MAPI/PCBM interface, which would artificially prolong the observed decay time beyond the charge carrier lifetime through re-emission from the trap states[35]. A removal of the trap states at the interface by passivation with PbI_2 would in turn lead to reduced TRPL decay times, which is one possible interpretation of our TRPL data.

Golubev et al. numerically investigated the impact of buffer layers especially for a MAPI/C_{60} interface. They calculated the influence of defect states on the open circuit voltage, which increases for a smaller number of these states[36].

Furthermore, their numerical investigations were built on the experimental work of Liu et al., who reported a significant decrease in photoluminescence (PL) intensity and an increase in solar cell performance after placing a C_{60} layer on top of a perovskite[37,38]. The numerical studies showed that this performance increase is probably a result of higher charge carrier mobility at the perovskite/C_{60} interface, and therefore an improved charge transport across this interface[36]. This explains the decrease in PL by improved charge carrier extraction from the absorber, which leads to less radiative recombination and thus, lower PL intensity. The post-deposited PbI_2 layer could act in a similar way as the C_{60} buffer layer does, because the decay times at high intensities in our experiments were smaller as compared to the sample without post-deposition, while the open circuit voltage increased. These considerations would also match the research of Jacobsson et al., who studied the influence of

remnant lead iodide on the MAPI absorber[24]. They found that lead iodide excess can improve the charge carrier extraction and leads to a quenching of the PL. This would be a second possible interpretation of the observed reduction of TRPL decay times in combination with an improved open circuit voltage. Additional measurements in this respect are needed to lead to more conclusive results.

A different thought model explaining the performance increase for the pre/post-deposition schemes is displayed in Fig. 8. As discussed before, the stoichiometry has a direct influence on the MAPI doping[27]. The n-i-p structure showed improved performance when PbI_2 was pre-evaporated[10,13]. Even for fully converted PbI_2 layers, it could be expected that the first MAPI layers after PbI_2 pre-evaporation would possess a PbI_2-rich stoichiometry[27,39,40]. In the case of the p-i-n structure this would lead to n-doped areas of MAPI close to the HTL[27,39,40]. The other way around, a pre-deposition of MAI would lead to a p-doped absorber interface adjacent to the HTL.

Following this line of thought, the pre- and post-evaporations induce stoichiometry gradients in the absorber, which in turn result in doping gradients and a band bending of the absorber at the interfaces. If the band bending fits the alignment of the ETL and HTL, the charge carrier separation and migration to the corresponding contacts is supported. Otherwise the charge extraction is impeded. This would also mean that even if the layers of pre-deposited PbI_2 were fully converted to MAPI in the (inverted) p-i-n structure, this setup is not preferable due to the mismatching band bending. Transferring these considerations to the pre-evaporation of MAI and the post-evaporation of PbI_2 (Eva 4), the absorber would be p-doped on the NiO interface (MAI-rich), intrinsic in the bulk (stoichiometric) and n-doped at the PCBM interface (PbI_2-rich), a configuration which would support charge extraction. These scenarios are depicted schematically in Fig. 8.

While we are unable to distinguish between the two hypotheses or confirm them further at this point, we present them here in order to inspire further thoughts along this line and would like to encourage additional research in this direction. It is clear, that both effects could also occur to different extends in parallel.

Conclusion

This work showed that the pre-deposition of PbI_2 in the inverted p-i-n structure (Eva 2) is strongly detrimental for perovskite solar cell performance, in contrast to our previous results for solar cells in the regular n-i-p configuration. On the contrary, the pre-evaporation of MAI in combination with the post-evaporation of PbI_2 is beneficial (Eva 4) and showed the best solar cell efficiencies. While the pre-evaporation of MAI strongly improved the short circuit current density, the PbI_2 post-deposition mainly resulted in an increased fill factor and open circuit voltage.

Two thought models potentially explaining the influence of the sequential evaporations schemes on the measured performance have been portrayed. The first model presumes the evaporation of an unconverted PbI_2 layer to create an energy barrier for the holes in the p-i-n structure due to the mismatched band offset[24,29–33]. This would be beneficial at the ETL interface (post deposition of PbI_2), but not desirable at the HTL side. The second model assumes a conversion of pre- and post-evaporated layers, but with a remaining stoichiometry gradient, ultimately resulting in a doping profile within the absorber. By pre- and post-evaporation of MAI and/or PbI_2, it is possible to tune the doping of the MAPI at the top/bottom interface and therefore create a band bending which aids or hinders the charge carrier separation[13,21,27,39,40]. Both models are not in conflict with each other and in practice a combination of both effects is considered to be most likely.

For the first time different pre- and post-deposition sequences have been applied to MAPI solar cells in p-i-n configuration. Our results underline the importance to consider stoichiometry variations within the absorber and at the absorber interface during processing, especially in view of industrial in-line processing with non-stationary substrates. Together with our previous results, this work stresses the importance of initial and final steps of a co-evaporation process and sheds light onto the basic concepts of non-stationary processing schemes stimulating both exciting further scientific investigations and innovative technological processing options. We are confident that our results and lines of thought will enable and trigger a wide range of further research activities on dynamic and pre/post-evaporation schemes for co-evaporated solar cell absorbers.

Data availability

The datasets generated and analyzed during the current study are available from the corresponding author on reasonable request.

References

1. Manser, J. S., Christians, J. A. & Kamat, P. V. Intriguing optoelectronic properties of metal halide perovskites. *Chem. Rev.* **116**, 12956–13008. https://doi.org/10.1021/acs.chemrev.6b00136 (2016).
2. Mitzi, D. Introduction: Perovskites. *Chem. Rev. B* **119**, 3033–3035. https://doi.org/10.1021/acs.chemrev.8b00800 (2019).
3. Green, M. A. *et al.* Solar cell efficiency tables (version 59). *Prog. Photovoltaics Res. Appl.* **30**, 3–12. https://doi.org/10.1002/pip.3506 (2021).
4. Liu, M., Johnston, M. B. & Snaith, H. J. Efficient planar heterojunction perovskite solar cells by vapour deposition. *Nature* **501**, 395–398. https://doi.org/10.1038/nature12509 (2013).
5. Ávila, J., Momblona, C., Boix, P. P., Sessolo, M. & Bolink, H. J. Vapor-deposited perovskites: The route to high-performance solar cell production?. *Joule* **1**, 431–442. https://doi.org/10.1016/j.joule.2017.07.014 (2017).
6. del Rey, D. P., Boix, P. P., Sessolo, M., Hadipour, A. & Bolink, H. J. Interfacial modification for high-efficiency vapor-phase-deposited perovskite solar cells based on a metal oxide buffer layer. *J. Phys. Chem. Lett.* **9**, 1041–1046. https://doi.org/10.1021/acs.jpclett.7b03361 (2018).
7. Chen, C.-W. *et al.* Efficient and uniform planar-type perovskite solar cells by simple sequential vacuum deposition. *Adv. Mater.* **26**, 6647–6652. https://doi.org/10.1002/adma.201402461 (2014).

8. Chen, H. Two-step sequential deposition of organometal halide perovskite for photovoltaic application. *Adv. Func. Mater.* **27**, 1605654. https://doi.org/10.1002/adfm.201605654 (2017).

9. Caballero, R. *et al.* Cu deficiency in multi-stage co-evaporated CU(IN, GA)SE2 for solar cell applications: Microstructure and GA in-depth alloying. *Acta Mater.* **58**, 3468–3476. https://doi.org/10.1016/j.actamat.2010.02.021 (2010).

10. Heinze, K. L. *et al.* Importance of methylammonium iodide partial pressure and evaporation onset for the growth of co-evaporated methylammonium lead iodide absorbers. *Sci. Rep.* **11**, 15299. https://doi.org/10.1038/s41598-021-94689-1 (2021).

11. Wang, S. *et al.* Smooth perovskite thin films and efficient perovskite solar cells prepared by the hybrid deposition method. *J. Mater. Chem. A* **3**, 14631–14641. https://doi.org/10.1039/c5ta03593g (2015).

12. Pistor, P., Borchert, J., Fränzel, W., Csuk, R. & Scheer, R. Monitoring the phase formation of coevaporated lead halide perovskite thin films by in situ x-ray diffraction. *J. Phys. Chem. Lett.* **5**, 3308–3312. https://doi.org/10.1021/jz5017312 (2014).

13. Bækbo, M. J., Hansen, O., Chorkendorff, I. & Vesborg, P. C. K. Deposition of methylammonium iodide via evaporation - combined kinetic and mass spectrometric study. *RSC Adv.* **8**, 29899–29908. https://doi.org/10.1039/C8RA04851G (2018).

14. Hsiao, S.-Y. *et al.* Efficient all-vacuum deposited perovskite solar cells by controlling reagent partial pressure in high vacuum. *Adv. Mater.* **28**, 7013–7019. https://doi.org/10.1002/adma.201601505 (2016).

15. Sauerbrey, G. Verwendung von schwingquarzen zur wägung dünner schichten und zur mikrowägung. *Z. Phys.* **155**, 206–222. https://doi.org/10.1007/BF01337937 (1959).

16. Schaeffer, R. W. & Ardelean, M. Powder x-ray diffraction of oriented and intercalated lead iodide. *Powder Diffr.* **16**, 16–19. https://doi.org/10.1154/1.1332077 (2001).

17. Szafrański, M. & Katrusiak, A. Mechanism of pressure-induced phase transitions, amorphization, and absorption-edge shift in photovoltaic methylammonium lead iodide. *J. Phys. Chem. Lett.* **7**, 3458–3466. https://doi.org/10.1021/acs.jpclett.6b01648 (2016).

18. Laskin, A. & Cowin, J. P. Automated single-particle sem/edx analysis of submicrometer particles down to 0.1 μm. *Anal. Chem.* **73**, 1023–1029, https://doi.org/10.1021/ac0009604 (2001).

19. Tilley, R. *Perovskites: Structure-Property Relationships* (Wiley, 2016).

20. Maiberg, M., Bertram, F., Müller, M. & Scheer, R. Theoretical study of time-resolved luminescence in semiconductors. iv. Lateral inhomogeneities. *J. Appl. Phys.* **121**, 085703. https://doi.org/10.1063/1.4976102 (2017).

21. Kim, B.-S., Gil-Escrig, L., Sessolo, M. & Bolink, H. J. Deposition kinetics and compositional control of vacuum-processed $CH_3NH_3PBI_3$ perovskite. *J. Phys. Chem. Lett.* **11**, 6852–6859. https://doi.org/10.1021/acs.jpclett.0c01995 (2020).

22. Chen, C.-W. *et al.* Efficient and uniform planar-type perovskite solar cells by simple sequential vacuum deposition. *Adv. Mater.* **26**, 6647–6652, https://doi.org/10.1002/adma.201402461 (2014).

23. Parrott, E. S. *et al.* Growth modes and quantum confinement in ultrathin vapour-deposited MAPBI3 films. *Nanoscale* **11**, 14276–14284. https://doi.org/10.1039/C9NR04104D (2019).

24. Jacobsson, T. J. *et al.* Unreacted PBI2 as a double-edged sword for enhancing the performance of perovskite solar cells. *J. Am. Chem. Soc.* **138**, 10331–10343. https://doi.org/10.1021/jacs.6b06320 (2016).

25. Supasai, T., Rujisamphan, N., Ullrich, K., Chemseddine, A. & Dittrich, T. Formation of a passivating $CH_3NH_3PBI_3$/PBI2 interface during moderate heating of CH3NH3PBI3 layers. *Appl. Phys. Lett.* **103**, 183906. https://doi.org/10.1063/1.4826116 (2013).

26. Muscarella, L. A. *et al.* Crystal orientation and grain size: Do they determine optoelectronic properties of MAPBI3 perovskite?. *J. Phys. Chem. Lett.* **10**, 6010–6018. https://doi.org/10.1021/acs.jpclett.9b02757 (2019).

27. Ou, Q. *et al.* Band structure engineering in metal halide perovskite nanostructures for optoelectronic applications. *Nano Mater. Sci.* **1**, 268–287. https://doi.org/10.1016/j.nanoms.2019.10.004 (2019).

28. Eames, C. *et al.* Ionic transport in hybrid lead iodide perovskite solar cells. *Nat. Commun.* **6**, 7497. https://doi.org/10.1038/ncomms8497 (2015).

29. Hellmann, T. *et al.* The electronic structure of mapi-based perovskite solar cells: Detailed band diagram determination by photoemission spectroscopy comparing classical and inverted device stacks. *Adv. Energy Mater.* **10**, 2002129. https://doi.org/10.1002/aenm.202002129 (2020).

30. Pecoraro, A., De Maria, A., Delli Veneri, P., Pavone, M. & Muñoz-García, A. B. Interfacial electronic features in methyl-ammonium lead iodide and p-type oxide heterostructures new insights for inverted perovskite solar cells. *Phys. Chem. Chem. Phys.* **22**, 28401–28413. https://doi.org/10.1039/D0CP05328G (2020).

31. Zhang, J., Morbidoni, M., Huang, K., Feng, S. & McLachlan, M. A. Environmentally friendly, aqueous processed ZNO as an efficient electron transport layer for low temperature processed metal-halide perovskite photovoltaics. *Inorg. Chem. Front.* **5**, 84–89. https://doi.org/10.1039/C7QI00667E (2018).

32. Malinkiewicz, O. *et al.* Metal-oxide-free methylammonium lead iodide perovskite-based solar cells: The influence of organic charge transport layers. *Adv. Energy Mater.* **4**, 1400345. https://doi.org/10.1002/aenm.201400345 (2014). https://onlinelibrary.wiley.com/doi/pdf/10.1002/aenm.201400345.

33. Dachauer, R., Clemens, O., Lakus-Wollny, K., Mayer, T. & Jaegermann, W. Characterization of methylammonium lead iodide thin films fabricated by exposure of lead iodide layers to methylammonium iodide vapor in a closed crucible transformation process. *physica status solidi (a)* **216**, 1800894. https://doi.org/10.1002/pssa.201800894 (2019).

34. Lodeiro, L. *et al.* Methodological issues in first-principle calculations of $CH_3NH_3PBI_3$ perovskite surfaces: Quantum confinement and thermal motion. *ACS Omega* **5**, 29477–29491. https://doi.org/10.1021/acsomega.0c04420 (2020).

35. Maiberg, M., Hölscher, T., Zahedi-Azad, S. & Scheer, R. Theoretical study of time-resolved luminescence in semiconductors. iii. Trap states in the band gap. *Journal of Applied Physics* **118**, 105701. https://doi.org/10.1063/1.4929877 (2015).

36. Golubev, T., Liu, D., Lunt, R. & Duxbury, P. Understanding the impact of C_{60} at the interface of perovskite solar cells via drift-diffusion modeling. *AIP Adv.* **9**, 035026. https://doi.org/10.1063/1.5068690 (2019).

37. Liu, D. *et al.* Impact of ultrathin C_{60} on perovskite photovoltaic devices. *ACS Nano* **12**, 876–883. https://doi.org/10.1021/acsnano.7b08561 (2018).

38. Wojciechowski, K. *et al.* C60 as an efficient n-type compact layer in perovskite solar cells. *J. Phys. Chem. Lett.* **6**, 2399–2405. https://doi.org/10.1021/acs.jpclett.5b00902 (2015).

39. Kim, T. G., Seo, S. W., Kwon, H., Hahn, J. & Kim, J. W. Influence of halide precursor type and its composition on the electronic properties of vacuum deposited perovskite films. *Phys. Chem. Chem. Phys.* **17**, 24342–24348. https://doi.org/10.1039/C5CP04207K (2015).

40. Emara, J. *et al.* Impact of film stoichiometry on the ionization energy and electronic structure of $CH_3NH_3PBI_3$ perovskites. *Adv. Mater.* **28**, 553–559. https://doi.org/10.1002/adma.201503406 (2016).

Acknowledgements

Author contributions

R.H. carried out the experiments, analyzed the data, discussed the results and wrote the manuscript. K.L.H. helped with the experiments and analyzed the results. R.H. and K.L.H. equally contributed to the work. S.B. and

Competing interests
The authors declare no competing interests.

Additional information
Supplementary Information The online version contains supplementary material available at https://doi.org/10.1038/s41598-022-23132-w.

Correspondence and requests for materials should be addressed to K.L.H. or P.P.

Reprints and permissions information is available at www.nature.com/reprints.

Publisher's note Springer Nature remains neutral with regard to jurisdictional claims in published maps and institutional affiliations.

Concluding Discussion

The impact of substrate and nucleation conditions on the bulk absorber growth $[(Q_3)]$, will be discussed first. In [H2] the PbI_2 seed layer enhances $MAPbI_3$ crystallinity and/or preferential orientation compared to the statically co-evaporated layer as observed by the peak intensity in the *in situ* XRD. This effect is known and discussed for [H1] in section 4.2. Depositing an MAI precursor instead of PbI_2 further increases the $MAPbI_3$ peak intensity compared to the PbI_2 precursor in [H2]. This observation is made although a low sticking factor of the MAI on the substrate is expected [207]. Kim et al. determined the increase of MAI condensation on a QCM at a constant impingement rate to increase by 2.7 when PbI_2 is present compared to the case without a PbI_2 precursor [287]. Therefore, a reasonable condensation rate is still expected in our case for the isolated deposition of an MAI precursor and it is valid to assume the presence of an MAI precursor layer in our experiment to which the increase in perovskite peak intensity can be related.

Olthof et al. investigated four different substrate types and their influence of condensation behavior during co-evaporation of MAI and PbI_2 [211]. They found the catalytic activity of ITO substrates to cause dissociation of MAI and PbI_2 due to the reaction with surface -OH groups, leading to a very slow condensation due to the lack of N [211]. A MoO_3 substrate reduced the condensation of Pb when MAI dissociates were present and a stoichiometric perovskite deposition was only possible after establishing a surface passivation layer. The organic substrates PEIE (polyethylenimine ethoxylated) and and PEDOT:PSS (poly[3,4-ethylenedioxythiophene]:poly[styrene sulfonate]) actually enabled an improved condensation rate for MAI dissociates and allowed for perovskite growth right away. A stable stoichiometric perovskite deposition was reached immediately (PEIE, PEDOT:PSS), after the deposition of $10\,nm$ (ITO) and $30\,nm$ (MoO_3). Thus, the individual substrates require different thicknesses of surface passivation layers to enable stoichiometric growth.

The phenomenon of surface passivation may not only determine the composition, but also the orientation of the $MAPbI_3$ layer. Zhang et al. spin-coated $MAPbI_3$ layers using a sandwich approach by depositing MAI-PbI_2-MAI precursor layers in three deposition steps on a TiO_2 substrate [300]. They varied only the concentration of the solution for the first MAI layer and found a strong increase in preferential orientation in the final $MAPbI_3$ layer with an increasing MAI concentration. In parallel, the PbI_2 peak intensity decreased and the PbI_2 peak even disappeared for the highest MAI concentrations. Thus, the observed dependency of their spin-coated layer on the MAI precursor concentration was similar to the GIWAXS results in [H1] where different thicknesses of PbI_2 precursors heavily influenced the perovskite orientation. The perovskite component CsBr has also been successfully employed as a precursor and buffer layer on a NiO HTL [301]. The CsBr was suggested to relieve the lattice mismatch between NiO and $MA_{1-x}FA_xPbI_3$ and induce a higher order of crystal growth in the perovskite.

Hence, the influence of substrate and nucleation conditions on the bulk perovskite growth $[(Q_3)]$ as observed in our work and the literature may be understood as follows. In [H1] and [H2] both MAI and PbI_2 precursor layers induce a stronger preferential orientation in the perovskite bulk than the perovskite that is grown directly on the respectively investigated substrates. This may be due to the

passivating functionality of MAI and PbI_2, preventing lattice stress and suppressing a high defect concentration in the perovskite lattice which would otherwise have been induced by the substrate which exhibits different lattice constants than the perovskite [302]. Both MAI and PbI_2 precursor layers may provide lattice-stress-free perovskite growth conditions due to their reaction towards perovskite formation with the incoming species.

To explain the optoelectronic behavior induced by the interfacial composition and aiming to shed light on (Q_4), two thought models are proposed in [H2] on the basis of j-V curves and TRPL (see section 3.4). The first thought model proposes that a residual interface layer like PbI_2 could lead to hole blocking. The second thought model suggests that the self-doping mechanism of $MAPbI_3$ leads to advantageous band bending.

Li et al. performed first-principles calculations to find the best $NiO/MAPbI_3$ interface bonds for charge transport [302]. They compared MAI- and PbI_2-terminations of $MAPbI_3$ at the NiO interface and found the PbI_2-terminated interface in $MAPbI_3$-(001) direction to yield the best performing solar cell device. They assigned this to low valence band offset (high conduction band offset) which is beneficial for effective hole transport (electron blocking). However, the calculated current density of their final theoretical device was 3 orders of magnitude below the current density measured in actual devices. A recent DFT study by Zhang et al. also observed a strong beneficial effect on charge extraction of the NiO-PbI_2 interaction compared to the NiO-MAI interaction at the $NiO/MAPbI_3$ interface [303]. According to their calculations, the PbI-O interactions yield the lowest Pb-I bond length distortion at the interface compared to the bulk (this reduces the likelihood of deep trap states at the interface), the lowest valence band offset and consequently best charge transport. Considering these theoretical studies, an MAI rich interface as in [H2] statistically favoring MAI-NiO interactions at the interface is expected to downgrade the device performance in general. However, Zhang et al. also note that the formation of PbI_2-NiO bonds is energetically more favorable compared to MAI-NiO bonds [303], which could lead to PbI_2-NiO bonds at the interface even under MAI rich conditions.

Other works have studied not the interfacial behavior via the individual interface bonds, but the effect of stoichiometric ratios and self-doping on the band alignment between $MAPbI_3$ and transport layers. Cui et al. [292] and Wang et al. [115] measured different shifts of E_f relative to the $MAPbI_3$ band edges (conduction band minimum, CBM and valence band maximum, VBM) depending on the MAI/PbI_2 ratios in the perovskite bulk. Cui et al. determined a distance of E_f from the CBM of $1.05\,eV$, $0.48\,eV$ and $0.32\,eV$ for MAI/PbI_2 ratios in the final layer of ~ 1.1, ~ 0.95 and ~ 0.91, respectively, at a constant band gap of $1.55\,eV$ [292]. Wang et al. also observed a relative rise in E_f with an increasing share of PbI_2 [115] and both works observed n-doping in this situation and p-doping for the case of MAI excess. Cui et al. used this effect to replace the absorber (i) in an n-i-p structure by an n/p perovskite homojunction to create an internal electric field in the perovskite to aid the charge transport [292]. They verified the internal electric field by Kelvin probe force microscopy. Accordingly, MAI rich nucleation at the HTL interface and PbI_2 rich final deposition at the ETL interface in [H2] are likely to induce the same phenonemon, yielding a shift in E_f relative to the band edges in the perovskite bulk and inducing an internal

electric field across the perovskite layer.

Li et al. prepared co-evaporated MAPbI$_3$ layers with a continuous grading of the MAI/PbI$_2$ ratio by ramping the deposition rates of MAI and PbI$_2$, respectively [40]. They asserted the CBM and VBM as well as the E_f at different positions in the layer and observed a gradient of E_f with respect to the band edges within the MAPbI$_3$ absorber, as postulated by Cui and Wang [115, 292]. They used this approach to prepare n-i-p and p-i-n PSCs and found MAI rich initial growth and PbI$_2$ rich final growth to be detrimental in the n-i-p structure, but highly effective in terms of PSC efficiency in the p-i-n structure. Accordingly, the inverse dynamic growth employing PbI$_2$ rich initial growth was successful in the n-i-p structure, yielding maximum efficiencies above 20 % in both device structures. Compared to Li et al. who deposited a stoichiometric gradient throughout the whole absorber layer [40], the work in [H2] shows that short dynamic evaporation steps at the beginning/end of the absorber deposition may be sufficient to optimize the perovskite properties.

In conclusion, for the first thought model to be sensible, a segregated PbI$_2$ layer covering the complete interfacial area would need to exist in order to force the carriers through a PbI$_2$ layer and thereby enable hole blocking. However, the existence of a residual PbI$_2$ layer at the interface was not conclusively shown for the best devices in our works [H1, H2], by Li et al. [40] or by Xu et al. [286]. Therefore, at the time being, our second proposed thought model seems to be more likely compared to the first, since band bending induced by stoichiometric variations has been postulated and verified by several groups. Therefore, the influence of interfacial precursors and consequently local perovskite stoichiometry on the optoelectronic properties [(Q_4)] may be determined by the reduction of perovskite lattice stress as well as bulk defects and the induced band bending by the self-doping mechanism in metal halide perovskites.

4.4 Stoichiometry Variations of Co-Evaporated APbX$_3$

Opening Remarks

We have shown that the local composition in MAPbI$_3$ can be optimized in terms of MAI/PbI$_2$ ratio to improve the growth and optoelectronic properties. The question remains if the conclusions drawn in [H1] and [H2] can be generalized and extrapolated to other perovskite compositions. The main interest in perovskite absorbers has shifted from MAPbI$_3$ to FAPbI$_3$ as explained in section 2.2. Therefore, the follow-up investigations [H3,H4] aim to provide a basis for the application of the principles determined for MAPbI$_3$ in [H1] and [H2] to perovskite absorbers based on FAPbI$_3$.

By (Q_1) the stoichiometric range for bulk single-phase growth and/or segregation is ascertained. In MAPbI$_3$, the bulk stoichiometry can influence the intrinsic stability and segregation of PbI$_2$ can be observed at low excess [215] while high MAI excess is needed for secondary phases to form [283]. Nonetheless, the tetragonal room-temperature MAPbI$_3$ phase can be grown under a broad range of stoichiometric conditions and its stability is mainly a long-term issue due to the volatile MAI.

On the other hand, FAPbI$_3$ suffers from polymorphism at room temperature, i.e. competing cubic α and hexagonal δ crystal phases between 151 K and 420 K and preferred growth of/transition to the δ phase [71, 78] (see section 2.2). For PSCs, the growth process needs to be conducted so that the cubic α phase becomes favored during growth and the δ phase is suppressed. During co-evaporation of FAPbI$_3$, the δ phase is energetically favored and Borchert et al. found that an annealing step is normally necessary to convert the film to the α phase [72].

However, some studies have shown there can be a shift in preferential phase growth to the α phase at lower temperatures depending on the stoichiometry. Solution-based approaches have been conducted previous to [H3], which investigated the influence of AX/PbX$_2$ ratios on the growth of (Cs,FA)PbI$_3$ [304] and FAPbI$_3$ [84], unveiling a significant influence of stoichiometric excess/deficiency on the grown phases and their performance as active materials in diodes. Only one study published during our work on [H3] by Roß et al. investigated FAPbI$_3$ PSCs prepared via co-evaporation with low FAI excess and found this to be beneficial for stabilization of the α phase at room temperature [80]. For CsPbI$_3$, Becker et al. showed that the 3D perovskite γ phase can be fabricated at only 50°C (compared to the commonly necessary post-annealing at 300°C [305, 306]) via PVD by evaporating an excess of CsI [23]. Ma et al. showed that an excess of CsBr stabilized CsPbI$_2$Br against air exposure [307]. Cho et al. obtained the highest efficiency and stability for (Cs,FA,MA)Pb(I,Br)$_3$ PSCs by preparing a PbI$_2$ deficient absorber [291].

Clearly, evidence towards the beneficial influence of bulk stoichiometric variations on the absorber growth of several perovskite compounds based on FAPbI$_3$ exists for several preparation methods. Nonetheless, a systematic variation via PVD that shows the stoichiometric range for the different perovskite compounds based on FAPbI$_3$ is missing. Accordingly, the stoichiometric range for single-phase and/or segregated growth addressed by (Q_1) has not been exhausted for evaporated absorbers based on FAPbI$_3$. Therefore, in [H3] the AX/PbX$_2$ ratio is varied for A-cations A and halides X in mixed absorbers FAPbI$_3$, (Cs,FA)PbI$_3$

and $(Cs,FA)Pb(I,Br)_3$ during co-evaporation of FAI, CsI, PbI_2 and $PbBr_2$. The preferential phase formation, segregation and crystallinity are investigated and the stoichiometrical and compositional phase space of $APbX_3$ is quantified.

Check for updates

Stoichiometry dependent phase evolution of co-evaporated formamidinium and cesium lead halide thin films†

Karl L. Heinze, [ID] *[a] Patrick Wessel,[a] Melissa Mauer,[a] Roland Scheer[a] and Paul Pistor [ID] *[ab]

Due to its scalability, thermal evaporation is an important processing route for perovskites in order to ensure the transition from research to commercialization. In this study, we focus on vacuum co-deposition of (i) $FAPbI_3$, (ii) $(Cs,FA)PbI_3$ and (iii) $(Cs,FA)Pb(I,Br)_3$ at room temperature and investigate the influence of stoichiometrical variations on the development of α and δ phases. Considering the standard perovskite term $APbX_3$, where A = FA and/or Cs and X = I and/or Br, we use EDX to determine the specific ratios of A/Pb, Cs/FA as well as X/Pb, respectively. We find, that at room temperature, the $FAPbI_3$ δ phase is not easily suppressed. But, in both, $FAPbI_3$ and $(Cs,FA)PbI_3$, more AX leads to a strong increase in α phase growth while more PbI_2 leads to an increase in δ phase. Incorporation of Cs slightly reduces the observed AX/PbX_2 threshold, at which the δ phase is suppressed. Finally, when Br is introduced to the layer, this threshold is reduced far below 3.

1 Introduction

The popularity of organic–inorganic perovskite materials in research has skyrocketed since their discovery as solar cell absorbers in 2009.[1] Since then, maximum solar cell efficiencies have surpassed 25% for single-junction solar cells and above 29% for monolithic perovskite/silicon tandems during 2021.[2] Modern lead halide perovskite materials are versatile semiconductors, with diode efficiencies also climbing to above 23%.[3] The unstable and hygroscopic initial absorber material $MAPbI_3$ (MA: methylammonium)[4–6] has nowadays been widely replaced by thermally more stable $FAPbI_3$ (FA: formamidinium) or multi-cationic mixtures.[7–9] Optoelectronically favorable, photoactive cubic "α" phase $FAPbI_3$ suffers from a self-driven phase transition to its hexagonal "δ" phase counterpart under ambient conditions, resulting in an unstable device operation.[10–12] Several experimental series have been conducted in the past trying to mitigate this problem and to stabilize $FAPbI_3$-based perovskites for efficient optoelectronic devices. These relied mainly on shifting the Goldschmidt-Tolerance factor of $FAPbI_3$ to a value below 1 by incorporating the smaller cations MA^+,[13–15] Cs^+[16–18] and even Rb^+.[19]

Another approach has been ventured by grain surface passivation with the large organic molecule SF-PEA (sulfonyl fluoride-functionalized phenethylammonium salt) for $FAPbI_3$[20] and by PEAI (Phenetylammonium iodide) for $CsPbI_3$.[21] Optimizing the stoichiometry in view of the AX (FAX, MAX, CsX) to BX_2 (PbX_2) ratio has been shown to improve phase stability and photovoltaic performance for $CsPbIBr_2$ absorbers.[22,23] Stoichiometry also strongly influences grain size, crystal properties and photovoltaic performance at room temperature for the compounds $(Cs,FA)PbI_3$[24] and $(Cs,FA)Pb(I,Br)_3$.[8] Building on these previous findings, our current investigation is aligned towards finding optimal stoichiometry parameters for the phase stabilization of co-evaporated $FAPbI_3$ thin films.

A critical concern in perovskite layer preparation can be the temperature. Standard recipes for metal–halide perovskite layers for optoelectronic devices often rely on a post-annealing step after preparation, leading to a defect reduction and often to a transition to the preferred photoactive phase. Reported annealing temperatures are between 100 °C and 180 °C for wet-chemical[25–27] as well as preparation *via* evaporation.[8,28,29] However, submitting layers to these temperatures for longer periods of time to stabilize their crystal structure can also lead to thermal decomposition and outgassing of organic components.[30,31] Additionally, the above-mentioned annealing temperatures lie far above the operating temperatures of standard diodes (41 °C)[32] and solar cells (50 °C),[33,34] which could mean a reversion of the previous crystal structure transition is to be expected at operating temperatures due to a resulting stress by reduction of lattice parameters.[35,36]

[a] *Thin Film Photovoltaics, Martin-Luther-University Halle-Wittenberg, Von-Danckelmann-Platz 3, 06120, Halle (Saale), Germany.*
E-mail: karl.heinze@physik.uni-halle.de

[b] *Universidad de Pablo de Olavide, Carretera de Utrera 1, 41013, Sevilla, Spain.*
E-mail: ppis@upo.es

A more sustainable stabilization could be achieved by preparing the respective photoactive layers solely at temperatures closer to the operating regime and out of reach of thermally activated phase transitions. Therefore, in our current work we focus on the stoichiometry dependent phase evolution of the photoactive α phase at room temperature.

In the past, slight variations concerning the absorber stoichiometry have been investigated, with contradictory results. Some groups found a PbI$_2$ excess to be advantageous for the absorber stability and device performance,[37–39] while others found a slight PbI$_2$ deficiency to improve the long-term stability of MAPbI$_3$ as well as mixed-cation perovskites.[40,41] The impact of a more pronounced variation of the AX/PbX$_2$ ratio has been studied for MAPbI$_3$,[42,43] but only few approaches have been made for FAPbI$_3$[44] and (Cs,FA)PbI$_3$.[24] To the best of our knowledge, the only studies performed on stoichiometry control via co-evaporation were on FAPbI$_3$[45] and (Cs,FA)Pb(I,Br)$_3$.[8]

Even though it is clear that stoichiometry variations of lead halide perovskites based on formamidinium play an important role in determining the crystalline phase distribution and potentially the final optoelectronic properties of these layers, this property is ignored to a great extent. In fact, it seems that systematic investigations of the phases present in the FAX/PbX$_2$ system that could lead to the presentation of a pseudobinary phase diagram are still missing up to now. Importantly, only few of the above-mentioned works determine the elemental composition of their layers after preparation. Especially for thermally evaporated, post-annealed samples, the impingement rate onto the sample and incorporation into the layer will not be the same.[45,46] There has been clear evidence for the influence of substrate type and temperature on the crystallisation properties[45,47,48] raising the question if the substrate choice influences growth by stoichiometry control.

The goal of this study is to systematically investigate the phase evolution of formamidinium-based perovskite compounds with various stoichiometries synthesized by co-evaporation at room temperature in order to achieve a clear understanding of the preferential phase growth for the different material fluxes and to set a framework for further investigation. To achieve this, we have conducted three series of experiments, in which we (i) varied first the FAI/PbI$_2$ ratio in ternary FAPbI$_3$ perovskites (ii) then studied variations of these absorbers with added amounts of CsI and (iii) finally added also Br and studied absorbers with different compositions with general compositions around (Cs,FA)Pb(I,Br)$_3$.

Similar studies on the influence of stoichiometry of wet-chemically prepared ternary FAPbI$_3$[44] and quartenary (Cs,FA)PbI$_3$[24] have been performed for perovskite diodes via spin-coating and low temperature annealing, but did not analyze the phase growth behaviour in detail. We build on these studies with the intent to transfer them to vacuum-based processing. The work aims at the identification of crucial compositions in the respective phase diagrams and an improved understanding of compositionally driven preferential growth of the cubic FAPbI$_3$ perovskite. For our experiments, we perform co-evaporation, which is advantageous due to its scalability and can provide the stepping stone to industrializiation for perovskite thin films, since it generally offers good control on film growth, stoichiometry and thickness. Our in situ X-ray diffraction setup enables us to monitor the crystal growth in real-time under vacuum conditions, as we have shown in previous studies.[49,50,51] However, the basis for this study are the θ–θ scans performed under vacuum just after deposition. We co-evaporated FAI, PbI$_2$, PbBr$_2$ and CsI in order to synthesize FAPbI$_3$ and (Cs,FA)PbI$_3$ as well as (Cs,FA)Pb(I,Br)$_3$ thin films in high vacuum and at room temperature. Their crystallinity and phase evolution are then analyzed with an X-ray diffraction system directly attached to the evaporation chamber. This way, we were able to conduct the synthesis and phase characterization in the same vacuum chamber without exposing the films to ambient conditions/humidity, which is important considering the phase instability of these perovskites. The principal set of parameter variations was conducted through changes of the relative evaporation fluxes, therefore varying perovskite composition along the Cs/FA, AX/PbX$_2$ and I/Br axes. We determined the elemental composition via EDX spectroscopy.

2 Experimental details

Substrates

For all processes we used glass substrates provided by Berliner Glas. The substrates were cleaned in an ultrasonic bath, subsequently in water – using 1% EMAG EM-080 cleaning soap – and isopropanol for 15 min. each. Then, a 130 nm thick ITO layer was sputtered on the glass, before 25 nm of NiO was deposited via e-beam evaporation inside the same vacuum chamber. The samples were then transferred to a glovebox. This glovebox is attached to a second evaporation chamber, in which the perovskite layers were deposited.

Perovskite deposition

CsI, PbI$_2$ (both 99.999%, Thermo Scientific), FAI (>99.5%, Ossila) and PbBr$_2$ (99.999%, Sigma) were handled in a glovebox attached to the vacuum chamber and used as received. The perovskite layers were deposited by physical vapor deposition in a co-evaporation process. CsI, PbI$_2$, FAI and PbBr$_2$ were nominally deposited at 0.6–0.8 Å s^{-1}, 0.5–1 Å s^{-1}, 0.1–0.85 Å s^{-1} and 0.08–0.12 Å s^{-1} respectively. The total film thickness was monitored using a quartz crystal microbalance. The base pressure of the system is 1.5–2 × 10^{-5} mbar due to the Kapton® windows that allow a transmission of X-rays for the in situ X-ray diffraction measurement. The chamber pressure was monitored with an Edwards WRGS-NW35 wide range gauge. A sketch of the evaporation system with the in situ X-ray diffraction (XRD) setup is depicted in Fig. S1 in the ESI.†

X-Ray diffraction (XRD) measurement

XRD was measured in situ through exchangeable Kapton® windows in the evaporation chamber by diffraction of Cu-K$_\alpha$ radiation with a wavelength of 1.54 Å generated at 1.4 kW (35 kV, 40 mA). Three Dectris Mythen 1 K detector modules are assembled in a row enabling the measurement of 2θ angles covering a range of 28°. The K$_\beta$ radiation is attenuated through

a Ni filter to 5% of the K_α intensity. For $\theta–\theta$ scans from 10 to 50°, 41 single scans with a 28° range were recorded. For every scan, source and detector are rearranged, so that the detector center corresponds to the 2θ angle. A $\theta–\theta$ scan consists of the respective central 1° from the 41 single scans. Fitting of the XRD peaks was performed with PDXL version 2.8.1.1 by Rigaku inc. employing a split pseudo-Voigt peak fit. The calculated errors were used for the error bars in the graphs in this publication.

Film characterization

SEM was performed with a Zeiss Supra 40 VP. Grain size areas were calculated from the SEM images shown in this manuscript using ImageJ by tracing the apparent grain boundaries. The grain area was approximated to be circular $(A = \pi \cdot (d/2)^2)$, so the averaged pseudo-diameter d could be used as reference for comparison. For the EDX measurements, a Bruker detector employing the ESPRIT Compact Software was used. The EDX measurements were conducted with an accelerating voltage of 10 kV, a working distance of 8 mm, and a magnification of 500. For quantification, Pb M-lines and I, Br and Cs L-lines were used. Background correction was done by a standardless peak to background (P/B) ZAF fitting. The errors calculated by Bruker's Compact program were used for Gaussian error propagation to calculate atomic ratio errors. PL measurements were conducted on a LabRAM HR Evolution using a wavelength of 532 nm, an objective with 50-fold magnification at 0.01% intensity.

3 Results

The composition of our films was determined from measuring solely the I/Pb/Cs/Br signals, because of the difficulties to quantitatively evaluate lighter elements such as H,C,N in standard EDX detectors. We calculate the A/B cation ratio indirectly from the I/Pb ratio, assuming that each A cation (FA,Cs) brings along one halide X anion (Br, I or Cl), and each Pb cation is associated with two X anions. Following the standard perovskite formula ABX_3, an I/Pb ratio of 3 is therefore characteristic for a stoichiometric layer with an AI/BI_2 ratio of 1. An I/Pb below 3 indicates an excess of PbI_2 and a deficiency of AI in comparison to the stoichiometric perovskite. I/Pb above 3 corresponds to an AI excess and a deficiency of PbI_2. The common term for this is shown in (1), where n represents the AI content relative to PbI_2.

$$FA_nPbI_{2+n} \quad \text{and} \quad (Cs,FA)_nPbI_{2+n} \tag{1}$$

As mentioned above, the FA content cannot be determined directly *via* EDX. Consequently, we use the I/Pb ratio to indirectly determine n. I/Pb = 2.5 corresponds to a PbI_2 excess of 100%, which would give $n = 0.5$. An I/Pb = 4 represents an AI excess of 100% and $n = 2$. Using the Pb content as reference and normalizing it to 1, the AI/PbI_2 ratios can be calculated *via* (2).

$$I - 2 \cdot Pb - Cs - FA = 0 \rightarrow \frac{FA + Cs}{Pb} = \frac{I - 2}{Pb} \tag{2}$$

The PbI_2 excess E_{PbI_2} and AI-cation excess E_A values are given by (3). Note, that E_A and E_{PbI_2} each only exist, if their respective

value is greater than 0.

$$E_{PbI_2} = \frac{3 \cdot Pb - I}{I - 2 \cdot Pb} \quad \text{and} \quad E_A = \frac{I}{Pb} - 3 \tag{3}$$

In the following, we will use the I/Pb ratios measured *via* EDX in order to express the AI/BI_2 ratio in our evaporated layers. At first, we will investigate the impact of the AI/BI_2 ratio (the FAI/PbI_2 ratio) on the phase evolution in ternary $FAPbI_3$ thin films with different FAI/PbI_2 ratios in a set of $FAPbI_3$ thin films with FAI/PbI_2 ratios between 2.4 and 5.4. Later on, we will study the influence of additionally co-evaporating CsI in a second set of $(Cs,FA)PbI_3$ thin films with $(CsI + FAI)/PbI_2$ ratios (A/B ratios) between 2.4 and 4.3 and Cs/FA ratios from 0.03 to 0.57. Finally, we will briefly investigate the influence of Br/I ratios from 0.14 to 0.24.

Fig. 1 shows a group of $FAPbI_3$ (blue) and a group of $(Cs,FA)PbI_3$ (purple) $\theta–\theta$ diffractograms measured directly after the thin film synthesis. The respective atomic ratios are given at the top of each diffractogram, in which the first number represents I/Pb. The second number, only displayed for $(Cs,FA)PbI_3$, gives the Cs/FA ratios. Within the $FAPbI_3$ and $(Cs,FA)PbI_3$ groups, respectively, the I/Pb ratio increases from bottom to top.

In general, three distinct phases with varying contributions can be identified in these diffractograms: the two phases of the polymorphic $FAPbI_3$ perovskite (cubic α $FAPbI_3$ and hexagonal δ $FAPbI_3$) and the secondary phase PbI_2. Their corresponding most intense peaks are indexed in the graph. We observe that for increasing I/Pb ratios, the main peaks associated with the $FAPbI_3$ α phase grow. These are namely the α-(100) (short: α1), (200) (short: α2) and (210) peaks. In parallel, the intensity of the δ (001) peak (short: δ_{FA}) decreases. The same trend is observed for the $(Cs,FA)PbI_3$ mixed perovskite. In the following, the peak
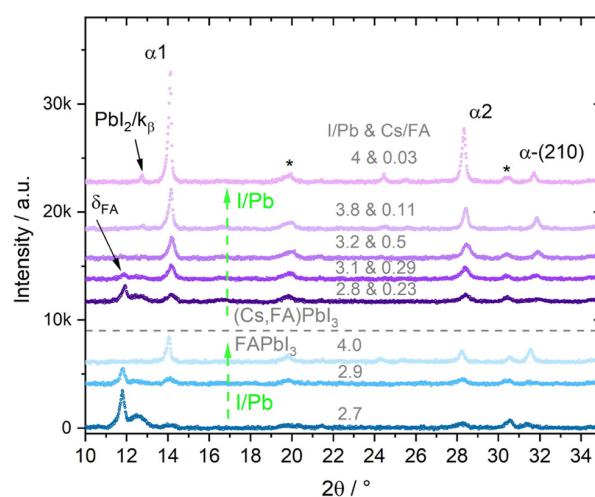

Fig. 1 $\theta–\theta$ diffractograms of $FAPbI_3$ (bottom three plots in blue) and $(Cs,FA)PbI_3$ (purple and pink plots) perovskites with different I/Pb and Cs/FA ratios. $FAPbI_3$ and $(Cs,FA)PbI_3$ α phase peaks are represented by α1 and α2 labels (corresponding to (100) and (200) peaks) as well as α-(210) label. δ_{FA} represents the δ (100) peak. PbI_2 marks the PbI_2 (001) peak. The PbI_2 (001) appears at the same position as the K_β of the α1 peak. The * marks ITO substrate peaks.
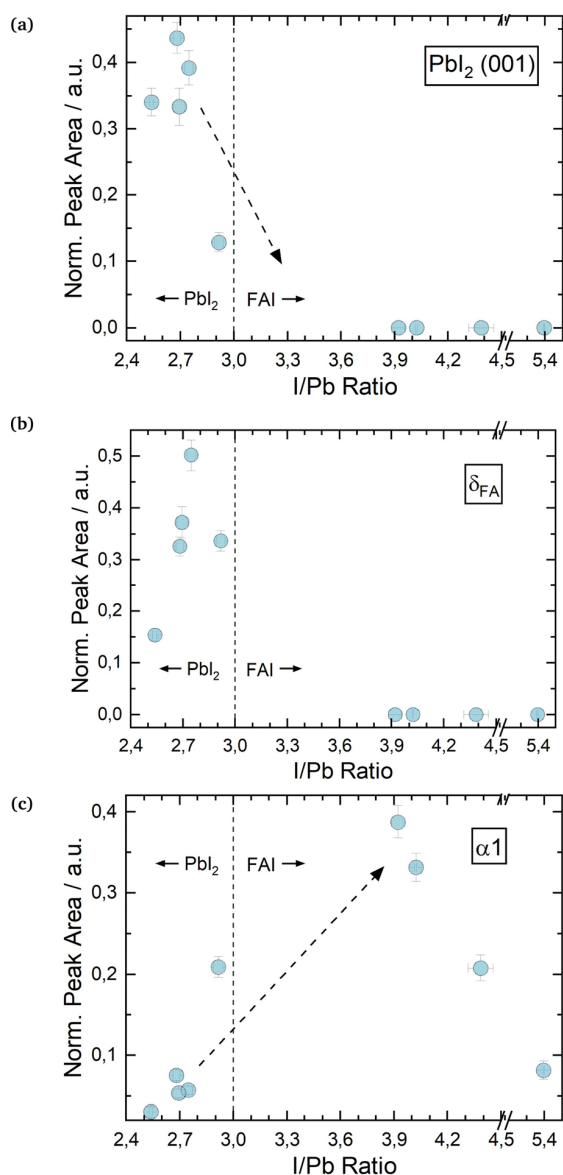
Fig. 2 Changes in θ–θ scan peak properties for varying I/Pb ratios in FAPbI$_3$: PbI$_2$ (001) peak area (a), δ_{FA} (b) and α 1 peak areas (c). All peak areas are normalized to the X-ray intensity through Kapton® windows. Sample EDX spectra for FAPbI$_3$ are shown in the ESI,† in Fig. S6 and S8.

area proportions of the different phases for both FAPbI$_3$ and (Cs,FA)PbI$_3$ will be assessed in detail with respect to the I/Pb ratio. Here, the peak areas extracted from the θ–θ scans are to a first approximation assumed to be proportional to the amount of respective phases present in the investigated layer. Peak area intensities are normalized with respect to the incident X-ray intensity in order to reduce the impact of X-ray attenuation.

Fig. 2a shows the change in PbI$_2$ (001) X-ray diffraction (XRD) peak area over a range of I/Pb ratios for the first set of FAPbI$_3$ absorbers. The scattered vertical line splits PbI$_2$ rich and FAI rich domains. The dotted arrows provide a guide to the eye for a suggested, likely course of y-value development. For the

calculation of error bar values, see the experimental details. We note that in several experiments we were not able to grow FAPbI$_3$ layers with a small FAI excess by adjusting the respective FAI and PbI$_2$ fluxes, as determined via EDX. Whether this was just a coincidence or is a systematic feature of the FAI/PbI$_2$ phase diagram has to be confirmed. Roß et al. report slight FAI excess in their grown layers, but do not confirm this via e.g. EDX or XPS.[47]

Finally, photoluminescence (PL) of the thin films was measured in air (Fig. S2 and S3 in the ESI†). Peak positions determined via Gauss fits are depicted in Fig. S5 in the ESI.† We observed peaks in the range from 1.55 eV to 1.6 eV, corresponding to a slightly blue-shifted photoluminescence with respect to the α phase of FAPbI$_3$. A similar energy shift is also observed by Ma et al. in FAPbI$_3$ samples with different α/δ phase contributions, and is thoroughly discussed in ref. 44. We have to note that PL measurements had to be carried out a posteriori in air, and an effect of the air humidity on the samples cannot be excluded (e.g. with respect to the α/δ phase transition). However, for a comparative analysis and for completeness, these results have been added to the ESI.†

As one would expect, PbI$_2$ segregates in PbI$_2$ rich layers (I/Pb smaller than 3). For stoichiometric and FAI-rich layers, no significant amounts of PbI$_2$ are observed. It follows, that an excess of PbI$_2$ during co-evaporation leads to the segregation of an increasing amount of PbI$_2$ as a secondary phase, which is intuitive. The absence of crystalline PbI$_2$ in the FAI-rich layers suggests the complete reaction of the deposited PbI$_2$ with FAI.

Interestingly, the evolution of the δ_{FA} peak roughly follows the peak area development of the PbI$_2$ (Fig. 2b), with increasing amounts of the δ phase for PbI$_2$-rich layers and no δ phase for FAI-rich layers. Ma et al. prepared FAPbI$_3$ via spin coating with an FAI excess of up to 300% and low annealing temperatures of only 60 °C. They observed a full suppression of the δ phase for 100% FAI excess upwards, similar to our results.[44]

Inversely to the δ phase, in Fig. 2b the α1 peak area initially increases for an increasing I/Pb ratio reaching a maximum at 3.9. For even higher I/Pb ratios, the α1 peak area decreases again, possibly because the large excess of FAI hinders the formation of well-formed FAPbI$_3$ crystal lattices. The α1 FWHM takes the opposite course, with a minimum at 3.9, supporting the idea of decreasing crystallinity/crystallite sizes at larger I/Pb ratios. (Fig. S15 in the ESI†). This trend is confirmed by the SEM images shown in Fig. 3. Fig. 3a shows a blurry surface and a morphology with small grain sizes of 49 nm in average for a sample with I/Pb of 2.5. When the I/Pb ratio is increased to 2.95, the surface remains rough, but an average grain size of 74 nm can be observed. Finally, Fig. 3c depicts 164 nm grain sizes in average with a smooth surface on a FAPbI$_3$ sample with I/Pb of 3.9 (Fig. S22, ESI†).

It should be noted, that only for the highest FAI excess did we detect a distinct crystalline FAI phase in our XRD (see Fig. S6 in the ESI†). For the other cases, we assume that the excess FAI is incorporated into the perovskite crystal lattice. This in turn causes a change of the lattice constants, which we observed as a shift of the α1 peak positions to smaller diffraction angles with
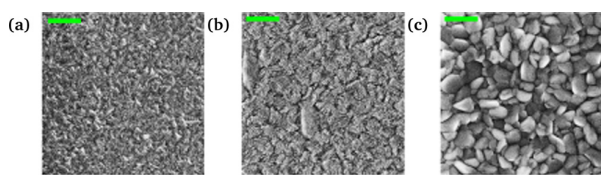
© 2022 The Author(s). Published by the Royal Society of Chemistry

Fig. 3 FA_nPbI_{2+n} samples with I/Pb ratios of 2.5 (a), 2.95 (b) and 3.9 (c). The green scalebar corresponds to 500 nm.

greater I/Pb ratios (Fig. S17 in the ESI†). Point or interstitial defects would lead to a dilation of the lattice, an increase of the lattice constants and thus a reduction of the respective diffraction angle. Accordingly, the 2θ $\alpha1$ angle increases for a smaller I/Pb ratio due to vacancies and a shrinkage of the lattice. Rothmann et al. observed PbI_2 and $FAPbI_3$ grains growing without grain boundaries, showing that both materials can intergrow and thus influence each other's lattice parameters.[52]

The smaller A cation Cs is expected to stabilize the α perovskite phase,[16,53] and in the second set of experiments we investigated a range of mixtures of both A-cations with Cs/FA ratios from 0.03 to 0.57. In line with the results above, the effect of varying I/Pb ratios will be discussed first. We observe similar trends for the three investigated phases. Fig. 4a shows the PbI_2 (001) peak for varying I/Pb ratios. Again and as expected, the PbI_2 (001) peak area is large for I/Pb ratios below 3 (PbI_2-rich layers), decreases for a rise in I/Pb ratios and eventually drops to zero for AI rich layers. The vanishing PbI_2 (001) signal indicates the complete conversion of the evaporated PbI_2 into the perovskite $(Cs,FA)PbI_3$. Similar to the first series, no unreacted CsI or FAI could be observed in the XRD. While the XRD signal of the organic FAI in general is weak and makes the detection of segregated FAI phases rather difficult, the absence of a CsI signal suggests that this compound is also completely incorporated into the perovskite phase (or formed an amorphous phase undetected by XRD). The δ_{FA} peak area decreases with increasing I/Pb, but was only fully suppressed at an AI excess of 90% (Fig. 4b). Yuan et al. prepared $(Cs_{0.1}FA_{0.9})_{1+n}P$-$bI_{3+n}$ via spin coating with excesses of $(Cs_{0.1}FA_{0.9})$.[24] They only observed a full suppression of the δ_{FA} phase for 100% FA excess upwards, in good agreement with our results.[24] In a similar experiment, Becker et al. observed yellow δ and dark γ (distorted α) phase $CsPbI_3$ growth via evaporation depending on the stoichiometry.[23] At PbI_2 rich conditions they observed the δ phase while at CsI rich conditions γ-$CsPbI_3$ was observed. They also suggested an intercalation mechanism of CsI into the layer, stabilizing the dark γ phase.

Fig. 4c shows the development of the $\alpha1$ peak area for $(Cs,FA)PbI_3$. Again, the $\alpha1$ peak area behaves similar as for $FAPbI_3$, suggesting similar preferential phase selection mechanisms for the single and mixed-cation absorber types. This can also by seen by comparing $\delta_{FA}/\alpha1$ relative peak areas for single- and double-cation perovskite, as shown in Fig. 5. The $\alpha1$ peak area is lowest for high PbI_2 contents and shows an increase for larger I/Pb ratios. This trend to an enhanced crystallinity is supported by a drop of the FWHM for the $\alpha1$ peak with increasing I/Pb (Fig. S18 in the ESI†). Interestingly, the maximum $\alpha1$ peak intensity and the
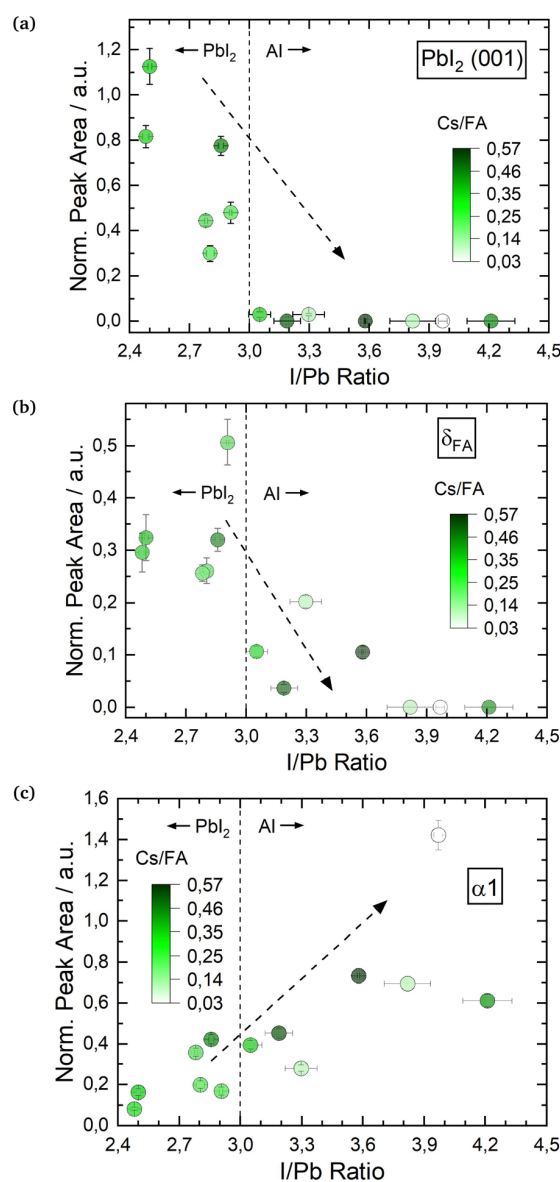

Fig. 4 Changes in $\theta-\theta$ peak properties of $(Cs,FA)PbI_3$ in dependence of I/Pb ratio: PbI_2 (001) peak area (a), δ_{FA} (b) and α 1 peak areas (c). All peak areas are normalized to the X-ray intensity through Kapton® windows. Sample EDX spectra for $(Cs,FA)PbI_3$ are shown in the ESI,† in Fig. S9–S11.

minimal FWHM lie at an I/Pb ratio of 3.9 to 4, which corresponds well to the values observed with $FAPbI_3$. The morphology is validated by SEM images shown in Fig. 6. An average grain size of 39 nm can be observed in Fig. 6a with I/Pb of 2.61. The average grain size increases to 105 nm in Fig. 6b when I/Pb reaches 3.03. Increasing I/Pb to 4.1 yields the largest grain sizes with pseudo diameters of 204 nm (Fig. S23, ESI†). So far, $FAPbI_3$ and $(Cs,FA)PbI_3$ investigations showed similar trends of the phase evolution with respect to the AI/PbI_2 ratio. It is worth noticing, that we always only observe perovskite peaks from a single phase, indicating a good homogeneous mixing of the two types of A cations. The insertion of Cs resulted in a small shift to larger
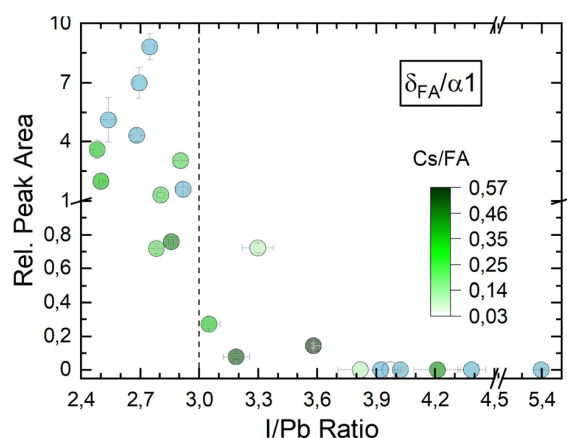
Fig. 5 $\delta_{FA}/\alpha 1$ peak ratio for FAPbI$_3$ as well as $\delta_{FA}/\alpha 1$ peak ratio for (Cs,FA)PbI$_3$ – each with respect to I/Pb ratios.

diffraction angles, *e.g.* $\alpha 1$ which was detected at 14.2 in comparison to 14.1 for the $\alpha 1$ peak of FAPbI$_3$ (Fig. S19 in the ESI†), as would be expected from the smaller lattice constant resulting from alloying with Cs.[54] We also observed a small $\alpha 1$ peak shift for an increasing I/Pb ratio for FAPbI$_3$ (Fig. S17 in the ESI†), but did not see the same for the $\alpha 1$ peak in (Cs,FA)PbI$_3$ (Fig. S19 in the ESI†).

Furthermore, we observed an increase of the $\alpha 1/\alpha 2$ peak ratio in (Cs,FA)PbI$_3$ with increasing I/Pb ratios (Fig. S20 in the ESI†), for which we do not yet have a clear explanation. For different Cs/FA ratios, the atomic form factor in the perovskite lattice changes, leading to different theoretical predictions for the different peak intensities and the $\alpha 1/\alpha 2$ peak ratio. For example, the peak ratio of the α-(100)/α-(200) peaks for the pure ternary CsPbI$_3$ and FAPbI$_3$ perovskite phases are 0.4[54] and 1.21,[55] respectively. However, the $\alpha 1/\alpha 2$ peak ratio does not seem to be directly and solely linked to the Cs/FA ratio. An increasing $\alpha 1/\alpha 2$ peak ratio could therefore possibly indicate that FA-cations are better incorporated at higher I/Pb ratios, and segregate preferentially in the δ phase of FAPbI$_3$ for lower I/Pb ratios.

In the third series of experiments, we introduced Br to the perovskite structure by additionally co-evaporating PbBr$_2$. This opens another path in the multi-dimensional phase space, with a multitude of variable parameters, of which this work can and will only scratch the surface. We will focus on showing, that co-mixing of Br leads to a significant stabilization of the growth
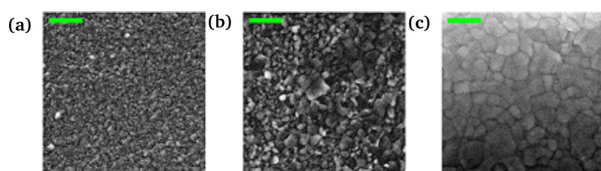

Fig. 6 (Cs,FA)$_n$PbI$_{2+n}$ samples with Cs/FA ratios of 0.05, 0.05 and 0.08 and I/Pb ratios of 2.61 (a), 3.03 (b) and 4.07 (c). The scalebar represents 500 nm.
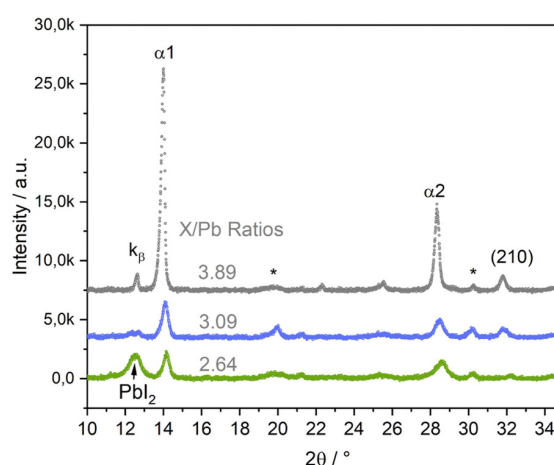

Fig. 7 $\theta-\theta$ scans of (Cs,FA)Pb(I,Br)$_3$ layers with different X/Pb ratios (X = I + Br). I/Br ratios vary between 0.13 and 0.24, as listed in Table S1 in the ESI.† EDX spectra for each sample are shown in Fig. S12 and Fig. 8c in the ESI.† The * marks ITO peaks.

of the perovskite α phase. In the following, the X/Pb ratio, in which X = I + Br, will replace the I/Pb ratio. In this series, we prepared samples with slightly varying Br/I ratios between 0.13 and 0.24. Fig. 7 shows selected $\theta-\theta$ diffractograms of (Cs,FA)Pb(I,Br)$_3$ samples with different X/Pb ratios of 2.64 (low), 3.09 (medium) and 3.89 (high). The original data along with Cs/FA and Br/I ratios are presented in Table S1 in the ESI,† the respective EDX spectra are shown in Fig. S12–S14 in the ESI.† Afterwards, PL measurements of all three samples were conducted in air (Fig. S4 in the ESI†). Positions of the PL peaks are compared with FAPbI$_3$ and (Cs,FA)PbI$_3$ samples in Fig. S5 in the ESI.†

Again, $\alpha 1$ and $\alpha 2$ peaks represent the (100) and (200) peaks of the perovskite α phase, respectively. α-(210) also correspond to the α phase, while PbI$_2$ indicates the phase's (001) peak. At medium and high X/Pb no PbI$_2$ or PbBr$_2$ residues are visible. With increasing X/Pb, the $\alpha 1$, $\alpha 2$, and (210) peak areas increase, indicating an increase of the share of perovskite in the layer. The $\alpha 1$ peak area is highest for the sample with highest X/Pb. The peak at 12.7 corresponds to the $\alpha 1$ K$_\beta$ peak. While there is a large PbI$_2$ peak visible in the sample with low X/Pb, no δ_{FA} peak can be observed, indicating a full suppression of the δ phase even for low X/Pb ratios. No PbBr$_2$ peak was observed, suggesting preferential incorporation of Br for perovskite growth.

At even smaller X/Pb ratios, small peaks corresponding to the δ phase could be observed. An example for a layer with X/Pb of 2.54 can be found in Fig. S21 in the ESI.† This means that inclusion of Br does not generally lead to a complete δ suppression, but substantially lowers the AX content limit, at which the δ phase can be suppressed. This is a clear difference in comparison to the samples without Br, where the δ_{FA} peak was observed at I/Pb ratios of up to 3.6 (Fig. 4b). The SEM images of samples with Br are conclusive. At low X/Pb, supposedly PbI$_2$ platelets surrounded by the smallest perovskite crytallites with slim, long shapes are grown. Although lighter spots, that can indicate PbX$_2$ rich domains in the
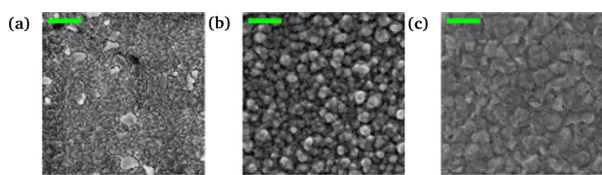
Fig. 8 (Cs,FA$_n$Pb(I,Br)$_{2+n}$) samples with X/Pb ratios of 2.64 (a), 3.09 (b) and 3.89 (c) and Br/I ratios of 0.2, 0.24 and 0.13, respectively. Detailed EDX data are presented in Table S1 in the ESI.† The scalebar represents 500 nm.

previously discussed SEM images in Fig. 3a and 6a, were visible, no such dominant segregation between PbX$_2$ rich and perovskite phases was seen without Br. This could hint to a stronger tendency towards perovskite growth, when Br is included, thus modifying the lattice parameters and making intergrowth of perovskite and PbX$_2$ rich phases less likely. At medium X/Pb in Fig. 8b, the average crystallite sizes increase considerably as they take round, pillar-like shapes. At highest X/Pb, the surface consists only of large grains and appears to be smoothed by the coverage of organic excess (Fig. S24 in the ESI†). The organic excess becomes apparent when considering the dark pinholes in Fig. 8c, that appear after several seconds of irradiation by the electron beam in organic rich layers.[52,56]

4 Discussion

We have observed stoichiometry-dependent trends in the preferential phase distribution during the growth of formamidinium-based perovskites and evaluated these trends along the X/Pb, Cs/FA and Br/I axes. In the following discussion, for simplicity, we will not discuss FAPbI$_3$ and (Cs,FA)PbI$_3$ separately.

In our experiments a clear correlation between the perovskite growth and the AX/PbX$_2$ ratio was found, with increasing crystallite sizes and an increasing relative content of the α perovskite phase share for an excess of AX. This phenomenon has been observed for wet-chemical[24,44] as well as evaporated FAPbI$_3$[45] and (Cs,FA)Pb(I,Br)$_3$,[8] layers, but up to now, only superficial explanations have been proposed for this mechanism including the creation of interstitial defects[23] or defect and surface passivation[44] similar to the effect that large organic cations have.[21] Even though degradation mechanisms[10,11,57–59] of FAPbI$_3$ α to δ phase are well explored, to the best of our knowledge, no calculations or theories explaining the simultaneous growth of α and δ phases of FAPbI$_3$ exist.

In a stoichiometric absorber, the FAPbI$_3$ δ phase is favored at room temperature due to the oversized FA$^+$ cation, as has been shown by many groups.[47,60–63] Yet, freshly grown layers often contain large shares of the α phase and this share is increased by including a larger amount of A-cations.

A possible explanation for the observed co-existence could be local compositional deviations, as has been shown to occur for mixed-halide-[64] and mixed-cation-perovskites.[65] During co-evaporation, local compositional deviations could result from island-like growth-behaviour due to an increased adsorption coefficient at certain surfaces,[66,67] e.g. favoring FAI rich growth where FAI is already present at the surface. This would lead to

crystallites with different AX/PbX$_2$ ratios and thus potentially to different preferential crystal phases.

The question remains how the composition impacts the tendency of the material to grow in one phase or the other. Oner et al. investigated surface energy and defect formation energy caused by different types of surface-terminations in α FAPbI$_3$ and found FAI-terminated surfaces to be the most energetically favorable and resilient to defect formation, more so than PbI$_2$-terminated ones.[68] An excess of FAI could therefore inhibit the formation of unfavorable defects and decrease the formation energy for α FAPbI$_3$. A similar effect has been calculated to occur for iPAmH$^+_{2/15}$FAI$_{14/15}$PbI$_{46/15}$,[60] where the formation energy for the α phase was decreased below the value for the δ phase by overstoichiometric addition of the large cation. We speculate, that surface passivation and defect formation resulting from FAI excess and consequently including the FA$^+$ and I$^-$ ions could be less favorable in the δ phase than in the α phase. These defects could include theoretically predicted I$_3^-$ trimers,[61] interstitials FA$_i$ and I$_i$ or the antisite defect FA$_{Pb}$, resulting in a stretched scaffold, large enough to hold FA$^+$ cations due to reduced surface stress. The decrease in lattice constant in Fig. S17 and S19 in the ESI† likely also points in this direction.

The incorporation of Br in combination with Cs significantly stabilized the growth of the (Cs,FA)PbI$_3$ α phase even for low Br/I in our experiments. This can be ascribed to a strong reduction of lattice strain in the (111) direction in FAPbI$_3$ by the additional components.[69] Amongst others, Zheng et al. observed a similar structural stabilization of FAPbI$_3$ with MABr and assigned the beneficial effects to a more compact lattice by the smaller A cation and halide.[15]

In general terms, we investigated the phase relations of polymorphic FA-based perovskite thin films and their preference to grow in the desired, photo-active α perovskite phase along three parameter axes: the X/Pb ratio, the Cs/FA ratio and the I/Br ratio. While the incorporation of Br successfully suppressed the growth of the photo-inactive δ phase, the incorporation of Br will also significantly impact the bandgap, and might not be desired in all applications. Contrary to our expectations, the Cs/FA variation did not significantly impact the segregation of δ domains in the film. However, a strong impact of the X/Pb ratio on the α/δ relation was observed. As a consequence, special attention has to be paid to the X/Pb ratio in vacuum-based deposition of FA-based perovskites (and perovskites in general).

Nevertheless, in our contribution, we solely investigated the impact on the crystal lattice and phase relations. Obviously, the X/Pb ratio also strongly affects the opto-electronic properties,[47,70] charge carrier densities[71] and stability of the films, which also has to be taken into account for a complete solar cell device optimization. This has proven to be a complex task and seems to depend on several yet unknown factors. E.g., Chiang et al. found an optimized efficiency for evaporated (Cs,FA)Pb(I,Br)$_3$ solar cells at an X/Pb ratio of 2.95, reducing crystallinity, but improving long-term structural stability by the excess of PbI$_2$ in the layer.[29] Ma et al. concluded excess PbI$_2$ to be beneficial, but also observed increasing efficiency over time via degradation to PbI$_2$ and resulting passivation.[72] Cho et al. investigated (Cs,FA,MA)Pb(I,Br)$_3$ solar cells

and found the optimum X/Pb ratio to be at about 3.4, noticing an enhanced optical and cell stability for overstoichiometric samples,[71] while Roß *et al.* produce FAPbI$_3$ solar cells with PbI$_2$ and FAI excess, respectively, showing similar efficiencies. In a more general approach it was shown, that unreacted PbI$_2$ is detrimental for (Cs,FA,MA)Pb(I,Br)$_3$ solar cells,[40] hinting towards a natural benign effect of A-cation excess in perovskite absorbers. According to several groups, the effect of X/Pb at specific interfaces has to be considered, where PbI$_2$ is beneficial at the ETL interface[51,73,74] and A-cations at the HTL interface.[73,75]

5 Conclusions

In summary, we investigated the influence of compositional variations on the growth of FA$_n$PbI$_{2+n}$ and double-cations (Cs,FA)$_n$PbI$_{2+n}$ as well as (Cs,FA)$_n$Pb(I,Br)$_{2+n}$ perovskites and the occurence of possible secondary phases at room temperature. The results from our systematic study show consistently, that it is possible to preferentially grow the α phase and suppress the δ phase for all absorber types when the AX/PbX$_2$ cation ratio is high enough. Without Cs, the threshold for suppression was found to be between I/Pb ratios of 3 to 3.9 The incorporation of Cs reduced the threshold to 3.6. However, solely through the introduction of Cs, the δ phase could not be completely suppressed for stoichiometric absorbers.

Apart from the preferential α phase growth at higher I/Pb ratios, the respective peak intensities increased while the FWHM decreased and the observed crystallite sizes increased. The introduction of Br strongly enhanced the suppression of the δ phase even for smaller AX/PbX$_2$ ratios. The threshold for δ phase suppression was then substantially reduced to a AX/PbX$_2$ ratio of 2.6, showing the potential of α phase stabilization by mixing halides. These results lead to three generalized design rules for the preferential growth of the α phase in formamidinium-based lead halide perovskites: (i) FAI-rich synthesis; (ii) small beneficial effect due to the incorporation of CsI (iii) strong impact upon the addition of the smaller halide anion Br.

Author contributions

K. H. and P. W. prepared samples and collected and analyzed the experimental data equally, while P. P. guided the experimental work. M. M. provided additional PL measurements. R. S. and P. P. provided structural guidance, valuable discussions and important input. K. H. and P. P. composed the mansucript. All authors redacted and discussed the manuscript.

Conflicts of interest

The authors have no conflicts of interest to declare.

References

1 A. Kojima, K. Teshima, Y. Shirai and T. Miyasaka, *J. Am. Chem. Soc.*, 2009, **131**, 6050–6051.

2 NREL, Best Research-Cell Efficiency Chart, 2022, https://www.nrel.gov/pv/cell-efficiency.html, Library Catalog: www.nrel.gov.

3 Y.-H. Kim, S. Kim, A. Kakekhani, J. Park, J. Park, Y.-H. Lee, H. Xu, S. Nagane, R. B. Wexler, D.-H. Kim, S. H. Jo, L. Martínez-Sarti, P. Tan, A. Sadhanala, G.-S. Park, Y.-W. Kim, B. Hu, H. J. Bolink, S. Yoo, R. H. Friend, A. M. Rappe and T.-W. Lee, *Nat. Photonics*, 2021, **15**, 148–155.

4 M. J. Bækbo, O. Hansen, I. Chorkendorff and P. C. K. Vesborg, *RSC Adv.*, 2018, **8**, 29899–29908.

5 B. Conings, J. Drijkoningen, N. Gauquelin, A. Babayigit, J. D'Haen, L. D'Olieslaeger, A. Ethirajan, J. Verbeeck, J. Manca, E. Mosconi, F. D. Angelis and H.-G. Boyen, *Adv. Energy Mater.*, 2015, **5**, 1500477.

6 B. C. ORegan, P. R. F. Barnes, X. Li, C. Law, E. Palomares and J. M. Marin-Beloqui, *J. Am. Chem. Soc.*, 2015, **137**, 5087–5099.

7 S. Li, Z. Liu, Z. Qiao, X. Wang, L. Cheng, Y. Zhai, Q. Xu, Z. Li, K. Meng and G. Chen, *Adv. Funct. Mater.*, 2020, 2005846.

8 R. Ji, Z. Zhang, C. Cho, Q. An, F. Paulus, M. Kroll, M. Löffler, F. Nehm, B. Rellinghaus, K. Leo and Y. Vaynzof, *J. Mater. Chem. C*, 2020, **8**, 7725–7733.

9 S.-H. Turren-Cruz, A. Hagfeldt and M. Saliba, *Science*, 2018, **362**, 449–453.

10 E. J. Juarez-Perez, L. K. Ono and Y. Qi, *J. Mater. Chem. A*, 2019, **7**, 16912–16919.

11 S. Thampy, B. Zhang, J.-G. Park, K.-H. Hong and J. W. P. Hsu, *Mater. Adv.*, 2020, **1**, 3349–3357.

12 M. P. U. Haris, S. Kazim, M. Pegu, M. Deepa and S. Ahmad, *Phys. Chem. Chem. Phys.*, 2021, **23**, 9049–9060.

13 A. Binek, F. C. Hanusch, P. Docampo and T. Bein, *J. Phys. Chem. Lett.*, 2015, **6**, 1249–1253.

14 N. Pellet, P. Gao, G. Gregori, T.-Y. Yang, M. K. Nazeeruddin, J. Maier and M. Grätzel, *Angew. Chem., Int. Ed.*, 2014, **53**, 3151–3157.

15 X. Zheng, C. Wu, S. K. Jha, Z. Li, K. Zhu and S. Priya, *ACS Energy Lett.*, 2016, **1**, 1014–1020.

16 Z. Li, M. Yang, J.-S. Park, S.-H. Wei, J. J. Berry and K. Zhu, *Chem. Mater.*, 2016, **28**, 284–292.

17 J.-W. Lee, D.-H. Kim, H.-S. Kim, S.-W. Seo, S. M. Cho and N.-G. Park, *Adv. Energy Mater.*, 2015, **5**, 1501310.

18 B. Charles, M. T. Weller, S. Rieger, L. E. Hatcher, P. F. Henry, J. Feldmann, D. Wolverson and C. C. Wilson, *Chem. Mater.*, 2020, **32**, 2282–2291.

19 M. Saliba, T. Matsui, K. Domanski, J.-Y. Seo, A. Ummadisingu, S. M. Zakeeruddin, J.-P. Correa-Baena, W. R. Tress, A. Abate, A. Hagfeldt and M. Grätzel, *Science*, 2016, 206–209.

20 C. Shen, Y. Wu, S. Zhang, T. Wu, H. Tian, W.-H. Zhu and L. Han, *Solar RRL*, 2020, **4**, 2000069.

21 Z. Zhang, R. Ji, M. Kroll, Y. J. Hofstetter, X. Jia, D. Becker-Koch, F. Paulus, M. Löffler, F. Nehm, K. Leo and Y. Vaynzof, *Adv. Energy Mater.*, 2021, **11**, 2100299.

22 Q. Ma, S. Huang, S. Chen, M. Zhang, C. F. J. Lau, M. N. Lockrey, H. K. Mulmudi, Y. Shan, J. Yao, J. Zheng, X. Deng, K. Catchpole, M. A. Green and A. W. Y. Ho-Baillie, *J. Phys. Chem. C*, 2017, **121**, 19642–19649.

23 P. Becker, J. A. Márquez, J. Just, A. Al-Ashouri, C. Hages, H. Hempel, M. Jošt, S. Albrecht, R. Frahm and T. Unold, *Adv. Energy Mater.*, 2019, **9**, 1900555.

24 Z. Yuan, Y. Miao, Z. Hu, W. Xu, C. Kuang, K. Pan, P. Liu, J. Lai, B. Sun, J. Wang, S. Bai and F. Gao, *Nat. Commun.*, 2019, **10**, 2818.

25 M. Saliba, T. Matsui, J.-Y. Seo, K. Domanski, J.-P. Correa-Baena, M. Khaja Nazeeruddin, S. M. Zakeeruddin, W. Tress, A. Abate, A. Hagfeldt and M. Grätzel, *Energy Environ. Sci.*, 2016, **9**, 1989–1997.

26 S. K. Yadavalli, Z. Dai, M. Hu, Q. Dong, W. Li, Y. Zhou, R. Zia and N. P. Padture, *Acta Mater.*, 2020, **193**, 10–18.

27 H. Min, M. Kim, S.-U. Lee, H. Kim, G. Kim, K. Choi, J. H. Lee and S. I. Seok, *Science*, 2019, **366**, 749–753.

28 J. Borchert, R. L. Milot, J. B. Patel, C. L. Davies, A. D. Wright, L. Martínez Maestro, H. J. Snaith, L. M. Herz and M. B. Johnston, *ACS Energy Lett.*, 2017, **2**, 2799–2804.

29 Y.-H. Chiang, M. Anaya and S. D. Stranks, *ACS Energy Lett.*, 2020, **5**, 2498–2504.

30 J. Feng, Y. Jiao, H. Wang, X. Zhu, Y. Sun, M. Du, Y. Cao, D. Yang and S. F. Liu, *Energy Environ. Sci.*, 2021, **14**, 3035–3043.

31 T. Burwig, K. Heinze and P. Pistor, *Phys. Rev. Mater.*, 2022, **6**, 065404.

32 L. Zhao, K. M. Lee, K. Roh, S. U. Z. Khan and B. P. Rand, *Adv. Mater.*, 2019, **31**, 1805836.

33 D. Faiman, *Prog. Photovoltaics Res. Appl.*, 2008, **16**, 307–315.

34 H. Wang, X. Cheng and H. Yang, *IEEE J. Photovolt.*, 2020, **10**, 729–739.

35 N. Rolston, K. A. Bush, A. D. Printz, A. Gold-Parker, Y. Ding, M. F. Toney, M. D. McGehee and R. H. Dauskardt, *Adv. Energy Mater.*, 2018, **8**, 1802139.

36 J. Zhao, Y. Deng, H. Wei, X. Zheng, Z. Yu, Y. Shao, J. E. Shield and J. Huang, *Sci. Adv.*, 2017, 1–8.

37 B. Shi, X. Yao, F. Hou, S. Guo, Y. Li, C. Wei, Y. Ding, Y. Li, Y. Zhao and X. Zhang, *J. Phys. Chem. C*, 2018, **122**, 21269–21276.

38 A. S. Yerramilli, Y. Chen, D. Sanni, J. Asare, N. D. Theodore and T. L. Alford, *Org. Electron.*, 2018, **59**, 107–112.

39 N. Ueoka and T. Oku, *ACS Appl. Mater. Interfaces*, 2018, **10**, 44443–44451.

40 G. Tumen-Ulzii, C. Qin, D. Klotz, M. R. Leyden, P. Wang, M. Auffray, T. Fujihara, T. Matsushima, J.-W. Lee, S.-J. Lee, Y. Yang and C. Adachi, *Adv. Mater.*, 2020, **32**, 1905035.

41 F. Liu, Q. Dong, M. K. Wong, A. B. Djurišić, A. Ng, Z. Ren, Q. Shen, C. Surya, W. K. Chan, J. Wang, A. M. C. Ng, C. Liao, H. Li, K. Shih, C. Wei, H. Su and J. Dai, *Adv. Energy Mater.*, 2016, **6**, 1502206.

42 R. Kottokkaran, H. A. Gaonkar, H. A. Abbas, M. Noack and V. Dalal, *J. Mater. Sci.: Mater. Electron.*, 2019, **30**, 5487–5494.

43 S.-Y. Hsiao, H.-L. Lin, W.-H. Lee, W.-L. Tsai, K.-M. Chiang, W.-Y. Liao, C.-Z. Ren-Wu, C.-Y. Chen and H.-W. Lin, *Adv. Mater.*, 2016, **28**, 7013–7019.

44 F. Ma, J. Li, W. Li, N. Lin, L. Wang and J. Qiao, *Chem. Sci.*, 2017, **8**, 800–805.

45 M. Roß, L. Gil-Escrig, A. Al-Ashouri, P. Tockhorn, M. Jošt, B. Rech and S. Albrecht, *ACS Appl. Mater. Interfaces*, 2020, **12**, 39261–39272.

46 K. B. Lohmann, J. B. Patel, M. U. Rothmann, C. Q. Xia, R. D. J. Oliver, L. M. Herz, H. J. Snaith and M. B. Johnston, *ACS Energy Lett.*, 2020, **5**, 710–717.

47 M. Roß, S. Severin, M. B. Stutz, P. Wagner, H. Köbler, M. Favin-Lévêque, A. Al-Ashouri, P. Korb, P. Tockhorn, A. Abate, B. Stannowski, B. Rech and S. Albrecht, *Adv. Energy Mater.*, 2021, **11**, 2101460.

48 S. Olthof and K. Meerholz, *Sci. Rep.*, 2017, **7**, 40267.

49 P. Pistor, J. Borchert, W. Fränzel, R. Csuk and R. Scheer, *J. Phys. Chem. Lett.*, 2014, **5**, 3308–3312.

50 T. Burwig, W. Fränzel and P. Pistor, *J. Phys. Chem. Lett.*, 2018, **9**, 4808–4813.

51 K. L. Heinze, O. Dolynchuk, T. Burwig, J. Vaghani, R. Scheer and P. Pistor, *Sci. Rep.*, 2021, **11**, 15299.

52 M. U. Rothmann, J. S. Kim, J. Borchert, K. B. Lohmann, C. M. OLeary, A. A. Sheader, L. Clark, H. J. Snaith, M. B. Johnston, P. D. Nellist and L. M. Herz, *Science*, 2020, **370**, 1–7.

53 J. Huang, P. Xu, J. Liu and X.-Z. You, *Small*, 2017, **13**, 1603225.

54 G. Murtaza and I. Ahmad, *Phys. B: Condens. Matter*, 2011, **406**, 3222–3229.

55 D. H. Fabini, C. C. Stoumpos, G. Laurita, A. Kaltzoglou, A. G. Kontos, P. Falaras, M. G. Kanatzidis and R. Seshadri, *Angew. Chem.*, 2016, **128**, 15618–15622.

56 J. Ran, O. Dyck, X. Wang, B. Yang, D. B. Geohegan and K. Xiao, *Adv. Energy Mater.*, 2020, **10**, 1903191.

57 P. Raval, R. M. Kennard, E. S. Vasileiadou, C. J. Dahlman, I. Spanopoulos, M. L. Chabinyc, M. Kanatzidis and G. N. Manjunatha Reddy, *ACS Energy Lett.*, 2022, 1534–1543.

58 S. P. Dunfield, L. Bliss, F. Zhang, J. M. Luther, K. Zhu, M. F. A. M. van Hest, M. O. Reese and J. J. Berry, *Adv. Energy Mater.*, 2020, **10**, 1904054.

59 L. Ma, D. Guo, M. Li, C. Wang, Z. Zhou, X. Zhao, F. Zhang, Z. Ao and Z. Nie, *Chem. Mater.*, 2019, **31**, 8515–8522.

60 B.-w Park, H. W. Kwon, Y. Lee, D. Y. Lee, M. G. Kim, G. Kim, K.-j Kim, Y. K. Kim, J. Im, T. J. Shin and S. I. Seok, *Nat. Energy*, 2021, **6**, 419–428.

61 A. Ruth, M. Holland, A. Rockett, E. Sanehira, M. D. Irwin and K. X. Steirer, *Crystals*, 2022, **12**, 88.

62 C. Wu, K. Chen, D. Y. Guo, S. L. Wang and P. G. Li, *RSC Adv.*, 2018, **8**, 2900–2905.

63 K. Nishimura, D. Hirotani, M. A. Kamarudin, Q. Shen, T. Toyoda, S. Iikubo, T. Minemoto, K. Yoshino and S. Hayase, *ACS Appl. Mater. Interfaces*, 2019, **11**, 31105–31110.

64 C. G. Bischak, C. L. Hetherington, H. Wu, S. Aloni, D. F. Ogletree, D. T. Limmer and N. S. Ginsberg, *Nano Lett.*, 2017, **17**, 1028–1033.

65 R. Chatterjee, I. M. Pavlovetc, K. Aleshire, G. V. Hartland and M. Kuno, *ACS Energy Lett.*, 2018, **3**, 469–475.

66 L. I. Maissel, R. Glang and P. P. Budenstein, *J. Electrochem. Soc.*, 1971, **118**, 114C.

67 E. S. Parrott, J. B. Patel, A.-A. Haghighirad, H. J. Snaith, M. B. Johnston and L. M. Herz, *Nanoscale*, 2019, **11**, 14276–14284.

68 S. M. Oner, E. Sezen, M. S. Yordanli, E. Karakoc, C. Deger and I. Yavuz, *J. Phys. Chem. Lett.*, 2022, **13**, 324–330.

69 E. G. Moloney, V. Yeddu and M. I. Saidaminov, *ACS Mater. Lett.*, 2020, **2**, 1495–1508.

70 D. P. McMeekin, G. Sadoughi, W. Rehman, G. E. Eperon, M. Saliba, M. T. Hörantner, A. Haghighirad, N. Sakai, L. Korte, B. Rech, M. B. Johnston, L. M. Herz and H. J. Snaith, *Science*, 2016, **351**, 151–155.

71 S. H. Cho, J. Byeon, K. Jeong, J. Hwang, H. Lee, J. Jang, J. Lee, T. Kim, K. Kim, M. Choi and Y. S. Lee, *Adv. Energy Mater.*, 2021, **11**, 2100555.

72 Z. Ma, D. Huang, Q. Liu, G. Yan, Z. Xiao, D. Chen, J. Zhao, Y. Xiang, C. Peng, H. Li, M. Zhang, W. Zhang, L. Duan and Y. Huang, *J. Energy Chem.*, 2022, **66**, 152–160.

73 J. Li, H. A. Dewi, H. Wang, J. Zhao, N. Tiwari, N. Yantara, T. Malinauskas, V. Getautis, T. J. Savenije, N. Mathews, S. Mhaisalkar and A. Bruno, *Adv. Funct. Mater.*, 2021, **31**, 2103252.

74 T. J. Jacobsson, J.-P. Correa-Baena, E. Halvani Anaraki, B. Philippe, S. D. Stranks, M. E. F. Bouduban, W. Tress, K. Schenk, J. Teuscher, J.-E. Moser, H. Rensmo and A. Hagfeldt, *J. Am. Chem. Soc.*, 2016, **138**, 10331–10343.

75 Z. Hu, Q. An, H. Xiang, L. Aigouy, B. Sun, Y. Vaynzof and Z. Chen, *ACS Appl. Mater. Interfaces*, 2020, **12**, 54824–54832.

Concluding Discussion

[H3] extensively addresses (Q_1) by providing a firm grasp on the stoichiometrical and compositional phase space of $FAPbI_3$. The results in [H3] show clearly that the $FAPbI_3((Cs,FA)PbI_3$ α phase can be promoted instead of the δ phase at room temperature if a sufficient excess of A-cations is incorporated or I is partially substituted with Br. This was determined via the X/Pb ratio.

Therefore, the works by Roß et al. on co-evaporation [80] and Ma et al. [84] and Yuan et al. [304] on spin-coated preparation, exhibiting the partial suppression of δ phase growth in $FAPbI_3$ by FAI excess are confirmed by [H3]. In addition, in [H3] the bulk growth in $FAPbI_3$ is investigated within a broader stoichiometrical range and it is shown via XRD that a further increase of the A-cation excess leads to a stronger suppression of the δ phase and finally, at high excess, to an exclusive α phase growth. Stoichiometric ranges for exclusive α phase growth are given. For $FAPbI_3$, exclusive α phase growth is observed for I/Pb ratios from 3 to 3.9 and above. At an I/Pb ratio of 5.4 the segregation of FAI is visible. Ma et al. observed the step-wise shift in preferential growth of the δ phase towards the α phase with increasing FAI/PbI_2 ratio from 0.9 to 2 (I/Pb ratio of 2.9 to 4) and identified the segregation of FA_3PbI_5 at an FAI/PbI_2 ratio of 3 (I/Pb ratio of 5) [84]. They related the increase in α phase share in the film to a reduction in colloidal size in the solution and therefore a reduction in grain size, which may lead to a relative increase of the total free energy (surface and bulk) of the δ phase [84]. This is the opposite of the observation in [H3], where the grain size is shown to increase for a higher FAI content. This clearly demonstrates the impact of different film formation phenomena on perovskites deposited by solution-based and vapor phase techniques. However, the similarity remains - as for $MAPbI_3$ - that excess PbI_2 segregates and excess FAI does not, but rather seems to be integrated into the perovskite. On a side note, excess FAX (X=I, Br) has been shown to lead to the formation of 2D Ruddlesden-Popper $FA_{n+1}Pb_nX_{3n+1}$ phases which exhibit distinct optical properties [308]. This family of phases is neglected here, but may be interesting for optoelectronic devices due to their optical tunability and the reduction of halide migration and segregation [309].

Roß et al. compared stoichiometric $FAPbI_3$ to absorbers with 15 % of PbI_2 excess and FAI excess, respectively, and observed the formation of PbI_2 even for excess FAI on MeO-2PACz ([2-(3,6-Dimethoxy9H-carbazol-9-yl)ethyl]phosphonic Acid) [80]. However, they determined the stoichiometry from the evaporation rates and did not measure the stoichiometry in the as-prepared film. Therefore, the condensation behavior of the evaporated materials on the substrate was neglected and the film resulting from excess FAI deposition rates might even have been rich in PbI_2. However, their study is a reminder that the substrate strongly influences film formation, as deposition on the unwashed MeO-2PACz supposedly allowed for a larger condensation rate of FAI leading to the shift towards preferential growth of the α phase [80] as discussed above. They also observed an increase in XRD peak intensity under FAI excess which is maintained during annealing at 100°C, indicating improved crystallinity as in [H3].

When FAI is partially substituted with CsI in [H3], the I/Pb threshold ratio above which exclusive α phase occurs decreases to 3.6 and again an increase in crystallite sizes is observed. Yuan et al. employed a solution-based approach investigating $(Cs,FA)PbI_3$ for LEDs and observed a suppression of the δ phase

between (CsI+FAI)/PbI_2 ratios of 1.5 and 2 (I/Pb ratios of 3.5 to 4) after annealing at 100°C [304]. Similar to Ma et al., they also notice a decrease in colloidal sizes in the solution with an increasing excess of (CsI+FAI), but the implication for crystallite sizes is not as clear.

The partial substitution of I with Br for (Cs,FA)Pb(I,Br)$_3$ resulted in the complete suppression of the δ phase for all films with X/Pb (X=I+Br) ratios above 2.64 in [H3]. Below an X/Pb ratio of 3, PbI_2 segregated and Br was preferentially incorporated into the perovskite crystal lattice. Above an X/Pb ratio of 3, no PbX_2 was observed. The quantification of stoichiometric ranges in which certain phases are preferred and/or others segregate is a novelty provided by [H3] and a huge leap towards answering (Q_1).

[H3] does not give a final explanation for the preferred α phase formation at given stoichiometric conditions. Oner et al. performed first-principles calculations for FAPbI$_3$ and found the lowest grain surface energies, corresponding to the most stable grain surfaces, for surfaces terminated with FAI compared to PbI_2-/I-/PbI-terminated surfaces [82]. They found FAI-terminated surfaces invoked the highest average defect formation energies compared to the other surface terminations. In fact, all considered defect formation energies were calculated to be above 1.5 eV in FAI-terminated surfaces. A stabilization of the α phase by FAI excess in [H3] may thus be correlated to grain surface passivation by the FAI.

Since an annealing step is necessary to drive the δ→α phase transition normally, a certain activation energy is required to grow the α phase. Therefore, the question remains why the α phase is formed preferentially in the first place for an excess of FAI in [H3]. Park et al. showed via DFT calculations that when the large cation iPAmH$^+$ (isopropylammonium iodide) was introduced to FAPbI$_3$ via solution-based preparation, it passivated the grain boundary of the FAPbI$_3$ grains, greatly reducing the formation energy of the α phase compared to the δ phase as well as lowering the defect formation in general [81]. Therefore, grain boundary passivation by FAI as postulated by Oner et al. may not only be correlated to stabilization, but also to reduced formation energy of the α phase.

PSCs are not discussed in [H3]. The impact of bulk stoichiometry on the PSC performance [(Q_2)] is investigated for FAPbI$_3$ by Roß et al. [80]. In their approach, the maximum single efficiency is obtained for FAI excess and the highest average efficiency of 14.7 % is measured for the stoichiometric absorber although all the average efficiencies are close to 14.5 % in a p-i-n structure using ITO/MeO-2PACz/perovskite/C$_{60}$/BCP/Cu [80]. In a sequential solution-based approach by Cho et al. the hysteresis was reduced and the overall efficiency and stability of FAI-rich (Cs,FA,MA)Pb(I,Br)$_3$ was significantly improved by incorporating a ~50 % excess of the organic component as measured in the final film [291]. The optimized efficiency of 20.5 % was attributed to the enhanced suppression of Pb-I antisite defects compared to compositions with ~30 % excess and balanced stoichiometry. During the stability test 95 % of the initial efficiency were maintained in the optimized device at constant operation under 1 sun compared to a few hours for the device with balanced stoichiometry. They employed an n-i-p device structure using ITO/SnO$_2$/perovskite/Spiro-MeOTAD/Au. Roß et al. and Cho et al. demonstrated improved j_{sc} and slightly reduced V_{OC} in their devices with organic excess, thus generally suggesting that excess of organic components in the bulk may be able to push the PSC efficiencies further[(Q_2)]. In comparison

to other works optimizing PSC devices by varying deposition techniques, intermediate steps, dopants or optimized transport layers [157], the approach to vary the bulk stoichiometry aiming for greater PSC efficiencies is very rare and should be pursued more when considering the discussed results.

4.5 Sequential Evaporation of APbX$_3$

Opening Remarks

In [H1–H3] stoichiometry-driven reactions in various APbX$_3$ thin films were investigated and the growth behavior during static and dynamic evaporation were analyzed via *in situ* XRD. In particular, the influence of PbI$_2$ and MAI seed layers on the formation and properties of the interface and bulk were studied in standard *n-i-p* and inverted *p-i-n* PSC structures. For MAPbI$_3$ PSCs prepared at room temperature, the limited diffusion reaction determined an optimum PbI$_2$ seed layer thickness, above which the efficiency decreased, indicating an unreacted PbI$_2$ layer at the interface due to the existence of a diffusion barrier. Such a diffusion reaction barrier can be overcome and some works have successfully demonstrated full conversion of the PbI$_2$ precursor layer to the perovskite phase during sequential evaporation by a post-annealing step for MAPbI$_3$ [275, 310] and FAPbI$_3$ [186, 311].

For (Cs,FA)PbI$_3$, one of the to-date maximum efficiencies for evaporated PSCs has been achieved via sequential thermal evaporation of PbI$_2$, FAI and CsI in this order [39]. Nonetheless, further optimization is necessary and a study showcasing the limits of the diffusion-driven reactions at the interfaces during deposition and throughout the bulk during post-annealing is missing so far. In addition, no variations of the sequence order have been investigated for (Cs,FA)PbI$_3$ and (Cs,FA)Pb(I,Br)$_3$ albeit the positive influence on charge transport as determined for interfacial reactions and gradients in MAPbI$_3$ PSCs in 4.2 and 4.3.

Therefore, [H4] investigates the variation of deposition sequence and reaction of precursors during sequential thermal evaporation. It aims to understand the phase formation and diffusion reactions in order to optimize the growth conditions to obtain single-phase perovskite thin film layers for (Cs,FA)PbI$_3$ and (Cs,FA)Pb(I,Br)$_3$.

RESEARCH ARTICLE

physica
status
solidi a

Check for updates

www.pss-a.com

Structural Evolution of Sequentially Evaporated (Cs,FA)Pb(I,Br)₃ Perovskite Thin Films via In Situ X-Ray Diffraction

Karl L. Heinze, Tobias Schulz, Roland Scheer, and Paul Pistor*

Evaporation of perovskite thin films for solar cell applications is a solvent-free, well controllable, and scalable deposition path with promising prospects for commercialization. Compared to commonly applied simultaneous co-evaporation of various halide precursor salts, sequential evaporation followed by an annealing step allows to better control the amount of deposited precursors, and has the potential to largely improve reproducibility. In this work, Cs/formamidinium (FA)-based lead iodide perovskites are deposited via sequential evaporation in a vacuum chamber and the phase formation and evolution of different precursor-stacking sequences and annealing conditions are investigated with in situ X-ray diagnostics. In addition, some Br is added to investigate the effect of halide intermixing. The stacking sequence is found to strongly influence the formation of dominant phases as well as the preferential orientation and HGHmorphology of the as-deposited films. These variations in turn affect the diffusion and conversion during thermal annealing and ultimately the conversion ratio of the final perovskite layers. For example, it is found that starting the stacking sequences with the A cations (CsI, FAI) favors a fast and complete conversion of the perovskite phase. However, the result is the formation of perovskite layers with large voids.

1. Introduction

Perovskite solar cells (PSCs) have almost reached the power conversion efficiency (PCE) of silicon-based solar cells (26.1% and 26.8%, respectively[1,2]). However, to date, the most prominent

K. L. Heinze, T. Schulz, R. Scheer
Thin Film Photovoltaics
Martin-Luther-University Halle-Wittenberg
Von-Danckelmann-Platz 3, 06120 Halle (Saale), Germany

P. Pistor
Center for Nanoscience and Sustainable Technologies (CNATS)
Universidad Pablo de Olavide
Carretera de Utrera 1, 41013 Sevilla, Spain
E-mail: ppis@upo.es

The ORCID identification number(s) for the author(s) of this article can be found under https://doi.org/10.1002/pssa.202300690.

deposition technique is spin-coating, which bears two main disadvantages. Spin-coating cannot be upscaled to produce devices on large areas for industrial applications, and solvents such as dimethylformamide or dimethylsulfoxide are needed.[3,4] These solvents are toxic[5] and costly, have a bad environmental footprint,[6] can cause damage to underlying layers[7] and thus their usage is ideally minimized.

A completely solvent-free perovskite synthesis can be realized by evaporation via physical vapor deposition (PVD), which allows for homogeneous large area growth on various substrate morphologies.[8–12] Compared to co-evaporation, sequential evaporation enables good crystallinity and better process control.[8,13,14] Feng et al. have shown that homogenous formamidinium (FA)-based perovskite layers can be deposited with a sequential roll-to-roll process on large areas, and applying an optimized low temperature annealing at 60 °C a high PCE of 21.3% could be obtained.[6] A record PCE of 24% for sequentially deposited CsFAPbI₃ was reported by Li et al. in 2022.[15] In sequential lead halide perovskite deposition, usually the inorganic components, typically PbI₂, are deposited first, and their properties and morphologies might therefore strongly influence subsequent perovskite formation. For sequential wet-chemical processing routes, i.e., the so-called two-step-deposition methods, many reports focus on the optimization of the inorganic precursor deposition in view of solar cell performance, emphasizing its significance. There, solvent additives or variations of different preparation techniques are used to obtain optimal morphologies,[16–18] and the consensus is that a highly oriented and porous PbI₂ precursor layer favors a full conversion to the perovskite phase leading to high-performance PSCs.[19–23]

However, few reports exist regarding the optimization of the inorganic precursor deposition in the context of PVD. Instead of a solution penetrating the inorganic precursor, during sequential evaporation a condensed organic (e.g., formamidinium iodide [FAI]) layer is formed, and solid-state diffusion determines the reaction kinetics. As a consequence, optimal precursor morphologies for a fast and complete conversion into high-quality perovskite layers might be different for vacuum-based approaches as compared to a solution-based conversion step. Using PVD, Hoerantner et al. speculate that the porosity of PbI₂ could be

advantageous for its conversion to MAPbI$_3$.[24] Li et al. maximized their PCE by enhancing the crystallinity of their PbI$_2$ seed layer and produced a smoother and more condensed surface by incorporating a small amount of CsI and PbCl$_2$.[15] Wang et al. employ spin-coated PbI$_2$/PbCl$_2$ and find larger precursor grains to be beneficial for perovskite formation during FAI evaporation.[14] The optimization of the PbI$_2$ precursor layer is even more important, as PbI$_2$ is a highly versatile material with many different polytypes[25] and morphologies, and its full potential for optimized sequential evaporation is still to be unfolded.

Solid-state diffusion through PbI$_2$ is driven by concentration gradients. However, there is still limited knowledge and understanding about the interdiffusion during the annealing of the precursors for perovskite conversion. As the lead halide salts share a similar octagonal lead halide configuration in the lead halide recursor as in the final perovskite phase, the conversion is sometimes called intercalation of the A cation. For MAPbI$_3$, Eames et al. found that primarily I$^-$ and MA$^+$ diffused within the perovskite lattice, while the Pb^{2+} ions mostly remained stationary.[26] This effect has been scarcely discussed for FA-based perovskites up to now and our experiments are specifically designed to elaborate on this knowledge gap.

Therefore, we investigate the sequential deposition of $(\text{Cs}, \text{FA})\text{Pb}(\text{I}, \text{Br})_3$ thin films via sequential thermal evaporation of the precursors in a vacuum chamber followed by an annealing step. We prepare perovskite absorbers using different sequences of the components FAI, cesium iodide (CsI), lead iodide (PbI$_2$), and lead bromide (PbBr$_2$) and analyze the crystal structure evolution of the different phases present during deposition and post annealing. For this purpose, we use an in situ X-ray diffraction (XRD) setup,[27] which allows us to observe the evolution of crystalline phases during growth and annealing. In the first part of this work, the iodine-based perovskite $(\text{Cs}, \text{FA})\text{PbI}_3$ is synthesized comparing two different precursor stacks: the conventional one starting with the B cation (Sequence B, PbI$_2$–FAI–CsI) and an alternative approach where the PbI$_2$ is deposited last (Sequence A, CsI–FAI–PbI$_2$). We detect large differences in the preferred phase formation, phase evolution during annealing, and morphology using in situ XRD, scanning electron microscopy (SEM), and energy-dispersive X-ray spectroscopy (EDX) measurements. The in situ XRD allows us to distinguish between the growth of two different PbI$_2$ polytypes: the hexagonal 2H phase and the rhombohedral 6R phase. Our results give evidence that the different precursor configurations can have a large impact on the conversion and final perovskite formation. In addition, we explore different options to optimize conversion into the perovskite phase such as nonstoichiometric precursor ratios, the deposition of split/multiple precursor layer stacks or the variation of the precursor morphologies by varying the substrate temperature during deposition. Finally, we investigate how the introduction of small amounts of Br in the form of PbBr$_2$ affects the aforementioned and analyze two different precursor sequences for the deposition of the mixed-halide perovskite $(\text{Cs}, \text{FA})\text{Pb}(\text{I}, \text{Br})_3$: one similar to sequence B, where the lead halides are deposited first (PbBr$_2$–PbI$_2$–FAI–CsI) and one where they are evaporated first and last, respectively (PbBr$_2$–FAI–CsI–PbI$_2$). We observe a strong effect of the sequence on the formation of preliminary Br-rich and

I-rich phases and their reaction speed toward a single mixed-halide perovskite phase.

2. Results

In total, we have conducted three different experimental series. In the first set of experiments, we compare different stacking orders of the precursors for the sequential formation of $(\text{Cs}, \text{FA})\text{PbI}_3$, namely depositing the A cations first (sequence A: CsI–FAI–PbI$_2$) and B cation first (sequence B: PbI$_2$–FAI–CsI). This is followed by precursor sequences where the PbI$_2$ layer is split into two parts with different ratios (sequence with split PbI$_2$), one of them at the bottom of the precursor stack, and the other on top (see **Figure 1**). Based on these simple experiments, we conduct a second series of experiments in the attempt to improve the conversion of the precursors into a perovskite film by comparing different processing conditions where the PbI$_2$ layer is deposited first (in that sense, variation of sequence B): PbI$_2$ layers synthesized at different process conditions (substrate temperature, wet-chemical deposition) and by applying overstoichiometric (os) amounts of FAI. The single component thicknesses were 21, 224, and 261 nm for CsI, FAI, and PbI$_2$ in each respective sequence. Details can be found in the Experimental Section.
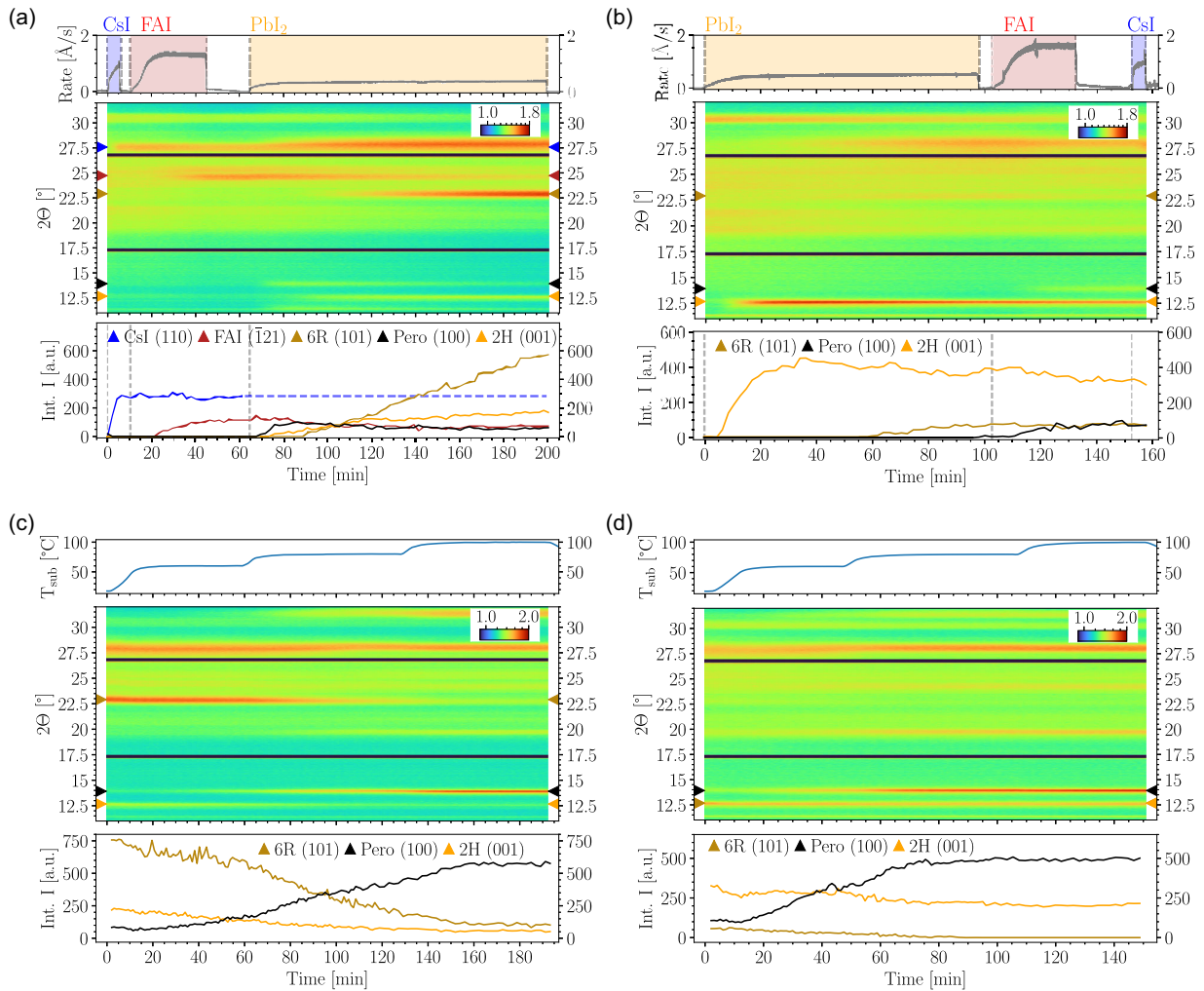
Finally, we briefly investigate how the addition of PbBr$_2$ as a source of Br to the precursor layer stack impacts the film formation and perovskite conversion in the last series of experiments. In these layer stacks, CsI and FAI thicknesses were again 21 and 224 nm, respectively, while 106 nm of PbI$_2$ and 115 nm of PbBr$_2$ were evaporated. We will start with the thorough analysis of the phase formation and evolution through deposition and annealing of the precursor stack with the A cation at the bottom (sequence A).

2.1. Precursor Order I: CsI/FAI First, PbI$_2$ Last (Sequence A)

Sequence A is a novelty for sequential evaporation of perovskites and thus promises to give valuable insight into the growth and reaction dynamics of the layer stack. The in situ diffractograms recorded during the deposition of sequence A are depicted as color plots in **Figure 2**a. Here, the XRD intensity is color coded and the x/y axes correspond to the process time and the 2Θ angle, respectively. Above the color plot, the respective deposition rates of CsI (blue background), FAI (red), and PbI$_2$ (yellow) are shown. Below the color plot, the peak area (given as integrated intensity: Int. I) evolution of the most relevant peaks for each precursor component and phase is depicted. The representative peaks
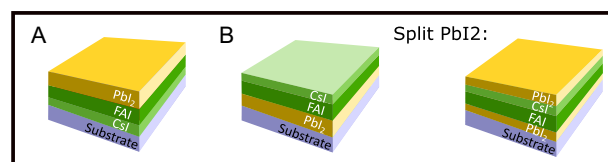
Figure 1. Schematic layer stacks after evaporating A, B, and split PbI$_2$ sequences. The layers providing A cations CsI and FAI are shown in light and dark green, respectively. PbI$_2$ layers are yellow.

ADVANCED
SCIENCE NEWS
www.advancedsciencenews.com

physica **pss** **a**
status
solidi

www.pss-a.com

Figure 2. Process diagrams for evaporation of sequences a) A and b) B: The diagrams include rates of CsI–FAI–PbI$_2$ (blue, red, and yellow backgrounds, respectively–top), in situ XRD color plot (center) and development of integrated peak intensities (Int. I–bottom). Corresponding 2Θ peak positions for evaluated peaks from the literature are displayed as triangles next to the color plot. In sequence A, CsI (110) Int. I is continued as a constant dashed line during PbI$_2$ deposition since evaluation is made impossible due to superposition with (Cs, FA)PbI$_3$ (200) (labeled Pero) and PbI$_2$ 6R (104) peaks, both broad near 28°.[25,29,31] In sequence B, FAI and CsI Int. I are not shown, since their intensities are too low. Process diagrams of sequences c) A and d) B during annealing: The diagrams show substrate temperature (top), in situ XRD color plot (center) and integrated intensity (Int. I) peak development (bottom). The sample temperature is increased from 60 to 100 °C over 150 min to fully convert the layer stack to the perovskite α phase.

shown here are marked by triangles next to the color plot, according to the literature value of their respective 2Θ positions. Before evaporation, substrate peaks at 20°, 21.5°, 30.5°, and 35.4° are visible, mainly from the cubic indium tin oxide (ITO) phase.[28] These are attenuated during the evaporation process due to absorption of X-rays in the deposited layers. To evaluate the formed crystalline phases in more detail, Θ–Θ scans of the layers directly after deposition and after annealing (i.e. at the end of each color plot) are shown in Figure S4 (Supporting Information). During the first evaporation step, the characteristic (110) peak of the cubic CsI phase appears at 27.6°.[29] Throughout the later stages of this process, superposition of this peak with peaks from other phases impedes its quantification, and as a simplification we assumed its intensity to be constant during PbI$_2$ deposition (indicated by the dashed line). After 22 min, the FAI monoclinic crystal phase becomes visible with its main peak at 24.7° corresponding to the ($\bar{1}$21) lattice plane.[30] Subsequently, during PbI$_2$ evaporation, first the characteristic (100) peak of the FAPbI$_3$ perovskite α phase at 13.9° appears[31] after approximately 70 min of processing time. At this point, we cannot determine, if the perovskite α phase contains low amounts of Cs, so we will refer to the α phase as (Cs, FA)PbI$_3$ (labeled Pero in Figure 2). Please note that, while we do observe a low intensity peak at 11.5°, close to the (001) peak of the FAPbI$_3$ δ phase,[32] we assume that no δ phase is formed, as explained in the SI on the basis of Figure S1 (Supporting

Information). FAI and $(Cs, FA)PbI_3$ peaks decrease in intensity slightly starting at 80 min and shortly after the (001) peak of the hexagonal PbI_2 2H phase at 12.7° forms.[33]

Starting at 90 min, a peak at 22.9° dominates during PbI_2 evaporation and the 2H (001) peak shrinks. The newly observed peak at 22.9° is strongly shifted compared to the 2H (100) peak at 22.5°.[33] We deduce that the PbI_2 phase not only undergoes a change in preferential orientation, but a different phase starts to grow. We allocate this to the PbI_2 6R phase (see Figure S2, Supporting Information), which exhibits one of its main peaks at 22.9°, stemming from its (101) lattice plane. The 6R phase has been observed to develop via evaporation under vacuum conditions.[25] In our experiment, the 6R (101) peak then grows linearly, making up all the crystalline PbI_2 phase growth visible in the diffractograms. The 6R (104) peak at 28.3° also develops clearly, but cannot be quantified due to superposition with the CsI (110) and $(Cs, FA)PbI_3$ (200) peaks. The transition from the growth of the 2H to the growth of the 6R polytype is a trend observed in many of our PbI_2 layers grown under vacuum (Figure S3, Supporting Information). For a summary of the most relevant peaks, see **Table 1**.

To investigate the conversion into the perovskite thin film resulting from sequence A, the layer was annealed at three different temperatures (Figure 2c). The top graph shows the substrate temperature, while the peak area development is displayed at the bottom. At 60 °C, a slow reaction between the three precursor layers takes place, resulting in a slow increase of the $(Cs, FA)PbI_3$ (100) peak intensity. Increasing the substrate temperature to 80 °C enhances this reaction, as $(Cs, FA)PbI_3$ (110) and (210) peaks appear at 19.7° and 31.4°, respectively. At the same time, the triple peak at 28° begins to narrow down to a single peak. This hints toward an amorphization of CsI or, more likely, diffusion of CsI into the perovskite layer. We suspect the $(Cs, FA)PbI_3$ (200) peak to be dominant at 28° due to PbI_2 conversion to the perovskite phase. Simultaneously, the 2H (001) and 6R (101) PbI_2 peaks begin to decrease in intensity. After approximately 150 min and at a temperature of 100 °C, the reactions described earlier are concluded and peak developments come to a halt in the timescale visible in our experiment. Perovskite peaks dominate the resulting layer and only slight traces of residual PbI_2 and FAI remain visible.

2.2. Precursor Order II: PbI$_2$ First (Sequence B)

Sequence B is the usual deposition order for sequentially evaporated perovskites and the logical counterpart to sequence A. We investigate this sequence via in situ XRD to expand the understanding on the reaction kinetics between precursor layers during evaporation and annealing. For sequence B PbI_2, FAI, and CsI were evaporated sequentially in this order. The in situ process diagram is shown in Figure 2b. Upon PbI_2 evaporation, a strong 2H (001) peak develops, which saturates after 30–40 min and then decreases in intensity slightly, while the 6R (101) and (104) peaks, respectively, evolve. FAI evaporation starting at 102 min leads to the formation of $FAPbI_3$ as can be seen by the low intensity $(Cs, FA)PbI_3$ (100) peak. Neither FAI nor CsI peaks appear in the XRD during their respective evaporation step, suggesting either strong diffusion and reactivity and/or low crystallinity of the unreacted species.

During annealing of sequence B (Figure 2d), the layer stack reacts well and all major perovskite peaks develop, increasing in intensity with each temperature step (60 °C, 80 °C, and 100 °C). Still, a small residual 2H (001) peak remains. FAI re-evaporation is an unlikely cause for remaining PbI_2, since we were only able to evaporate FAI above 140 °C in vacuum. At standard conditions, FAI has been shown to evaporate at 230 °C.[30] In consequence, the incomplete reaction of the layer stack is not a result of FAI desorption, but indicates that the provided heat does not enhance diffusion enough to fully react the layer stack during our experiment. This is consistent with the correct stoichiometry of annealed films (as correct by EDX, see the next paragraphs).

2.3. SEM and EDX

The characteristics of sequences A and B are further investigated by SEM and EDX measurements. The SEM cross section of sequence A in **Figure 3**a shows a homogeneous bulk with distinct properties at the surface and the substrate interface. At the surface small, bright crystallites and platelets can be seen. These are assigned to PbI_2 surface species. At the NiO interface, clearly visible voids suggest a peculiar upward diffusion behavior of the A cations into the PbI_2. We use EDX to

Table 1. Overview of relevant reference 2Θ diffraction peaks for the evaporated components. 2H and 6R refer to different polytypes of the PbI_2 compound with hexagonal and rhombohedral crystal structures, respectively. I-rich (IPer) and Br-rich (BrPer) perovskite phases do not correspond exactly to the $FAPbI_3$ and $FAPbBr_3$ phases and XRD peaks given here, since IPer and BrPer phases might include varying shares of the respective other halide, resulting in a shift of the peak positions. Additionally, the incorporation of CsI leads to a small shift to higher diffraction angles.

Material	Crystal Structure	Space Group	Lattice Plane	XRD 2Θ Angle	Source
CsI	Cubic	Pm-3m (221)	(110)	27.6°	[29]
FAI	Monoclinic	P21/a (14)	($\bar{1}$21) (002)	24.7°, 25.6°	[30]
PbI$_2$	2H	P-3m1 (164)	(001) (002)	12.7°, 25.5°	[33]
PbI$_2$	6R	R-3m (166)	(101) (104)	22.9°, 28.3°	[25]
FAPbI$_3$	Cubic	Pm-3m (221)	(100) (110) (111) (200) (210)	13.9°, 19.7°, 24.2°, 28.0°, 31.4°	[31]
PbBr$_2$	Orthorhombic	Pnam (62)	(200) (111) (220)	22.0°, 22.7°, 29°	[40]
FAPbBr$_3$	Cubic	Pm-3m (221)	(100) (110) (200)	14.8°, 20.9°, 29.8°	[67]
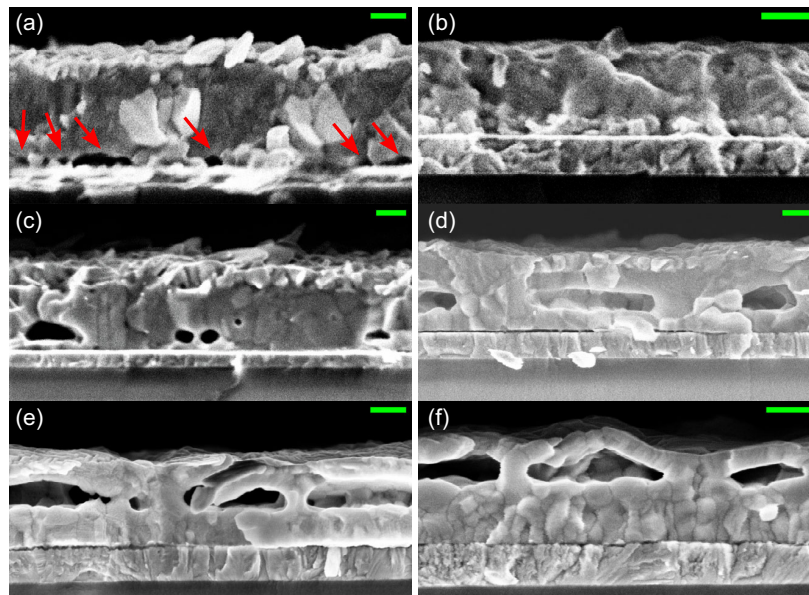
Figure 3. Scanning electron microscopy (SEM) cross sections after annealing. a) Sequence A (CsI-FAI-PbI$_2$). Voids at the interface to the substrate are marked by red arrows. b) Sequence B (PbI$_2$-FAI-CsI) after annealing. c–f) Processes with split PbI$_2$ (sequence [x]PbI$_2$–FAI–CsI–(1–x)PbI$_2$) after annealing with $x = 10\%$, 30%, 50%, 70%. The green scale bar represents 200 nm.

Table 2. Ratios of X/Pb determined via EDX for different evaporation sequences for the perovskite films after annealing. X corresponds to I for sequences resulting in (Cs, FA)PbI$_3$ and represents the sum of I and Br for mixed-halide processes Br-1 and Br-split. Please note that the quantification of the Br halide with EDX exhibits a relatively large experimental error. For a stoichiometric perovskite, an X/Pb ratio of 3 is expected.

Sequence	Materials	X/Pb ratios
A	CsI–FAI–PbI$_2$	3.04
B	PbI$_2$–FAI–CsI	3.08
Br-1	PbBr$_2$–PbI$_2$–FAI–CsI	3.47
Br-split	PbBr$_2$–FAI–CsI–PbI$_2$	3.27

quantify the stoichiometry in our samples. Since the organic components in FAI cannot be quantified well with our EDX system, we use the I/Pb ratio as a manner to quantify the composition. Measurements for sequences A and B are shown in **Table 2**. The sample from sequence A exhibits a near-perovskite stoichiometry, in good agreement with the XRD results.

The SEM image of sequence B in Figure 3b depicts a bulk with visibly larger crystallites compared to A, while exhibiting a thin, separated layer close to the substrate. As this layer appears brighter in the SEM image, we assume that it is PbI$_2$ rich. Therefore, the unreacted crystalline PbI$_2$, observed by XRD, is located at the NiO interface, as one could expect from the evaporation sequence. Similar to sequence A, the EDX measurements in Table 2 show a near-perovskite stoichiometry. Considering the PbI$_2$ at the bottom and the I/Pb ratio of 3, this suggests some remaining unreacted FAI and CsI resulting from lack of

diffusion. Noticeably, no voids are visible at the NiO interface, supporting the idea of an A cation-dominated diffusion.

2.4. Precursor Order III: PbI$_2$ at the Top and at the Bottom (Sequence with Split PbI$_2$)

To investigate the A cation diffusion behavior more deeply and in an attempt to achieve a more homogeneous film formation, we tested splitting the evaporated PbI$_2$ layer and depositing different shares x (and $1-x$) of PbI$_2$ first (and last): (x)PbI$_2$–FAI–CsI–($1-x$)PbI$_2$. We achieved a full reaction to the perovskite α phase with $x = 10\%$, 30%, 50%, and 70% according to XRD (Figure S5–S7, Supporting Information). However, we were not able to suppress the void formation, as long as part of the PbI$_2$ was evaporated last. Instead, the position of the voids moved upward in the perovskite layer with increasing x. As can be seen in the respective SEM images (Figure 3c–f), the voids mark the position of the FAI layer prior to annealing.

2.5. Modifications of Sequence B (PbI$_2$ First)

So far it was found that sequences A and precursor order III caused void formation and can therefore lead to mechanical destabilization of the layer. Consequently, we explored several modified paths for sequence B to achieve full conversion to the perovskite phase. To drive the conversion of the residual, unreacted PbI$_2$ in sequence B, we I) supplied an os amount of FAI, II) used cooled ($-30\,°C$) and heated (100, 170 °C) substrates only during PbI$_2$ deposition to benignly alter the PbI$_2$ properties and (III) employed the spin-coating technique to fabricate a completely different PbI$_2$. A schematic overview of the modifications is provided in **Figure 4**.

I: oversupply FAI (Bos)   overs. FAI (Bpost)   II: $T_{Substrate}$ during PbI_2 III: spin-coated PbI_2
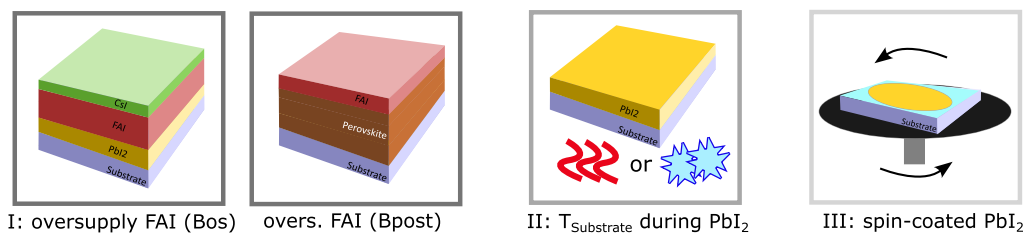
Figure 4. Schematic overview of modifications of sequence B (PbI_2 first). From left to right: I: oversupply of FAI during deposition (Bos) or as a post treatment (Bpost); II: substrate temperature during PbI_2 deposition; and III: spin-coated PbI_2.

2.5.1. I: Oversupply of FAI

To provide an oversupply of FAI, we deposited the full PbI_2 layer first, but drove further reaction either by directly evaporating an os amount of FAI in the sequence Bos: PbI_2–(os)FAI–CsI or by post depositing additional FAI in the sequence Bpost: PbI_2–FAI–CsI–(post)FAI. Both modifications successfully lead to a full conversion of the layer to the α perovskite phase, as can be seen in Figure S8 (Supporting Information). In the cross-sectional SEM images of Bos and Bpost (Figure S9, Supporting Information), the layer stack is fully reacted. We observe a dependence of the crystallite size on the position in the layer, with larger grains toward the top. This is assumed to be related to a stoichiometry gradient in the layer. As has been shown previously, a larger concentration of A cations can lead to an increase in crystallite size.[34–36] Additionally, the pinholes in the top layer caused by the electron beam point to an organic-rich stoichiometry. Therefore, we assume that the reaction in our layers is still diffusion-limited and the FAI is not distributed completely homogeneously.

2.5.2. II: Substrate Temperature during PbI_2 Deposition

In our evaporation process, PbI_2 tends to grow with weak preferential orientation and in a porous manner (SEM cross section in Figure S10, Supporting Information). Similar behavior was observed by other groups by growth of porous, polycrystalline PbI_2 films with small crystallite sizes.[24,37,38] Other publications have shown that PbI_2 can be evaporated as a compact layer with strong preferential orientation[6] and low roughness.[15] In an attempt to ameliorate the PbI_2 properties for the diffusion reaction process, we deposited PbI_2 at different substrate temperatures (−30, 100, and 170 °C; SEM in Figure S11, Supporting Information). Both heating and cooling resulted in strongly 2H-dominated growth modes of PbI_2. However, none of the layer stacks were fully converted to the perovskite phase, even though the PbI_2 morphology and texture was strongly altered (Figure S12 and S13, Supporting Information). So far, only sequence A and the processes with split PbI_2 resulted in fully converted layers without excess A cations. All of these exhibit 6R growth giving rise to the idea that the diffusion–reaction kinetics of the perovskite conversion benefit from the presence of this PbI_2 species.

2.5.3. III: Spin-Coated PbI_2

In an additional experiment, we first spin-coated a layer of PbI_2 and achieved a more homogeneous, smooth PbI_2 growth (SEM

cross section in Figure S14, Supporting Information). For this sample, high-intensity perovskite peaks appear already during evaporation of FAI and CsI. Here, the perovskite peaks during evaporation are much larger than for evaporated PbI_2 in sequence B. Subsequently, we observe a clear $(Cs, FA)PbI_3$ (100) peak shift during evaporation of CsI (Figure S15, Supporting Information). In the SEM cross section of the finished layer, large columnar perovskite crystallites can be seen (Figure S16, Supporting Information). In contrast to the previous attempts with evaporated PbI_2, here the perovskite crystallites stretch through the full layer. The qualities of an evaporated PbI_2 precursor could potentially be improved by co-evaporating CsBr or $PbCl_2$ and CsI, as has been successful in other works.[15,39] Further ideas will be touched upon in the discussion section. We conclude that the PbI_2 morphology strongly impacts the reaction and diffusion dynamics of the perovskite conversion. The results with spin-coated PbI_2 show that the A cations' diffusion–leading to perovskite conversion–can be optimized and a compact PbI_2 host structure can be beneficial for the transport and diffusion of the FAI.

2.6. Mixed I/Br Perovskites

Halide diffusion is a relevant aspect when preparing homogeneously mixed perovskite $(Cs, FA)Pb(I, Br)_3$ and ensuring the stability of a single stable phase. We prepared mixed I/Br perovskite compositions in two different sets of evaporation sequences (see Table 2).

2.6.1. Precursor Order I: Lead Halides PbX_2 First (Br-1)

For the sequence Br-1, we evaporated the sequence $PbBr_2$–PbI_2–FAI–CsI. During evaporation, the components crystallize with a strong preferential orientation, as can be seen in the process diagram in **Figure 5**a (Additional Θ–Θ scans in Figure S17, Supporting Information). First, orthorhombic $PbBr_2$ (200), (111), and (220) peaks appear at 22.0°, 22.7°, and 29°, respectively.[40] Upon PbI_2 evaporation, some PbI_2 is incorporated into the $PbBr_2$ structure as we observe in a peak shift of $PbBr_2$ (111) peak by 0.07° (Figure S18, Supporting Information). The $PbBr_2$ incentivizes the PbI_2 to grow only in the 2H phase, as only the correspondent (001) and (002) peaks appear.[33] Peaks corresponding to the 6R polytype do not evolve. We were able to confirm these observations concerning preferential orientation and polytype during evaporation of an additional process, where only $PbBr_2$–PbI_2 were deposited (Figure S19, Supporting
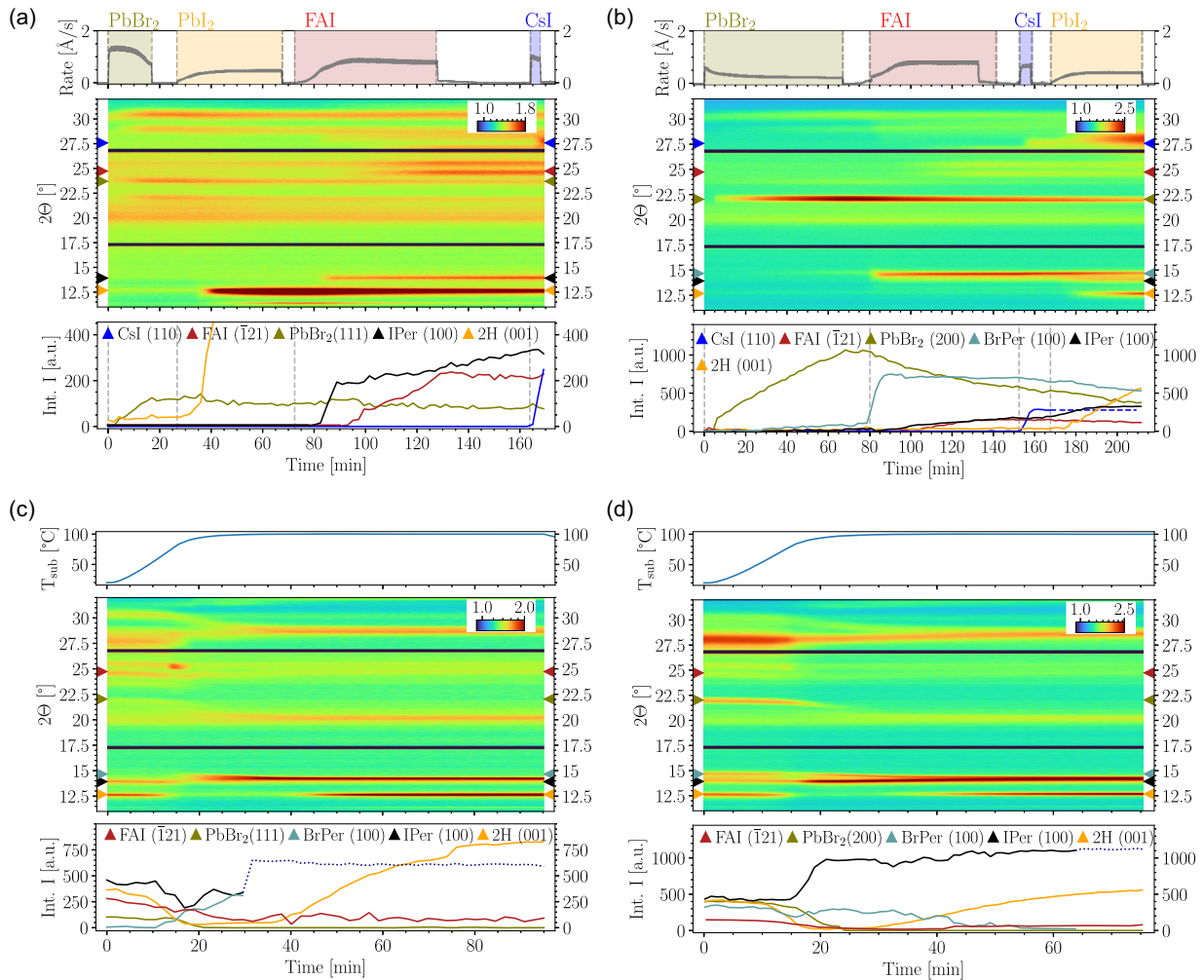
Figure 5. Upper: process diagrams for evaporation of sequences a) Br-1 and b) Br-split including rates during single component deposition (top), in situ XRD color plot (center) and representative peak evaluation (bottom) given as the integrated intensity (Int. I) of each peak over time. Triangles next to the color plot give literature 2Θ positions for the evaluated experimental peaks. In sequence Br-split, CsI (110) Int. I is continued as a dashed line due to superposition with IPer (200) and 6R (104) peaks, both broad near 28°.[25,29,31] Lower: process diagrams for annealing of c) Br-1 and d) Br-split consisting of substrate temperature (top), in situ XRD color plot (center) and Int. I of significant peaks.

Information). In Br-1, the 2H (001) Int. I increases quickly during PbI$_2$ evaporation and decreases upon the subsequent evaporation of the A cations (detailed development shown in Figure S18, Supporting Information). During the FAI-deposition step, I-rich (Cs, FA)Pb(I, Br)$_3$ perovskite (IPer) (100) and (200) peaks are formed first.[31] Subsequently, the monoclinic FAI phase is formed, manifested through the appearance of a double peak at 24.7° and 25.6°.[30] Upon CsI evaporation, we observe no shift in the IPer (100) peak (Figure S20, Supporting Information) and CsI crystallizes, noticeable for example by the cubic phase (110) peak.

During annealing of Br-1 (Figure 5c), the 2H (001) peak is the first to rapidly lose intensity, indicating the commencement of the perovskite formation. After 13 min, FAI ($\bar{1}$21) disappears and 2 min later the perovskite (111) peak at 24.2° takes its place.[31] Also after 13 min, FAI (002) shows an intensity jump,

hinting toward a recrystallization of the FAI in its orthorhombic phase.[30] CsI starts reacting after 17 min at 88 °C, as can be seen from the disappearance of its (110) peak.

All initial peaks exhibit a shift to lower angles due to thermal expansion. However, the PbBr$_2$ (111) peak shifts stronger than expected only from thermal expansion, indicating an incorporation of PbI$_2$ into the lattice (Figure S21 and S22, Supporting Information).[41] After 15 min and at 80 °C, the Br-rich (Cs, FA)Pb(I, Br)$_3$ perovskite phase (BrPer) (100) peak at 14.6° increases at the expense of the IPer (100) peak. Both peaks begin shifting toward each other (Figure S23, Supporting Information) and cannot be distinguished from 30 min onward (dotted line in Figure 5c). Further, BrPer and IPer peaks combine at around 20° and 29°, respectively, indicating that a single mixed perovskite (Cs, FA)Pb(I, Br)$_3$ phase has formed. Up until the end of the annealing, the double halide perovskite (100) intensity declines

**ADVANCED
SCIENCE NEWS**

www.advancedsciencenews.com

pss
physica status solidi a

www.pss-a.com

slowly, while the 2H (100) intensity increases monotonously, indicating a slow recrystallization and/or decomposition process.

2.6.2. Precursor Order II: Lead Halides PbX_2 First and Last (Br-Split)

We then evaporated the sequence Br-split: $PbBr_2$–FAI–CsI–PbI_2 (process diagram in Figure 5b and Θ–Θ scans in Figure S17, Supporting Information). After deposition of $PbBr_2$ and throughout FAI evaporation, both components quickly react to form both BrPer (100) and IPer (100) peaks. Later during FAI evaporation, an unreacted FAI phase forms. In contrast to Br-1, part of the deposited CsI is immediately incorporated into the BrPer phase, as indicated by a BrPer (100) peak shift toward higher angles (Figure S24, Supporting Information). Upon PbI_2 deposition, BrPer and IPer peaks clearly shift away from each other (Figure S24, Supporting Information), while the IPer (100) Int. I benefits from the I-rich evaporation step. After approximately 170 min, the 2H (001) peak evolves and grows quickly. Whether 2H or 6R PbI_2 growth dominates cannot be determined due to superposition of the 6R (104) peak with the perovskite peaks at 28°–29°. While no 6R (101) peak is observed, a strong 2H (001) texture is induced in this sequence, as can be seen by its linear growth in Int. I.

During annealing of Br-split (Figure 5d), a conversion of the precursors to a highly oriented mixed-halide $(Cs, FA)Pb(I, Br)_3$ phase can be observed. After 10 min and at 50 °C, the Int. I of the 2H (001) and $PbBr_2$ (200) peaks begin to decrease. Similar to Br-1, the peaks from both lead halide phases shift due to thermal expansion of the respective lattices and halide mixing (Figure S22, Supporting Information). After 25 min and at 98 °C, they disappear completely. The PbI_2 2H (001) peak returns 5 min later and increases in size until the end of the annealing.

BrPer (100) and IPer (100) peaks shift toward each other starting at 17 min and 70 °C (Figure S25, Supporting Information). The IPer (100) peak is strongly intensified. Both phases cannot be distinguished anymore after 65 min. It should be noted that the combined phase is formed much slower than in the Br-1 evaporation sequence.

The SEM images of Br-split and Br-1 are shown in **Figure 6**. As observed for the sequences with split PbI_2, the deposition of FAI in between the lead halide layers in the sequence Br-split leads to void formation in the final film. In the top-view, unreacted PbI_2 forming island-type structures can be observed. Br-1 shows large crystallites throughout the whole interface and especially at the top. Still, the cross section displays PbI_2 residues at the substrate interface, which was to be expected from the in situ XRD results displayed in Figure 5c.

3. Discussion

We investigated the crystal growth and phase formation during variations of sequential evaporation and annealing processes for the preparation of $(Cs, FA)PbI_3$ and $(Cs, FA)Pb(I, Br)_3$ using in situ XRD.

The approach to deposit A cations first via sequence A, as demonstrated for $(Cs, FA)PbI_3$ in this work, is a novelty in the field of sequential perovskite evaporation. We observed that on top of the CsI/FAI stack, the PbI_2 precursor layer grew in the PbI_2 6R polytype, which, to the best of our knowledge, has not been reported for evaporated perovskite layers so far. Sequence A enabled complete transformation of the stoichiometric precursor layers into the perovskite, but also favored the formation of voids. These are potentially disadvantageous, as they could mechanically destabilize the perovskite layer. We reproduced this behavior in the sequence with split PbI_2, where the voids shifted upward according to the thickness of the first PbI_2 layer and the position of the FAI layer.

In sequence B, we deposited a PbI_2 precursor layer first, which preferentially grew in the 2H polytype, transitioning to 6R later during deposition. We observed a good reactive behavior of the stoichiometric layer stack without void formation, but residual PbI_2 remained at the substrate interface even after prolonged annealing. This could not be avoided even in variations of this precursor sequence, where we deliberately changed the substrate temperature during PbI_2 deposition to see if we could stimulate the growth of PbI_2 with morphologies better suited for the conversion into perovskites. Finally, we were able to achieve full conversion into the perovskite phase for nonstoichiometric samples
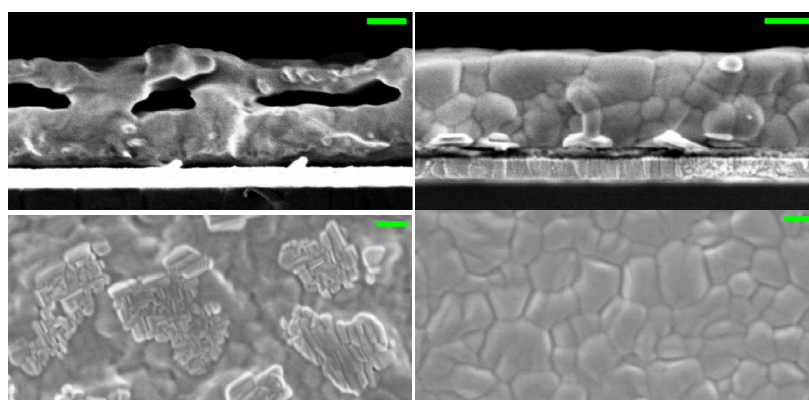
Figure 6. SEM cross sections (top) and top views (bottom) of Br-split (left) and Br-1 (right) after annealing. The green scale bars correspond to 200 nm. Similarly to the processes with split PbI_2, Br-split displays voids from FAI diffusion and PbI_2 as well as $PbBr_2$ fixture. Br-1 exhibits large crystallites and unreacted PbI_2 at the substrate interface.

with the precursor sequence B by evaporating an excess of FAI during the same sequence (Bos) or as a post treatment (Bpost). While this is an interesting way to achieve the full conversion into the perovskite phase (no residual PbI_2), the impact of stoichiometry and precursor morphologies on the opto-electronic properties are still an open question and require further analysis.

3.1. FAI-Dominated Diffusion Leads to Voids

Our results strongly indicate that the reaction between FAI and PbI_2 is dominated by FAI diffusion into the PbI_2 layer. In sequences A and the sequence with split PbI_2, this is clearly visible in the respective SEM images, where the FAI diffusion resulted in voids. Similar to MAI, FAI exhibits Volmer–Weber island growth (Figure S26, Supporting Information and refs. [42–44]). Therefore, the observed voids in sequence A could be explained by PbI_2 pillars growing next to FAI islands, thereby reaching the substrate interface and supporting the upward diffusion behavior of FAI. FAI from the substrate interface could diffuse into the PbI_2 host structure along these pillars, resulting in voids at the substrate interface.

A similar stack to our sequence with split PbI_2 was prepared by Yang et al. They evaporated an alternating sequence $PbCl_2$–MAI–$PbCl_2$–MAI, but did not observe voids in their layer after annealing.[45] Comparing our sequence with split PbI_2 to Yang's work, it seems the A cation growth behavior is not decisive for the success of the diffusion reaction and perovskite transformation, since both MAI and FAI intrinsically exhibit island growth. However, the difference could originate from the properties of the lead halide layer. $PbCl_2$ can grow smoother than PbI_2[44] or reduce roughness in PbI_2 as an additive,[15] possibly enabling a homogeneous reaction along the surface in Yang's work. The PbI_2 evaporated in this work exhibits a rough surface and could amplify the island growth of FAI, resulting in void formation in the final film prepared via the sequence with split PbI_2.

Sequence B is a well-known approach for sequential perovskite deposition. We observed that sequence B provided a less favorable perovskite conversion, making an excess of FAI necessary in the sequences Bos and Bpost to achieve a full conversion of the PbI_2 layer. For $MAPbI_3$, some groups used an excess of A cations to transform the lead halide precursor layer and removed the excess A cation by annealing or washing.[42,46] Sequence B has been used for perovskite device preparation and the effect of excess FAI on the optoelectronic properties has been shown to be advantageous for diodes and solar cells up to a certain excess value.[34,35,47] However, other works have been successful in depositing a stoichiometric layer stack and fully converting it to the perovskite phase. Feng et al. deposited highly textured 2H PbI_2 and addressed underconversion by optimizing the post annealing temperature to drive FAI diffusion.[6] In a noteworthy work, Moser et al. evaporated a PbI_2/CsBr precursor layer and achieved full conversion depositing FAI via chemical vapor deposition (CVD).[39] Very recently, CsBr has been proposed to enhance diffusion and facilitate the full perovskite transformation in sequentially evaporated films.[48] Full reaction was achieved more slowly in thicker layers of up to 400 nm as compared to multiply deposited layer stacks, and it was argued that this is due to diffusion limiting the reaction.[48]

● FAI ● PbI_2 ● CsI ■ Perovskite
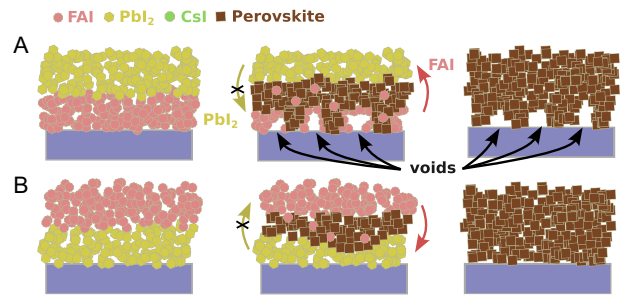
Figure 7. Simplified illustration of the proposed diffusion mechanism in a FAI–PbI_2 layer stack as in sequence A (top row) and a PbI_2–FAI stack as in sequence B (bottom row). CsI is left out for simplicity. The left column presents the initial growth of layers during deposition, the center column illustrates the first reaction between the two layers and the right column shows a fully transformed perovskite layer after, e.g., annealing.

From our work and the aforementioned literature results, we suggest a simple mechanism (**Figure 7**): Upon contacting, FAI and PbI_2 layers react to form the perovskite $FAPbI_3$, through which further FAI components will diffuse due to a concentration gradient and react with the PbI_2 on the other side and so on. This is made possible by the capacity of $FAPbI_3$ to hold and transport excess FAI.[34–36] The PbI_2 provides the host structure for the interdiffusion of FAI and the properties of the PbI_2 host structure are therefore expected to directly influence the diffusion behavior of the FAI. It is unlikely that the FAI diffuses through the PbI_2 without reacting, since the enthalpy of formation of $FAPbI_3$ should be lower than that of its educts.[49,50] CsI diffusion only takes place through already-formed $FAPbI_3$, since CsI and PbI_2 do not interdiffuse or react to $CsPbI_3$, unless 200 °C are applied, as confirmed by annealing of a layer stack in our in situ chamber by us (Figure S27, Supporting Information) and reported elsewhere.[51] This type of diffusion reaction has been termed intercalation for MAI into PbI_2,[52,53] but has not been described as clearly for the FAI into PbI_2 diffusion/reaction process.[6,15,54]

In consequence of the suggested mechanism, in both sequences A and B, the diffusion and conversion into perovskite of the precursor stack depends strongly on the properties and morphology of the PbI_2 precursor, including important factors such as porosity, surface texture, preferential orientation, and polytype (2H or 6R). In the following, we will discuss the impact of these different PbI_2 properties on the reaction behavior of the layer stack.

3.2. PbI_2 Polytypes Influence Perovskite Formation

In our work, the different observed PbI_2 polytypes are expected to impact the diffusion/reaction processes involved in the perovskite conversion. In sequence A, when the PbI_2 was grown on top of the FAI precursor, the A cation precursor strongly promoted the growth of PbI_2 in the 6R polytype. In the sequences with split PbI_2, the 6R growth was also enhanced in comparison to sequence B during evaporation of the second PbI_2 layer, when this contributed 70% and 90% of the total PbI_2. In sequence B, PbI_2 is growing on top of the hole-transport layer (HTL) (NiO),

favoring 2H PbI_2. During conversion, the 6R part of the PbI_2 layer was first converted, while parts of the 2H did not fully react. Obviously, this could be incentivized by the fact that the 6R-rich domain is located on top of the 2H domain (growth only at later process time) and thereby close to the A cation supply. Still, our results indicate that the 6R polytype could be preferable for the perovskite conversion.

The dependence of PbI_2 conversion on the favored polytype is scarcely discussed in perovskite literature, since other polytypes than 2H are rarely observed. Dhamaniya et al. use a solution additive to fabricate a PbI_2 precursor layer with similar structure as the 6R polytype observed in our work.[55] They observe faster perovskite conversion during wet-chemical treatment and attribute this to higher porosity, surface roughness, and surface area of the new structure. Malevu et al. compare the influence of PbI_2 6R and 12R precursors on final perovskite device efficiency, but don't include the most common 2H polytype and their structural observations are limited.[56] To the best of our knowledge, no other reports exist investigating other PbI_2 polytypes than 2H for sequential deposition, not to mention evaporation.

In our experiments, the preferential orientation of the 6R polytype did not seem to play a role, since (101) favored growth dominated in sequence A, while (104) dominated in the sequence with split PbI_2 and both enabled fully converted layer stacks. In sequence B, weakly oriented 2H PbI_2 remained partially unconverted, while strongly oriented spin-coated 2H PbI_2 enabled good conversion. Still, evaporated, strongly oriented 2H PbI_2 did not enable full conversion as we showed by deposition of PbI_2 at different substrate temperatures. Other works have concluded orientational properties of the precursor layer to be a decisive factor for conversion. For $(Cs, FA)PbI_3$, a highly textured PbI_2 precursor layer was fabricated by Li et al, which included $PbCl_2$ and CsI to enable an isotropic growth of the precursor and full perovskite conversion.[15] Another group used a vapor treatment to promote face-up orientation of the PbI_6^{4-} octahedra to enhance diffusion of MAI and conversion of PbI_2 to $MAPbI_3$.[38] Possibly, the influence of orientation on perovskite conversion is stronger for the 2H than for the 6R polytype.

We observed full conversion to the perovskite phase for both 2H and 6R polytypes in different preferential orientations. Thus, we suspect PbI_2 porosity to also play a role in the diffusion reaction. In sequence B, porosity could inhibit FAI diffusion into the PbI_2 by forming diffusion bottle necks or promoting Volmer–Weber island growth of the FAI. In sequence A, the predeposited FAI layer could suppress island growth of the PbI_2 and enable more homogeneous Stranski–Krastanov layer-plus-island or even Frank–van der Merwe layer-by-layer PbI_2 growth, resulting in a more compact structure for further reaction.

Several works have shown porosity of the PbI_2 precursor plays a role in two-step spin-coating, where a porous layer is mainly seen as an advantage for easier infiltration by the organic cation solution.[21,57–59] Astonishingly in blade-coating, compactness has been observed to be more favorable for conversion.[60] However, porosity versus compactness is a blank slate in the field of sequential evaporation and uniform quantification is needed. We strongly encourage further research in this direction, since porosity could be a major difference maker, as it has proven to be for wet-chemical sequential deposition processing. One option to potentially improve the compactness of the evaporated lead halide layers that we currently contemplate is the evaporation of small amounts $PbCl_2$ in the future.

3.3. Halide Exchange in Mixed-Halide Layer Stacks

Next, we investigated two mixed-halide sequences. We showed that both Br-1 and Br-split sequences yield a single mixed-halide perovskite $(Cs, FA)Pb(I, Br)_3$ phase.

Both processes exhibited two I-/Br-rich perovskite phases that combined during annealing. Interestingly, the halide exchange reaction between these initial perovskite phases exhibited different speeds for both sequences. When the A cations were between $PbBr_2$ and PbI_2 in Br-split, Br-rich, and I-rich perovskite phases already formed during evaporation and coexisted significantly longer during annealing compared to Br-1. In Br-1, $PbBr_2$ and PbI_2 were located adjacent to each other and only an I-rich perovskite phase was observed during evaporation. During annealing, a Br-rich phase formed briefly, but quickly combined with the I-rich phase to form a single perovskite phase. We suspect this to be caused by the low thickness of the initial Br-rich layer, since the perovskite phase is not in direct contact with the $PbBr_2$, which provides Br to the perovskite. During annealing of Br-1, $PbBr_2$ exchanges Br^- ions with I^- ions, enriching the perovskite phase with Br and rendering a segregated PbI_2 phase in the final film.

In Br-split in contrast, the two initial perovskite phases combined comparably slowly. Therefore, it seems that less energy is needed to incorporate Br into an existing I-rich perovskite lattice, than to combine Br- and I-rich perovskite phases. This makes sense, since, in Br-split, both Br^- and the larger I^- ions have to diffuse through the perovskite, whereas this was only Br^- in sequence Br-1. This is supported by previous results, according to which the conversion from $MAPbI_3$ to $MAPbBr_3$ is energetically easier than the opposite direction.[61] Additionally, the diffusion coefficients of Br^- ions in $MAPbI_3$ were found to be an order of magnitude larger than for I^- ions in $MAPbBr_3$,[62] adding to the idea that the diffusion of I^- ions slows down the formation of the mixed-halide perovskite in Br-1.

3.4. Absence of δ Phase

In this work in general, we did not once observe a $FAPbI_3$ δ phase during growth and annealing of our layers using in situ XRD. Feng et al. showed similar results, but do not discuss this effect.[6] However, the δ phase is the preferred configuration at room temperature and is usually reported to form during co-evaporation, requiring a hot annealing step at 145–170 °C for the conversion into the α phase.[11,63–65] By employing sequential evaporation and avoiding δ phase formation in the first place, the annealing temperature could be reduced to 100 °C in our work and even 80 °C in others.[6] This could even be further optimized by creating optimal diffusion reaction conditions through precursor engineering.[15,44] At first glance, the favored α phase growth could be an intrinsic effect of the diffusion reaction, requiring less energy to transform hexagonal PbI_2 to the cubic perovskite phase than the δ phase, even though the latter is also hexagonal. Nonetheless, we speculate that this behavior is incentivized by

the diffusion limitation of FAI into PbI_2 at room temperature, but not into $FAPbI_3$. It follows, that an excess of FAI is present at the interface and during initial perovskite formation, favoring the α phase.[34–36,65] Still, several open questions in this regard remain, and we hope that this work encourages further investigation in this line.

4. Conclusion

We have prepared $(Cs, FA)PbX_3$ perovskite layers using a scarcely explored deposition process via sequential thermal evaporation and annealing in a vacuum chamber. This processing route enables ease of scalability and a well-defined stoichiometry control, because the thickness of each individual component can be determined individually. We tested different precursor orders, ratios, and deposition conditions to study their impact on the perovskite conversion dynamics. We observe a barely known PbI_2 6R polytype, and found that this polytype might enhance the conversion. We used in situ XRD to monitor the phase evolution of perovskite components CsI, FAI, PbI_2, and $PbBr_2$ during deposition at room temperature and post annealing at 100 °C.

For $(Cs, FA)PbI_3$, we focused on two sequences: PbI_2–FAI–CsI (sequence A) and CsI–FAI–PbI_2 (sequence B). In sequence A, PbI_2 grew mainly in its 6R polytype and the stoichiometric layer was fully converted to the perovskite α phase after annealing. However, in the SEM images, we observed voids at the interface to the substrate. Further, when we evaporated different shares of PbI_2 as first and last layers, respectively, we observed void formation at different positions in the stoichiometric layer according to the position of the FAI precursor. In sequence B, PbI_2 growth was dominated by its 2H polytype and void formation did not occur. However, the stoichiometric layer could not be fully converted to the perovskite phase during annealing, unless we deposited an os amount of FAI during the sequence or post deposition.

From the void formation, we deduce that it is FAI that dominantly diffuses into the PbI_2, while PbI_2 mainly remains at its initial location. CsI will then diffuse into the perovskite lattice. It follows that FAI diffusion and perovskite formation strongly depend on the layer properties and morphology of PbI_2 precursor. Although we cannot pinpoint one decisive property to influence the strong difference in diffusion and reaction behavior in sequences A and B, we assign it to a combination of PbI_2 polytype, (surface) orientation, roughness, and porosity and strongly encourage further research in this direction.

For the deposition of $(Cs, FA)Pb(I, Br)_3$, we investigated two evaporation sequences: $PbBr_2$–PbI_2–FAI–CsI (Br-1) and $PbBr_2$–FAI–CsI–PbI_2 (Br-split). During evaporation, we observed the formation of an I-rich perovskite phase in Br-1, but in total two distinct perovskite phases (I-rich and Br-rich) in Br-split. This resulted in a much faster transition to a single mixed-halide phase in Br-1 compared to Br-split. We relate this to the sterically favored integration of Br^- ions into the I-rich lattice in Br-1, compared to the integration of I^- ions into the Br-rich lattice as in the Br-split experiment.

Astonishingly, we observed no δ phase in all samples throughout sequential evaporation at room temperature and annealing. Therefore, no additional thermal energy is needed to induce the phase transformation from δ to α phase. Consequently,

compared to co-evaporation, a far lower annealing temperature is needed for the perovskite formation, which, in combination with the simplified process control, might provide an important asset in large-scale industrial processing, making sequential evaporation a promising path for further research.

5. Experimental Section

Substrates: We used commercial glass substrates coated with ITO (15 Ωsq, provided by Kintec). Cleaning was done in an ultrasonic bath, subsequently in water with 1% EMAG EM-080 cleaning soap, isopropyl alcohol (IPA), and acetone for 15 min each. For sequences A and B, to produce conditions for perovskite growth on an HTL, a 25 nm thick NiO layer was deposited via e-beam evaporation. Due to an adjustment in process conduct, instead of NiO, Poly(triaryl amine) or Poly[bis (4-phenyl)(2,4,6-trimethylphenyl)amine] (PTAA) was spin-coated from a 5 mg ml⁻¹ solution in toluene with 2,3,5,6-tetrafluoro-7,7,8,8-tetracyano-quinodimethane doping for all other samples. After HTL deposition, the samples were transferred to a glove box attached to the in situ evaporation chamber, in which the perovskite layers were evaporated.

Perovskite Deposition: The evaporated materials CsI, PbI_2 (both 99.999%, Thermo Scientific), FAI (>99.5%, Ossila), and $PbBr_2$ (99.999%, Sigma) were handled in a glove box attached to the evaporation chamber and used as received. We sequentially deposited perovskite layers via thermal evaporation. CsI, FAI, PbI_2, and $PbBr_2$ were deposited at 0.5–1, 0.8–1.6, 0.5–1.6, and $0.7 - 1.2 Ås^{-1}$, respectively. For sequences A, processes with split PbI_2 and B the CsI, FAI, and PbI_2 thicknesses were 21, 224, and 261 nm, resulting in a final nominal composition of $(Cs_{0.1}FA_{0.9})PbI_3$ with a theoretical bandgap energy of 1.5 eV.[66] When preparing I/Br mixed-halide layers, CsI and FAI thicknesses were kept the same and 115 nm of $PbBr_2$ and 106 nm of PbI_2 were evaporated yielding the final nominal composition $(Cs_{0.1}FA_{0.9})Pb(I_{0.6}Br_{0.4})_3$ with a theoretical bandgap energy of 1.72 eV.[66] Thicknesses were monitored using a quartz crystal microbalance. The base pressure of the system was $3 - 4 \cdot 10^{-5}$ mbar owing to the Kapton windows that allow a transmission of X-rays for the in situ XRD measurement. The chamber pressure was monitored with an Edwards WRGS-NW35 wide range gauge and increased to up to 1×10^{-4} mbar during the processes due to thermal radiation of the heated material sources.

XRD Measurement: During evaporation, XRD was measured in situ through exchangeable Kapton windows in the walls of the evaporation chamber. We used Cu-K$_\alpha$ radiation with a wavelength of 1.54Å generated at 1.4 kW (35 kV, 40 mA). A linear detector consisting of three Dectris Mythen 1 K modules enabled the measurement of a 28° angular 2Θ range. This was set from 8° to 36° during our experiments. The occurring K$^\beta$ radiation was attenuated by a Ni filter to 5% of the K$^\alpha$ intensity. Using the same setup, we measured Θ–Θ scans from 10° to 50°. Peak fitting for calculation of the integrated peak area (Int. I) was performed with PDXL version 2.8.1.1 by Rigaku Inc., using a split pseudo-Voigt peak fit.

Film Characterization: SEM was measured using a Zeiss Supra 40 VP. Cross section and top-view images were taken at 1–3 kV employing a secondary electron in-lens detector. In the same SEM, we used a Bruker detector with the EDX analysis program ESPRIT. EDX measurements were done at 10 kV, a working distance of 8 mm, and a magnification of 500. For quantification, Pb M-lines and I, Br, and Cs L-lines were used. A standardless peak to background (P/B) Z-atomic number, A-absorption correction factor, F-fluorescence correction factor (ZAF) fitting was applied for background correction.

Supporting Information

Supporting Information is available from the Wiley Online Library or from the author.

Acknowledgements

Conflict of Interest

The authors declare no conflict of interest.

Author Contributions

K.H. and T.S. equally contributed to this work. K.H., T.S., and P.P. developed the experimental procedure. P.P guided the scientific progress. K.H. and T.S. deposited the thin films, and conducted and evaluated the experiments. K.H., T.S., P.P., and R.S. discussed and interpreted the results. K.H. wrote the main part of the manuscript.

Keywords

[1] M. A. Green, E. D. Dunlop, M. Yoshita, N. Kopidakis, K. Bothe, G. Siefer, X. Hao, *Prog. Photovolt.: Res. Appl.* **2023**, *31*, 651.

[2] NREL, Best Research-Cell Efficiency Chart, **2023** https://www.nrel.gov/pv/cell-efficiency.html.

[3] J. Wu, X. Xu, Y. Zhao, J. Shi, Y. Xu, Y. Luo, D. Li, H. Wu, Q. Meng, *ACS Appl. Mater. Interfaces* **2017**, *9*, 26937.

[4] Y. Zhang, M. Chen, Y. Zhou, W. Li, Y. Lee, H. Kanda, X.-X. Gao, R. Hu, K. G. Brooks, R. Zia, S. Kinge, N. P. Padture, M. K. Nazeeruddin, *Adv. Energy Mater.* **2020**, *10*, 2001300.

[5] R. Vidal, J.-A. Alberola-Borràs, S. N. Habisreutinger, J.-L. Gimeno-Molina, D. T. Moore, T. H. Schloemer, I. Mora-Seró, J. J. Berry, J. M. Luther, *Nat. Sustain.* **2021**, *4*, 277.

[6] J. Feng, Y. Jiao, H. Wang, X. Zhu, Y. Sun, M. Du, Y. Cao, D. Yang, S. F. Liu, *Energy Environ. Sci.* **2021**, *14*, 3035.

[7] S. Wang, X. Li, J. Wu, W. Wen, Y. Qi, *Curr. Opin. Electrochem.* **2018**, *11*, 130.

[8] J. Ávila, C. Momblona, P. P. Boix, M. Sessolo, H. J. Bolink, *Joule* **2017**, *1*, 431.

[9] J. Li, H. Wang, X. Y. Chin, H. A. Dewi, K. Vergeer, T. W. Goh, J. W. M. Lim, J. H. Lew, K. P. Loh, C. Soci, T. C. Sum, H. J. Bolink, N. Mathews, S. Mhaisalkar, A. Bruno, *Joule* **2020**, *4*, 1035.

[10] K. Hamada, K. Yonezawa, K. Yamamoto, T. Taima, S. Hayase, N. Ooyagi, Y. Yamamoto, K. Ohdaira, *Jpn. J. Appl. Phys.* **2019**, *58*, SB SBBF06.

[11] J. Borchert, R. L. Milot, J. B. Patel, C. L. Davies, A. D. Wright, L. Martínez Maestro, H. J. Snaith, L. M. Herz, M. B. Johnston, *ACS Energy Lett.* **2017**, *2*, 2799.

[12] G. Nogay, F. Sahli, J. Werner, R. Monnard, M. Boccard, M. Despeisse, F.-J. Haug, Q. Jeangros, A. Ingenito, C. Ballif, *ACS Energy Lett.* **2019**, *4*, 844.

[13] M. Kam, Y. Zhu, D. Zhang, L. Gu, J. Chen, Z. Fan, *Sol. RRL* **2019**, *3*, 1900050.

[14] S. Wang, L. Tan, J. Zhou, M. Li, X. Zhao, H. Li, W. Tress, L. Ding, M. Graetzel, C. Yi, *Joule* **2022**, *6*, 1344.

[15] H. Li, J. Zhou, L. Tan, M. Li, C. Jiang, S. Wang, X. Zhao, Y. Liu, Y. Zhang, Y. Ye, W. Tress, C. Yi, *Sci. Adv.* **2022**, *8*, 28.

[16] Z. Zhou, J. Liang, Z. Zhang, Y. Zheng, X. Wu, C. Tian, Y. Huang, J. Wang, Y. Yang, A. Sun, Z. Chen, C.-C. Chen, *ACS Appl. Mater. Interfaces* **2022**, *14*, 49886.

[17] M. F. Mohamad Noh, N. A. Arzaee, I. N. Nawas Mumthas, A. Aadenan, H. Alessa, M. N. Alghamdi, H. Moria, N. A. Mohamed, A. R. B. Mohd Yusoff, M. A. Mat Teridi, *Electrochim. Acta* **2022**, *402*, 139530.

[18] Y. Xiang, Z. Ma, Y. Huang, W. Zhang, C. Peng, H. Li, *ACS Appl. Energy Mater.* **2021**, *4*, 12091.

[19] D. Huang, Q. Liu, Z. Ma, Y. Li, G. Yan, S. Hou, Z. Du, J. Yang, Y. Chen, S. Tang, H. Zhou, Y. Xiang, W. Zhang, Y. Huang, Y. Mai, *Sci. China Mater.* **2023**, *66*, 1313.

[20] Y. Yun Kim, E. Young Park, T.-Y. Yang, J. Hong Noh, T. Joo Shin, N. Joong Jeon, J. Seo, *J. Mater. Chem. A* **2018**, *6*, 12447.

[21] J.-J. Yan, Y. Li, Y. Chang, P. Jiang, C.-W. Wang, *Superlattices Microstruct.* **2016**, *94*, 196.

[22] Y. Wu, A. Islam, X. Yang, C. Qin, J. Liu, K. Zhang, W. Peng, L. Han, *Energy Environ. Sci.* **2014**, *7*, 2934.

[23] J. Burschka, N. Pellet, S.-J. Moon, R. Humphry-Baker, P. Gao, M. K. Nazeeruddin, M. Grätzel, *Nature* **2013**, *499*, 316.

[24] M. T. Hoerantner, E. L. Wassweiler, H. Zhang, A. Panda, M. Nasilowski, A. Osherov, R. Swartwout, A. E. Driscoll, N. S. Moody, M. G. Bawendi, K. F. Jensen, V. Bulović, *ACS Appl. Mater. Interfaces* **2019**, *11*, 32928.

[25] R. S. Mitchell, *Z. für Krist. – Cryst. Mater.* **1959**, *111*, 372.

[26] C. Eames, J. M. Frost, P. R. F. Barnes, B. C. O'Regan, A. Walsh, M. S. Islam, *Nat. Commun.* **2015**, *6*, 7497.

[27] G. Kaune, S. Hartnauer, R. Scheer, *Phys. Status Solidi A* **2014**, *211*, 1991.

[28] N. Nadaud, N. Lequeux, M. Nanot, J. Jové, T. Roisnel, *J. Solid State Chem.* **1998**, *135*, 140.

[29] I. V. Aleksandrov, A. F. Goncharov, I. N. Makarenko, S. M. Stishov, *Phys. Rev. B* **1991**, *43*, 6194.

[30] A. A. Petrov, E. A. Goodilin, A. B. Tarasov, V. A. Lazarenko, P. V. Dorovatovskii, V. N. Khrustalev, *Acta Crystallogr. Sect. E: Crystallogr. Commun.* **2017**, *73*, 569.

[31] D. H. Fabini, C. C. Stoumpos, G. Laurita, A. Kaltzoglou, A. G. Kontos, P. Falaras, M. G. Kanatzidis, R. Seshadri, *Angew. Chem.* **2016**, *128*, 15618.

[32] C. C. Stoumpos, C. D. Malliakas, M. G. Kanatzidis, *Inorg. Chem.* **2013**, *52*, 9019.

[33] T. Minagawa, *Acta Crystallogr. Sect. A: Cryst. Phys. Diffract. Theoret. Gen. Crystallogr.* **1975**, *31*, 823.

[34] F. Ma, J. Li, W. Li, N. Lin, L. Wang, J. Qiao, *Chem. Sci.* **2017**, *8*, 800.

[35] Z. Yuan, Y. Miao, Z. Hu, W. Xu, C. Kuang, K. Pan, P. Liu, J. Lai, B. Sun, J. Wang, S. Bai, F. Gao, *Nat. Commun.* **2019**, *10*, 2818.

[36] K. L. Heinze, P. Wessel, M. Mauer, R. Scheer, P. Pistor, *Mater. Adv.* **2022**, *3*, 8695.

[37] J. Fang, D. Lin, W. Huang, X. Wang, H. Li, S. Li, G. Xie, D. Wang, L. Qiu, *J. Alloys Compd.* **2023**, *955*, 170255.

[38] Z. Li, J. Li, H. Cao, Y. Qian, J. Zhai, Y. Qiu, L. Yang, S. Yin, *ACS Appl. Mater. Interfaces* **2021**, *13*, 45496.

[39] T. Moser, K. Artuk, Y. Jiang, T. Feurer, E. Gilshtein, A. N. Tiwari, F. Fu, *J. Mater. Chem. A* **2020**, *8*, 21973.

[40] H. E. Swanson, E. Tatge, *Natl. Bur. Stand. U.S.A.* **1953**, *2*, 44.

[41] S. I. Levkovets, O. Y. Khyzhun, G. L. Myronchuk, P. M. Fochuk, M. Piasecki, I. V. Kityk, A. O. Fedorchuk, V. I. Levkovets, L. V. Piskach, O. V. Parasyuk, *J. Electron Spectrosc. Relat. Phenom.* **2017**, *218*, 13.

[42] Q. Guesnay, F. Sahli, C. Ballif, Q. Jeangros, *APL Mater.* **2021**, *9*, 100703.

[43] E. S. Parrott, J. B. Patel, A.-A. Haghighirad, H. J. Snaith, M. B. Johnston, L. M. Herz, *Nanoscale* **2019**, *11*, 14276.

[44] S. Wang, L. K. Ono, M. R. Leyden, Y. Kato, S. R. Raga, M. V. Lee, Y. Qi, *J. Mater. Chem. A* **2015**, *3*, 14631.

[45] D. Yang, Z. Yang, W. Qin, Y. Zhang, S. F. Liu, C. Li, *J. Mater. Chem. A* **2015**, *3*, 9401.

[46] G. Li, J. Y. L. Ho, M. Wong, H.-S. Kwok, *Phys. Status Solidi – Rapid Res. Lett.* **2016**, *10*, 153.

[47] R. Ji, Z. Zhang, C. Cho, Q. An, F. Paulus, M. Kroll, M. Löffler, F. Nehm, B. Rellinghaus, K. Leo, Y. Vaynzof, *J. Mater. Chem. C* **2020**, *8*, 7725.

[48] J. Yan, J. Zhao, H. Wang, M. Kerklaan, L. J. Bannenberg, B. Ibrahim, T. J. Savenije, L. Mazzarella, O. Isabella, *ACS Appl. Energy Mater.* **2023**, *6*, 10265.

[49] I. L. Ivanov, A. S. Steparuk, M. S. Bolyachkina, D. S. Tsvetkov, A. P. Safronov, A. Y. Zuev, *J. Chem. Thermodyn.* **2018**, *116*, 253.

[50] A. Luongo, B. Brunetti, S. Vecchio Ciprioti, A. Ciccioli, A. Latini, *J. Phys. Chem. C* **2021**, *125*, 21851.

[51] K. Yonezawa, K. Yamamoto, M. Shahiduzzaman, Y. Furumoto, K. Hamada, T. S. Ripolles, M. Karakawa, T. Kuwabara, K. Takahashi, S. Hayase, T. Taima, *Jpn. J. Appl. Phys.* **2017**, *56*, 04CS11.

[52] M. Shahiduzzaman, K. Yonezawa, K. Yamamoto, T. S. Ripolles, M. Karakawa, T. Kuwabara, K. Takahashi, S. Hayase, T. Taima, *ACS Omega* **2017**, *2*, 4464.

[53] S. Ngqoloda, C. J. Arendse, T. F. Muller, P. F. Miceli, S. Guha, L. Mostert, C. J. Oliphant, *ACS Appl. Energy Mater.* **2020**, *3*, 2350.

[54] Y. Wang, L. Duan, M. Zhang, Z. Hameiri, X. Liu, Y. Bai, X. Hao, *Sol. RRL* **2022**, *6*, 2200234.

[55] B. P. Dhamaniya, P. Chhillar, A. Kumar, K. Chandratre, S. Mahato, K. P. Ganesan, S. K. Pathak, *ACS Omega* **2020**, *5*, 31180.

[56] T. D. Malevu, B. S. Mwankemwa, K. G. Tshabalala, M. Diale, R. O. Ocaya, *J. Mater. Sci.: Mater. Electron.* **2018**, *29*, 13011.

[57] N. Li, Z. Zhu, C.-C. Chueh, H. Liu, B. Peng, A. Petrone, X. Li, L. Wang, A. K.-Y. Jen, *Adv. Energy Mater.* **2017**, *7*, 1601307.

[58] H. A. Abbas, R. Kottokkaran, B. Ganapathy, M. Samiee, L. Zhang, A. Kitahara, M. Noack, V. L. Dalal, *APL Mater.* **2015**, *3*, 016105.

[59] A. Liu, K. Liu, H. Zhou, H. Li, X. Qiu, Y. Yang, M. Liu, *Sci. Bull.* **2018**, *63*, 1591.

[60] S. Razza, F. Di Giacomo, F. Matteocci, L. Cinà, A. L. Palma, S. Casaluci, P. Cameron, A. D'Epifanio, S. Licoccia, A. Reale, T. M. Brown, A. Di Carlo, *J. Power Sources* **2015**, *277*, 286.

[61] P. Pistor, T. Burwig, C. Brzuska, B. Weber, W. Fränzel, *J. Mater. Chem. A* **2018**, *6*, 11496.

[62] A. Osherov, Y. Feldman, I. Kaplan-Ashiri, D. Cahen, G. Hodes, *Chem. Mater.* **2020**, *32*, 4223.

[63] Y. Huang, X. Lei, T. He, Y. Jiang, M. Yuan, *Adv. Energy Mater.* **2022**, *12*, 2100690.

[64] M. U. Rothmann, J. S. Kim, J. Borchert, K. B. Lohmann, C. M. O'Leary, A. A. Sheader, L. Clark, H. J. Snaith, M. B. Johnston, P. D. Nellist, L. M. Herz, *Science* **2020**, *370*, 6516.

[65] M. Roß, S. Severin, M. B. Stutz, P. Wagner, H. Köbler, M. Favin-Lévêque, A. Al-Ashouri, P. Korb, P. Tockhorn, A. Abate, B. Stannowski, B. Rech, S. Albrecht, *Adv. Energy Mater.* **2021**, *11*, 2101460.

[66] D. P. McMeekin, G. Sadoughi, W. Rehman, G. E. Eperon, M. Saliba, M. T. Hörantner, A. Haghighirad, N. Sakai, L. Korte, B. Rech, M. B. Johnston, L. M. Herz, H. J. Snaith, *Science* **2016**, *351*, 151.

[67] F. C. Hanusch, E. Wiesenmayer, E. Mankel, A. Binek, P. Angloher, C. Fraunhofer, N. Giesbrecht, J. M. Feckl, W. Jaegermann, D. Johrendt, T. Bein, P. Docampo, *J. Phys. Chem. Lett.* **2014**, *5*, 2791.

Concluding Discussion

A great advantage of sequential evaporation in [H4] is the absence of the δ phase during preparation. FAI and PbI_2 are expected to react immediately forming the perovskite phase close to the interface. The FAI is not transported through the PbI_2, but only through the perovskite. Due to the perovskite's ability to contain excess FAI and allow for its diffusion, the perovskite formation at the interface is postulated to be rich in FAI. As determined in section 4.4, this incentivizes δ phase suppression. Accordingly, a fast diffusion reaction occurs at the beginning due to the large concentration gradient of FAI driving the diffusion through the perovskite structure. Logically, the diffusion is slowed down during the perovskite formation throughout the layer stack since the gradient is flattened. Surprisingly, the observation that the δ phase is intrinsically suppressed during sequential evaporation has not been a topic of discussion, yet, but is confirmed by a recent study by Lin et al. [312].

(Q_3), which adresses the perpetuation of initial perovskite crystallization towards the bulk, should be considered here, since the initial preference to grow in the α phase is perpetuated to later stages of the preparation in [H4]. In addition, it can be speculated that dynamic preparation of absorbers based on $FAPbI_3$ should be conceivable, possibly bearing several advantages compared to co-evaporation: (i) δ phase suppression at lower temperatures similar to sequential evaporation (ii) modification of interface properties by stoichiometric variation (iii) more reliable diffusion reaction to the perovskite phase as during complete sequential evaporation due to the lower thickness of the precursor layers.

Henceforth, thoughts are developed towards the influence of interface stoichiometric and compositional modifications on the PSC performance $[(Q_4)]$. The diffusion limitation of FAI may be expected to induce a gradient in A/B cation ratio, even though this was only suggested by the SEM images for the schemes with overstoichiometric FAI deposition, namely Bos and Bpost in [H4]. Still, e.g. in sequence B (PbI_2-FAI-CsI), the ratio of FAI to PbI_2 may be anticipated to decrease monotonously from the surface to the substrate. It follows that the preparation of layers with modified interfaces or graded absorber layers - as Li et al. have done via co-evaporation for $MAPbI_3$ [40] - may be possible via sequential evaporation by controlling the diffusion. Feng et al. controlled the diffusion reaction of sequentially deposited films via thermal evaporation by varying the post-deposition annealing temperature [220]. Their deposition sequence was PbI_2-FAI-CsI in an *n-i-p* device structure. The optimum annealing temperature was 60°C, minimizing the segregated PbI_2 in the final layer and optimizing optoelectronic properties. Still, residual PbI_2 was observed via XRD (not via SEM) in their optimized absorber and may be attributed to a thin layer at the interface to the ETL due to the sequential process conduct. Therefore, a stoichiometric gradient within their layer is likely to have existed. In a successful work by Wang et al. they employed spin-coated PbI_2 and subsequent evaporation of FAI in an *n-i-p* device for above 24 % efficiency showing a strong signal of residual PbI_2 [186]. For their champion device with an efficiency above 24 % Li et al. evaporated the PbI_2 first (and improved diffusion by co-evaporating a small amount of $PbCl_2$) in a sequential process for devices in the *n-i-p* structure [39]. They optimized the annealing time so that the perovskite's orientation was as homogeneous as possible. Their annealing stretched beyond the full conversion of the layer to the

perovskite phase and ended when the layer again began to decompose, presumably this enabled passivation by the excess PbI_2. Therefore, a grading of their final layer may not be assumed as easily.

To-date, all works investigating sequential evaporation for PSCs evaporate the lead halide first, mostly in an *n-i-p* structure [39, 218, 310–314]. Nonetheless, PSCs based on $FAPbI_3$ have been investigated in the *p-i-n* structure [201] and in a rather successful work by Li et al. they reach 20 % efficiency by enhancing the precursor reaction by vapor-treatment of the PbI_2 precursor [315]. Still, a residual PbI_2 peak is observed in the XRD. Consequently, even though the highest efficiencies for sequentially prepared devices have been achieved in *n-i-p* devices and some evidence exists towards advantageous influence of residual PbI_2 layers at the ETL/perovskite interfaces in the above mentioned works, the influence of interface modification on PSC performance [(Q_4)] should be studied in more detail.

Finally, the diffusion limitations during sequential evaporation [(Q_5)] are studied in [H4] and the formation of a single-phase perovskite thin film from sequentially evaporated precursors is shown via XRD for sequences A and split PbI_2 (PbI_2-FAI-CsI-PbI_2). Nonetheless, the SEM image of sequence A shows crystallites with distinct properties suggesting separated phases in the thin film. The sequence with split PbI_2 allows for full conversion, but enhances the void formation in the layer. From these results and the literature discussed above, sequence B (PbI_2-FAI-CsI) may be the only practical sequence. Even though a full layer conversion proved difficult via sequence B for $(Cs,FA)PbI_3$ in [H4], other groups have succeeded by different variations in their processing scheme as discussed above.

An interesting study published during review of [H4] was performed by Lin et al. on the sequential evaporation of $FAPbI_3$ via sequence B [312]. They found the α phase to hinder the diffusion of FAI and its distribution throughout the layer stack, leaving segregated PbI_2 at the substrate interface. Therefore, a transformation to the δ phase was induced by exposing the layer to high humidity which enabled a complete diffusion reaction of the layer stack, before a final annealing step was performed transforming the layer back to the α phase. The improved diffusion was ascribed to the greater interplanary distance of the face-sharing PbI_6^{4-} octahedra in the δ phase and the reaction between FAI and H_2O, forming FA^+ and I^- [312] which have higher diffusibility compared to FAI [316], consequently lowering the calculated diffusion barrier for FA^+ [312]. Their final optimized devices achieved up to 22 % efficiency in an *n-i-p* structure.

However, other groups have succeeded at preparing high performance PSCs via sequence B modifying only the PbI_2 by incorporating low amounts of CsBr [186, 201], CsI [39] and/or $PbCl_2$ [39, 310], through vapor treatment [315] or by solution-based preparation [186]. Thus, several paths exist towards full transformation to the α phase for layer stacks deposited via sequence B and their individual advantages will have to be determined in future studies.

4.6 Additional Results

4.6.1 Thermal Decomposition of FAPbI₃

Opening Remarks

Few measurements have been conducted to investigate the thermal decomposition behavior of FAPbI$_3$ and the determined values for the activation energy E range from 95 to 115 kJmol^{-1} and the frequency factor A from 7 to 15. This is owed to the application of different preparational methods and heating schemes during decomposition between the previous works [317–319] of which none uses thermal evaporation. To test the limits of FAPbI$_3$ prepared via thermal evaporation and to enable a comparison to the previous work by Burwig et al. [320] FAI and PbI$_2$ are co-evaporated and, among others, several isothermal decomposition experiments are conducted using the *in situ* XRD in [H5].

Closing Discussion

The determined activation energy E=125.1 kJmol^{-1} and frequency factor A=21.1 were used to calculate the rate constant of the thermal decomposition k via the equation $k = A \exp E/RT$ with the temperature T and the universal gas constant R. With this approach, a direct comparison of MAPbI$_3$ and FAPbI$_3$, each prepared as a thin film via co-evaporation and decomposed under vacuum, is enabled and the decomposition temperature of FAPbI$_3$ was found to be higher than for MAPbI$_3$ by about 45°C. Therefore, under operational conditions in a solar cell, at which 85°C can be reached [63,64], FAPbI$_3$ may exhibit significantly higher long-term stability as an absorber compared to MAPbI$_3$.

4.6.2 Co-Evaporated Cs₂AgBiBr₆ Quartenary Perovskite

Opening Remarks

Two relevant drawbacks of perovskites such as MAPbI$_3$ or (Cs,FA)Pb(I,Br)$_3$ are that these compounds contain the toxic element Pb and exhibit limited stability due to their organic components. Therefore, Pb-free inorganic perovskite compounds with band gaps in the visible region could have an advantage. When replacing Pb with Sn, the band gap is slightly lowered and many advantageous properties are preserved, but the Sn^{2+} quickly oxidizes to Sn^{4+}, decomposing the perovskite. The quartenary perovskite Cs$_2$AgBiBr$_6$ has a good stability against moisture, light and heat [321–323] and exhibits a band gap of 1.9 eV, therefore making it potentially interesting in a perovskite solar cell. [H6] investigates the co-evaporation of the quartenary perovskite and its application in solar cells and was presented at the 36th EUPVSEC conference.

Closing Discussion

The presented solar cells made from co-evaporated Cs$_2$AgBiBr$_6$ showed an efficiency of 0.5 % compared to 10 % of MAPbI$_3$ in the same structure. This is attributed to a low short-circuit current density, which has previously been observed in the literature [20, 322, 324]. In a TEM microscopy image the co-evaporated

layers exhibited large voids in the bulk which may be caused by the volatilization of $BiBr_3$ or other growth-related reasons. To exclude the volatilization of $BiBr_3$ the high annealing temperature of 250°C could be optimized. The results in [H6] showcase the possibility and comparable ease to deposit $Cs_2AgBiBr_6$ via co-evaporation, but convincing efficiencies remain absent. However, efficiencies of $Cs_2AgBiBr_6$ solar cells have reached 6.4 % in 2022 by lowering the band gap to 1.64 eV [325], revealing there is still room for improvement in this direction. In addition, the material remains an excellent contender for the application in high energy photon and X-ray detectors [326–328].

4.7 Conclusions and Outlook

This work has provided several novel approaches and results concerning the thermal evaporation of MHPs and contributed towards closing the knowledge gap between solution-based and vapor phase deposition methods. The compositional and stoichiometrical phase space of bulk $MAPbI_3$ and absorbers based on $FAPbI_3$ were explored $[(Q_1)]$. For both materials, excess PbI_2 segregates immediately and excess A-cation species do not crystallize as a separate phase up to very high excess values. For $MAPbI_3$, an increased crystallinity of the 3D tetragonal perovskite phase was observed for PbI_2 rich conditions as well as MAI rich bulk conditions, which may be connected to the influence of the substrate on nucleation behavior. In general, MAI excess is expected to contribute to higher crystallinity with a higher probability. An increasing excess of FAI increasingly promotes the 3D cubic perovskite phase (α phase) while suppressing the non-perovskite hexagonal phase (δ phase) in $FAPbI_3$ at room temperature. However, the observed crystallinity is not the only decisive factor when considering the influence of stoichiometry on PSC performance $[(Q_2)]$. A certain range of MAI/PbI_2 or FAI/PbI_2 ratios situated around the stoichiometric ratio of three seems to exist in which the preparation of high-efficiency PSCs is possible. However, the efficiency rapidly degrades outside of this range for $MAPbI_3$ (extensive experiments for $FAPbI_3$ are missing).

A vital idea introduced within this thesis is the variation of co-evaporation by dynamic processing. The dynamic evaporation approaches pursued in this thesis for $MAPbI_3$ allowed to determine the strong benign effect of seed layers towards bulk crystallization $[(Q_3)]$ and the paramount influence of interface tuning/modification by the pre- and post-evaporation of the components MAI and PbI_2 on PSC performance $[(Q_4)]$. However, the interfacial reaction itself may even play a secondary role, but the self-doping mechanism in perovskites can induce advantageous band bending towards the interfaces that can be exploited.

Finally, the possibilities and limits of sequential evaporation were explored $[(Q_5)]$ and the diffusion mechanism dominated by the FAI in absorbers based on $FAPbI_3$ was showcased by various previously unexplored precursor deposition sequences. Most pivotal, the δ phase was completely absent showing that sequential evaporation clearly favors α phase growth. From the results obtained and discussed in this thesis, the only viable sequence is based on the evaporation of the lead halide first (sequence B), since otherwise mechanically critical voids are generated by the upwards diffusion of the FAI. However, the lead halide layer needs to be prepared or treated in a certain way to allow for a sufficient diffusion reaction in sequence B.

Since perovskites based on $FAPbI_3$ are the current standard, in the future, more effort should be put in researching their preparation via evaporation for efficient upscaling. Abzieher et al. discuss the prospect of vapor phase deposition for industrial scale production of PSCs and find a strong discrepancy between (i) the focus of research facilities on solution-based approaches (over 99 % of publications on PSCs in 2021 have used solution-based approaches) (ii) the high performance of evaporated PSCs compared to the scarce amount of research invested (above 24 % vs. 26.1 % for a solution-based approach [2]) (iii) the well-balanced investments of upcoming industrial PSC producers towards fabrication via solution and vapor deposition techniques and (iv) the heavy focus of established thin

film industry (module and equipment manufacturers) on vapor deposition [329]. In addition, Abzieher et al. strongly encourage research on processing schemes other than co-evaporation such as sequential evaporation to tackle disadvantages exhibited by co-evaporation compared to solution preparation, e.g. small crystallite sizes. Sequential evaporation facilitates good process control by decoupling the monitoring of deposition and film formation. It also offers an alternative crystallization path which may be the reason why it has enabled the highest efficiencies by far out of all vapor phase deposition techniques, mainly by improving the V_{OC} [39].

However, even though (i) the self-doping effect has been observed in FAPbI$_3$ [330] (ii) the sequential deposition approach intrinsically suggests gradients of the AX and BX$_2$ components in the reacted layer (iii) the best results have been obtained in the n-i-p structure which would favor the potential band bending induced by sequence B [39, 186], the advantageous band bending unveiled by dynamic processing [H1, H2] [40, 286] has not been utilized for sequentially evaporated perovskites based on FAPbI$_3$, yet. Therefore, to further improve PSCs prepared via sequential evaporation, the knowledge obtained on interfacial tuning by dynamic processing in this thesis should be considered.
In consequence, several specific suggestions can be made on possible continuations of the work in this thesis:

1. The diffusion behaviour of FAI and PbI$_2$ during sequential evaporation should be quantified further by using different precursors, precursor thicknesses and annealing temperatures. Mixing PbI$_2$ with other precursors (e.g. PbBr$_2$, PbCl$_2$ and/or CsI, CsBr) is expected to yield a significant improvement of the diffusion behavior. In any case, the morphology of the deposited PbX$_2$ precursor layer needs to be controlled in detail.

2. The success that dynamic evaporation has had in the context of MAPbI$_3$ PSCs may transfer to similar success for PSCs based on FAPbI$_3$. Therefore, the implications of local stoichiometric deviations and Fermi-level grading resulting from dynamic and sequential evaporation ought to be studied.

3. More generally, the influence of stoichiometry on the behavior of PSC devices based on FAPbI$_3$ should be defined in more detail. Explicit comparisons of PSCs with a range of different stoichiometries (excess/deficiency of FAI) in the final film may enable improved performance and stability. Specifically, films rich in FAI have not been investigated in great detail, yet.

5 Summary

In this thesis, the limits and prospects of the thermal evaporation of organic-inorganic metal halide perovskites (MHPs) for photovoltaic applications were explored. The main goal of this thesis was to explore untapped potentials of physical vapor deposition techniques and introduce variations of the processing conditions by e.g. dynamizing the (co-)evaporation schemes, to analyze the phase evolution during film formation with an *in situ* XRD setup attached to the evaporation chamber and relate this to optoelectronic properties of the deposited perovskite absorber film.

In [H1], the impact of bulk and initial growth conditions on $MAPbI_3$ crystal growth and its implications in *n-i-p* solar cells was examined. During co-evaporation of MAI and PbI_2 the growth of $MAPbI_3$ is initiated by PbI_2 nucleation. This subsequently increases the otherwise low MAI condensation rate on the substrate, so that, after the formation of an initial PbI_2 seed layer, subsequently the perovskite is formed. Optimum bulk growth conditions were obtained with a PbI_2 deposition rate of $0.2\,Å$ per second and an intermediate chamber pressure of $7.5 \times 10^{-5}\,mbar$. With these conditions, maximum solar cell efficiencies of $14\,\%$ were achieved with low hysteresis for perovskite solar cells in an $ITO/SnO_2/C_{60}/MAPbI_3/PTAA/Au$ architecture. Subsequently, a novel dynamic co-evaporation scheme was introduced that enables a better control of the initial nucleation by deliberately evaporating PbI_2 seed layers with different thicknesses prior to the previously optimized co-evaporation for bulk perovskite growth. This dynamic evaporation allows for the layer-depth-dependent control of stoichiometry and is only possible via evaporation. A thin initial PbI_2 precursor layer proved to be crucial for the preparation of efficient solar cells, while an MAI-rich initial phase at the start of the perovskite growth led to non-functional devices. The impact of the PbI_2 seed layer was discussed in the context of improved interface properties and/or improved bulk growth as a result of favorable initial nucleation.

In continuation to [H1], the dynamic evaporation approach was transferred to *p-i-n* solar cells in [H2]. By comparing the above results for standard *n-i-p* devices with solar cells in the inverted structure, the impact of bulk and interface properties could be untangled. Several novel dynamic evaporation schemes were conducted including the deposition of thin PbI_2 and MAI precursors and post-deposition of a thin PbI_2 layer. Astonishingly, in the *p-i-n* device the PbI_2 precursor layer (with optimized thickness according to [H1]) yielded lower efficiency compared to cells with $MAPbI_3$ absorbers prepared via standard co-evaporation. However, an MAI precursor layer improved the efficiency compared to standard co-evaporation and additional post-deposition of a PbI_2 layer produced the highest efficiency. Based on these results and the discussed literature, the precursor layers induce improved crystallinity by preventing lattice stress that would otherwise be induced by lattice mismatch of the substrate and the perovskite. These results were interpreted in view of an improved charge extraction, with two hypothetical models involving charge carrier blocking at the interface and band bending through stoichiometry variations.

The combined interpretation of these two works lead to the conclusion and important finding that dynamic processing including pre/post-deposition of excess MAI/PbI_2 is a very favorable approach towards optimized solar cell absorbers,

emphasizing the importance of initial process conditions and the need for MAI-rich interfaces at the interface to the hole transport layer, and PbI_2-rich interfaces at the electron extracting side. The likely cause for enhanced charge extraction is the beneficial band-bending towards the interfaces between perovskite and charge extraction layers produced by the locally enhanced stoichiometry-induced self-doping effect of MHPs: An excess of PbI_2 causes n-doping while an excess of MAI causes p-doping [115, 292]. Therefore, p-doping near the hole transporting layer (HTL) improves hole extraction and electron blocking towards the HTL and n-doping near the electron transporting layer (ETL) improves electron extraction and hole blocking towards the ETL.

Subsequently, in [H3] the phase space for the to-date most prominent perovskite absorbers based on $FAPbI_3$ was explored through systematic compositional variations. The bulk stoichiometry during co-evaporation was varied in terms of the AX/BX_2 ratio (determined via the X/Pb ratio from EDX) for growth of $FAPbI_3$, $(Cs,FA)PbI_3$ and $(Cs,FA)Pb(I,Br)_3$ absorbers. For X/Pb ratios below 3, the excess PbX_2 clearly formed a segregated crystalline phase in all compositions and for X/Pb above 3 no crystalline PbX_2 was observed by XRD. In contrast to this, an excess of FAI and/or CsI did not lead to the observation of any secondary phase segregations, indicating an intercalation of FAI and CsI into the perovskite structure and/or their accumulation at grain boundaries. For compositions without Br, the δ phase was clearly identified for stoichiometric compositions during growth at room temperature. However, when an overstoichiometric amount of FAI was incorporated into $FAPbI_3$, within a certain I/Pb threshold range the α phase became preferred and the formation of the detrimental δ phase could successfully be suppressed. With inclusion of CsI, the threshold for full suppression of the δ phase was possible at an I/Pb ratio of about 3.6. With an increased share of A-cations, the observed crystallinity also increased. Further, the use of Br reduced the threshold to 2.6, supposedly due to the strong stabilization of the α phase by Br. For PbX_2 excess in $(Cs,FA)Pb(I,Br)_3$, Br was incorporated into the perovskite structure and PbI_2 segregated. These findings provide a clear picture of the compositional range for single-phase perovskite growth and the positive impact of (i) FAI-rich synthesis, (ii) Cs- and (iii) Br-incorporation. The benefit of these synthesis paths lies in the possibility to grow at room temperature and omit any post-annealing for the formation of the α phase. The effect leading to the suppression of the δ phase formation was discussed in this thesis and was assigned to the lower energy of FAI-terminated grain surfaces in the α phase (than in the δ phase) compared to arbitrary chemical surface-terminations [82]. This is in line with literature work showing that conditions (i)-(iii) also positively influence solar cell [23, 80, 291] and diode efficiencies [84, 304].

The final publication [H4] investigated the perovskite formation from sequentially evaporated precursors in a variety of sequences during evaporation and annealing up to 100°C. The initial reaction between the AX species (CsI and FAI) and PbI_2 was assigned to the FAI, since CsI and PbI_2 only reacted at far higher temperatures. Sequence A (CsI-FAI-PbI_2) allowed for full conversion of the layer stack to the perovskite phase, but exhibited voids at the interface to the substrate, suggesting upwards diffusion of the FAI. In four experiments with split evaporation of different shares x of the total amount of PbI_2 in the sequence $xPbI_2$-FAI-CsI-$(1-x)PbI_2$, this diffusion behavior was confirmed. Therein, the

formed voids shifted within the layer according to the original position of the FAI within the evaporated stacks. Layers prepared via sequence B (PbI$_2$-FAI-CsI) exhibited no voids, but the complete conversion of the layer stack proved to be less simple. Although alterations of the PbI$_2$ deposition aiming at the improvement of the PbI$_2$ morphology in favor of a complete conversion of the PbI$_2$ precursor were attempted, the latter was only achieved with an overstoichiometric share of FAI. Successful methods for the modification of PbI$_2$ precursors and the performance of solar cells with sequentially evaporated perovskite absorbers from the literature were discussed and related to the efforts undertaken in [H4].

This thesis successfully explored the stoichiometric and compositional phase space of MHPs based on MAPbI$_3$ and FAPbI$_3$ prepared by static and dynamic evaporation. In summary, the influence of bulk and interface stoichiometry on crystal growth and solar cell performance were studied. Dynamic evaporation was successfully used for the first time to induce band bending by self-doping which can be exploited for improved charge transport in MAPbI$_3$. The phase space for exclusive FAPbI$_3$ α phase growth from physical vapor deposition methods was established and methods based on stoichiometry engineering and sequential deposition were developed to successfully suppress the δ phase. These findings bear fundamental insights into the absorber formation from the vapor phase and give important guidelines for the future prosperous development of perovskite absorbers from dry, vacuum-based deposition methods with a large up-scaling potential.

List of Figures

List of Tables

References

[1] E. A. Katz, *Helvetica Chimica Acta* **2020**, *103*, 6 e2000061, _eprint: https://onlinelibrary.wiley.com/doi/pdf/10.1002/hlca.202000061.

[2] NREL, Best Research-Cell Efficiency Chart, **2023**, URL `https://www.nrel.gov/pv/cell-efficiency.html`.

[3] A. Kojima, K. Teshima, Y. Shirai, T. Miyasaka, *Journal of the American Chemical Society* **2009**, *131*, 17 6050, publisher: American Chemical Society.

[4] G. Flora, D. Gupta, A. Tiwari, *Interdisciplinary Toxicology* **2012**, *5*, 2 47.

[5] R. Pandey, S. Bhattarai, K. Sharma, J. Madan, A. K. Al-Mousoi, M. K. A. Mohammed, M. K. Hossain, *ACS Applied Electronic Materials* **2023**, *5*, 10 5303, publisher: American Chemical Society.

[6] J. Zhao, Z. Zhang, G. Li, M. H. Aldamasy, M. Li, A. Abate, *Advanced Energy Materials* **2023**, *13*, 13 2204233, _eprint: https://onlinelibrary.wiley.com/doi/pdf/10.1002/aenm.202204233.

[7] S. Ma, G. Yuan, Y. Zhang, N. Yang, Y. Li, Q. Chen, *Energy & Environmental Science* **2022**, *15*, 1 13, publisher: Royal Society of Chemistry.

[8] C.-H. Chen, S.-N. Cheng, L. Cheng, Z.-K. Wang, L.-S. Liao, *Advanced Energy Materials* **2023**, *13*, 14 2204144, _eprint: https://onlinelibrary.wiley.com/doi/pdf/10.1002/aenm.202204144.

[9] S. P. Dunfield, L. Bliss, F. Zhang, J. M. Luther, K. Zhu, M. F. A. M. van Hest, M. O. Reese, J. J. Berry, *Advanced Energy Materials* **2020**, *10*, 26 1904054, _eprint: https://onlinelibrary.wiley.com/doi/pdf/10.1002/aenm.201904054.

[10] C. C. Boyd, R. Cheacharoen, T. Leijtens, M. D. McGehee, *Chemical Reviews* **2019**, *119*, 5 3418, publisher: American Chemical Society.

[11] D. Bryant, N. Aristidou, S. Pont, I. Sanchez-Molina, T. Chotchunangatchaval, S. Wheeler, J. R. Durrant, S. A. Haque, *Energy & Environmental Science* **2016**, *9*, 5 1655, publisher: Royal Society of Chemistry.

[12] H. Zhu, S. Teale, M. N. Lintangpradipto, S. Mahesh, B. Chen, M. D. McGehee, E. H. Sargent, O. M. Bakr, *Nature Reviews Materials* **2023**, *8*, 9 569.

[13] D. B. Ritzer, T. Abzieher, A. Basibüyük, T. Feeney, F. Laufer, S. Ternes, B. S. Richards, S. Bergfeld, U. W. Paetzold, *Progress in Photovoltaics: Research and Applications* **2022**, *30*, 4 360, _eprint: https://onlinelibrary.wiley.com/doi/pdf/10.1002/pip.3489.

[14] T. J. Jacobsson, A. Hultqvist, A. García-Fernández, A. Anand, A. Al-Ashouri, A. Hagfeldt, A. Crovetto, A. Abate, A. G. Ricciardulli, A. Vijayan, A. Kulkarni, A. Y. Anderson, B. P. Darwich, B. Yang, B. L. Coles, C. A. R. Perini, C. Rehermann, D. Ramirez, D. Fairen-Jimenez, D. Di Girolamo, D. Jia, E. Avila, E. J. Juarez-Perez, F. Baumann, F. Mathies, G. S. A. González, G. Boschloo, G. Nasti, G. Paramasivam, G. Martínez-Denegri,

H. Näsström, H. Michaels, H. Köbler, H. Wu, I. Benesperi, M. I. Dar, I. Bayrak Pehlivan, I. E. Gould, J. N. Vagott, J. Dagar, J. Kettle, J. Yang, J. Li, J. A. Smith, J. Pascual, J. J. Jerónimo-Rendón, J. F. Montoya, J.-P. Correa-Baena, J. Qiu, J. Wang, K. Sveinbjörnsson, K. Hirselandt, K. Dey, K. Frohna, L. Mathies, L. A. Castriotta, M. H. Aldamasy, M. Vasquez-Montoya, M. A. Ruiz-Preciado, M. A. Flatken, M. V. Khenkin, M. Grischek, M. Kedia, M. Saliba, M. Anaya, M. Veldhoen, N. Arora, O. Shargaieva, O. Maus, O. S. Game, O. Yudilevich, P. Fassl, Q. Zhou, R. Betancur, R. Munir, R. Patidar, S. D. Stranks, S. Alam, S. Kar, T. Unold, T. Abzieher, T. Edvinsson, T. W. David, U. W. Paetzold, W. Zia, W. Fu, W. Zuo, V. R. F. Schröder, W. Tress, X. Zhang, Y.-H. Chiang, Z. Iqbal, Z. Xie, E. Unger, *Nature Energy* **2022**, *7*, 1 107, number: 1 Publisher: Nature Publishing Group.

[15] C. He, G. Zha, C. Deng, Y. An, R. Mao, Y. Liu, Y. Lu, Z. Chen, *Crystal Research and Technology* **2019**, *54*, 5 1900011, _eprint: https://onlinelibrary.wiley.com/doi/pdf/10.1002/crat.201900011.

[16] L. Ma, Z. Yan, X. Zhou, Y. Pi, Y. Du, J. Huang, K. Wang, K. Wu, C. Zhuang, X. Han, *Nature Communications* **2021**, *12*, 1 2023, number: 1 Publisher: Nature Publishing Group.

[17] D. B. Straus, S. Guo, R. J. Cava, *Journal of the American Chemical Society* **2019**, *141*, 29 11435, publisher: American Chemical Society.

[18] Y. Fu, M. P. Hautzinger, Z. Luo, F. Wang, D. Pan, M. M. Aristov, I. A. Guzei, A. Pan, X. Zhu, S. Jin, *ACS Central Science* **2019**, *5*, 8 1377, publisher: American Chemical Society.

[19] Y. Zhou, H. Xue, Y.-H. Jia, G. Brocks, S. Tao, N. Zhao, *Advanced Functional Materials* **2019**, *29*, 48 1905739, _eprint: https://onlinelibrary.wiley.com/doi/pdf/10.1002/adfm.201905739.

[20] F. Igbari, R. Wang, Z.-K. Wang, X.-J. Ma, Q. Wang, K.-L. Wang, Y. Zhang, L.-S. Liao, Y. Yang, *Nano Letters* **2019**, *19*, 3 2066, publisher: American Chemical Society.

[21] V. M. Goldschmidt, *Naturwissenschaften* **1926**, *14*, 21 477.

[22] D. B. Mitzi, K. Liang, *Journal of Solid State Chemistry* **1997**, *134*, 2 376.

[23] P. Becker, J. A. Márquez, J. Just, A. Al-Ashouri, C. Hages, H. Hempel, M. Jošt, S. Albrecht, R. Frahm, T. Unold, *Advanced Energy Materials* **2019**, *9*, 22 1900555, _eprint: https://onlinelibrary.wiley.com/doi/pdf/10.1002/aenm.201900555.

[24] K. Achyutha, M. N. Satyanarayan, *Physica B: Condensed Matter* **2021**, *603* 412418.

[25] M. Becker, T. Klüner, M. Wark, *Dalton Transactions* **2017**, *46*, 11 3500, publisher: Royal Society of Chemistry.

[26] A. Omura, Y. Moritomo, *Applied Physics Express* **2012**, *5*, 5 057101, publisher: IOP Publishing.

[27] X. Zheng, C. Wu, S. K. Jha, Z. Li, K. Zhu, S. Priya, *ACS Energy Letters* **2016**, *1*, 5 1014, publisher: American Chemical Society.

[28] C. J. Bartel, C. Sutton, B. R. Goldsmith, R. Ouyang, C. B. Musgrave, L. M. Ghiringhelli, M. Scheffler, *Science Advances* **2019**, *5*, 2 eaav0693, publisher: American Association for the Advancement of Science Section: Research Article.

[29] W. Travis, E. N. K. Glover, H. Bronstein, D. O. Scanlon, R. G. Palgrave, *Chemical Science* **2016**, *7*, 7 4548, publisher: Royal Society of Chemistry.

[30] M. R. Filip, F. Giustino, *Proceedings of the National Academy of Sciences* **2018**, *115*, 21 5397, publisher: Proceedings of the National Academy of Sciences.

[31] M. R. Filip, G. E. Eperon, H. J. Snaith, F. Giustino, *Nature Communications* **2014**, *5*, 1 5757, number: 1 Publisher: Nature Publishing Group.

[32] S. F. Hoefler, G. Trimmel, T. Rath, *Monatshefte für Chemie - Chemical Monthly* **2017**, *148*, 5 795.

[33] R. Padmavathy, A. Amudhavalli, R. Rajeswarapalanichamy, K. Iyakutti, *Zeitschrift für Naturforschung A* **2019**, *74*, 10 905, publisher: De Gruyter.

[34] R. Prasanna, A. Gold-Parker, T. Leijtens, B. Conings, A. Babayigit, H.-G. Boyen, M. F. Toney, M. D. McGehee, *Journal of the American Chemical Society* **2017**, *139*, 32 11117, publisher: American Chemical Society.

[35] W. Shockley, H. J. Queisser, *Journal of Applied Physics* **1961**, *32*, 3 510.

[36] J. H. Noh, S. H. Im, J. H. Heo, T. N. Mandal, S. I. Seok, *Nano Letters* **2013**, *13*, 4 1764, publisher: American Chemical Society.

[37] D. Zhang, H. Zhang, H. Guo, F. Ye, S. Liu, Y. Wu, *Advanced Functional Materials* **2022**, *32*, 27 2200174, _eprint: https://onlinelibrary.wiley.com/doi/pdf/10.1002/adfm.202200174.

[38] Y. Chen, Q. Meng, Y. Xiao, X. Zhang, J. Sun, C. B. Han, H. Gao, Y. Zhang, Y. Lu, H. Yan, *ACS Applied Materials & Interfaces* **2019**, *11*, 47 44101, publisher: American Chemical Society.

[39] H. Li, J. Zhou, L. Tan, M. Li, C. Jiang, S. Wang, X. Zhao, Y. Liu, Y. Zhang, Y. Ye, W. Tress, C. Yi, *Science Advances* **2022**, *8*, 28.

[40] J. Li, H. A. Dewi, H. Wang, J. Zhao, N. Tiwari, N. Yantara, T. Malinauskas, V. Getautis, T. J. Savenije, N. Mathews, S. Mhaisalkar, A. Bruno, *Advanced Functional Materials* **2021**, *31*, 42 2103252, _eprint: https://onlinelibrary.wiley.com/doi/pdf/10.1002/adfm.202103252.

[41] N. Li, A. Feng, X. Guo, J. Wu, S. Xie, Q. Lin, X. Jiang, Y. Liu, Z. Chen, X. Tao, *Advanced Energy Materials* **2022**, *12*, 7 2103241, _eprint: https://onlinelibrary.wiley.com/doi/pdf/10.1002/aenm.202103241.

[42] E. A. Duijnstee, V. M. Le Corre, M. B. Johnston, L. J. A. Koster, J. Lim, H. J. Snaith, *Physical Review Applied* **2021**, *15*, 1 014006, publisher: American Physical Society.

[43] D. Li, D. Zhang, K.-S. Lim, Y. Hu, Y. Rong, A. Mei, N.-G. Park, H. Han, *Advanced Functional Materials* **2020**, *n/a*, n/a 2008621, _eprint: https://onlinelibrary.wiley.com/doi/pdf/10.1002/adfm.202008621.

[44] M. Saliba, T. Matsui, J.-Y. Seo, K. Domanski, J.-P. Correa-Baena, M. Khaja Nazeeruddin, S. M. Zakeeruddin, W. Tress, A. Abate, A. Hagfeldt, M. Grätzel, *Energy & Environmental Science* **2016**, *9*, 6 1989, publisher: Royal Society of Chemistry.

[45] E. Smecca, Y. Numata, I. Deretzis, G. Pellegrino, S. Boninelli, T. Miyasaka, A. L. Magna, A. Alberti, *Physical Chemistry Chemical Physics* **2016**, *18*, 19 13413, publisher: Royal Society of Chemistry.

[46] J.-W. Lee, D.-H. Kim, H.-S. Kim, S.-W. Seo, S. M. Cho, N.-G. Park, *Advanced Energy Materials* **2015**, *5*, 20 1501310, _eprint: https://onlinelibrary.wiley.com/doi/pdf/10.1002/aenm.201501310.

[47] G. E. Eperon, S. D. Stranks, C. Menelaou, M. B. Johnston, L. M. Herz, H. J. Snaith, *Energy & Environmental Science* **2014**, *7*, 3 982, publisher: Royal Society of Chemistry.

[48] T. Baikie, Y. Fang, J. M. Kadro, M. Schreyer, F. Wei, S. G. Mhaisalkar, M. Graetzel, T. J. White, *Journal of Materials Chemistry A* **2013**, *1*, 18 5628, publisher: Royal Society of Chemistry.

[49] J. Xie, Y. Liu, J. Liu, L. Lei, Q. Gao, J. Li, S. Yang, *Journal of Power Sources* **2015**, *285* 349.

[50] T. J. Jacobsson, L. J. Schwan, M. Ottosson, A. Hagfeldt, T. Edvinsson, *Inorganic Chemistry* **2015**, *54*, 22 10678, publisher: American Chemical Society.

[51] X. Guo, C. McCleese, C. Kolodziej, A. C. S. Samia, Y. Zhao, C. Burda, *Dalton Transactions* **2016**, *45*, 9 3806, publisher: Royal Society of Chemistry.

[52] M. N. F. Hoque, N. Islam, Z. Li, G. Ren, K. Zhu, Z. Fan, *ChemSusChem* **2016**, *9*, 18 2692, _eprint: https://onlinelibrary.wiley.com/doi/pdf/10.1002/cssc.201600949.

[53] W. Kong, Z. Ye, Z. Qi, B. Zhang, M. Wang, A. Rahimi-Iman, H. Wu, *Physical Chemistry Chemical Physics* **2015**, *17*, 25 16405, publisher: Royal Society of Chemistry.

[54] C. Motta, F. El-Mellouhi, S. Sanvito, *Scientific Reports* **2015**, *5*, 1 12746, number: 1 Publisher: Nature Publishing Group.

[55] M. Senno, S. Tinte, *Physical Chemistry Chemical Physics* **2021**, *23*, 12 7376, publisher: Royal Society of Chemistry.

[56] A. A. Bakulin, O. Selig, H. J. Bakker, Y. L. Rezus, C. Müller, T. Glaser, R. Lovrincic, Z. Sun, Z. Chen, A. Walsh, J. M. Frost, T. L. C. Jansen, *The Journal of Physical Chemistry Letters* **2015**, *6*, 18 3663, publisher: American Chemical Society.

[57] K. Momma, F. Izumi, *Journal of Applied Crystallography* **2008**, *41*, 3 653, publisher: International Union of Crystallography.

[58] M. Szafrański, A. Katrusiak, *The Journal of Physical Chemistry Letters* **2016**, *7*, 17 3458, publisher: American Chemical Society.

[59] M. T. Weller, O. J. Weber, P. F. Henry, A. M. D. Pumpo, T. C. Hansen, *Chemical Communications* **2015**, *51*, 20 4180, publisher: Royal Society of Chemistry.

[60] C. Quarti, E. Mosconi, F. De Angelis, *Chemistry of Materials* **2014**, *26*, 22 6557, publisher: American Chemical Society.

[61] R. E. Wasylishen, O. Knop, J. B. Macdonald, *Solid State Communications* **1985**, *56*, 7 581.

[62] H. Mashiyama, Y. Kawamura, E. Magome, Y. Kubota, *Journal of the Korean Physical Society* **2003**, *42*, 9 1026, publisher: The Korean Physical Society.

[63] D. B. Khadka, Y. Shirai, M. Yanagida, K. Uto, K. Miyano, *Solar Energy Materials and Solar Cells* **2022**, *246* 111899.

[64] I. Mesquita, L. Andrade, A. Mendes, *ChemSusChem* **2019**, *12*, 10 2186, _eprint: https://onlinelibrary.wiley.com/doi/pdf/10.1002/cssc.201802899.

[65] S. Singh, C. Li, F. Panzer, K. L. Narasimhan, A. Graeser, T. P. Gujar, A. Köhler, M. Thelakkat, S. Huettner, D. Kabra, *The Journal of Physical Chemistry Letters* **2016**, *7*, 15 3014, publisher: American Chemical Society.

[66] G. D. Cody, T. Tiedje, B. Abeles, B. Brooks, Y. Goldstein, *Physical Review Letters* **1981**, *47*, 20 1480.

[67] B. J. Foley, D. L. Marlowe, K. Sun, W. A. Saidi, L. Scudiero, M. C. Gupta, J. J. Choi, *Applied Physics Letters* **2015**, *106*, 24 243904.

[68] K. P. O'Donnell, X. Chen, *Applied Physics Letters* **1991**, *58*, 25 2924.

[69] S. Masi, A. F. Gualdrón-Reyes, I. Mora-Seró, *ACS Energy Letters* **2020**, *5*, 6 1974, publisher: American Chemical Society.

[70] J. Huang, P. Xu, J. Liu, X.-Z. You, *Small* **2017**, *13*, 10 1603225, _eprint: https://onlinelibrary.wiley.com/doi/pdf/10.1002/smll.201603225.

[71] C. C. Stoumpos, C. D. Malliakas, M. G. Kanatzidis, *Inorganic Chemistry* **2013**, *52*, 15 9019.

[72] J. Borchert, R. L. Milot, J. B. Patel, C. L. Davies, A. D. Wright, L. Martínez Maestro, H. J. Snaith, L. M. Herz, M. B. Johnston, *ACS Energy Letters* **2017**, *2*, 12 2799.

[73] S. Sun, Z. Deng, Y. Wu, F. Wei, F. H. Isikgor, F. Brivio, M. W. Gaultois, J. Ouyang, P. D. Bristowe, A. K. Cheetham, G. Kieslich, *Chemical Communications* **2017**, *53*, 54 7537, publisher: The Royal Society of Chemistry.

[74] V. C. A. Taylor, D. Tiwari, M. Duchi, P. M. Donaldson, I. P. Clark, D. J. Fermin, T. A. A. Oliver, *The Journal of Physical Chemistry Letters* **2018**, *9*, 4 895, publisher: American Chemical Society.

[75] J. M. Frost, K. T. Butler, F. Brivio, C. H. Hendon, M. van Schilfgaarde, A. Walsh, *Nano Letters* **2014**, *14*, 5 2584, publisher: American Chemical Society.

[76] A. Binek, F. C. Hanusch, P. Docampo, T. Bein, *The Journal of Physical Chemistry Letters* **2015**, *6*, 7 1249, publisher: American Chemical Society.

[77] D. H. Fabini, C. C. Stoumpos, G. Laurita, A. Kaltzoglou, A. G. Kontos, P. Falaras, M. G. Kanatzidis, R. Seshadri, *Angewandte Chemie* **2016**, *128*, 49 15618.

[78] X. Dong, L. Chao, T. Niu, Y. Li, P. Guo, W. Hui, L. Song, Z. Wu, Y. Chen, *Solar RRL* **2022**, *6*, 7 2200060, _eprint: https://onlinelibrary.wiley.com/doi/pdf/10.1002/solr.202200060.

[79] P. Raval, R. M. Kennard, E. S. Vasileiadou, C. J. Dahlman, I. Spanopoulos, M. L. Chabinyc, M. Kanatzidis, G. N. Manjunatha Reddy, *ACS Energy Letters* **2022**, 1534–1543, publisher: American Chemical Society.

[80] M. Roß, S. Severin, M. B. Stutz, P. Wagner, H. Köbler, M. Favin-Lévêque, A. Al-Ashouri, P. Korb, P. Tockhorn, A. Abate, B. Stannowski, B. Rech, S. Albrecht, *Advanced Energy Materials* **2021**, *11*, 35 2101460.

[81] B.-w. Park, H. W. Kwon, Y. Lee, D. Y. Lee, M. G. Kim, G. Kim, K.-j. Kim, Y. K. Kim, J. Im, T. J. Shin, S. I. Seok, *Nature Energy* **2021**, *6*, 4 419, number: 4 Publisher: Nature Publishing Group.

[82] S. M. Oner, E. Sezen, M. S. Yordanli, E. Karakoc, C. Deger, I. Yavuz, *The Journal of Physical Chemistry Letters* **2022**, *13*, 1 324, publisher: American Chemical Society.

[83] M. Hasanzadeh Azar, M. Mohammadi, N. T. Rezaei, S. Aynehband, L. Shooshtari, R. Mohammadpour, A. Simchi, *ACS Applied Nano Materials* **2021**, *4*, 8 7788, publisher: American Chemical Society.

[84] F. Ma, J. Li, W. Li, N. Lin, L. Wang, J. Qiao, *Chemical Science* **2017**, *8*, 1 800.

[85] N. Li, Z. Zhu, C.-C. Chueh, H. Liu, B. Peng, A. Petrone, X. Li, L. Wang, A. K.-Y. Jen, *Advanced Energy Materials* **2017**, *7*, 1 1601307.

[86] W. S. Yang, J. H. Noh, N. J. Jeon, Y. C. Kim, S. Ryu, J. Seo, S. I. Seok, *Science* **2015**, *348*, 6240 1234, publisher: American Association for the Advancement of Science.

[87] Z. Li, M. Yang, J.-S. Park, S.-H. Wei, J. J. Berry, K. Zhu, *Chemistry of Materials* **2016**, *28*, 1 284, publisher: American Chemical Society.

[88] P. Guo, A. Mannodi-Kanakkithodi, J. Gong, Y. Xia, C. C. Stoumpos, D. H. Cao, B. T. Diroll, J. B. Ketterson, G. P. Wiederrecht, T. Xu, M. K. Y. Chan, M. G. Kanatzidis, R. D. Schaller, *Nature Communications* **2019**, *10*, 1 482, number: 1 Publisher: Nature Publishing Group.

[89] S. Draguta, O. Sharia, S. J. Yoon, M. C. Brennan, Y. V. Morozov, J. S. Manser, P. V. Kamat, W. F. Schneider, M. Kuno, *Nature Communications* **2017**, *8*, 1 200, number: 1 Publisher: Nature Publishing Group.

[90] G. Mannino, I. Deretzis, E. Smecca, A. La Magna, A. Alberti, D. Ceratti, D. Cahen, *The Journal of Physical Chemistry Letters* **2020**, *11*, 7 2490, publisher: American Chemical Society.

[91] S. De Wolf, J. Holovsky, S.-J. Moon, P. Löper, B. Niesen, M. Ledinsky, F.-J. Haug, J.-H. Yum, C. Ballif, *The Journal of Physical Chemistry Letters* **2014**, *5*, 6 1035, publisher: American Chemical Society.

[92] I. L. Braly, H. W. Hillhouse, *The Journal of Physical Chemistry C* **2016**, *120*, 2 893, publisher: American Chemical Society.

[93] E. T. Hoke, D. J. Slotcavage, E. R. Dohner, A. R. Bowring, H. I. Karunadasa, M. D. McGehee, *Chemical Science* **2015**, *6*, 1 613, publisher: Royal Society of Chemistry.

[94] S. Akin, E. Akman, S. Sonmezoglu, *Advanced Functional Materials* **2020**, *30*, 28 2002964, _eprint: https://onlinelibrary.wiley.com/doi/pdf/10.1002/adfm.202002964.

[95] Z. Xie, S. Sun, Y. Yan, L. Zhang, R. Hou, F. Tian, G. G. Qin, *Journal of Physics: Condensed Matter* **2017**, *29*, 24 245702, publisher: IOP Publishing.

[96] S. Pang, H. Hu, J. Zhang, S. Lv, Y. Yu, F. Wei, T. Qin, H. Xu, Z. Liu, G. Cui, *Chemistry of Materials* **2014**, *26*, 3 1485, publisher: American Chemical Society.

[97] N. Pellet, P. Gao, G. Gregori, T.-Y. Yang, M. K. Nazeeruddin, J. Maier, M. Grätzel, *Angewandte Chemie International Edition* **2014**, *53*, 12 3151, _eprint: https://onlinelibrary.wiley.com/doi/pdf/10.1002/anie.201309361.

[98] R. Jono, H. Segawa, *Chemistry Letters* **2019**, *48*, 8 877.

[99] G. E. Eperon, T. Leijtens, K. A. Bush, R. Prasanna, T. Green, J. T.-W. Wang, D. P. McMeekin, G. Volonakis, R. L. Milot, R. May, A. Palmstrom, D. J. Slotcavage, R. A. Belisle, J. B. Patel, E. S. Parrott, R. J. Sutton, W. Ma, F. Moghadam, B. Conings, A. Babayigit, H.-G. Boyen, S. Bent, F. Giustino, L. M. Herz, M. B. Johnston, M. D. McGehee, H. J. Snaith, *Science* **2016**, *354*, 6314 861, publisher: American Association for the Advancement of Science.

[100] A. M. Igual-Muñoz, J. Ávila, P. P. Boix, H. J. Bolink, *Solar RRL* **2020**, *4*, 2 1900283, _eprint: https://onlinelibrary.wiley.com/doi/pdf/10.1002/solr.201900283.

[101] Q. Gao, H. Sahin, J. Kang, S.-H. Wei, *Physical Review B* **2021**, *104*, 6 064204, publisher: American Physical Society.

[102] E. S. Parrott, T. Green, R. L. Milot, M. B. Johnston, H. J. Snaith, L. M. Herz, *Advanced Functional Materials* **2018**, *28*, 33 1802803, _eprint: https://onlinelibrary.wiley.com/doi/pdf/10.1002/adfm.201802803.

[103] A. Rajagopal, R. J. Stoddard, H. W. Hillhouse, A. K.-Y. Jen, *Journal of Materials Chemistry A* **2019**, *7*, 27 16285, publisher: The Royal Society of Chemistry.

[104] Y. J. Ahn, S. G. Ji, J. Y. Kim, *Journal of the Korean Ceramic Society* **2021**.

[105] K. Xiao, Y.-H. Lin, M. Zhang, R. D. J. Oliver, X. Wang, Z. Liu, X. Luo, J. Li, D. Lai, H. Luo, R. Lin, J. Xu, Y. Hou, H. J. Snaith, H. Tan, *Science* **2022**, *376*, 6594 762, publisher: American Association for the Advancement of Science.

[106] G. E. Eperon, C. E. Beck, H. J. Snaith, *Materials Horizons* **2016**, *3*, 1 63, publisher: Royal Society of Chemistry.

[107] P. Würfel, *Physik der Solarzellen*, Spektrum, 2 edition, **2000**.

[108] L. M. Pazos-Outón, T. P. Xiao, E. Yablonovitch, *The Journal of Physical Chemistry Letters* **2018**, *9*, 7 1703, publisher: American Chemical Society.

[109] P. Fassl, V. Lami, F. J. Berger, L. M. Falk, J. Zaumseil, B. S. Richards, I. A. Howard, Y. Vaynzof, U. W. Paetzold, *Matter* **2021**, *4*, 4 1391.

[110] J. M. Richter, M. Abdi-Jalebi, A. Sadhanala, M. Tabachnyk, J. P. H. Rivett, L. M. Pazos-Outón, K. C. Gödel, M. Price, F. Deschler, R. H. Friend, *Nature Communications* **2016**, *7*, 1 13941, number: 1 Publisher: Nature Publishing Group.

[111] F. Zhang, B. Yang, X. Mao, R. Yang, L. Jiang, Y. Li, J. Xiong, Y. Yang, R. He, W. Deng, K. Han, *ACS Applied Materials & Interfaces* **2017**, *9*, 17 14827, publisher: American Chemical Society.

[112] A. Y. Alsalloum, B. Turedi, X. Zheng, S. Mitra, A. A. Zhumekenov, K. J. Lee, P. Maity, I. Gereige, A. AlSaggaf, I. S. Roqan, O. F. Mohammed, O. M. Bakr, *ACS Energy Letters* **2020**, *5*, 2 657.

[113] W.-J. Yin, T. Shi, Y. Yan, *Applied Physics Letters* **2014**, *104*, 6 063903.

[114] S. Ilahi, *Physica B: Condensed Matter* **2023**, *652* 414612.

[115] Q. Wang, Y. Shao, H. Xie, L. Lyu, X. Liu, Y. Gao, J. Huang, *Applied Physics Letters* **2014**, *105*, 16 163508.

[116] D. Forgács, M. Sessolo, H. J. Bolink, *Journal of Materials Chemistry A* **2015**, *3*, 27 14121, publisher: Royal Society of Chemistry.

[117] C. Momblona, L. Gil-Escrig, E. Bandiello, E. M. Hutter, M. Sessolo, K. Lederer, J. Blochwitz-Nimoth, H. J. Bolink, *Energy & Environmental Science* **2016**, *9*, 11 3456, publisher: Royal Society of Chemistry.

[118] T. Hellmann, C. Das, T. Abzieher, J. A. Schwenzer, M. Wussler, R. Dachauer, U. W. Paetzold, W. Jaegermann, T. Mayer, *Advanced Energy Materials* **2020**, *10*, 42 2002129, _eprint: https://onlinelibrary.wiley.com/doi/pdf/10.1002/aenm.202002129.

[119] M. Cai, N. Ishida, X. Li, X. Yang, T. Noda, Y. Wu, F. Xie, H. Naito, D. Fujita, L. Han, *Joule* **2018**, *2*, 2 296.

[120] C. Wehrenfennig, G. E. Eperon, M. B. Johnston, H. J. Snaith, L. M. Herz, *Advanced Materials* **2014**, *26*, 10 1584, _eprint: https://onlinelibrary.wiley.com/doi/pdf/10.1002/adma.201305172.

[121] S. Wang, W.-b. Xiao, F. Wang, *RSC Advances* **2020**, *10*, 54 32364, publisher: Royal Society of Chemistry.

[122] P. Piatkowski, B. Cohen, S. Kazim, S. Ahmad, A. Douhal, *Physical Chemistry Chemical Physics* **2016**, *18*, 39 27090, publisher: Royal Society of Chemistry.

[123] J. He, R. Long, *The Journal of Physical Chemistry Letters* **2018**, *9*, 22 6489, publisher: American Chemical Society.

[124] A. A. Zhumekenov, M. I. Saidaminov, M. A. Haque, E. Alarousu, S. P. Sarmah, B. Murali, I. Dursun, X.-H. Miao, A. L. Abdelhady, T. Wu, O. F. Mohammed, O. M. Bakr, *ACS Energy Letters* **2016**, *1*, 1 32, publisher: American Chemical Society.

[125] W. Rehman, R. L. Milot, G. E. Eperon, C. Wehrenfennig, J. L. Boland, H. J. Snaith, M. B. Johnston, L. M. Herz, *Advanced Materials* **2015**, *27*, 48 7938, _eprint: https://onlinelibrary.wiley.com/doi/pdf/10.1002/adma.201502969.

[126] P. Piatkowski, B. Cohen, C. S. J. Ponseca, M. Salado, S. Kazim, S. Ahmad, V. Sundström, A. Douhal, *The Journal of Physical Chemistry Letters* **2016**, *7*, 1 204, publisher: American Chemical Society.

[127] W. S. Yang, B.-W. Park, E. H. Jung, N. J. Jeon, Y. C. Kim, D. U. Lee, S. S. Shin, J. Seo, E. K. Kim, J. H. Noh, S. I. Seok, *Science* **2017**, *356*, 6345 1376, publisher: American Association for the Advancement of Science.

[128] N. Liu, C. Yam, *Physical Chemistry Chemical Physics* **2018**, *20*, 10 6800, publisher: Royal Society of Chemistry.

[129] T. Leijtens, G. E. Eperon, A. J. Barker, G. Grancini, W. Zhang, J. M. Ball, A. R. Srimath Kandada, H. J. Snaith, A. Petrozza, *Energy & Environmental Science* **2016**, *9*, 11 3472, publisher: Royal Society of Chemistry.

[130] P. Yadav, M. I. Dar, N. Arora, E. A. Alharbi, F. Giordano, S. M. Za-keeruddin, M. Grätzel, *Advanced Materials* **2017**, *29*, 40 1701077, _eprint: https://onlinelibrary.wiley.com/doi/pdf/10.1002/adma.201701077.

[131] H.-S. Kim, N.-G. Park, *The Journal of Physical Chemistry Letters* **2014**, *5*, 17 2927, publisher: American Chemical Society.

[132] N.-G. Park, M. Grätzel, T. Miyasaka, K. Zhu, K. Emery, *Nature Energy* **2016**, *1*, 11 1, number: 11 Publisher: Nature Publishing Group.

[133] D.-H. Kang, N.-G. Park, *Advanced Materials* **2019**, *31*, 34 1805214, _eprint: https://onlinelibrary.wiley.com/doi/pdf/10.1002/adma.201805214.

[134] C. Li, A. Guerrero, Y. Zhong, A. Gräser, C. A. M. Luna, J. Köhler, J. Bis-quert, R. Hildner, S. Huettner, *Small* **2017**, *13*, 42 1701711.

[135] D. Barboni, R. A. D. Souza, *Energy & Environmental Science* **2018**, *11*, 11 3266, publisher: Royal Society of Chemistry.

[136] L. McGovern, M. H. Futscher, L. A. Muscarella, B. Ehrler, *The Journal of Physical Chemistry Letters* **2020**, *11*, 17 7127, publisher: American Chemical Society.

[137] D.-Y. Son, S.-G. Kim, J.-Y. Seo, S.-H. Lee, H. Shin, D. Lee, N.-G. Park, *Journal of the American Chemical Society* **2018**, *140*, 4 1358, publisher: American Chemical Society.

[138] Z. Li, C. Xiao, Y. Yang, S. P. Harvey, D. Hoe Kim, J. A. Christians, M. Yang, P. Schulz, S. U. Nanayakkara, C.-S. Jiang, J. M. Luther, J. J. Berry, M. C. Beard, M. M. Al-Jassim, K. Zhu, *Energy & Environmental Science* **2017**, *10*, 5 1234, publisher: Royal Society of Chemistry.

[139] P. Calado, A. M. Telford, D. Bryant, X. Li, J. Nelson, B. C. O'Regan, P. R. F. Barnes, *Nature Communications* **2016**, *7*, 1 13831, number: 1 Publisher: Nature Publishing Group.

[140] S. van Reenen, M. Kemerink, H. J. Snaith, *The Journal of Physical Chemistry Letters* **2015**, *6*, 19 3808, publisher: American Chemical Society.

[141] A.-N. Cho, N.-G. Park, *ChemSusChem* **2017**, *10*, 19 3687, _eprint: https://onlinelibrary.wiley.com/doi/pdf/10.1002/cssc.201701095.

[142] M. Ye, C. He, J. Iocozzia, X. Liu, X. Cui, X. Meng, M. Rager, X. Hong, X. Liu, Z. Lin, *Journal of Physics D: Applied Physics* **2017**, *50*, 37 373002, publisher: IOP Publishing.

[143] Y. Bai, X. Meng, S. Yang, *Advanced Energy Materials* **2018**, *8*, 5 1701883, _eprint: https://onlinelibrary.wiley.com/doi/pdf/10.1002/aenm.201701883.

[144] G. A. Sepalage, S. Meyer, A. Pascoe, A. D. Scully, F. Huang, U. Bach, Y.-B. Cheng, L. Spiccia, *Advanced Functional Materials* **2015**, *25*, 35 5650, _eprint: https://onlinelibrary.wiley.com/doi/pdf/10.1002/adfm.201502541.

[145] K.-H. Jung, J.-Y. Seo, S. Lee, H. Shin, N.-G. Park, *Journal of Materials Chemistry A* **2017**, *5*, 47 24790, publisher: The Royal Society of Chemistry.

[146] F. Wu, R. Pathak, Q. Qiao, *Catalysis Today* **2021**, *374* 86.

[147] S. R. Pering, P. J. Cameron, *Materials Advances* **2022**, *3*, 21 7918, publisher: Royal Society of Chemistry.

[148] B. Conings, J. Drijkoningen, N. Gauquelin, A. Babayigit, J. D'Haen, L. D'Olieslaeger, A. Ethirajan, J. Verbeeck, J. Manca, E. Mosconi, F. D. Angelis, H.-G. Boyen, *Advanced Energy Materials* **2015**, *5*, 15 1500477, _eprint: https://onlinelibrary.wiley.com/doi/pdf/10.1002/aenm.201500477.

[149] Y. Li, X. Xu, C. Wang, C. Wang, F. Xie, J. Yang, Y. Gao, *The Journal of Physical Chemistry C* **2015**, *119*, 42 23996.

[150] J. Zhao, B. Cai, Z. Luo, Y. Dong, Y. Zhang, H. Xu, B. Hong, Y. Yang, L. Li, W. Zhang, C. Gao, *Scientific Reports* **2016**, *6*, 1 21976, number: 1 Publisher: Nature Publishing Group.

[151] P. Toloueinia, H. Khassaf, A. Shirazi Amin, Z. M. Tobin, S. P. Alpay, S. L. Suib, *ACS Applied Energy Materials* **2020**, *3*, 9 8240, publisher: American Chemical Society.

[152] Z. Zhu, V. G. Hadjiev, Y. Rong, R. Guo, B. Cao, Z. Tang, F. Qin, Y. Li, Y. Wang, F. Hao, S. Venkatesan, W. Li, S. Baldelli, A. M. Guloy, H. Fang, Y. Hu, Y. Yao, Z. Wang, J. Bao, *Chemistry of Materials* **2016**, *28*, 20 7385, publisher: American Chemical Society.

[153] J. A. Christians, P. A. Miranda Herrera, P. V. Kamat, *Journal of the American Chemical Society* **2015**, *137*, 4 1530, publisher: American Chemical Society.

[154] A. M. A. Leguy, Y. Hu, M. Campoy-Quiles, M. I. Alonso, O. J. Weber, P. Azarhoosh, M. van Schilfgaarde, M. T. Weller, T. Bein, J. Nelson, P. Docampo, P. R. F. Barnes, *Chemistry of Materials* **2015**, *27*, 9 3397, publisher: American Chemical Society.

[155] S. N. Habisreutinger, T. Leijtens, G. E. Eperon, S. D. Stranks, R. J. Nicholas, H. J. Snaith, *Nano Letters* **2014**, *14*, 10 5561, publisher: American Chemical Society.

[156] S. Wang, M. Sina, P. Parikh, T. Uekert, B. Shahbazian, A. Devaraj, Y. S. Meng, *Nano Letters* **2016**, *16*, 9 5594, publisher: American Chemical Society.

[157] Y. Huang, X. Lei, T. He, Y. Jiang, M. Yuan, *Advanced Energy Materials* **2022**, *12*, 4 2100690.

[158] D. Lin, Y. Gao, T. Zhang, Z. Zhan, N. Pang, Z. Wu, K. Chen, T. Shi, Z. Pan, P. Liu, W. Xie, *Advanced Functional Materials* **2022**, *32*, 48 2208392, _eprint: https://onlinelibrary.wiley.com/doi/pdf/10.1002/adfm.202208392.

[159] R. T. Wang, A. F. Xu, W. Li, Y. Li, G. Xu, *The Journal of Physical Chemistry Letters* **2021**, *12*, 22 5332, publisher: American Chemical Society.

[160] K. L. Svane, A. C. Forse, C. P. Grey, G. Kieslich, A. K. Cheetham, A. Walsh, K. T. Butler, *The Journal of Physical Chemistry Letters* **2017**, *8*, 24 6154, publisher: American Chemical Society.

[161] H. Xie, Z. Wang, Z. Chen, C. Pereyra, M. Pols, K. Gałkowski, M. Anaya, S. Fu, X. Jia, P. Tang, D. J. Kubicki, A. Agarwalla, H.-S. Kim, D. Prochowicz, X. Borrisé, M. Bonn, C. Bao, X. Sun, S. M. Zakeeruddin, L. Emsley, J. Arbiol, F. Gao, F. Fu, H. I. Wang, K.-J. Tielrooij, S. D. Stranks, S. Tao, M. Grätzel, A. Hagfeldt, M. Lira-Cantu, *Joule* **2021**, *5*, 5 1246.

[162] N. Aristidou, I. Sanchez-Molina, T. Chotchuangchutchaval, M. Brown, L. Martinez, T. Rath, S. A. Haque, *Angewandte Chemie International Edition* **2015**, *54*, 28 8208, _eprint: https://onlinelibrary.wiley.com/doi/pdf/10.1002/anie.201503153.

[163] Y. Ouyang, Y. Li, P. Zhu, Q. Li, Y. Gao, J. Tong, L. Shi, Q. Zhou, C. Ling, Q. Chen, Z. Deng, H. Tan, W. Deng, J. Wang, *Journal of Materials Chemistry A* **2019**, *7*, 5 2275, publisher: The Royal Society of Chemistry.

[164] F. T. F. O'Mahony, Y. Hui Lee, C. Jellett, S. Dmitrov, D. T. J. Bryant, J. R. Durrant, B. C. O'Regan, M. Graetzel, M. K. Nazeeruddin, S. A. Haque, *Journal of Materials Chemistry A* **2015**, *3*, 14 7219, publisher: Royal Society of Chemistry.

[165] Y. Guo, C. Li, Y. Xue, C. Geng, D. Tian, *Materials Research Express* **2018**, *5*, 2 026203.

[166] A. Senocrate, T. Acartürk, G. Yeong Kim, R. Merkle, U. Starke, M. Grätzel, J. Maier, *Journal of Materials Chemistry A* **2018**, *6*, 23 10847, publisher: Royal Society of Chemistry.

[167] A. Alberti, I. Deretzis, G. Pellegrino, C. Bongiorno, E. Smecca, G. Mannino, F. Giannazzo, G. G. Condorelli, N. Sakai, T. Miyasaka, C. Spinella, A. La Magna, *ChemPhysChem* **2015**, *16*, 14 3064, _eprint: https://onlinelibrary.wiley.com/doi/pdf/10.1002/cphc.201500374.

[168] E. J. Juarez-Perez, L. K. Ono, M. Maeda, Y. Jiang, Z. Hawash, Y. Qi, *Journal of Materials Chemistry A* **2018**, *6*, 20 9604, publisher: Royal Society of Chemistry.

[169] R. K. Gunasekaran, D. Chinnadurai, A. R. Selvaraj, R. Rajendiran, K. Senthil, K. Prabakar, *ChemPhysChem* **2018**, *19*, 12 1507, _eprint: https://onlinelibrary.wiley.com/doi/pdf/10.1002/cphc.201800002.

[170] S. Wang, Y. Jiang, E. J. Juarez-Perez, L. K. Ono, Y. Qi, *Nature Energy* **2016**, *2*, 1 1, number: 1 Publisher: Nature Publishing Group.

[171] M. Kroll, S. Dilara Öz, Z. Zhang, R. Ji, T. Schramm, T. Antrack, Y. Vaynzof, S. Olthof, K. Leo, *Sustainable Energy & Fuels* **2022**, *6*, 13 3230, publisher: Royal Society of Chemistry.

[172] R. Guo, D. Han, W. Chen, L. Dai, K. Ji, Q. Xiong, S. Li, L. K. Reb, M. A. Scheel, S. Pratap, N. Li, S. Yin, T. Xiao, S. Liang, A. L. Oechsle, C. L. Weindl, M. Schwartzkopf, H. Ebert, P. Gao, K. Wang, M. Yuan, N. C. Greenham, S. D. Stranks, S. V. Roth, R. H. Friend, P. Müller-Buschbaum, *Nature Energy* **2021**, *6*, 10 977, number: 10 Publisher: Nature Publishing Group.

[173] T. Leijtens, G. E. Eperon, N. K. Noel, S. N. Habisreutinger, A. Petrozza, H. J. Snaith, *Advanced Energy Materials* **2015**, *5*, 20 1500963, _eprint: https://onlinelibrary.wiley.com/doi/pdf/10.1002/aenm.201500963.

[174] J. Burschka, N. Pellet, S.-J. Moon, R. Humphry-Baker, P. Gao, M. K. Nazeeruddin, M. Grätzel, *Nature* **2013**, *499*, 7458 316.

[175] H. Tsai, W. Nie, J.-C. Blancon, C. C. Stoumpos, R. Asadpour, B. Harutyunyan, A. J. Neukirch, R. Verduzco, J. J. Crochet, S. Tretiak, L. Pedesseau, J. Even, M. A. Alam, G. Gupta, J. Lou, P. M. Ajayan, M. J. Bedzyk, M. G. Kanatzidis, A. D. Mohite, *Nature* **2016**, *536*, 7616 312, number: 7616 Publisher: Nature Publishing Group.

[176] A. R. Bowring, L. Bertoluzzi, B. C. O'Regan, M. D. McGehee, *Advanced Energy Materials* **2018**, *8*, 8 1702365, _eprint: https://onlinelibrary.wiley.com/doi/pdf/10.1002/aenm.201702365.

[177] D. W. deQuilettes, W. Zhang, V. M. Burlakov, D. J. Graham, T. Leijtens, A. Osherov, V. Bulović, H. J. Snaith, D. S. Ginger, S. D. Stranks, *Nature Communications* **2016**, *7*, 1 11683, number: 1 Publisher: Nature Publishing Group.

[178] Y. Deng, S. Xu, S. Chen, X. Xiao, J. Zhao, J. Huang, *Nature Energy* **2021**, *6*, 6 633, number: 6 Publisher: Nature Publishing Group.

[179] F. Brivio, C. Caetano, A. Walsh, *The Journal of Physical Chemistry Letters* **2016**, *7*, 6 1083, publisher: American Chemical Society.

[180] X. Tang, M. van den Berg, E. Gu, A. Horneber, G. J. Matt, A. Osvet, A. J. Meixner, D. Zhang, C. J. Brabec, *Nano Letters* **2018**, *18*, 3 2172, publisher: American Chemical Society.

[181] C. G. Bischak, C. L. Hetherington, H. Wu, S. Aloni, D. F. Ogletree, D. T. Limmer, N. S. Ginsberg, *Nano Letters* **2017**, *17*, 2 1028, publisher: American Chemical Society.

[182] J. S. Yun, J. Seidel, J. Kim, A. M. Soufiani, S. Huang, J. Lau, N. J. Jeon, S. I. Seok, M. A. Green, A. Ho-Baillie, *Advanced Energy Materials* **2016**, *6*, 13 1600330, _eprint: https://onlinelibrary.wiley.com/doi/pdf/10.1002/aenm.201600330.

[183] S. J. Yoon, M. Kuno, P. V. Kamat, *ACS Energy Letters* **2017**, *2*, 7 1507, publisher: American Chemical Society.

[184] A. Rajagopal, Z. Yang, S. B. Jo, I. L. Braly, P.-W. Liang, H. W. Hillhouse, A. K.-Y. Jen, *Advanced Materials* **2017**, *29*, 34 1702140, _eprint: https://onlinelibrary.wiley.com/doi/pdf/10.1002/adma.201702140.

[185] R. Wang, T. Huang, J. Xue, J. Tong, K. Zhu, Y. Yang, *Nature Photonics* **2021**, *15*, 6 411.

[186] S. Wang, L. Tan, J. Zhou, M. Li, X. Zhao, H. Li, W. Tress, L. Ding, M. Graetzel, C. Yi, *Joule* **2022**, *6*, 6 1344.

[187] G. Niu, W. Li, F. Meng, L. Wang, H. Dong, Y. Qiu, *Journal of Materials Chemistry A* **2014**, *2*, 3 705, publisher: Royal Society of Chemistry.

[188] S. Ito, S. Tanaka, K. Manabe, H. Nishino, *The Journal of Physical Chemistry C* **2014**, *118*, 30 16995, publisher: American Chemical Society.

[189] A. Donakowski, D. W. Miller, N. C. Anderson, A. Ruth, E. M. Sanehira, J. J. Berry, M. D. Irwin, A. Rockett, K. X. Steirer, *ACS Energy Letters* **2021**, *6*, 2 574, publisher: American Chemical Society.

[190] W.-A. Quitsch, D. W. deQuilettes, O. Pfingsten, A. Schmitz, S. Ognjanovic, S. Jariwala, S. Koch, M. Winterer, D. S. Ginger, G. Bacher, *The Journal of Physical Chemistry Letters* **2018**, *9*, 8 2062, publisher: American Chemical Society.

[191] L. T. Schelhas, Z. Li, J. A. Christians, A. Goyal, P. Kairys, S. P. Harvey, D. Hoe Kim, K. H. Stone, J. M. Luther, K. Zhu, V. Stevanovic, J. J. Berry, *Energy & Environmental Science* **2019**, *12*, 4 1341, publisher: Royal Society of Chemistry.

[192] I. M. Pavlovetc, M. C. Brennan, S. Draguta, A. Ruth, T. Moot, J. A. Christians, K. Aleshire, S. P. Harvey, S. Toso, S. U. Nanayakkara, J. Messinger, J. M. Luther, M. Kuno, *ACS Energy Letters* **2020**, *5*, 9 2802, publisher: American Chemical Society.

[193] K. Domanski, B. Roose, T. Matsui, M. Saliba, S.-H. Turren-Cruz, J.-P. Correa-Baena, C. Roldan Carmona, G. Richardson, J. M. Foster, F. D. Angelis, J. M. Ball, A. Petrozza, N. Mine, M. K. Nazeeruddin, W. Tress, M. Grätzel, U. Steiner, A. Hagfeldt, A. Abate, *Energy & Environmental Science* **2017**, *10*, 2 604, publisher: Royal Society of Chemistry.

[194] H. Tsai, R. Asadpour, J.-C. Blancon, C. C. Stoumpos, O. Durand, J. W. Strzalka, B. Chen, R. Verduzco, P. M. Ajayan, S. Tretiak, J. Even, M. A. Alam, M. G. Kanatzidis, W. Nie, A. D. Mohite, *Science* **2018**, *360*, 6384 67, publisher: American Association for the Advancement of Science.

[195] K. A. Bush, A. F. Palmstrom, Z. J. Yu, M. Boccard, R. Cheacharoen, J. P. Mailoa, D. P. McMeekin, R. L. Z. Hoye, C. D. Bailie, T. Leijtens, I. M. Peters, M. C. Minichetti, N. Rolston, R. Prasanna, S. Sofia, D. Harwood, W. Ma, F. Moghadam, H. J. Snaith, T. Buonassisi, Z. C. Holman, S. F. Bent, M. D. McGehee, *Nature Energy* **2017**, *2*, 4 1, number: 4 Publisher: Nature Publishing Group.

[196] S. L. Hamukwaya, H. Hao, Z. Zhao, J. Dong, T. Zhong, J. Xing, L. Hao, M. M. Mashingaidze, *Coatings* **2022**, *12*, 2 252, number: 2 Publisher: Multidisciplinary Digital Publishing Institute.

[197] N.-G. Park, K. Zhu, *Nature Reviews Materials* **2020**, *5*, 5 333, number: 5 Publisher: Nature Publishing Group.

[198] T. Soto-Montero, W. Soltanpoor, M. Morales-Masis, *APL Materials* **2020**, *8*, 11 110903.

[199] Y. Li, F. Z. Liu, M. Waqas, T. L. Leung, H. W. Tam, X. Q. Lan, B. Tu, W. Chen, A. B. Djurišić, Z. B. He, *Small Methods* **2018**, *2*, 7 1700387, _eprint: https://onlinelibrary.wiley.com/doi/pdf/10.1002/smtd.201700387.

[200] M. R. Leyden, L. K. Ono, S. R. Raga, Y. Kato, S. Wang, Y. Qi, *Journal of Materials Chemistry A* **2014**, *2*, 44 18742, publisher: The Royal Society of Chemistry.

[201] T. Moser, K. Artuk, Y. Jiang, T. Feurer, E. Gilshtein, A. N. Tiwari, F. Fu, *Journal of Materials Chemistry A* **2020**, *8*, 42 21973.

[202] G. Tong, J. Zhang, T. Bu, L. K. Ono, C. Zhang, Y. Liu, C. Ding, T. Wu, S. Mariotti, S. Kazaoui, Y. Qi, *Advanced Energy Materials* **2023**, *13*, 21 2300153, _eprint: https://onlinelibrary.wiley.com/doi/pdf/10.1002/aenm.202300153.

[203] M. Liu, M. B. Johnston, H. J. Snaith, *Nature* **2013**, *501*, 7467 395, number: 7467 Publisher: Nature Publishing Group.

[204] J. Borchert, H. Boht, W. Fränzel, R. Csuk, R. Scheer, P. Pistor, *Journal of Materials Chemistry A* **2015**, *3*, 39 19842, publisher: Royal Society of Chemistry.

[205] C.-W. Chen, H.-W. Kang, S.-Y. Hsiao, P.-F. Yang, K.-M. Chiang, H.-W. Lin, *Advanced Materials* **2014**, *26*, 38 6647, _eprint: https://onlinelibrary.wiley.com/doi/pdf/10.1002/adma.201402461.

[206] J. Teuscher, A. Ulianov, O. Müntener, M. Grätzel, N. Tétreault, *ChemSusChem* **2015**, *8*, 22 3847, _eprint: https://onlinelibrary.wiley.com/doi/pdf/10.1002/cssc.201500972.

[207] M. J. Bækbo, O. Hansen, I. Chorkendorff, P. C. K. Vesborg, *RSC Advances* **2018**, *8*, 52 29899, publisher: Royal Society of Chemistry.

[208] J. Borchert, I. Levchuk, L. C. Snoek, M. U. Rothmann, R. Haver, H. J. Snaith, C. J. Brabec, L. M. Herz, M. B. Johnston, *ACS Applied Materials & Interfaces* **2019**, *11*, 32 28851, publisher: American Chemical Society.

[209] X. Zhou, X. Li, Y. Liu, F. Huang, D. Zhong, *Applied Physics Letters* **2016**, *108*, 12 121601, publisher: American Institute of Physics.

[210] H. Xu, Y. Wu, J. Cui, C. Ni, F. Xu, J. Cai, F. Hong, Z. Fang, W. Wang, J. Zhu, L. Wang, R. Xu, F. Xu, *Physical Chemistry Chemical Physics* **2016**, *18*, 27 18607, publisher: Royal Society of Chemistry.

[211] S. Olthof, K. Meerholz, *Scientific Reports* **2017**, *7*, 1 40267, number: 1 Publisher: Nature Publishing Group.

[212] L. Cojocaru, K. Wienands, T. W. Kim, S. Uchida, A. J. Bett, S. Rafizadeh, J. C. Goldschmidt, S. W. Glunz, *ACS Applied Materials & Interfaces* **2018**, *10*, 31 26293, publisher: American Chemical Society.

[213] E. S. Parrott, J. B. Patel, A.-A. Haghighirad, H. J. Snaith, M. B. Johnston, L. M. Herz, *Nanoscale* **2019**, *11*, 30 14276.

[214] K. B. Lohmann, J. B. Patel, M. U. Rothmann, C. Q. Xia, R. D. J. Oliver, L. M. Herz, H. J. Snaith, M. B. Johnston, *ACS Energy Letters* **2020**, *5*, 3 710.

[215] T. J. Jacobsson, J.-P. Correa-Baena, E. Halvani Anaraki, B. Philippe, S. D. Stranks, M. E. F. Bouduban, W. Tress, K. Schenk, J. Teuscher, J.-E. Moser, H. Rensmo, A. Hagfeldt, *Journal of the American Chemical Society* **2016**, *138*, 32 10331, publisher: American Chemical Society.

[216] M. U. Rothmann, J. S. Kim, J. Borchert, K. B. Lohmann, C. M. O'Leary, A. A. Sheader, L. Clark, H. J. Snaith, M. B. Johnston, P. D. Nellist, L. M. Herz, *Science* **2020**, *370*, 6516 1.

[217] Y.-H. Chiang, M. Anaya, S. D. Stranks, *ACS Energy Letters* **2020**, *5*, 8 2498, publisher: American Chemical Society.

[218] M. Kam, Y. Zhu, D. Zhang, L. Gu, J. Chen, Z. Fan, *Solar RRL* **2019**, *3*, 7 1900050.

[219] J. Yan, J. Zhao, H. Wang, M. Kerklaan, L. J. Bannenberg, B. Ibrahim, T. J. Savenije, L. Mazzarella, O. Isabella, *ACS Applied Energy Materials* **2023**, publisher: American Chemical Society.

[220] J. Feng, Y. Jiao, H. Wang, X. Zhu, Y. Sun, M. Du, Y. Cao, D. Yang, S. F. Liu, *Energy & Environmental Science* **2021**, *14*, 5 3035.

[221] L. I. Maissel, R. Glang, *Handbook of Thin Film Technology*, McGraw-Hill Book Company, New York, USA, **1971**, publisher: IOP Publishing.

[222] H. Frey, H. R. Khan, *Handbook of Thin-Film Technology*, Springer-Verlag, Esslingen, Schwäbisch-Gmünd, **2015**.

[223] H. Hertz, *Annalen der Physik* **1882**, *253*, 10 177, _eprint: https://onlinelibrary.wiley.com/doi/pdf/10.1002/andp.18822531002.

[224] M. Knudsen, *Annalen der Physik* **1915**, *352*, 13 697, _eprint: https://onlinelibrary.wiley.com/doi/pdf/10.1002/andp.19153521306.

[225] I. Langmuir, *Physikalische Zeitschrift* **1913**, 1273–1280.

[226] M. Volmer, *Kinetik der Phasenbildung*, Theodor Steinkopff Verlag, Dresden, **1939**.

[227] S. Dushman, *Scientific Foundations of Vacuum Technique*, John Wiley And Sons, Inc., New York, London, 2 edition, **1949**.

[228] D. W. Pashley, *The Philosophical Magazine: A Journal of Theoretical Experimental and Applied Physics* **1959**, *4*, 39 324, publisher: Taylor & Francis _eprint: https://doi.org/10.1080/14786435908233344.

[229] I. Stranski, L. Krastanov, *Ber. Akad. Wiss. Wien* **1938**, *146* 797.

[230] K. Reichelt, X. Jiang, *Thin Solid Films* **1990**, *191*, 1 91.

[231] Luxel, **2023**, URL https://luxel.com/product-category/evaporation-sources/radak-2/radak-ii-radak-2/.

[232] CreaTec, **2023**, URL https://createc.de/index.php?index=1&menuid=28&lng=de&id=50.

[233] MBraun, **2023**, URL https://www.mbraun.com/us/products/coating/vacuum.html.

[234] L. Spieß, H. Behnken, C. Genzel, R. Schwarzer, G. Teichert, *Moderne Röntgenbeugung*, Springer, 3 edition, **2009**.

[235] W. Demtröder, *Experimentalphysik 3 - Atome, Moleküle, Festkörper*, Springer-Verlag, Kaiserslautern, 4 edition, **2010**.

[236] J. Skaar, Braggs lov, URL https://snl.no/Braggs_lov.

[237] I. V. Aleksandrov, A. F. Goncharov, I. N. Makarenko, S. M. Stishov, *Physical Review B* **1991**, *43*, 7 6194.

[238] A. Amendola, *ICDD Grant-in-Aid*, Polytechnic Institute of Brooklyn, Brooklyn, New York, USA, **1959**.

[239] A. A. Petrov, E. A. Goodilin, A. B. Tarasov, V. A. Lazarenko, P. V. Dorovatovskii, V. N. Khrustalev, *Acta Crystallographica Section E: Crystallographic Communications* **2017**, *73*, 4 569.

[240] T. Minagawa, *Acta Crystallographica Section A: Crystal Physics, Diffraction, Theoretical and General Crystallography* **1975**, *31*, 6 823.

[241] R. S. Mitchell, *Zeitschrift für Kristallographie - Crystalline Materials* **1959**, *111*, 1-6 372.

[242] H. E. Swanson, E. Tatge, *Standard X-ray Diffraction Powder Patterns*, National Bureau of Standards, **1953**.

[243] F. C. Hanusch, E. Wiesenmayer, E. Mankel, A. Binek, P. Angloher, C. Fraunhofer, N. Giesbrecht, J. M. Feckl, W. Jaegermann, D. Johrendt, T. Bein, P. Docampo, *The Journal of Physical Chemistry Letters* **2014**, *5*, 16 2791.

[244] H. Analytical, Particle Size and Strain Analysis by X-Ray Diffraction, **2002**.

[245] H. Klug, L. Alexander, *X-Ray Diffraction Procedures for Polycrystalline and Amorphous Materials*, Wiley, 2 edition, **1974**.

[246] L. E. Mundt, L. T. Schelhas, *Advanced Energy Materials* **2020**, *10*, 26 1903074.

[247] D. T. Moore, H. Sai, K. W. Tan, D.-M. Smilgies, W. Zhang, H. J. Snaith, U. Wiesner, L. A. Estroff, *Journal of the American Chemical Society* **2015**, *137*, 6 2350, publisher: American Chemical Society.

[248] R. Munir, A. D. Sheikh, M. Abdelsamie, H. Hu, L. Yu, K. Zhao, T. Kim, O. E. Tall, R. Li, D.-M. Smilgies, A. Amassian, *Advanced Materials* **2017**, *29*, 2 1604113, _eprint: https://onlinelibrary.wiley.com/doi/pdf/10.1002/adma.201604113.

[249] K. H. Stone, A. Gold-Parker, V. L. Pool, E. L. Unger, A. R. Bowring, M. D. McGehee, M. F. Toney, C. J. Tassone, *Nature Communications* **2018**, *9*, 1 3458, number: 1 Publisher: Nature Publishing Group.

[250] M. L. Petrus, Y. Hu, D. Moia, P. Calado, A. M. A. Leguy, P. R. F. Barnes, P. Docampo, *ChemSusChem* **2016**, *9*, 18 2699, _eprint: https://onlinelibrary.wiley.com/doi/pdf/10.1002/cssc.201600999.

[251] W. Tan, A. R. Bowring, A. C. Meng, M. D. McGehee, P. C. McIntyre, *ACS Applied Materials & Interfaces* **2018**, *10*, 6 5485, publisher: American Chemical Society.

[252] J. Yang, B. D. Siempelkamp, D. Liu, T. L. Kelly, *ACS Nano* **2015**, *9*, 2 1955, publisher: American Chemical Society.

[253] M. Tolan, *X-Ray Scattering from Soft-Matter Thin Films: Materials Science and Basic Research*, Springer, Berlin, Heidelberg, **1999**.

[254] U. Pietsch, V. Holý, T. Baumbach, *High-Resolution X-Ray Scattering: From Thin Films and Lateral Nanostructures*, Springer, Berlin, Heidelberg, **2004**.

[255] M. Tariq, O. Dolynchuk, T. Thurn-Albrecht, *Macromolecules* **2019**, *52*, 23 9140, publisher: American Chemical Society.

[256] R. F. Egerton, *Physical Principles of Electron Microscopy*, Springer, **2005**.

[257] T. E. Everhart, R. F. M. Thornley, *Journal of Scientific Instruments* **1960**, *37*, 7 246.

[258] M. U. Rothmann, W. Li, Y. Zhu, A. Liu, Z. Ku, U. Bach, J. Etheridge, Y.-B. Cheng, *Advanced Materials* **2018**, *30*, 25 1800629, _eprint: https://onlinelibrary.wiley.com/doi/pdf/10.1002/adma.201800629.

[259] J. A. Bearden, *X-Ray Wavelengths*, Review of Modern Physics, **1967**.

[260] S. S. Hegedus, W. N. Shafarman, *Progress in Photovoltaics: Research and Applications* **2004**, *12*, 2-3 155, _eprint: https://onlinelibrary.wiley.com/doi/pdf/10.1002/pip.518.

[261] K. Miyano, N. Tripathi, M. Yanagida, Y. Shirai, *Accounts of Chemical Research* **2016**, *49*, 2 303, publisher: American Chemical Society.

[262] I. Montoya De Los Santos, H. J. Cortina-Marrero, M. A. Ruíz-Sánchez, L. Hechavarría-Difur, F. J. Sánchez-Rodríguez, M. Courel, H. Hu, *Solar Energy* **2020**, *199* 198.

[263] H. J. Snaith, A. Abate, J. M. Ball, G. E. Eperon, T. Leijtens, N. K. Noel, S. D. Stranks, J. T.-W. Wang, K. Wojciechowski, W. Zhang, *The Journal of Physical Chemistry Letters* **2014**, *5*, 9 1511, publisher: American Chemical Society.

[264] T. Kirchartz, J. A. Márquez, M. Stolterfoht, T. Unold, *Advanced Energy Materials* **2020**, *10*, 26 1904134, _eprint: https://onlinelibrary.wiley.com/doi/pdf/10.1002/aenm.201904134.

[265] M. Stolterfoht, C. M. Wolff, J. A. Márquez, S. Zhang, C. J. Hages, D. Rothhardt, S. Albrecht, P. L. Burn, P. Meredith, T. Unold, D. Neher, *Nature Energy* **2018**, *3*, 10 847, number: 10 Publisher: Nature Publishing Group.

[266] V. Sarritzu, N. Sestu, D. Marongiu, X. Chang, S. Masi, A. Rizzo, S. Colella, F. Quochi, M. Saba, A. Mura, G. Bongiovanni, *Scientific Reports* **2017**, *7*, 1 44629, number: 1 Publisher: Nature Publishing Group.

[267] P. Wurfel, *Journal of Physics C: Solid State Physics* **1982**, *15*, 18 3967.

[268] C. M. Wolff, F. Zu, A. Paulke, L. P. Toro, N. Koch, D. Neher, *Advanced Materials* **2017**, *29*, 28 1700159, _eprint: https://onlinelibrary.wiley.com/doi/pdf/10.1002/adma.201700159.

[269] F. Staub, H. Hempel, J.-C. Hebig, J. Mock, U. W. Paetzold, U. Rau, T. Unold, T. Kirchartz, *Physical Review Applied* **2016**, *6*, 4 044017, publisher: American Physical Society.

[270] M. Maiberg, Ph.D. thesis, Martin-Luther-Universität Halle-Wittenberg, Halle, **2016**.

[271] T. Hölscher, Ph.D. thesis, MLU Halle-Wittenberg, Halle, **2015**.

[272] Z. Li, T. R. Klein, D. H. Kim, M. Yang, J. J. Berry, M. F. A. M. van Hest, K. Zhu, *Nature Reviews Materials* **2018**, *3*, 4 1, number: 4 Publisher: Nature Publishing Group.

[273] S. Razza, S. Castro-Hermosa, A. Di Carlo, T. M. Brown, *APL Materials* **2016**, *4*, 9 091508.

[274] Y. Deng, X. Zheng, Y. Bai, Q. Wang, J. Zhao, J. Huang, *Nature Energy* **2018**, *3*, 7 560, number: 7 Publisher: Nature Publishing Group.

[275] M. T. Hoerantner, E. L. Wassweiler, H. Zhang, A. Panda, M. Nasilowski, A. Osherov, R. Swartwout, A. E. Driscoll, N. S. Moody, M. G. Bawendi, K. F. Jensen, V. Bulović, *ACS Applied Materials & Interfaces* **2019**, *11*, 36 32928.

[276] Q. Guesnay, F. Sahli, C. Ballif, Q. Jeangros, *APL Materials* **2021**, *9*, 10 100703, publisher: American Institute of Physics.

[277] S.-Y. Hsiao, H.-L. Lin, W.-H. Lee, W.-L. Tsai, K.-M. Chiang, W.-Y. Liao, C.-Z. Ren-Wu, C.-Y. Chen, H.-W. Lin, *Advanced Materials* **2016**, *28*, 32 7013, _eprint: https://onlinelibrary.wiley.com/doi/pdf/10.1002/adma.201601505.

[278] P. Guo, Q. Ye, X. Yang, J. Zhang, F. Xu, D. Shchukin, B. Wei, H. Wang, *Journal of Materials Chemistry A* **2019**, *7*, 6 2497, publisher: Royal Society of Chemistry.

[279] J. A. Christians, P. Schulz, J. S. Tinkham, T. H. Schloemer, S. P. Harvey, B. J. Tremolet De Villers, A. Sellinger, J. J. Berry, J. M. Luther, *Nature Energy* **2018**, *3*, 1 68.

[280] R. Szostak, A. de Souza Gonçalves, J. N. de Freitas, P. E. Marchezi, F. L. de Araújo, H. C. N. Tolentino, M. F. Toney, F. das Chagas Marques, A. F. Nogueira, *Chemical Reviews* **2023**, *123*, 6 3160, publisher: American Chemical Society.

[281] G. Tumen-Ulzii, C. Qin, D. Klotz, M. R. Leyden, P. Wang, M. Auffray, T. Fujihara, T. Matsushima, J.-W. Lee, S.-J. Lee, Y. Yang, C. Adachi, *Advanced Materials* **2020**, *32*, 16 1905035, _eprint: https://onlinelibrary.wiley.com/doi/pdf/10.1002/adma.201905035.

[282] F. Liu, Q. Dong, M. K. Wong, A. B. Djurišić, A. Ng, Z. Ren, Q. Shen, C. Surya, W. K. Chan, J. Wang, A. M. C. Ng, C. Liao, H. Li, K. Shih, C. Wei, H. Su, J. Dai, *Advanced Energy Materials* **2016**, *6*, 7 1502206, _eprint: https://onlinelibrary.wiley.com/doi/pdf/10.1002/aenm.201502206.

[283] T. Gallet, R. G. Poeira, E. M. Lanzoni, T. Abzieher, U. W. Paetzold, A. Redinger, *ACS Applied Materials & Interfaces* **2021**, *13*, 2 2642, publisher: American Chemical Society.

[284] J. R. Klein, O. Flender, M. Scholz, K. Oum, T. Lenzer, *Physical Chemistry Chemical Physics* **2016**, *18*, 16 10800.

[285] Z. Song, S. C. Watthage, A. B. Phillips, B. L. Tompkins, R. J. Ellingson, M. J. Heben, *Chemistry of Materials* **2015**, *27*, 13 4612.

[286] H. Xu, F. Xu, W. Wang, Y. Zhu, Z. Fang, B. Yao, F. Hong, J. Cui, F. Xu, R. Xu, C.-C. Chen, L. Wang, *Organic Electronics* **2019**, *69* 329.

[287] B.-S. Kim, L. Gil-Escrig, M. Sessolo, H. J. Bolink, *The Journal of Physical Chemistry Letters* **2020**, *11*, 16 6852, publisher: American Chemical Society.

[288] Z. Ahmad, M. A. Najeeb, R. A. Shakoor, A. Alashraf, S. A. Al-Muhtaseb, A. Soliman, M. K. Nazeeruddin, *Scientific Reports* **2017**, *7*, 1 15406, number: 1 Publisher: Nature Publishing Group.

[289] H. Lee, S. Gaiaschi, P. Chapon, A. Marronnier, H. Lee, J.-C. Vanel, D. Tondelier, J.-E. Bourée, Y. Bonnassieux, B. Geffroy, *ACS Energy Letters* **2017**, *2*, 4 943, publisher: American Chemical Society.

[290] B. Fernandez, L. Lobo, P. Tyagi, V. Stoichkov, J. Kettle, R. Pereiro, *Talanta* **2019**, *192* 317.

[291] S. H. Cho, J. Byeon, K. Jeong, J. Hwang, H. Lee, J. Jang, J. Lee, T. Kim, K. Kim, M. Choi, Y. S. Lee, *Advanced Energy Materials* **2021**, *11*, 17 2100555, _eprint: https://onlinelibrary.wiley.com/doi/pdf/10.1002/aenm.202100555.

[292] P. Cui, D. Wei, J. Ji, H. Huang, E. Jia, S. Dou, T. Wang, W. Wang, M. Li, *Nature Energy* **2019**, *4*, 2 150.

[293] R. A. Street, S. E. Ready, F. Lemmi, K. S. Shah, P. Bennett, Y. Dmitriyev, *Journal of Applied Physics* **1999**, *86*, 5 2660.

[294] M. I. Saidaminov, A. L. Abdelhady, B. Murali, E. Alarousu, V. M. Burlakov, W. Peng, I. Dursun, L. Wang, Y. He, G. Maculan, A. Goriely, T. Wu, O. F. Mohammed, O. M. Bakr, *Nature Communications* **2015**, *6*, 1 7586, number: 1 Publisher: Nature Publishing Group.

[295] K. Wang, C. Wu, Y. Hou, D. Yang, T. Ye, J. Yoon, M. Sanghadasa, S. Priya, *Energy & Environmental Science* **2020**, *13*, 10 3412, publisher: Royal Society of Chemistry.

[296] Z. Zheng, S. Wang, Y. Hu, Y. Rong, A. Mei, H. Han, *Chemical Science* **2022**, *13*, 8 2167, publisher: Royal Society of Chemistry.

[297] J.-Y. Jeng, Y.-F. Chiang, M.-H. Lee, S.-R. Peng, T.-F. Guo, P. Chen, T.-C. Wen, *Advanced Materials* **2013**, *25*, 27 3727, _eprint: https://onlinelibrary.wiley.com/doi/pdf/10.1002/adma.201301327.

[298] F. D. Giacomo, A. Fakharuddin, R. Jose, T. M. Brown, *Energy & Environmental Science* **2016**, *9*, 10 3007, publisher: Royal Society of Chemistry.

[299] Y. Wang, W. Chen, L. Wang, B. Tu, T. Chen, B. Liu, K. Yang, C. W. Koh, X. Zhang, H. Sun, G. Chen, X. Feng, H. Y. Woo, A. B. Djurišić, Z. He, X. Guo, *Advanced Materials* **2019**, *31*, 35 1902781, _eprint: https://onlinelibrary.wiley.com/doi/pdf/10.1002/adma.201902781.

[300] X. Zhang, J. Ye, L. Zhu, H. Zheng, G. Liu, X. Liu, B. Duan, X. Pan, S. Dai, *Nanoscale* **2017**, *9*, 14 4691.

[301] B. Zhang, J. Su, X. Guo, L. Zhou, Z. Lin, L. Feng, J. Zhang, J. Chang, Y. Hao, *Advanced Science* **2020**, *7*, 11 1903044.

[302] L. Li, J. Mi, Y. Yong, B. Mao, W. Shi, *Journal of Materials Chemistry C* **2018**, *6*, 30 8226.

[303] S. Zhang, J. Su, H. Yuan, Z. Lin, L. Guo, Y. Hao, J. Chang, *Surfaces and Interfaces* **2023**, *43* 103575.

[304] Z. Yuan, Y. Miao, Z. Hu, W. Xu, C. Kuang, K. Pan, P. Liu, J. Lai, B. Sun, J. Wang, S. Bai, F. Gao, *Nature Communications* **2019**, *10*, 1 2818.

[305] T. Burwig, W. Fränzel, P. Pistor, *The Journal of Physical Chemistry Letters* **2018**, *9*, 16 4808, publisher: American Chemical Society.

[306] R. J. Sutton, G. E. Eperon, L. Miranda, E. S. Parrott, B. A. Kamino, J. B. Patel, M. T. Hörantner, M. B. Johnston, A. A. Haghighirad, D. T. Moore, H. J. Snaith, *Advanced Energy Materials* **2016**, *6*, 8 1502458, _eprint: https://onlinelibrary.wiley.com/doi/pdf/10.1002/aenm.201502458.

[307] Q. Ma, S. Huang, S. Chen, M. Zhang, C. F. J. Lau, M. N. Lockrey, H. K. Mulmudi, Y. Shan, J. Yao, J. Zheng, X. Deng, K. Catchpole, M. A. Green, A. W. Y. Ho-Baillie, *The Journal of Physical Chemistry C* **2017**, *121*, 36 19642, publisher: American Chemical Society.

[308] B. A. Rosales, L. E. Mundt, T. G. Allen, D. T. Moore, K. J. Prince, C. A. Wolden, G. Rumbles, L. T. Schelhas, L. M. Wheeler, *Nature Communications* **2020**, *11*, 1 5234, bandiera_abtest: a Cc_license_type: cc_by Cg_type: Nature Research Journals Number: 1 Primary_atype: Research Publisher: Nature Publishing Group Subject_term: Electronic materials;Materials for energy and catalysis;Optical materials and structures Subject_term_id: electronic-materials;materials-for-energy-and-catalysis;optical-materials-and-structures.

[309] J. Cho, P. S. Mathew, J. T. DuBose, P. V. Kamat, *Advanced Materials* **2021**, *33*, 48 2105585, _eprint: https://onlinelibrary.wiley.com/doi/pdf/10.1002/adma.202105585.

[310] W.-G. Choi, D.-W. Kang, S. Na, C.-G. Park, F. P. Gokdemir, T. Moon, *Nanoscale Research Letters* **2018**, *13*, 1 9.

[311] W.-G. Choi, S. Na, C.-G. Park, T. Moon, *Solar Energy* **2019**, *178* 56.

[312] D. Lin, J. Fang, X. Yang, X. Wang, S. Li, D. Wang, G. Xie, H. Li, X. Wang, L. Qiu, *Small* **2023**, *n/a*, n/a 2307960.

[313] M. A. Reinoso, C. A. Otálora, G. Gordillo, *Materials* **2019**, *12*, 9 1394, number: 9 Publisher: Multidisciplinary Digital Publishing Institute.

[314] A. Ng, Z. Ren, Q. Shen, S. H. Cheung, H. C. Gokkaya, G. Bai, J. Wang, L. Yang, S. K. So, A. B. Djurišić, W. W.-f. Leung, J. Hao, W. K. Chan, C. Surya, *Journal of Materials Chemistry A* **2015**, *3*, 17 9223, publisher: The Royal Society of Chemistry.

[315] Z. Li, J. Li, H. Cao, Y. Qian, J. Zhai, Y. Qiu, L. Yang, S. Yin, *ACS Applied Materials & Interfaces* **2021**, *13*, 38 45496.

[316] W. Fan, K. Deng, Y. Shen, Y. Bai, L. Li, *Angewandte Chemie* **2022**, *134*, 42 e202211259.

[317] V. L. Pool, B. Dou, D. G. Van Campen, T. R. Klein-Stockert, F. S. Barnes, S. E. Shaheen, M. I. Ahmad, M. F. A. M. van Hest, M. F. Toney, *Nature Communications* **2017**, *8*, 1 14075, number: 1 Publisher: Nature Publishing Group.

[318] E. J. Juarez-Perez, L. K. Ono, Y. Qi, *Journal of Materials Chemistry A* **2019**, *7*, 28 16912, publisher: Royal Society of Chemistry.

[319] A. Luongo, B. Brunetti, S. Vecchio Ciprioti, A. Ciccioli, A. Latini, *The Journal of Physical Chemistry C* **2021**, *125*, 40 21851.

[320] T. Burwig, P. Pistor, *Physical Review Materials* **2021**, *5*, 6 065405, publisher: American Physical Society.

[321] L. Dong, S. Sun, Z. Deng, W. Li, F. Wei, Y. Qi, Y. Li, X. Li, P. Lu, U. Ramamurty, *Computational Materials Science* **2018**, *141* 49.

[322] C. Wu, Q. Zhang, Y. Liu, W. Luo, X. Guo, Z. Huang, H. Ting, W. Sun, X. Zhong, S. Wei, S. Wang, Z. Chen, L. Xiao, *Advanced Science* **2018**, *5*, 3 1700759, _eprint: https://onlinelibrary.wiley.com/doi/pdf/10.1002/advs.201700759.

[323] F. Igbari, Z.-K. Wang, L.-S. Liao, *Advanced Energy Materials* **2019**, *9*, 12 1803150, _eprint: https://onlinelibrary.wiley.com/doi/pdf/10.1002/aenm.201803150.

[324] M. Wang, P. Zeng, S. Bai, J. Gu, F. Li, Z. Yang, M. Liu, *Solar RRL* **2018**, *2*, 12 1800217, _eprint: https://onlinelibrary.wiley.com/doi/pdf/10.1002/solr.201800217.

[325] Z. Zhang, Q. Sun, Y. Lu, F. Lu, X. Mu, S.-H. Wei, M. Sui, *Nature Communications* **2022**, *13*, 1 3397, number: 1 Publisher: Nature Publishing Group.

[326] L.-Z. Lei, Z.-F. Shi, Y. Li, Z.-Z. Ma, F. Zhang, T.-T. Xu, Y.-T. Tian, D. Wu, X.-J. Li, G.-T. Du, *Journal of Materials Chemistry C* **2018**, *6*, 30 7982, publisher: The Royal Society of Chemistry.

[327] J. A. Steele, W. Pan, C. Martin, M. Keshavarz, E. Debroye, H. Yuan, S. Banerjee, E. Fron, D. Jonckheere, C. W. Kim, W. Baekelant, G. Niu, J. Tang, J. Vanacken, M. Van der Auweraer, J. Hofkens, M. B. J. Roeffaers, *Advanced Materials* **2018**, *30*, 46 1804450, _eprint: https://onlinelibrary.wiley.com/doi/pdf/10.1002/adma.201804450.

[328] B. Yang, W. Pan, H. Wu, G. Niu, J.-H. Yuan, K.-H. Xue, L. Yin, X. Du, X.-S. Miao, X. Yang, Q. Xie, J. Tang, *Nature Communications* **2019**, *10*, 1 1989, number: 1 Publisher: Nature Publishing Group.

[329] T. Abzieher, D. T. Moore, M. Roß, S. Albrecht, J. Silvia, H. Tan, Q. Jeangros, C. Ballif, M. Hoerantner, B.-S. Kim, H. J. Bolink, P. Pistor, J. Christoph Goldschmidt, Y.-H. Chiang, S. D Stranks, J. Borchert, M. D. McGehee, M. Morales-Masis, J. Patel, A. Bruno, U. Wilhelm Paetzold, *Energy & Environmental Science* **2024**.

[330] G. Paul, S. Chatterjee, H. Bhunia, A. J. Pal, *The Journal of Physical Chemistry C* **2018**, *122*, 35 20194, publisher: American Chemical Society.

Acknowledgements

I highly appreciate the opportunity provided for me by Prof. Roland Scheer to work in the Thin Film Photovoltaics research group at the MLU and I am thankful for his guidance and advice which enabled the making of this thesis. I want to express my sincere gratitude towards Dr. Paul Pistor, without whom this thesis would not have been possible. Thank you for your ideas, incentives, insight, commitment and patience - even after moving to Spain. I enjoyed working with Thomas Burwig, who introduced me to most of the experimental setups and to programming with Python and always offered a helping hand. Speaking of which, Dr. Torsten Hölscher cannot be left unmentioned, as the most disruptive experimental problems were solved by his crafty wits. Tobias Schulz, Robert Heidrich and Patrick Wessel were excellent master's students and co-workers and I wish them luck in pursuing their own Phds. I also want to thank Thomas Richter and Ulrich Fahnert for their untiring supply of samples. In addition, Dr. Bodo Fuhrmann and co-workers readily provided their aid at the IZM.

I am very grateful towards Dr. Heiko Kempa for providing a kind and respectful atmosphere for interdisciplinary exchange during meetings, breaks and the frequently organized "Tea Time" with his special tee. I want to thank Dr. Matthias Maiberg for his positivity, moral support and the shared interests, which provided a lot of energy and an enjoyable time. Chris Bluhm, Julia Horstmann, Merve Demir, Chang-Yun Song, Leonard Wägele and other co-workers contributed essential treats to the research group's open-minded and progressive mentality. Outside of the university environment, my family and Laura provided great encouragement. Finally, I want to thank the reviewers and the doctorate committee and hope they find joy engaging themselves in my work just as I found during its making.

Eidesstattliche Erklärung

Hiermit erkläre ich an Eides statt, dass ich, Karl Lukas Heinze, die vorliegende Arbeit "Synthesis and Phase Evolution of Evaporated Lead Halide Perovskites for Solar Cells: From *in situ* Analysis to Optoelectronic Properties" selbstständig und unter ausschließlicher Verwendung der angegebenen Literatur und Hilfsmittel erstellt habe. Alle wörtlichen oder sinngemäßen Zitate sind als solche gekennzeichnet. Die Arbeit wurde bisher in gleicher oder ähnlicher Form keiner anderen Prüfungsbehörde vorgelegt und auch nicht veröffentlicht.

Halle (Saale), den

Karl Lukas Heinze

M.Sc. Karl Lukas Heinze

Sex: Male
Nationality: German

Curriculum Vitae

Academic Education

PhD studies on perovskite solar cells at the MLU in Halle   Since May, 2019

Master's studies in Renewable Energies at the MLU   October, 2016 to April, 2019
  Grade: 1.5

Bachelor's studies in physics at the University of Hamburg   October, 2012 to April, 2016
  Grade: 2.4

Police Record
No previous convictions.

Halle, 1st of February, 2024